HILDE LEA LEIN

MECHANICAL PROPERTIES AND PHASE STABILITY OF OXYGEN PERMEABLE MEMBRANES $La_{0.5}Sr_{0.5}Fe_{1-x}Co_xO_{3-\delta}$

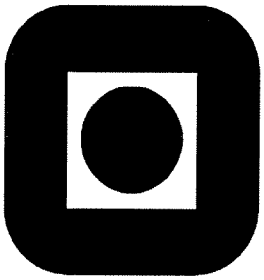

DEPARTMENT OF MATERIALS TECHNOLOGY

NORWEGIAN UNIVERSITY OF SCIENCE AND TECHNOLOGY

NTNU

IMT-REPORT 2005:69, IUK-THESIS 114

FEBRUARY 2005

This thesis has been submitted to

Department of Materials Technology

Norwegian University of Science and Technology

in partial fulfillment of the requirements for

the Norwegian academic degree

DOKTOR INGENIØR

February 2005

PREFACE

First of all, I want to thank my main supervisor Tor Grande for all help and guidance during this work. I'm very grateful for your excellent supervision, and your knowledge and experience have been of invaluable importance for my work. The never-ending enthusiasm, which I especially appreciate, has been a great motivation. And I'm also very thankful for giving me the opportunity to stay four months in US. Next, I want to thank my co-supervisor Kjell Wiik and also Mari-Ann Einarsrud for always being interested and supporting, and for having valuable comments to my work.

I also want to thank Edgar Lara-Curzio for inviting me to Oak Ridge National Laboratory (ORNL), and for all the interest in my work, the helpfulness and useful discussions. I wish to thank the staff at ORNL, especially Laura Riester and Raphalle Satet, for making the stay there fun and unforgettable.

Financial support from The Research Council of Norway, Statoil and Hydro is appreciated.

I will thank all my friends everywhere for support and friendship. And I will thank my colleagues in "Blokk 2", or lately "Blokk 1", for all the relevant and irrelevant discussions, the coffee brakes, outside-work-activities and just for making these years fun.

Finally, I want to thank my dear husband Sigvart and my family for invaluable support, encouragement and believe in what I have been doing.

TABLE OF CONTENT

SCIENTIFIC PAPERS

APPENDICES

LIST OF ACRONYMS

HTXRD	High Temperature X-Ray Diffraction
LSC	$La_{0.5}Sr_{0.5}CoO_{3-\delta}$
LSF	$La_{0.5}Sr_{0.5}FeO_{3-\delta}$
LSF25C75	$La_{0.5}Sr_{0.5}Fe_{0.25}Co_{0.75}O_{3-\delta}$
LSFC	$La_{0.5}Sr_{0.5}Fe_{0.5}Co_{0.5}O_{3-\delta}$
MIEC	Mixed Ionic and Electronic Conductivity
pO_2	Partial Pressure of Oxygen (O_2)
SEM	Scanning Electron Microscopy
SENB	Single Edge Notched Beam
SEVNB	Single Edge V-Notched Beam
SOFC	Solid Oxide Fuel Cell
TEC	Thermal Expansion Coefficient
XRD	X-Ray Diffraction
YSZ	Yttria-Stabilized Zirconia

1 SUMMARY

Ceramic membranes made from mixed oxygen-ionic and electronic conducting perovskite oxides can selectively separate oxygen from air at elevated temperatures. These membranes have several potential applications that require a continuous supply of oxygen. For example, they may be an alternative for cryogenic production of oxygen or alternative electrode materials in solid oxide fuel cells. Of particular significance is the partial oxidation of methane to syngas ($CO + H_2$). By combining air separation and partial oxidation of natural gas into a single step, the need for expensive oxygen production by cryogenic means may be eliminated. Combined with existing processes for gas-to-liquid production such as Fisher-Tropsch and methanol synthesis, the MIEC membrane technology represents a very attractive route for conversion of natural gas to liquid fuels.

The research in this field was initially concerned with the search for materials with the optimum oxygen flux. Today, the long term stability of the membranes is probably the main issue. The membranes have to be stable under operating conditions, which include mechanical stability and chemically compatibility with other materials like sealing and support materials. However, the current understanding of the long term chemical and mechanical reliability is poor and this is one of the major challenges for solid state ionic research. The aim of this work has been to investigate the mechanical properties and the chemical stability of $La_{0.5}Sr_{0.5}Fe_{1-x}Co_xO_{3-\delta}$ ($x = 0, 0.5, 1$) materials when they are exposed to thermal and chemical gradients.

The chemically induced stresses due to reduction of the valence state of the transition metals are of particular importance with respect to the mechanical stability. In paper I, the oxygen non-stoichiometry, investigated by thermo-gravimetrical analysis, and thermal end chemical expansion, studied by dilatometry and high temperature X-ray diffraction, of $La_{0.5}Sr_{0.5}Fe_{1-x}Co_xO_{3-\delta}$ materials are reported. The oxygen deficiency was observed to increase with decreasing partial pressure of oxygen and increasing temperature corresponding to expectations and previous reports. At ambient temperature the thermal expansion coefficient of the materials were in the range 15-$18 \cdot 10^{-6}$ K^{-1}. Above a certain temperature thermal reduction of the material take place, and the thermal expansion coefficient due to chemical expansion raise to 16-$36 \cdot 10^{-6}$ K^{-1}. The chemical expansion ε_c, defined as the linear expansion due to a change in partial pressure of oxygen at constant temperature, reached a maximum in the range 0.036-0.039 for the materials

studied at 800°C. The change in ionic radii of the transition metals is the main contribution to the chemical expansion. The crystal structure of the perovskite materials were shown to be slightly rhombohedral at ambient temperatures and a transition to cubic phase were observed above 300°C.

This non-linear thermal expansion behavior is a major challenge for the applications of the mixed conductor materials. $La_{0.5}Sr_{0.5}Fe_{1-x}Co_xO_{3-\delta}$ membranes in an oxygen partial pressure gradient will have different oxygen deficiency on either side of the membrane. The increasing oxygen deficiency is accompanied by a volume expansion as shown in paper I, and this will lead to chemically induced stresses. These stresses and the failure that might follow can be prevented by creep of the materials. Creep is also important due to dimensional stability. In paper II, the steady-state creep performance under compression of $La_{0.5}Sr_{0.5}Fe_{1-x}Co_xO_{3-\delta}$ ($x = 0.5$, 1) as a function of temperature, atmosphere, load and two different grain sizes is reported. The stress exponent found for the materials was close to unity and an unusual low inverse grain size exponent close to one was found for one of the materials. The activation energy of the two materials was not equal and the influence of secondary phases on the creep was discussed. The obtained creep behavior and microstructural investigation after measurements point to a diffusion related mechanism for the creep. Higher creep rates are found under reducing conditions and this suggest that creep relaxation of mechanical or chemical induced stresses may enhance the mechanical stability of oxygen permeable membranes.

In Paper III, the mechanical properties of $La_{0.5}Sr_{0.5}Fe_{1-x}Co_xO_{3-\delta}$ ($x = 0.5$, 0.75, 1) were investigated by several methods. Fracture strength was measured by four-point bending, fracture toughness was measured by SENB and SEVNB methods and finally Young's modulus were investigated by four-point bending and resonant ultrasound spectroscopy. Four-point bending showed a non-linear ferroelastic behavior at ambient temperature due to rhombohedral crystal structure. Above the ferroelastic to paraelastic transition temperature the materials showed elastic behavior, however, at temperatures from about 800°C a non-elastic respond was observed due to creep. The measured fracture strength and fracture toughness were observed to increase with increasing temperature, which was attributed to frozen-in stress gradients in the materials during cooling due to different oxygen stoichiometry. These stress gradients caused the low fracture strength and fracture toughness at ambient temperature. At higher temperatures, the stresses are assumed to relax resulting in a higher strength and fracture toughness. At high temperature, the non-linear respond made systematic errors in the calculated strength and fracture toughness. The Young's

modulus was measured from four-point bending and by resonant ultrasound spectroscopy for two of the materials. These data obtained by these two different methods were not in good agreement, which demonstrate the difficulty to obtain reliable data for the Young's modulus of such materials by four-point bending. The presented findings have demonstrated the importance of understanding ferroelasticity and chemically induced stresses in order to comprehend the mechanical properties of such mixed valence state perovskite materials.

A high oxygen flux is required in order to realize the oxygen permeable membrane technology. At the same the chemical stability of the materials in a pO_2 gradient must be good for a sufficient long period of time. The oxygen flux performance and the long term stability of $La_{0.5}Sr_{0.5}Fe_{1-x}Co_xO_{3-\delta}$ ($x = 0$, 0.5, 1) are the topics of Paper IV and V. Oxygen fluxes through the membranes are found as a function of oxygen gradient and temperature in a oxygen permeation cell using air and inert gas on each side. The oxygen flux was observed to increase with decreasing pO_2 on the secondary side until the surface exchange became rate limiting and the fluxes reach a constant value. By further increase of the pO_2 gradient, the flux seemed to decrease and this was attributed to the pO_2 dependence of the surface exchange coefficient. The apparent activation energy of the oxygen permeation was in good accordance with previous investigation of similar materials.

After about 5 week of exposure in an oxygen gradient at about 1150°C, the membranes were carefully examined by electron microscopy for evidence for kinetic demixing and decomposition. Dependent of the overall composition of the membrane, different secondary phases were formed at the primary surface of the membrane. For the cobalt containing materials, isolated grains or clusters of grains of cobalt oxide were formed. In case of the $La_{0.5}Sr_{0.5}FeO_{3-\delta}$ membrane, a dense and about 20 μm thick layer of the secondary phase $SrFe_{12}O_{19}$ was formed at the primary side. The overall (La+Sr)/(Fe+Co) ratio was also seen to influence on the phase formed at the primary side. Kinetic demixing was also demonstrated in all the membranes although the metal concentration profiles were not drastically changed from the initial concentrations. The formation of secondary phases was reflected in the (La+Sr)/(Fe+Co) ratio across the membrane. The largest deviation from the nominal stoichiometry was seen close to the surfaces indicating steeper chemical gradients close to the surfaces. These phenomena may strongly limit the long term stability of thinner membranes e. g. films on a porous substrate.

2 INTRODUCTION

2.1 Background

The demand for energy conversion without environmental polluting emissions causes the use of fuel cells more relevant. Large resources of natural gas make a potential to use fuel cells in power production, where electrochemical processes are used to produce electricity.[1-6] This provide many advantages compared to traditional energy conversion systems including high efficiency, reliability, fuel adaptability and low levels of SO_x and NO_x emissions.[1] Solid oxide fuel cells (SOFCs) consist of two porous electrodes separated by a dense pure oxygen-ion-conducting electrolyte, as shown in Figure 1.

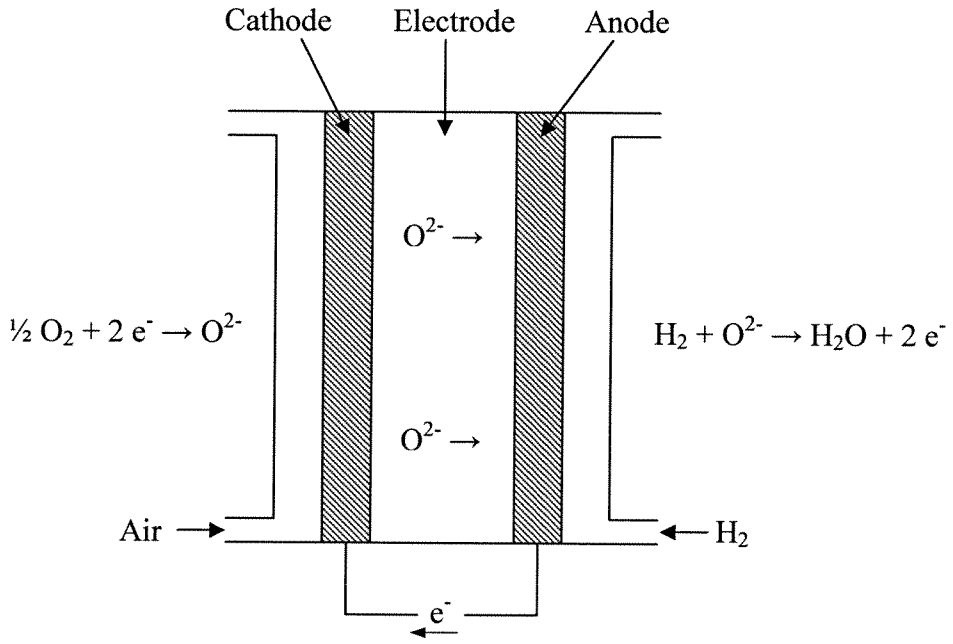

Figure 1: Operating principle of a solid oxide fuel cell. Redrawn from [7].

Such fuel cells convert H_2 to H_2O or CH_4 to CO_2 and H_2O. Oxygen gas flows over the cathode and is reduced to O^{2-} by combining with electrons from the external circuit. The O^{2-} ions diffuse through the solid electrolyte and react with the fuel gas at the anode, and electrons are liberated. Because of the high operating temperatures of typically 800-1000°C, they allow use of fuels such as natural gas without a separate external reformer.[1, 7]

There are numerous designs of SOFCs, e.g. tubular configuration, monolithic solid oxide fuel cells (MSOFCs) and planar (biopolar plate) design.[7-9] For all types of fuel cells, chemical stability, dimensional stability in different atmospheres and match of the thermal expansion coefficients within the different cell components are of importance.[7, 10] Electrolytes should have a high oxygen-ion conductivity, but as low electronic conductivity as possible. The most studied materials belong to the fluorite-type solid solutions MO_2-M'O or MO_2-M''$_2O_3$ where MO_2 is the basis oxide and M'O and M''$_2O_3$ the dopands. Yttria stabilized zirconia (YSZ) is the conventional electrolyte due to high ionic conductivity around operating temperatures and stability in oxidizing and reducing atmospheres.[7] However, Sr and Mg substituted $LaGaO_3$ is a future candidate as electrolyte due to higher oxygen conductivity.[11] Other promising materials are $BaCe_{0.9}Gd_{0.1}O_3$ and $CaAl_{0.7}Ti_{0.3}O_3$,[8] and Gd and Sm doped CeO_2.[12-14] The cathode promotes the reduction of oxygen gas to O^{2-}. Several metals such as Pt and Ag can be used as cathode material, but for SOFC the most commonly used materials are perovskites. The requirements are high electronic conductivity, nonnegligible anionic conductivity and high catalytic activity.[7] These requirements are fulfilled by most of the ABO_3 oxide systems, where A is a rare earth element and B is a transition metal (Fe, Ni, Co, Mn). In most cases, alkaline earth elements (Sr^{2+}, Ca^{2+}) are partially substituted at A site and various transition metals can be used simultaneous at B site, increasing the ionic and electronic conductivity.[7] $La_{1-x}Sr_xMnO_{3-\delta}$ materials are some of the most common cathode materials, but $La_{1-x}Sr_xCoO_{3-\delta}$ are also of interest.[15-16] Sr and Fe substituted $LaFeO_3$ materials also have properties which make them potential candidates as cathodes.[17-21] Anode materials require high stability in reducing atmosphere. Transition metals are best candidates due to high catalytic activity. However, the difference in thermal expansion coefficient between these metals and the electrolyte can make problems for porous metal layers during thermal cycling. Instead, fine-grained metal-YSZ cermets are sintered on the electrolyte surface. Ni is the most common metal followed by Fe and Ru.[7, 22] Interconnection materials are necessary to combine single cells to form stacks by connecting the cathode material of one cell to the anode material of the adjacent cell. Of special requirements are matching thermal expansion

coefficients (TEC) to the other cell components, resistance to thermal shock and gas tightness.[7] The most significant interconnect material is doped $LaCrO_3$. However, challenges are related to both the sintering[23] and to optimize the thermal expansion to avoid cracking during cycling.[6]

Even though there have been going on research on SOFCs for several decades there are still challenges with respect to materials technology. At present it is a drive to lower the operation temperature in order to utilize metallic interconnects instead of $LaCrO_3$ based materials. Lower operation temperature is only possible if also the electrolyte becomes thinner, and cells based on films in the range of microns supported by porous support are the state of the art cell design.[24-34] Lower operation temperature will also demand new electrode materials, particularly on the air side. With the new SOFC design, the mechanical performance of both the electrolyte and the porous support, which could be one of the electrode materials, becomes even more important.

Dense membranes with mixed oxygen ionic and electronic conductivity are receiving considerable attention due to possible applications for oxygen separation and partial oxidation.[7, 35-40] Separation of oxygen using a mixed ionic and electronic (MIEC) membrane is shown in Figure 2. The driving force for oxygen transport is the difference in oxygen partial pressure across the membrane. Since the MIEC membrane is dense and gas tight, the oxygen ions migrate selectively through the membrane. Dissociation and ionization of oxygen occurs at the high pO_2 surface, and the oxygen ions recombine to oxygen molecules at the low pO_2 side. The flux of oxygen ions is charge compensated by a simultaneous flux of electrons and holes. Thus, the MIEC membrane can operate without attachment of electrodes and external circuitry. The oxygen permeation rate is either controlled by the rate of solid state diffusion within the bulk or the oxygen exchange in either side of the membrane. In the bulk controlled regime, the flux will increase with increasing pO_2 gradient and decreasing membrane thickness. Below a characteristic thickness, L_c, the flux becomes controlled by surface exchange reactions.[7]

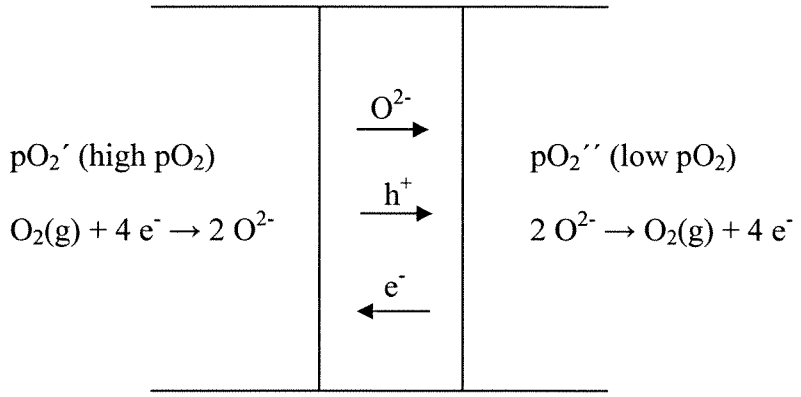

Figure 2: Principle of an oxygen permeable membrane in a pO_2 gradient.

Materials with oxygen-deficient perovskite and perovskite related structures have received much attention for the development of mixed conductors and new solid electrolytes. High fluxes in compositions like $La_{1-x}A_xCo_{1-y}B_yO_{3-\delta}$ (A = Sr, Ba, Ca and B = Fe, Cu, Ni) have widely been reported,[17,41-49] and these compositions are candidate materials for oxygen permeable membranes. Some of the challenges associated with MIEC materials are to achieve a sufficient oxygen permeation flux at an attractive temperature, the sealing to a support material and the long-term thermal and chemical stability. The oxygen fluxes can be improved by using thin film membranes, typically less than 25 μm thick,[32] due to reduced diffusional transport resistance. For sufficient mechanical stability, such membranes must be supported on a porous substrate. Thin dense layers of La-Sr-Fe-Co based perovskites have been deposited on porous support of MgO, Al_2O_3 or similar perovskites by tape casting, sputtering, vapor deposition or different coating methods.[12, 28, 30, 40, 50-53] The chemical gradient across membranes may lead to cation demixing and decomposition, and thin membranes give rise to faster degradation. This may degrade the membranes within the expected operating time. In addition, stresses on each side of the membrane due to a gradient in oxygen vacancy concentration might lead to failure.[54] Knowledge of mechanical properties such as fracture strength, fracture toughness and creep resistance is therefore essential.

2.2 Aim of the work

The aim of the present work has been to establish a fundamental understanding of chemical and mechanical degradation of $La_{0.5}Sr_{0.5}Fe_{1-x}Co_xO_{3-\delta}$ materials when they are exposed to thermal and chemical gradients. The specific chemical composition was chosen in order to give a cubic perovskite at ambient temperatures. It turned out that they were slightly rhombohedral and this gave an effect on the mechanical properties as shown in the thesis. The materials used in the study were also chosen due to their high electronic and ionic conductivity, and are of particular interest for oxygen separation at high temperatures. In such applications the materials will operate in an oxygen partial pressure gradient, and the influence of this gradient on the materials will be of particular importance. Chemical, thermal and mechanical stability of the materials are important for the utilization of such devices. They must be chemical compatible with supports, tolerate thermal cycling and have sufficient mechanical properties. Considerable mechanical stresses may be present due to chemically induced stresses and gradients in the oxygen activity across the membranes. Even small deviations from the nominal A:B ratio of 1:1 may cause formation of secondary phases, which can affect the properties.

The gradient in the chemical potential across the materials results in a gradient in the oxygen non-stoichiometry, accompanied by a gradient in chemical expansion due to changes in the unit cell volumes on the different sides. This difference causes a chemically induced stress and might lead to failure due to creep, kinetic demixing or fracture. To find clarify the effect of expansion at different temperatures and environments, the oxygen vacancy concentrations, thermal and chemical expansions of $La_{0.5}Sr_{0.5}Fe_{1-x}Co_xO_{3-\delta}$ ($x = 0$, 0.5, 0.75 and 1) materials in different atmospheres have been investigated as a function of temperature (Paper I).

High creep resistance is important for the dimensional stability of the devices. Creep relaxation may also to some extent be beneficial to avoid failure. For this reasons the creep performance of the materials in various atmospheres is of importance. Creep rates for $La_{0.5}Sr_{0.5}Fe_{1-x}Co_xO_{3-\delta}$ ($x = 0.5$ and 1) materials have been investigated as a function of load, temperature, atmosphere and grain size. The results give information of the mechanisms for creep and hence the dimensional stability (Paper II). Creep data are also of fundamental importance for the understanding of cation diffusion in the materials.

One of the main challenges for the applications is to prevent mechanical failure during fabrication and operation, and knowledge of mechanical properties is essential. Of special importance are the mechanical properties at operation temperatures, due to the desired long lifetime and estimation of reliability. The fracture strength, fracture toughness and Young's modulus have been investigated at room temperature and at elevated temperatures for $La_{0.5}Sr_{0.5}Fe_{1-x}Co_xO_{3-\delta}$ (x = 0.5, 0.75 and 1) materials (Paper III).

The physical and the chemical properties are controlled through the composition. For a material in a pO_2 gradient, kinetic demixing can occur due to cation diffusion and this can lead to degradation since local composition changes, secondary phases and perhaps morphological changes may destroy the functionality of the materials and give rise to a decrease in the lifetime. The understanding of the demixing process is of great fundamental and practical importance due to prediction of the durability and reliability of materials. Here, oxygen permeation has been investigated as a function of pO_2 gradient and temperature for $La_{0.5}Sr_{0.5}Fe_{1-x}Co_xO_{3-\delta}$ (x = 0, 0.5 and 1) materials (Paper IV). Formation of new phases on the surfaces after long time in a pO_2 gradient and cation demixing of the same materials have also been demonstrated, and this data is presented in Paper V.

2.3 The perovskite structure

Perovskites have the general formula ABO_3. The ideal structure consists of a cubic array of corner-sharing BO_6 octahedra where B often is a transition metal. The A cation is 12-coordinated to the anions and interstitial between the BO_6 octahedra. A is an alkali metal, an alkali earth metal or a rare earth ion.[7] The perovskite structure is shown in Figure 3a).

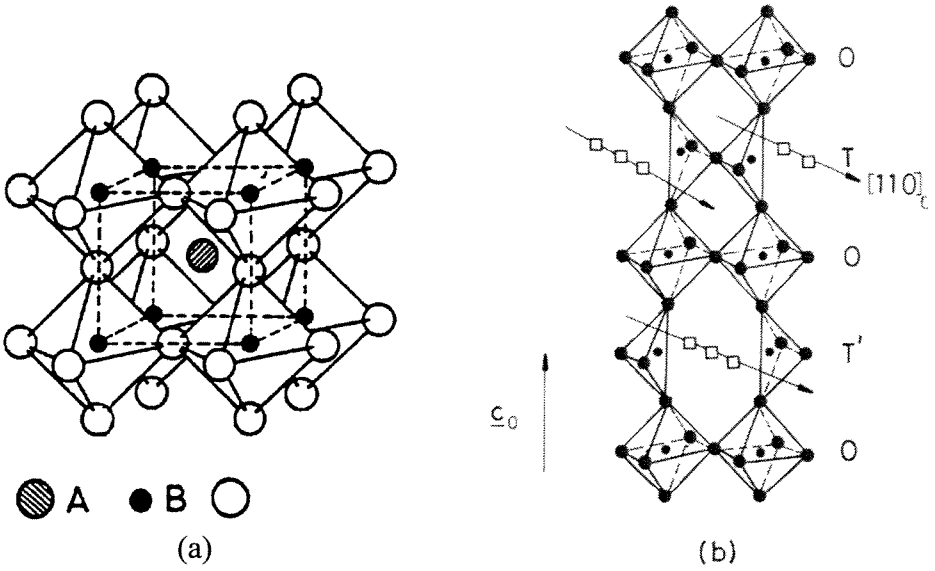

(a) (b)

Figure 3: a) The cubic perovskite structure and b) the brownmillerite structure.[55]

Different oxidation states for the cations are possible in the perovskite structure, e.g. $A^{I}B^{V}O_3$, $A^{II}B^{IV}O_3$ or $A^{III}B^{III}O_3$, where the sum of the valences of A and B cations is six. In many cases, the BO_6 octahedra are tilted or rotated due to the presence of a "small" A cation,[7] reducing the symmetry to tetragonal, orthorhombic or rhombohedral. The tolerance limits of the cationic radii are defined by the Goldsmidt factor, t, which is based on geometric considerations

$$t = \frac{r_A + r_B}{\sqrt{2(r_B + r_O)}} \tag{1}$$

where r_A, r_B and r_O are the radii of the respective ions.[7] Nominally the perovskite structure is stable between $1.05 < t < \sim 0.75$.[55] The ideal cubic perovskite lattice exists only for t close to 1, whereas the less symmetric perovskites have $t \neq 1$.

Non-stoichiometry is common in perovskite materials, and can arise from cation deficiency at A or B site, oxygen deficiency or oxygen excess.[55] Anion vacancy is more common than vacancies at cation sites, and the non-stoichiometry is usually written as $ABO_{3-\delta}$ according to the reaction

$$ABO_3 \rightarrow ABO_{3-\delta} + \frac{\delta}{2} O_2(g) \qquad (2)$$

Oxygen deficient perovskites are the most common, but metal deficient materials like $LaMnO_{3+\delta}$ are also known. Since the oxygen non-stoichiometry is determined by the sum of the valence state of the cations, δ can be increased by substituting a lower valent cation on A or B site. The oxygen ion conduction will be enhanced by increasing the oxygen deficiency. If B is a transition metal, its valence state will be temperature and oxygen partial pressure dependent. Changes in the valence state of transition metals will be compensated by a change in the non-stoichiometry. When $\delta = 0.5$, the brownmillerite structure may be formed, see Figure 3b), where one-sixth of anion sites are vacant. The oxygen vacancies are ordered in such a way that alternating layers of octahedral (O) and tetrahedral (T, T') coordinated B-cations are formed.[55] Other ordered structures are known with different numbers of octahedra between the tetrahedral layers. Many perovskite materials may order at low temperatures or at low partial pressures of oxygen. In $La_{1-x}Sr_xFeO_{3-\delta}$ several vacancy-ordered structures are known belonging to the series $A_nB_nO_{3n-1}$ ($n = 2, 3, 4, 8$).[56, 57]

Dann et al.[58] have investigated the crystal structure of $La_{1-x}Sr_xFeO_{3-\delta}$ ($0 \leq x \leq 1$, $0 \leq \delta \leq 0.5$) at room temperature. They found a cubic symmetry for $0.8 \leq x \leq 1$, rhombohedral symmetry for $0.4 \leq x \leq 0.7$ and orthorhombic symmetry for $0 \leq x \leq 0.2$. $La_{1-x}Sr_xCoO_{3-\delta}$ is rhombohedral for $0 \leq x \leq 0.5$ and cubic in the range $0.55 \leq x \leq 0.7$ at room temperature, according to Mineshige et al.[59] By increasing the temperature, most of the non-cubic perovskites go through a phase transition to a structure with higher symmetry. The tilting or deformation of the oxygen octahedra becomes unstable because of lattice vibrations. Fossdal et al.[60] found by high temperature x-ray diffraction a rhombohedral to cubic phase transition at 250 ± 50°C for $La_{0.5}Sr_{0.5}FeO_{3-\delta}$. $La_{0.5}Sr_{0.5}CoO_{3-\delta}$ has a rhombohedral angle of 60.1 at room temperature[59] and a phase transition to cubic symmetry at relative low temperature is expected.

The properties of the perovskite materials are controlled by the compositions. The magnetic properties vary between ferro-, antiferro- and paramagnetic, while the electrical properties vary between metallic, semi-conducting and insulating.

The total conductivity is the sum of the electrical-, hole- and ionic conductivity. The pO_2 dependence of the electrical conductivity for $La_{0.6}Sr_{0.4}Co_{0.2}Fe_{0.8}O_3$ at different temperatures is given in Figure 4.

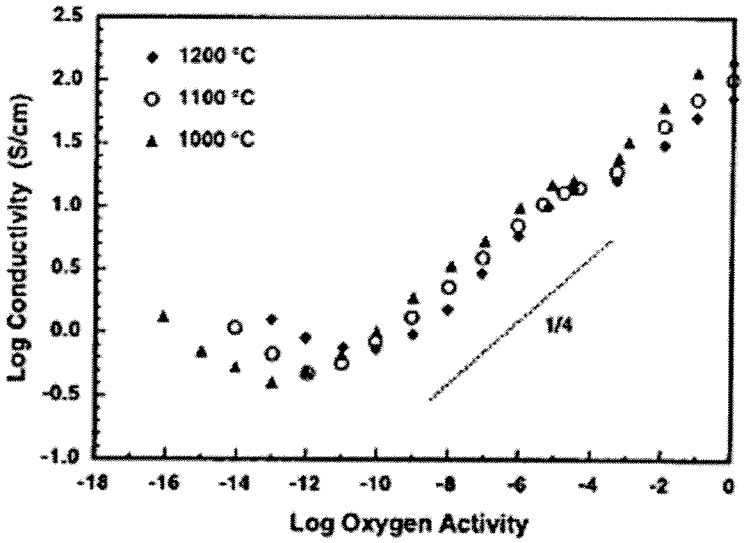

Figure 4: Electrical conductivity of $La_{0.6}Sr_{0.4}Co_{0.2}Fe_{0.8}O_3$ at different temperatures as a function of oxygen activity.[61]

On the high pO_2 side of the conductivity minimum, the materials exhibit p-type conductivity. On the low pO_2 side of the minimum, there is n-type conductivity.

The ionic conductivity is related to the defect chemistry since it depends on the concentration of oxygen vacancies. By increasing the temperature or reducing the oxygen partial pressure, the oxygen vacancy concentration will increase according to equation (2). The non-stoichiometry of $La_{0.3}Sr_{0.7}CoO_{3-\delta}$ as a function of pO_2 at different temperatures is shown in Figure 5.

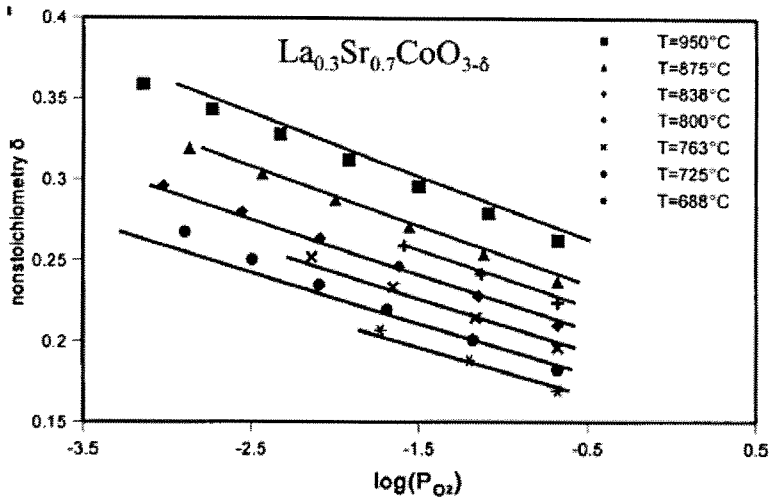

Figure 5: Plot of the oxygen non-stoichiometry, δ, in $La_{0.3}Sr_{0.7}CoO_{3-\delta}$ as a function of log pO_2 at different temperatures.[62]

2.4 Thermal and chemical expansion

Thermal expansion is the relative change in dimension as the temperature is increased or decreased due to anharmonic vibrations. Thermal expansion data are usually reported as the linear thermal expansion coefficient α defined as

$$\alpha = \frac{\Delta l / l_o}{\Delta T} \tag{3}$$

where Δl is the change in length from the length at ambient temperature, l_o, and ΔT is the change in temperature.[63] α is for most compositions positive and near linear with increasing temperature. The magnitude of α for perovskite materials at room temperature spans over a wide range. Typical values for $LaMO_3$ (M = transition metal) are between 7 and $30 \cdot 10^{-6}$ K^{-1} where the cobaltites have the highest values.[60, 64-75] By plotting data for $La_{1-x}Sr_xMO_3$ compositions as a function of Sr-doping on A-site with the B cation constant, there will be a clear increasing tendency with increasing doping concentration.[8, 70, 76-81] The same is seen for Co-doping on B-site in $La_{0.8}Sr_{0.2}Fe_{1-x}Co_xO_3$ [78] and $LaCr_{1-x}Co_xO_3$.[82] Here the thermal expansion is

close to linear with the substitution level. All these literature data are summarized in Figure 6.

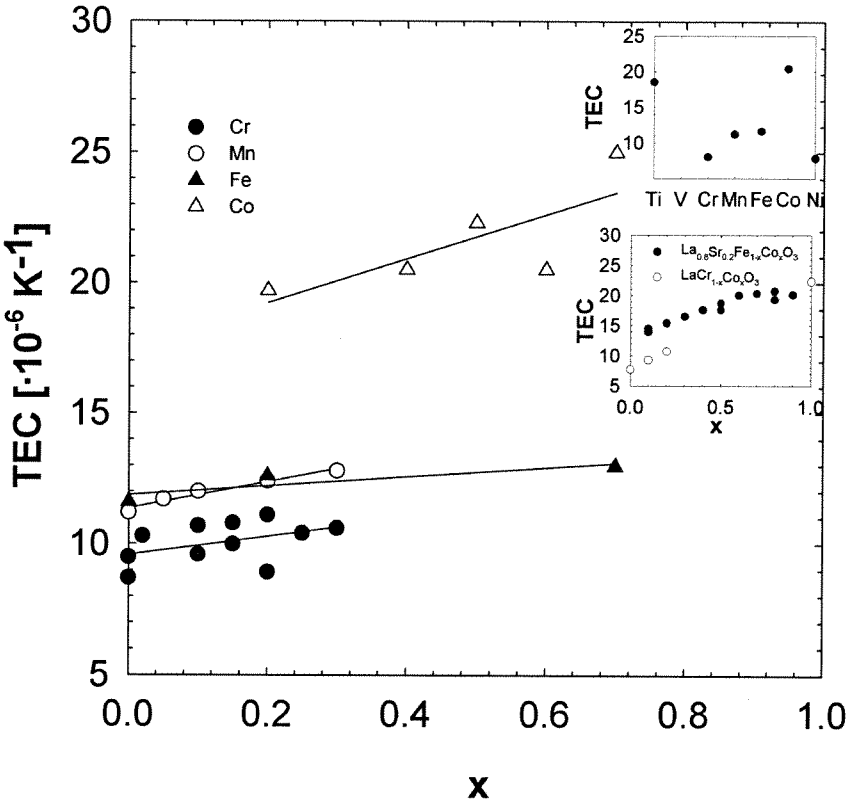

Figure 6: Thermal expansion coefficients (TEC) for $La_{1-x}Sr_xMO_3$ found in literature.[8, 70, 76-81] The upper small plot shows TEC for $LaMO_3$ as a function of position in the periodic table.[60, 64-75] The other small plot shows the relationship of Co-doping on B-site in $La_{0.8}Sr_{0.2}Fe_{1-x}Co_xO_3$ [78] and $LaCr_{1-x}Co_xO_3$.[82]

The oxygen deficiency in $La_{1-x}Sr_xFe_{1-y}Co_yO_{3-\delta}$ materials increases with increasing temperature and decreasing partial pressure of oxygen[7] according to the reaction

$$La_{1-x}Sr_xFe_{1-y}Co_yO_{3-\delta} \rightarrow La_{1-x}Sr_xFe_{1-y}Co_yO_{3-\delta'} + \frac{\delta' - \delta}{2}O_2(g) \qquad (4)$$

The gradual increase in the oxygen deficiency (δ) is accompanied by an expansion due to change in the unit cell volume with decreasing valence state of the transition metals. The trivalent and divalent cation are larger compared to the four-valent.[83] A weakening of the ionic bonds caused by removal of charged species will also contribute. This additional expansion is called chemical expansion. The contribution of chemical expansion to the thermal expansion is illustrated in Figure 7.

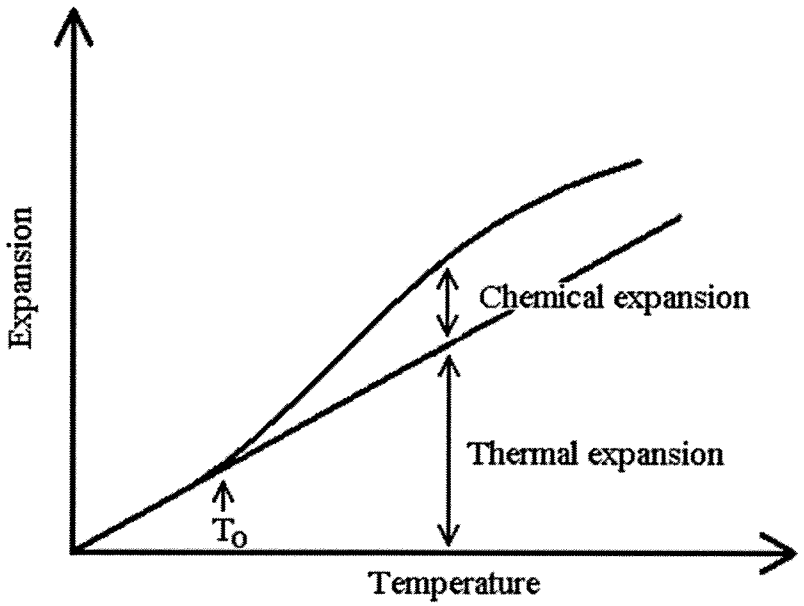

Figure 7: The contribution of chemical expansion to the thermal expansion. The onset of thermal reduction is T_o.

Above the onset temperature for reduction, T_o, the chemical expansion will contribute to a larger total thermal expansion coefficient until a maximum followed by a drop when all B cations are in the reduced state. This increase in thermal expansion coefficient above T_o has been shown for both $La_{1-x}Sr_xFeO_{3-\delta}$ [18, 84] and $La_{1-x}Sr_xCoO_{3-\delta}$ [62, 85-88] materials in addition to $La_{1-x}Sr_xFe_{1-y}Co_yO_{3-\delta}$.[78] The phenomenon is inherent for all mixed-valence materials forming oxygen vacancies by reducing the cations. Expansion coefficients at different temperatures for selected perovskite materials are given in Table 1.

Table 1: Thermal expansion coefficient, α, for some perovskite materials in air at room temperature (RT) and higher temperatures.

Material	$\alpha \cdot 10^{-6}$ [K^{-1}]	Temperature range [°C]	Ref
$LaCrO_3$	7.7	RT	82
$LaCr_{0.9}Co_{0.1}O_3$	9.3	rt	82
$LaCr_{0.8}Co_{0.2}O_3$	10.7		82
$LaCoO_3$	22.3		82
$La_{0.8}Sr_{0.2}Fe_{0.9}Co_{0.1}O_3$	14.5	200-900	78
$La_{0.8}Sr_{0.2}Fe_{0.8}Co_{0.2}O_3$	15.4	100-800	78
$La_{0.8}Sr_{0.2}Fe_{0.7}Co_{0.3}O_3$	16.5	100-900	78
$La_{0.8}Sr_{0.2}Fe_{0.6}Co_{0.4}O_3$	17.6	100-900	78
$La_{0.8}Sr_{0.2}Fe_{0.5}Co_{0.5}O_3$	18.7	100-900	78
$La_{0.8}Sr_{0.2}Fe_{0.4}Co_{0.6}O_3$	20.0	100-900	78
$La_{0.8}Sr_{0.2}Fe_{0.3}Co_{0.7}O_3$	20.3	100-900	78
$La_{0.8}Sr_{0.2}Fe_{0.2}Co_{0.8}O_3$	20.7	100-900	78
$La_{0.8}Sr_{0.2}Fe_{0.1}Co_{0.9}O_3$	20.1	100-900	78
$LaFeO_3$	11.6	200-420	60
$LaFeO_3$	10.9	480-920	60
$SrFe_{0.5}Co_{0.5}O_{3-\delta}$	18	27-477	89
$SrFe_{0.5}Co_{0.5}O_{3-\delta}$	33	527-827	89
$La_{0.3}Sr_{0.7}CoO_{3-\delta}$	19.6	27-367	45
$La_{0.3}Sr_{0.7}CoO_{3-\delta}$	28.8	367-747	45
$La_{0.5}Sr_{0.5}FeO_{3-\delta}$	16.9	20-400	90
$La_{0.5}Sr_{0.5}FeO_{3-\delta}$	18.4	700-1000	90
$La_{0.5}Sr_{0.5}Fe_{0.5}Co_{0.5}O_{3-\delta}$	16.9	20-400	90
$La_{0.5}Sr_{0.5}Fe_{0.5}Co_{0.5}O_{3-\delta}$	28.6	700-1000	90
$La_{0.5}Sr_{0.5}CoO_{3-\delta}$	17.9	20-400	90
$La_{0.5}Sr_{0.5}CoO_{3-\delta}$	30.7	700-1000	90

The chemical expansion can be represented by the linear strain, ε_c, and quantified or normalized by $\varepsilon_c/\Delta\delta$ [91] where

$$\varepsilon_c = \frac{L - L_0}{L_0} \tag{5}$$

Here, $\Delta\delta$ and $L\text{-}L_o$ are the change in oxygen deficiency and cell parameter between two partial pressures of oxygen at constant temperature. For materials containing different transition metal ions, the normalized chemical strain is expected to vary. The chemical expansion of perovskite materials

containing Co and Fe is significantly larger than for similar materials containing Cr. CeO_2 based materials, on the other hand, have significantly larger chemical expansion than perovskite based materials. Reported data in the literature are summarized in Table 2.

Table 2: Chemical expansion for different compositions found in the literature.

Composition	ε_c	$\Delta\delta$	$\varepsilon_c/\Delta\delta$	Temp[°C]	Ref.
$La_{0.5}Sr_{0.5}FeO_{3-\delta}$	0.0058	0.097	0.059	800	[60]
$La_{0.5}Sr_{0.5}Fe_{0.5}Co_{0.5}O_{3-\delta}$	0.0045	0.116	0.039	800	[90]
$La_{0.5}Sr_{0.5}Fe_{0.5}Co_{0.5}O_{3-\delta}$	0.0043	0.122	0.036	1000	[90]
$La_{0.5}Sr_{0.5}CoO_{3-\delta}$	0.0041	0.116	0.035	800	[90]
$La_{0.7}Ca_{0.3}CrO_{3-\delta}$	0.0036	0.101	0.036	1000	[92]
$La_{0.7}Ca_{0.3}Cr_{0.9}Al_{0.1}O_{3-\delta}$	0.0040	0.118	0.034	1000	[92]
$La_{0.6}Sr_{0.4}Fe_{0.2}Co_{0.8}O_{3-\delta}$	0.0039	0.180	0.022	800	[80]
$La_{0.8}Sr_{0.2}Cr_{0.97}V_{0.03}O_{3-\delta}$	0.0013	0.044	0.030	1000	[93]
$La_{0.3}Sr_{0.7}FeO_{3-\delta}$	0.0040	0.125	0.032	875	[79]
$La_{0.7}Sr_{0.3}Fe_{0.6}Ga_{0.4}O_{3-\delta}$	0.0015	0.035	0.044	875	[79]
$LaMnO_{3+\delta}$			0.024	700	[94]
$La_{0.8}Sr_{0.2}CrO_{3-\delta}$			0.024	1000	[93]
$Ce_{0.9}Gd_{0.1}O_{1.95-\delta}$	0.0090	0.18	0.050	1000	[91]
$Ce_{0.8}Gd_{0.2}O_{1.95-\delta}$	0.0112	0.17	0.066	1000	[91]

The thermal and chemical expansion and their temperature dependency are important due to connection to sealing and support materials in practical applications. Mismatch will cause stresses which may lead to cracking or delamination. Sealant materials such as $CaSiO_3$, $SrSiO_3$ and other Si-based glasses have thermal expansion coefficients in the range $9\text{-}14\cdot10^{-6}\ K^{-1}$ [95] while supports as Al_2O_3, MgO, stabilized ZrO_2 and $LaCrO_3$ have thermal expansion coefficients in the range $7\text{-}10\cdot10^{-6}\ K^{-1}$.[63, 68] Stresses caused by chemical expansion, may be allowed to relax during bending or extension depending on membrane geometry.[96] Otherwise, this may lead to damage and failure of the device.

2.5 Fracture strength, toughness and E-modulus

In solid oxide fuel cells, oxygen permeable membranes and high temperature electrochemical devices, the mechanical properties of the

materials are important. One of the main challenges for these applications is to prevent mechanical failure during operation, and the knowledge of mechanical properties is particularly important. Of specially importance are the mechanical properties of the materials at operation temperatures due to expected lifetime and estimation of reliability. Among the mechanical properties of interest are fracture strength, fracture toughness, Young's modulus and creep resistance.

Fracture strengths of perovskite materials found in literature are summarized in Table 3.

Table 3: Fracture strength for perovskite materials at room temperature (RT) and elevated temperatures.

Material	Strength at RT [MPa]	Strength at high T [MPa]	Test method	Ref.
$LaFeO_3$	202±18	235±38 (800°C)	4-point	97
$LaCoO_3$	53‡	~50‡ (850°C)	4-point	98
$La_{0.5}Sr_{0.5}CoO_{3-\delta}$	138±12	181±18 (800°C)	4-point	99
$La_{0.8}Sr_{0.2}CoO_3$	76‡	~57‡ (850°C)	4-point	98
$La_{0.5}Sr_{0.5}Fe_{0.5}Co_{0.5}O_{3-\delta}$	121±7	181±13 (800°C)	4-point	99
$La_{0.5}Sr_{0.5}Fe_{0.25}Co_{0.75}O_{3-\delta}$	71±7	61±20 (400°C) 121±11 (600°C) 120±11 (800°C)	4-point	99
$La_{0.8}Sr_{0.2}Fe_{0.8}Co_{0.2}O_3$	165	-	biaxial#	100
$La_{0.6}Sr_{0.4}Fe_{0.8}Co_{0.2}O_3$	155	-	biaxial#	100
$La_{0.4}Sr_{0.6}Fe_{0.8}Co_{0.2}O_3$	50*	-	biaxial#	100
$La_{0.2}Sr_{0.8}Fe_{0.8}Co_{0.2}O_3$	40*	-	biaxial#	100
$La_{0.8}Sr_{0.2}CrO_3$	49	67 (800°C)	biaxial	101
$La_{0.7}Sr_{0.3}CrO_3$	234	-	3-point	102
$La_{0.8}Ca_{0.2}CoO_3$	150	~63 (850°C)	4-point	98
$La_{0.75}Ca_{0.25}CrO_3$	122±26	~60 (800°C)	4-point	103
$La_{0.7}Ca_{0.3}CrO_3$	256	-	3-point	102
$La_{0.2}Sr_{0.8}Cr_{0.2}Fe_{0.8}O_3$	340	113 (1000°C) 178 (1000°C, 10^{-4}atm) 109 (1000°C, 10^{-12}atm)	C-ring	104, 105
$La_{0.8}Sr_{0.2}Cr_{0.2}Fe_{0.8}O_3$	243	-	biaxial#	106
$La_{0.6}Sr_{0.4}Cr_{0.2}Fe_{0.8}O_3$	138	-	biaxial#	106
$La_{0.7}Sr_{0.3}Cr_{0.8}Co_{0.2}O_3$	230	-	4-punkt	107
$La_{0.975}Ca_{0.025}CrO_3$ + 20wt% Y_2O_3	~170	~90 (1000°C)	4-point	108

Table 3: (continued) Fracture strength for perovskite materials at room temperature (RT) and elevated temperatures.

Material	Strength at RT [MPa]	Strength at high T [MPa]	Test method	Ref.
$La_{0.5}Sr_{0.5}MnO_3$	78	59 (200°C) 109 (400°C) 171 (600°C) 188 (700°C) 200 (800°C)	4-point	[109]
$La_{0.875}Sr_{0.125}MnO_3$	164	109 (400°C) 150 (800°C) 222 (1000°C)	3-point	[110]
$La_{0.5}Sr_{0.5}Mn_{0.96}Co_{0.04}O_3$	38	59 (300°C) 142 (450°C) 115 (600°C) 115 (750°C)	4-point	[109]
$LaCr_{0.9}Mg_{0.1}O_3$	140	247 (125°C) 87 (1000°C)	4-point	[111]
$La_{0.9}Sr_{0.1}Ga_{0.8}Mg_{0.2}O_3$	162±14	55±11 (900°C)	biaxial[#]	[112]
$La_{0.8}Sr_{0.2}Ga_{0.85}Mg_{0.15}O_3$	139±17	-	3-point	[113]

[‡] Materials with 10-13% porosity
[*]The materials showed extensive cracking after sintering
[#]Ball-on-ring geometry

The temperature dependency of the fracture strength is influenced by the crystal structure and phase transitions. For cubic and rhombohedral materials, the fracture strength is decreasing with increasing temperature.[98, 112, 114-115] The opposite has been reported in some cases, but this behavior is likely because of creep in the materials at high temperature, causing a non-elastic behavior and systematic errors in the measurements. Creep during four-point bending will give rise to overestimation of the strength. In addition, a loss of ferroelastic behavior at high temperatures could cause a reduction in the strength. Built-in stress gradients in the materials during cooling due to different oxygen stoichiometry can also affect the low temperature values.[99]

High fracture toughness increases the resistance with respect to crack-initiations and propagation, a necessity for practical use of the materials.

Fracture toughness of different perovskite materials found in literature is given in Table 4.

Table 4: Fracture toughness (K_{1C}) for perovskite materials at room temperature (RT) and higher temperatures.

Material	K_{1C} at RT [MPa·m$^{1/2}$]	K_{1C} at high T [MPa·m$^{1/2}$]	Test method	Ref.
$LaFeO_3$	2.5	2.2 (400°C) 3.1 (800°C)	SENB	97
$LaCoO_3$	1.3	-	SEVNB	116
$La_{0.8}Ca_{0.2}CoO_3$	2.2	1.0 (800°C)	SEVNB	116
$La_{0.5}Sr_{0.5}CoO_{3-\delta}$	1.5±0.3	2.9±0.4 (800°C)	SENB	99
$La_{0.5}Sr_{0.5}Fe_{0.5}Co_{0.5}O_{3-\delta}$	1.3±0.1	-	SENB	99
	1.2±0.1	1.5±0.2 (800°C)	SEVNB	
		2.3±0.2 (1000°C)	SEVNB	
$La_{0.8}Sr_{0.2}Co_{0.2}Fe_{0.8}O_3$	1.5	-	Vickers	117
$La_{0.2}Sr_{0.8}Co_{0.2}Fe_{0.8}O_3$	1.0-1.1	-	Vickers	117
$La_{0.2}Sr_{0.8}Cr_{0.2}Fe_{0.8}O_3$	0.9±0.3	0.1±0.015 (1000°C) 0.14±0.01 (1000°C, 10^{-4}atm) 0.12±0.012 (1000°C, 10^{-12}atm)	C-ring	104,105
$La_{0.975}Ca_{0.025}CrO_3$ + 20wt% Y_2O_3	2.1	1.9 (1000°C)	SENB	108
$La_{0.9}Sr_{0.1}Ga_{0.8}Mg_{0.2}O_3$	2.0-2.2	0.75 (600°C)	SENB	118
$LaCr_{0.9}Mg_{0.1}O_3$	2.8	3.9 (125°C) 1.9 (1000°C)	SENB	111

The temperature variations are in correspondence with the fracture strength. It is assumed that creep of the materials will influence the temperature dependency in the same way as for the fracture strength.

The Young's modulus will generally decrease with increasing temperature.[119-121] There are different techniques for determination of the Young's modulus in a material. A simple technique is the four-point bending by calculating the E-modulus from the slope of the stress-strain behavior.[63, 119] However, it is difficult to achieve good accuracy in determination of elastic constants by static methods.[119] Dynamic methods like resonance and ultrasonic wave propagation can give an order of magnitude greater accuracy. Young's modulus of perovskite materials found in literature obtained by different methods is given in Table 5.

Table 5: Young's modulus (E) for perovskite materials at room temperature (RT) and higher temperatures measured by different test methods, a. o. 4-point bending (4PB), resonant ultrasound spectroscopy (RUS).

Material	E at RT [GPa]	E at high T [GPa]	Test method	Ref.
$LaFeO_3$	213±14	206±24 (800°C)	4PB	97
$La_{0.5}Sr_{0.5}Fe_{0.5}Co_{0.5}O_{3-\delta}$	131±1	130±1 (800°C)	RUS	99
$La_{0.5}Sr_{0.5}CoO_{3-\delta}$	135±1	135 (800°C 126 (1000°C)	RUS	99
$LaCoO_3$	83±3$^{\$}$	-	4PB	98
$La_{0.8}Sr_{0.2}CoO_3$	86±13$^{\$}$	-	4PB	98
$La_{0.8}Ca_{0.2}CoO_3$	112±3	-	4PB	98
$La_{0.8}Sr_{0.2}Fe_{0.8}Co_{0.2}O_3$	161±2	-	Ultrasonic/ pulse-echo	100
$La_{0.6}Sr_{0.4}Fe_{0.8}Co_{0.2}O_3$	152±3	-	Ultrasonic/ pulse-echo	100
$La_{0.4}Sr_{0.6}Fe_{0.8}Co_{0.2}O_3$	167±9	-	Ultrasonic/ pulse-echo	100
$La_{0.2}Sr_{0.8}Fe_{0.8}Co_{0.2}O_3$	188±6	-	Ultrasonic/ pulse-echo	100
$BaTiO_3$	110	130 (100°C) 190 (150°C)	4PB	122
$La_{0.9}Sr_{0.1}Ga_{0.8}Mg_{0.2}O_3$	190	115 (600°C)	Ultrasonic/ pulse-echo	118
$La_{0.8}Sr_{0.2}Fe_{0.8}Cr_{0.2}O_3$	192±7	-	pulse-echo	106
$La_{0.6}Sr_{0.4}Fe_{0.8}Cr_{0.2}O_3$	139±2	-	pulse-echo	106
$La_{0.4}Sr_{0.6}Fe_{0.8}Cr_{0.2}O_3$	135	-	pulse-echo	106
$La_{0.2}Sr_{0.8}Fe_{0.8}Cr_{0.2}O_3$	128	-	pulse-echo	106
$La_{0.8}Sr_{0.2}Ga_{0.85}Mg_{0.15}O_3$	184±5	-	pulse-echo	113
$La_{0.9}Sr_{0.1}Mn_{0.96}Co_{0.04}O_3$	120	-	ultrasonic res. freq.	109
$La_{0.7}Sr_{0.3}Mn_{0.96}Co_{0.04}O_3$	118	-	ultrasonic res. freq.	109
$La_{0.5}Sr_{0.5}Mn_{0.96}Co_{0.04}O_3$	30	-	ultrasonic res. freq.	109

$ Estimated for 100% dense material using the method of Selçuk and Atkinson. [123]

2.6 Creep

Creep is a plastic deformation of a material under constant stress.[63, 124] Creep in ceramics takes place at high temperatures under relative low stresses with low strain rates. [119] In general, creep may be described by three different stages; primary, secondary and tertiary creep. The behavior in tension and compression is shown in Figure 8.

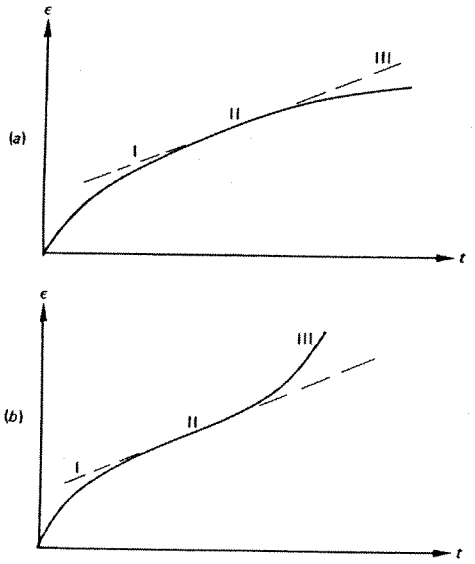

Figure 8: Typical creep curves. (a) Compression: the creep-rate decreases in time but a quasi-steady-state portion (II) can be found after the primary creep regime (I) and before the tertiary creep regime (III). (b) Tension: the creep-rate first decreases in the primary creep regime (I), a quasi-steady-state regime follows (II). The accelerating tertiary creep (III) leads to failure. [125]

The quasi-steady state regime is usually treated as a steady-state regime and its creep rate variation with stress and temperature is often taken as the state for the creep equation. The generalized steady-state creep relationship [126] for oxide materials is given in equation (6)

$$\dot{\varepsilon} = A\left(\frac{1}{d}\right)^{p} \left(pO_2\right)^{m} \sigma^{n} \exp\left(-\frac{Q}{RT}\right) \tag{6}$$

where $\dot{\varepsilon}$ is the steady-state creep rate, A is a constant, d is the grain size, p is the inverse grain size exponent, m is the oxygen partial pressure exponent, σ is the applied stress, n is the stress exponent, Q is the activation energy, R is the gas constant and T is the absolute temperature.

Depending on the materials in question, there are different mechanisms for creep controlled by viscoelastic effects, diffusion or porosity.[63] Strain can be achieved by transport of matter by diffusion (diffusion creep) or by shear along the grain boundaries (grain boundary sliding),[125] according to which mechanism provides the greater amount of strain. If the transport of matter occurs by lattice diffusion, it is called Nabarro-Herring creep and the creep varies with the inverse of grain size squared. If the transport of matter occurs by grain-boundary diffusion, it is Coble creep and the creep varies with the inverse grain size raised to the third power.[125]

The stress exponent, grain size exponent and the activation energy can provide information about the mechanisms of creep. A low stress exponent and an inverse grain size exponent of 2 indicates diffusion through grains (Nabarro-Herring creep) while an equivalent exponent of 3 indicates diffusion via grain boundaries (Coble creep). Coble creep is favored over Nabarro-Herring creep at low temperature because the activation energy for grain boundary diffusion is less than for diffusion through grains. In addition, Coble creep is favored for small grains.[63]

The activation energies obtained from creep measurements can be compared to activation energies for the different ions, and the rate determining specie can be found. Table 6 gives activation energies found in literature for cation diffusion in perovskite materials. Activation energies for oxygen diffusion are usually considerable lower than for cation diffusion, and the cations are rate determining.

Several studies of the creep performance of perovskite materials are available in the literature. Table 7 gives a summary of creep parameters obtained for perovskite materials.

Understanding and investigating of creep is important due to the request for dimensional stability of devices. By studying creep of at different conditions, the mechanisms and behavior can be understood. This may help finding materials with the best properties for the actual application.

Table 6: Literature values of activation energies for perovskite materials found by cation diffusion.

Composition	Method	Temp [°C]	Ea [kJ/mol]	Comment	Ref
$La_{0.75}Ca_{0.25}CrO_{3-\delta}$	Instanteous source method, Sr-nitr solution diff. couple	900-1400	318 261	bulk grain b.	[127]
$La_{0.7}Ca_{0.3}CrO_{3-\delta}$	SIMS, ^{50}Cr	900-1100	213 266	bulk grain b.	[128]
$LaCrO_3$	La^{3+} diff		480		[129]
$LaCrO_3$	Transient el. cond. La^{3+}	1300-1400	387		[130]
$YCrO_3$	Diff. couple Y^{3+}	1185-1446	272		[131]
$NdCrO_3$	Diff. couple Nd^{3+}	1200-1500	343		[132]
$La_{0.9}Sr_{0.1}FeO_3$	SIMS, Y^{3+}, Cr^{3+}	900-1100	Y:168±24 Cr:150±30 128±28	bulk grain b.	[133]
$La_{0.9}Sr_{0.1}Ga_{0.9}Mg_{0.1}O_{2.9}$	SIMS; ^{138}La, ^{84}Sr, ^{25}Mg	900-1400	434 145	bulk, high T bulk, low T	[134]
$LaFeO_3$	Diff. couple Fe^{3+}	950-1350	310±20		[135]
$YFeO_3$	Diff. couple	1220-1352	450±20		[136]
$GdFeO_3$	Diff. couple Gd_2O_3, Fe_2O_3	1200-1400	397±20		[137]
$La_{0.75}Ca_{0.25}CrO_{3-\delta}$	SIMS, ^{44}Ca	900-1100	219 123	bulk grain b.	[138]
$La_{0.75}Ca_{0.25}CrO_{3-\delta}$	Ca-Sr-interdiff.	900-1100	226 202	bulk grain b.	[138]

Table 7: Literature values for creep parameters of perovskite materials. GBS = grain boundary sliding, LD = lattice diffusion

Composition	Temp [°C]	n	Ea [kJ/mol]	p	m	Mechanism	Ref
$SrFeO_{3-d}$	800-1000	unity	260±30				139
$BaTiO_3$	1200-1300	1	720	2		GBS, LD	140
$BaTiO_3$	1150-1250	2	800				141
$SrTiO_3$ (single crystal)	1250-1520	3.5±0.1	730-770 <100> 620 <110>		differ <100> and <110>		142
$La_{0.9}Sr_{0.1}MnO_3$	1225	1.3 ± 0.2			0.37 (10^{-7}-10^{-4}) -0.19 (> 10^{-3})	GBS, LD cation/ox.vac. (pO_2-dep)	143
$La_{0.8}Sr_{0.2}MnO_3$	1165-1265	1.3 ± 0.2	530±40 (air)		0.26 (10^{-5}-10^{-3}) -0.19 (> 10^{-2})	GBS, LD cation/ox.vac. (pO_2-dep)	143
$La_{0.7}Sr_{0.3}MnO_3$	1225	1.3 ± 0.2			0.30 (> 10^{-4})	GBS, LD cation	143
$La_{0.9}Sr_{0.1}MnO_3$	1150-1300	unity	490			LD of cations	144
Sr-doped $LaMnO_3$	1150-1300					LD of cations	145
$(La_{0.9}Sr_{0.1})_zGa_{0.8}Mg_{0.2}O_3$ (z=1, 0.98, 0.95)	950-1350	1.49±0.10	426±9	3.1 z=0.98 1.9 z=0.95			146
$La_{0.8}Sr_{0.2}Ga_{0.85}Mg_{0.15}O_3$	1200-1300	unity	521±15			LD of cations	147-149
$SrCo_{0.8}Fe_{0.2}O_{3-d}$	850-975	unity 2.2-2.9	457 T<925 268 T>925	Unity		LD (low str), dislocation (high str)	150-152
$La_{0.2}Sr_{0.8}Fe_{0.8}Cr_{0.2}O_{3-d}$	1100-1200	1.4 (air)	566 (air) 532-479 885	2.3 2.07	 0.004 (>10^{-11}) -0.5 (<10^{-11})	LD (low str) power law (high str)	153-156

2.7 Oxygen permeable membranes

Ceramic membranes made from mixed oxygen-ionic and electronic conducting (MIEC) perovskite oxides allow selective separation of oxygen from air at elevated temperatures, typically above 700°C.[7] The oxygen permeation in a membrane is determined by either surface exchange processes on one or both of the surfaces, or solid-state oxygen ion bulk diffusion. The bulk diffusion depends on the temperature, oxygen partial pressure and microstructure of the bulk. The surface exchange depends in addition on catalytic activity, surface structure and area.[7] The oxygen transport through the bulk of a mixed conducting membrane is described by the Wagner equation[7]

$$j_{O_2} = -\frac{RT}{4^2 F^2 L} \int_{\ln P'_{O_2}}^{\ln P''_{O_2}} \frac{\sigma_{el}\sigma_{ion}}{\sigma_{el}+\sigma_{ion}} d\ln P_{O_2} \qquad (7)$$

where R is the gas constant, T is the temperature, L is the membrane thickness, σ_{el} and σ_{ion} are the electronic and the ionic conductivity, and P'_{O_2} and P''_{O_2} are the oxygen partial pressures on the different sides of the membrane.

For materials with high bulk diffusion or in the case of very thin membranes, the oxygen flux may be rate controlled by oxygen surface exchange. This transition from control by diffusion to control by surface exchange is defined by the characteristic or critical thickness, L_c, of the membrane.[7] L_c is reported to vary in the range 20 to 3000 μm depending on composition, temperature and pO_2.[157]

There are many studies of these properties for similar compositions in the literature. The first materials were $La_{1-x}Sr_xCo_{1-y}Fe_yO_{3-\delta}$, published by Teraoka et al.[158] Here, the permeation rates were found to change by substitution on A or B site. Other substitutions were also reported,[159] and gave rise to different effects on the permeability rates, shown in Table 8.

Table 8: Effect on cation substitution on the oxygen permeability for some perovskite oxides.[159]

Composition	Effect on permeability
$La_{0.6}A_{0.4}Co_{0.8}Fe_{0.2}O_{3-\delta}$	A: Ba > Ca > Sr > Na
$La_{0.6}Sr_{0.4}Co_{0.8}B_{0.2}O_{3-\delta}$	B: Cu > Ni > Co > Fe > Cr > Mn
$Ln_{0.6}Sr_{0.4}CoO_{3-\delta}$	Ln: Gd > Sm > Nd > Pr > La

Literature data on oxygen permeability for selected perovskite materials are given in Table 9. The data are for disc-shaped membranes with air on the high pO_2 side. The fluxes are normalized by the thickness of the membrane. The activation energies for the oxygen diffusion process are also given in the table. The temperature range for calculation of the activation energies are close to the given temperature for the reported oxygen flux. Generally, data in the literature exhibit large variation even for the apparently same materials. Such conflicting results reflect the experimental difficulties in measuring oxygen fluxes, e. g. the effective pO_2 gradient across the membrane and sample preparation.

The different oxygen partial pressures at the surfaces of membranes give an oxygen activity gradient through the membrane. This gradient will cause a gradient in oxygen non-stoichiometry and the subsequent difference in volume expansion will lead to a build-up of mechanical stresses. Hendriksen et al.[42] calculated strain and stress profiles in a $La_{0.6}Sr_{0.4}Co_{0.2}Fe_{0.8}O_{3-\delta}$ membrane at operating conditions (800°C, $pO_2 = 10^{-19}$ atm on the secondary side and air on the high pO_2 side). The calculated profiles are shown in Figure 9. The lattice expansion due to the pO_2 gradient is seen to result in an overall expansion of the membrane of ca. 0.35 %. Tensile stresses (up to 70 MPa) are built up at the primary side and compressive stresses (up to 15 MPa) at the secondary side. Here, any stress relaxation due to creep is not regarded. The tensile stress level is increased by increasing the membrane thickness. The failure mode proposed is fracture of the membrane due to the levels of these tensile stresses. However, in the case of membranes thinner than a few hundred μm, the membrane must be supported on a porous substrate and the relevant failure mode is rather a delamination between membrane and support.[42]

Table 9: Normalized oxygen permeability, jO_2, for disc-shaped membranes at different temperatures and different oxygen partial pressure at low pO_2 side found in literature. Gas on high pO_2 side is air.

Material	jO_2 [(ml/min·cm^2)·mm]	T [°C]	Ea [kJ/mol]	pO_2 [atm]	Ref.
$SrFeO_3$	0.91	996	90-110	$10^{-2.9}$	160
$SrFe_{0.67}Co_{0.33}O_3$	2.73	1000	100±7	He	157
$Sr_{0.97}Fe_{0.33}Co_{0.67}O_3$	4.2	992	90-110	$10^{-2.2}$	160
$La_{0.5}Sr_{0.5}FeO_{3-\delta}$	0.40	1147	105±4	He	161
$La_{0.5}Sr_{0.5}Fe_{0.5}Co_{0.5}O_{3-\delta}$	1.2	1147	88±9	He	161
$La_{0.5}Sr_{0.5}CoO_{3-\delta}$	2.2	1147	68±1	He	161
$La_{0.2}Sr_{0.8}Fe_{0.2}Co_{0.8}O_{3-\delta}$	1.1	975	82±6	He	41
$La_{0.7}Sr_{0.3}FeO_{3-\delta}$	2.0	1000	31±19	10^{-12}	17
$La_{0.7}Sr_{0.3}FeO_{3-\delta}$	0.23	1000	206±12	$10^{-2.1}$	17-18
$La_{0.5}Sr_{0.5}CoO_{3-\delta}$	0.31	890	150±5	$10^{-2.5}$	43
$La_{0.3}Sr_{0.7}CoO_{3-\delta}$	0.65	880		$10^{-2.5}$	44
$La_{0.3}Sr_{0.7}CoO_{3-\delta}$	0.53	880		$10^{-1.1}$	45
$La_{0.3}Sr_{0.7}CoO_{3-\delta}$	1.4	1000	57±2	$10^{-1.6}$	46
$Ba_{0.5}Sr_{0.5}Co_{0.8}Fe_{0.2}O_{3-\delta}$	2.4	950	41	$10^{-1.3}$	162
$Ba_{0.5}Sr_{0.5}Co_{0.8}Fe_{0.2}O_{3-\delta}$	1.4*	900	42	He	163
$SrCo_{0.8}Fe_{0.2}O_{3-\delta}$	1.9	950		$10^{-1.3}$	162
$LaSr_{0.5}Ni_{0.5}O_{3-\delta}$	0.10	950		$10^{-1.7}$	45
$LaGa_{0.5}Ni_{0.5}O_{3-\delta}$	0.013	950		$10^{-1.7}$	45
$La_{0.4}Ca_{0.6}FeO_3$	0.061	900	107±1	Ar	47
$La_{0.4}Ca_{0.6}Co_{0.5}Fe_{0.5}O_3$	0.11	900	120±10	Ar	47
$La_{0.6}Sr_{0.4}Co_{0.2}Fe_{0.8}O_3$	0.29	950	128±8	He	48
$La_{0.6}Sr_{0.4}Co_{0.2}Fe_{0.8}O_3$	0.46	1000		$10^{-2.5}$	49

*) Thickness not given.

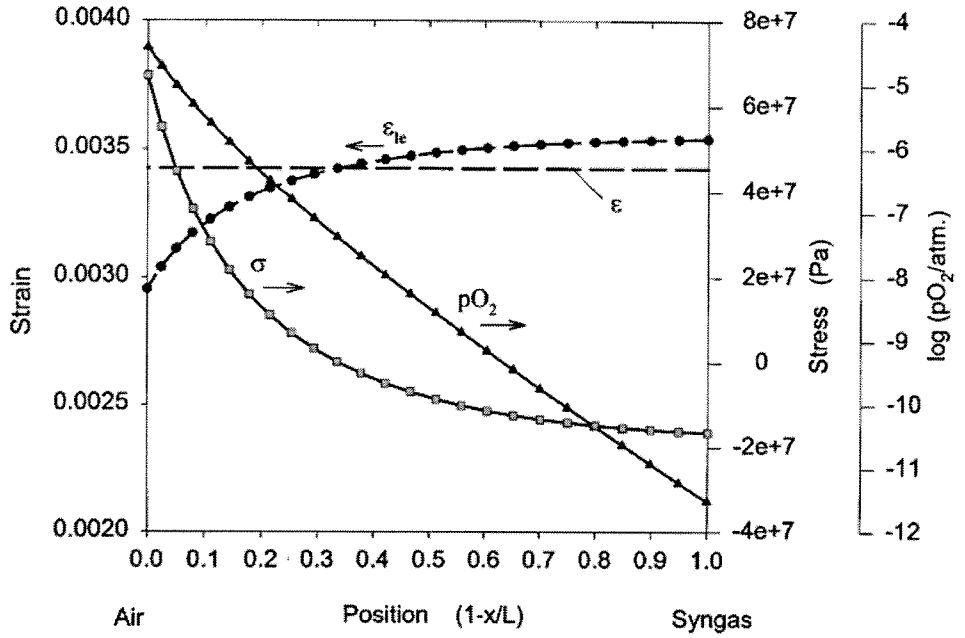

Figure 9: Calculated pO_2, strain and stress profiles across a $La_{0.6}Sr_{0.4}Co_{0.2}Fe_{0.8}O_{3-\delta}$ membrane exposed to a pO_2 of 10^{-19} atm at the low pO_2 side and a pO_2 of 0.2 atm at the high pO_2 side (T = 800°C). From Hendriksen et al.[42]

2.8 Stability of materials in potential gradient

Homogeneous materials can be exposed to thermodynamic potential gradients, for instance gradients in temperature, chemical or electrical gradients, or uniaxial pressure.[164-165] These gradients act as driving forces on atoms in a crystalline material and fluxes of atoms result. The fluxes may lead to three basic degradation phenomena of the materials.[165]

- The material, which was originally chemically homogeneous, becomes chemically inhomogeneous (kinetic demixing).
- Formation of new phases might take place, i.e. the initially single-phase material might decompose into new phases (kinetic decomposition).
- The original morphology of the material might become unstable and a new morphology might be established (morphological instability)

Membranes placed in potential gradients are not in equilibrium with their immediate surroundings and all three phenomena observed above are kinetic in nature. If the applied thermodynamic potential gradient is removed, the directed fluxes will disappear. Owing to diffusion processes the material will relax and again become homogeneous. The new phases will disappear, and the new morphology might become unstable and the old might be re-established.[164, 165]

Demixing of oxides in a pO_2 gradient is investigated for many binary and tertiary oxides. Martin[166] has shown the chemical potential gradients and the concentration profiles for cation fluxes, cation vacancies and electron holes for an $(A_{1-x}B_x)O$ oxide that is exposed to such a gradient. This is shown in Figure 10.

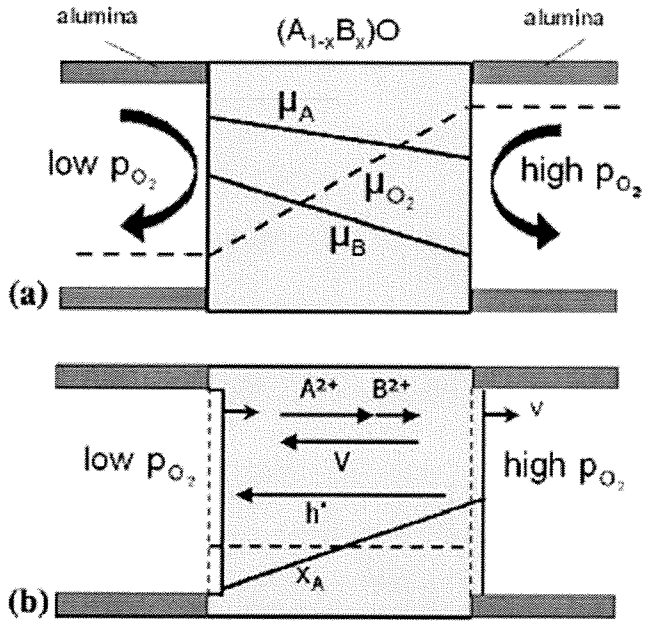

Figure 10: Schematic setup of an oxide that is exposed to an oxygen potential gradient. (a) Chemical potential gradients of the chemical components A, B, and O. (b) Fluxes of cations, A^{2+} and B^{2+}, cation vacancies, V, and electron holes, $h^{\cdot}$, and demixing profile of the faster component A and shift of the crystal surfaces.[166]

Gradients in the chemical potentials of the chemical components A and B (Figure 10a) are induced as a consequence of the Gibbs–Duhem relation

$$x_A d\mu_A + x_B d\mu_B + x_O d\mu_O = 0 \tag{8}$$

The cations are assumed to be mobile by means of cation vacancies in the cation sublattice of the oxide. Thus, the fluxes of cations and vacancies are coupled,

$$j_{A^{2+}} + j_{B^{2+}} + j_V = 0 \tag{9}$$

At the high pO_2 side, cations A^{2+} and B^{2+}, are oxidized by oxygen gas and new lattice molecules, AO and BO, of the oxide are produced. At the low pO_2 side the oxide molecules are reduced to cations and oxygen. As a consequence of these reactions, both oxide surfaces shift to the side of higher oxygen potential. If both cations have different mobilities, the originally homogeneous oxide will become inhomogeneous, as shown in Figure 10b). The faster of the two components A and B becomes enriched at the high pO_2 side, while the slower component is left behind and becomes enriched at the low pO_2 side. The equation for demixing at steady-state[165]

$$\left(\frac{1}{1-x_A} + \frac{D_A}{D_B}\frac{1}{x_A}\right) RT \ln \nabla x_A = \left(\frac{D_A}{D_B} - 1\right)\frac{1}{2}\nabla \mu_{O_2} \tag{10}$$

shows that the ratio D_A/D_B determines whether there is kinetic demixing and at which side of the oxide component A becomes enriched. If both components have the same diffusion coefficient, $D_A/D_B = 1$, there will be no demixing, while if $D_A/D_B > 1$, ∇x_A has the same sign as the oxygen potential gradient $\nabla \mu_{O_2}$, i.e., A becomes enriched at the high pO_2 side. If B is the faster component, $D_A/D_B < 1$, A becomes enriched at the low pO_2 side. The degree of demixing is dependent on the difference in mobility between the cations and the gradient in the driving force. A large difference in mobility and a thinner material increase the degree of demixing.[54, 164, 167-170]

The cation demixing in binary and tertiary oxides is widely reported. $(Co_{1-x}Ga_x)O$,[170] $(Co_xNi_{1-x})_{1-\delta}O$,[172-174] YSZ,[174-175] $(Mn_xFe_{1-x})_3O_4$,[176-177] (Co,Mg)O,[167, 175, 178] (Mn,Fe)O,[177] $Ni_{1-x}Ti_{x/2}O$,[178] $NiTiO_3$,[178] Co_2TiO_4 [178] are some of the examples. However, only limited studies on kinetic demixing and kinetic decomposition in perovskite materials are reported. Kim et al.[179] have investigated the low pO_2 side of $La_{0.36}Sr_{0.64}Co_{0.65}Cu_{0.35}O_{3-x}$ membrane, and found a perovskite phase enriched on La and Co in addition to grains of non-perovskite Sr-Cu oxide with minor amounts of La and Co. Diethelm et

al.[180] studied $La_{0.6}Ca_{0.4}Fe_{0.75}Co_{0.25}O_{3-\delta}$. After use of CH_4 at the low pO_2 side, they found decomposition to three layers. La was enriched, and Fe and Co was found as metallic clusters. On the high pO_2 side, they found (Ca and) Co oxide. The low pO_2 side of $La_{0.3}Sr_{0.7}CoO_{3-\delta}$ was investigated by van Doorn et al.[181] after 120h at 900°C. They found a thin porous layer mainly of $SrCO_3$ and a Sr enriched phase was discovered between surface layer and bulk. $La_{0.4}Ca_{0.6}Fe_{1-x}Co_xO_{3-\delta}$ (x = 0, 0.25 and 0.5) membranes [47] decomposed at secondary side, and an enrichment of transition metals was found. However, no composition change across the membrane was detected.

The physical and the chemical properties of this kind of materials are controlled through the composition. The occurrence of kinetic demixing and chemical decomposition results in a degradation since local composition changes. Secondary phases and perhaps morphological changes may destroy the functionality of the materials and give rise to a decrease in the lifetime.[171, 173-174, 177, 182-185] Therefore, the understanding of the demixing and decomposition processes is of great fundamental and practical importance due to prediction of the durability and reliability of these materials.

3 REFERENCES

1. S. C. Singhal, "Solid oxide fuel cells for stationary, mobile, and military applications", Solid State Ionics, 152-153 (2002) 405-410.
2. P. J. Gellings and H. J. M. Bouwmeester, "Solid state aspects of oxidation catalysis", Cat. Today, 58 (2000) 1-53.
3. S. P. S. Badwal and K. Foger, "Solid oxide electrolyte fuel cell review", Ceramics International, 22 (1996) 257-265.
4. R. M. Ormerod, "Solid oxide fuel cells", Chem. Soc. Rev., 32 (2003) 17-28.
5. S. M. Haile, "Fuel cell materials and components", Acta Mater., 51 (2003) 5981-6000.
6. H. U. Anderson, "Review of p-type doped perovskite materials for SOFC and other applications", Solid State Ionics, 52 (1992) 33-41.
7. H. J. M. Bouwmeester and A. J. Burgraaf, in: P.J. Gellings and H.J.M. Bouwmeester (Eds), The CRC Handbook of Solid State Electrochemistry, CRC Press, Inc., New York (1997).
8. N. G. Minh, "Ceramic Fuel Cells", J. Am. Ceram. Soc, 76 [3] (1993) 563-588.
9. B. C. H. Steele, "Oxygen transport and exchange in oxide ceramics", J. Power Sources, 49 (1994) 1-14.
10. P. Nauth and H. Tuller, "Solid-State Ionics: Roots, Status, and Future Prospects", J. Am. Ceram. Soc., 85 (2002) 1654-1680.
11. T. Arakawa, H. Kurachi and J. Shiokawa, "Physicochemical properties of rare earth perovskite oxides used as gas sensor materials", J. Mater. Sci., 20 (1985) 1207-1210.
12. L. G. Coocia, G. C. Tyrrell, J. A. Kilner, D. Waller, R. J. Chater and I. W. Boyd, "Pulsed laser deposition of novel materials for thin film solid oxide fuel cell applications: $Ce_{0.9}Gd_{0.1}O_{1.95}$, $La_{0.7}Sr_{0.3}CoO_y$ and $La_{0.7}Sr_{0.3}Co_{0.2}Fe_{0.8}O_y$", Appl. Surf. Sci., 96-98 (1996) 795-801.
13. D. Waller, J. A. Lane, J. A. Kilner and B. C. H. Steele, "The effect of thermal treatment on the resistance of LSCF electrodes on gadolinia doped ceria electrolytes", Solid State Ionics, 86-88 (1996) 767-772.
14. J. P. P. Huijsmans, F. P. F. van Berkel and G. M. Christie, "Intermediate temperature SOFC – a promise for the 21st century", J. Power Sources, 71 (1998) 107-110.
15. Y. Ohno, S. Nagata and H. Sato, "Effect of electrode materials on the properties of high-temperature solid electrolyte fuel cells", Solid State Ionics, 3/4 (1981) 439-442.
16. T. J. Gray, "Strontium ceramics for chemical applications", J. Power Sources., 6 (1981) 121-142.
17. J. E. ten Elshof, H. J. M. Bouwmeester and H. Verweij, "Oxygen transport through $La_{1-x}Sr_xFeO_{3-\delta}$ membranes. II. Permeation in air/CO, CO_2 gradients", Solid State Ionics, 89 (1996) 81-92.

18. J. E. ten Elshof, H. J. M. Bouwmeester and H. Verweij, "Oxygen transport through $La_{1-x}Sr_xFeO_{3-\delta}$ membranes. I. Permeation in air/He gradients", Solid State Ionics, 81 (1995) 97-109.
19. K. Huang, H. Y. Lee and J. B. Goodenough, "Sr- and Ni-doped $LaCoO_3$ and $LaFeO_3$ perovskites – New cathode materials for solid oxide fuel cells", J. Electrochem. Soc., 145 (1998) 3220-3227.
20. J. Mizusaki, T. Sasamoto, W. R. Cannon and H. K. Bowen, "Electronic conductivity, Seebeck coefficient, and defect structure of $LaFeO_3$", J. Am. Ceram. Soc., 65 (1982) 363-368.
21. J. Mizusaki, T. Sasamoto, W. R. Cannon and H. K. Bowen, "Electronic conductivity, Seebeck coefficient, and defect structure of $La_{1-x}Sr_xFeO_3$ (x = 0.1, 0.25)", J. Am. Ceram. Soc., 66 (1983) 247-252.
22. W. Z. Zhu and S. C. Deevi, "A review on the status of anode materials for solid oxide fuel cells", Mater. Sci. Eng., A362 (2003) 228-239.
23. N. Sakai, T. Kawada, H.Yokokawa, M.Dokiya and T. Iwata, "Thermal expansion of some chromium deficient lanthanum chromites", Solid State Ionics 40/41 (1990) 394-397.
24. B. A. Haberman and J. B. Young, "Three-dimensional simulation of chemically reacting gas flows in the porous support structure of an integrated-planar solid oxide fuel cell", Int. J. Heat Mass Transfer 47 (2004) 3617-3629.
25. S. de Souza, S. J. Visco and L. C. De Jonghe, "Thin-film solid oxide fuel cell with high performance at low-temperature", Solid State Ionics, 98 (1997) 57-61.
26. P. Charpentier, P. Fragnaud, D. M. Schleich and E. Gehain, "Preparation of thin film SOFCs working at reduced temperature", Solid State Ionics, 135 (2000) 373-380.
27. Y.-K. Lee, J.-Y. Kim, Y.-K. Lee, I. Kim, H.-S. Moon, J.-W. Park, C. P. Jacobson and S. J. Visco, "Conditioning effects on $La_{1-x}Sr_xMnO_3$-yttria stabilized zirconia electrodes for thin-film solid oxide fuel cells", J. Power Sources, 115 (2003) 219-228.
28. H. Middleton, S. Diethelm, R. Ihringer, D. Larrain, J. Sfeir and J. Van Herle, "Co-casting and co-sintering of porous MgO support plates with thin dense perovskite layers of $LaSrFeCoO_3$", J. Euro. Ceram. Soc., 24 (2004) 1083.
29. L. Hong, X. Chen and Z. Cao, "Preparation of a perovskite $La_{0.2}Sr_{0.8}CoO_{3-x}$ membrane on a porous MgO substrate", J. Euro. Ceram. Soc., 21 (2001) 2207-2215.
30. L. M. van der Haar and H. Verweij, "Homogeneous porous perovskite supports for thin dense oxygen separation membranes", J. Membr. Sci, 180 (2000) 147-155.
31. D. Perednis and L. J. Gauckler, "Solid oxide fuel cells with electrolytes prepared via spray pyrolysis", Solid State Ionics, 166 (2004) 229-239.
32. L. C. De Jonghe, C. P. Jacobson and S. J. Visco, "Supported electrolyte thin film synthesis of solid oxide fuel cells", Annu. Rev. Mater. Res., 33 (2003) 169-182.
33. Q. Fang and J. -Y. Zhang, "Preparation of $Ce_{1-x}Gd_xO_{2-0.5x}$ thin films by UV assisted sol–gel method", Surf. Coat. Tech., 151-152 (2002) 100-104.

34. J. W. Yan, Z. G. Lu, Y. Jiang, Y. L. Dong, C. Y. Yu and W. Z. Li, "Fabrication and testing of a doped lanthanum gallate electrolyte thin-film solid oxide fuel cell", J. Electrochem. Soc., 149 [9] (2002) A1132-A1135.
35. T. J. Mazanec, "Prospects for ceramic electrochemical reactors in industry", Solid State Ionics, 70/71 (1994) 11-19.
36. S. Carter, A. Selcuk, R. J. Chater, J. Kajda, J. A. Kilner and B. C. H. Steele, "Oxygen transport in selected nonstoichiometric perovskite-structure oxides", Solid State Ionics, 53-56 (1992) 597-605.
37. V. V. Kharton, E. N. Naumovich and A. V. Nikolaev, "Materials of high-temperature electrochemical oxygen membranes", J. Membr. Sci., 111 (1996) 149-157.
38. U. Balachandran, J. T. Dusek, S. M. Sweeney, R. B. Poeppel, R. L. Mieville, P. S. Maiya, M. S. Kleefisch, S. Y. Pei, T. P. Kobylinski, C. A. Udovich and A. C. Bose, "Methane to syngas via ceramic membranes", Am. Ceram. Soc. Bull., 74 (1995) 71-75.
39. U. Balachandran, B. Ma, P. S. Maiya, R. L. Mieville, J. T. Dusek, J. J. Picciolo, J. Guan, S. E. Dorris and M. Liu, "Development of mixed-conducting oxides for gas separation", Solid State Ionics, 108 (1998) 363-370.
40. M. Liu and D. Wang, "Preparation of $La_{1-z}Sr_zCo_{1-y}Fe_yO_{3-x}$ thin films, membranes, and coatings on dense and porous substrates", J. Mater. Res., 10 [12] (1995) 3210-3221.
41. C.-Y. Tsai, A. G. Dixon, Y. H. Ma, W. R. Moser and M. R. Pascucci, "Dense Perovskite, $La_{1-x}A'_xFe_{1-y}Co_yO_{3-\delta}$ (A' = Ba, Sr, Ca), Membrane Synthesis, Applications, and Characterization", J. Am. Ceram. Soc., 81 [6] (1998) 1437-1444.
42. P. V. Hendriksen, P. H. Larsen, M. Mogensen, F. W. Poulsen and K. Wiik, "Prospects and problems of dense oxygen permeable membranes", Catal. Today, 56 (2000) 283-295.
43. K. Huang and J. B. Goodenough, "Oxygen Permeation Through Cobalt-Containing Perovskites. Surface Oxygen Exchange vs. Lattice Oxygen Diffusion", J. Electrochem. Soc., 148 (2001) E203-E214.
44. V. V. Kharton and F. M. B. Marques, "Mixed ionic-electronic conductors: effects of ceramic microstructure on transport properties", Curr. Op. in Solid State and Mater. Sci., 6 (2002) 261-269.
45. V. V. Kharton, A. A. Yaremchenko, A. V. Kovalevsky, A. P. Viskup, E. N. Naumovich and P. F. Kerko, "Perovskite-type oxides for high-temperature oxygen separation membranes", J. Membr. Sci., 163 (1999) 307-317.
46. C. H. Chen, H. M. J. Bouwmeester, R. H. E. van Doorn, H. Kruidhof and A. J. Burggraaf, "Oxygen permeation of $La_{0.3}Sr_{0.7}CoO_{3-\delta}$", Solid State Ionics, 98 (1997) 7-13.
47. S. Diethelm, J. Van herle, P. H. Middleton and D. Favrat, "Oxygen permeation and stability of $La_{0.4}Ca_{0.6}Fe_{1-x}Co_xO_{3-\delta}$ (x = 0, 0.25, 0.5) membranes", J. Power Sources, 118 (2003) 270-275.
48. J. E. ten Elshof, H. J. M. Bouwmeester and H. Verweij, "Oxidative coupling of methane in a mixed-conducting perovskite membrane reactor", Appl. Catal. A, 130 (1995) 195-212.

49. J. A. Lane, S. J. Benson, D. Waller and J. A. Kilner, "Oxygen transport in $La_{0.6}Sr_{0.4}Co_{0.2}Fe_{0.8}O_{3-\delta}$", Solid State Ionics, 121 (1999) 201-208.
50. Wanqin Jin, Shiguang Li, Pei Huang, Nanping Xu and Jun Shi, "Preparation of an asymmetric perovskite-type membrane and its oxygen permeability"; J. Membr. Sci., 185 (2001) 237-243.
51. C. Xia, T.L. Ward, P. Atanasova and R.W. Schwartz, "Metal-organic chemical vapor deposition of Sr-Co-Fe-O films on porous substrates", J. Mater. Res., 13 [1] (1998) 173-179.
52. C. H. Chen, H. M J. Bouwmeester, H. Kruidhof, J. E. ten Elshof and A. J. Burggraaf, "Fabrication of $La_{1-x}Sr_xCoO_{3-\delta}$ thin layers on porous supports by a polymeric sol-gel process", J. Mater. Chem., 6 (1996) 815-819.
53. A. Abrutis, A. Teiserskis, G. Garcia, V. Kubilius, Z. Saltyte, Z. Salciunas, V. Faucheux, A. Figueras and S. Rushworth, "Preparation of dense, ultra-thin MIEC ceramic membranes by atmospheric spray-pyrolysis technique", J. Membr. Sci., 240 (2004) 113-122.
54. H. Schmalzried, "Behavior of (semiconducting) oxide crystals in oxygen potential gradients", Reactivity of Solids, 1 (1986) 117-137.
55. C. N. R. Rao and J. Gopalakrishnan, "New Directions in Solid State Chemistry", 2. ed., Cambridge University Press, Cambridge (1997).
56. E. Garcia-Gonzalez, M. Parras, J. M. Gonzalez-Calbet and M. Vallet-Regi, "A HREM study on $La_{1/3}Sr_{2/3}FeO_{3-\delta}$. 2. ($0.15 \leq y \leq 0.33$)", J. Solid State Chem., 125 (1995) 125-132.
57. J. P Hodges, S. Short, J. D. Jorgensen, X. Xiong, B. Dabrowski, S. M. Mini and C. W. Kimball, "Evolution of oxygen-vacancy ordered crystal structures in the perovskite series $Sr_nFe_nO_{3n-1}$ (n = 2, 4, 8 and infinity), and the relationship to electronic and magnetic properties", J. Solid State Chem., 151 (2000) 190-209.
58. S. E. Dann, D. B. Currie, M. T. Weller, M. F. Thomas and A. D. Al-Rawwas, "The Effect of Oxygen Stoichiometry on Phase Relations and Structure in the System $La_{1-x}Sr_xFeO_{3-\delta}$ ($0 \leq x \leq 1$, $0 \leq \delta \leq 0.5$)", J. Solid State Chem., 109 (1994) 134-144.
59. A. Mineshige, M. Inaba, TS. Yao, Z. Ogumi, K. Kikuchi and M. Kawase, "Crystal structure and metal-insulator transition of $La_{1-x}Sr_xCoO_3$", J. Solid State Chem., 121 (1996) 423-429.
60. A. Fossdal, M. Menon, I. Værnhus, K. Wiik, M.-A. Einarsrud and T. Grande, "Crystal structure and thermal expansion of $La_{1-x}Sr_xFeO_{3-\delta}$ materials", J. Am. Ceram. Soc., 87 [10] (2004) 1952-1958.
61. L-W. Tai, M. M. Nasrallah and H. U. Anderson, "Thermochemical Stability, Electrical Conductivity, and Seebeck Coefficient of Sr-Doped $LaCo_{0.2}Fe_{0.8}O_{3-\delta}$", J. Solid State Chem., 118 (1995) 117-124.
62. M. H. R. Lankhorst, H. J. M. Bouwmeester and H. Verweij, "High-Temperature Coulometric Titration of $La_{1-x}Sr_xCoO_{3-\delta}$: Evidence for the Effect of Electronic Band Structure on Nonstoichiometry Behavior", J. Solid State Chem., 133 (1997) 555-567.
63. D. W. Richerson, "Modern Ceramic Engineering", Marcel Dekker Inc., New York (1992).

64. M. M Nasrallah, J. D. Carter, H. U. Anderson and R. Koc, in: Proceedings of the Second International Symposium on Solid Oxide Fuel Cells. Commission of The European Communities, Luxembourg, 1991.
65. V. V. Kharton, A. A. Yaremchenko and E. N. Naumovich, "Research on the electrochemistry of oxygen ion conductors in the formed Soviet Union. II. Perovskite-related oxides", J. Solid State Electrochem. 3 (1999) 303-326.
66. M. Mori and Y. Hiei, "Thermal Expansion Behavior of Titanium-Doped La(Sr)CrO3 Solid Oxide Fuel Cell Interconnects", J. Am. Ceram. Soc., 84 [11] (2001) 2573-2578.
67. M. Mori, Y. Hiei and T. Yamamoto, "Control of the Thermal Expansion of Strontium-Doped Lanthanum Chromite Perovskites by B-site Doping for High-Temperature Solid Oxide Fuel Cell Separators", J. Am. Ceram. Soc., 84 [4] (2001) 781-786.
68. H. Hayashi, M. Watanabe and H. Inaba, "Measurement of thermal expansion coefficient of $LaCrO_3$", Thermichimica Acta, 359 (2000) 77-85.
69. N. Sakai and S. Stølen, "Heat capacity and thermodynamic properties of lanthanum(III) chromate(III): $LaCrO_3$, at temperatures from 298.15 K. Evaluation of the thermal conductivity", J. Chem. Thermodynamics, 27 (1995) 493-506.
70. S. Srilomsak, D. P. Schilling, H. U. Anderson, in: S. C. Singhal (Ed.), Proceedings of the First International Symposium on Solid Oxide Fuel Cells, The Electrochemical Society, Pennington, NJ, 1989.
71. C. S. Montross, H. Yokogawa and M. Dokiya, "Thermal stresses in planar solid oxide fuel cells due to thermal expansion differences", Br. Ceram. Trans., 101 [3] (2002) 85-93.
72. W. Ma, G. Xie and H. Wang, "Thermal Expansion Behavior of $La_{1-x}Sr_xMn_{1-y}Co_yO_{3-\delta}$ Perovskites", J. Mater. Sci. Technol., 18 [3] (2002) 286-287.
73. B. Yan, J. Zhang and J. Liu, "Thermal Expansion of $LaCoO_3$", J. Rare Earths", 22 [2] (2004) 259-262.
74. J. Hemberger, H. A. Krug von Nidda, V. Fritsch, J. Deisenhofer, S. Lobina, T. Rudolf, P. Lunkenheimer, F. Lichtenberg, A. Loidl, D. Bruns ans B. Büchner, "Evidence for Jahn-Teller distortions at the Antiferromagnetic transition in $LaTiO_3$", Phys. Rev. Lett., 91 [6] (2003) 066403.
75. M. Cwik, T. Lorenz, J. Baier, R. Müller, G. André, F. Bourée, F. Lichtenberg, A. Freimuth, R. Smitz, E. Müller-Hartmann and M. Braden, "Crystal and magnetic structure of $LaTiO_3$: Evidence for nondegenerate t_{2g} orbitals", Phys. Rew. B, 68 (2003) 060401.
76. P. Duran, J. Tartaj, F. Capel and C. Moure, "Formation, sintering and thermal expansion behavior of Sr- and Mg – doped LaCrO3 as AOFC interconnector prepared by the ethylene glycol polymerized complex solution synthesis method", J. Euro. Ceram. Soc., 24 (2004) 2619-2629.
77. J. W. Fergus, "Lanthanum chromite-based materials for solid oxide fuel cell interconnects", Solid State Ionics, 171 (2004) 1-15.
78. L.-W. Tai, M. M. Nasrallah, H. U. Anderson, D. M. Sparlin and S. R. Sehlin, "Structure and electrical properties of $La_{1-x}Sr_xCo_{1-y}Fe_yO_3$. Part 1. The system $La_{0.8}Sr_{0.2}Co_{1-y}Fe_yO_3$.", Solid State Ionics, 76 (1995) 259-271.

79. V. V. Kharton, A. A. Yaremchenko, M. V. Patrakeev, E. N Naumovich and F. M. B. Marques, "Thermal and chemical induced expansion of $La_{0.3}Sr_{0.7}(Fe,Ga)O_{3-\delta}$ ceramics", J Euro. Ceram. Soc, 23 (2003) 1417-1426.
80. S. Wang, M. Katsuki, M. Dokiya and T. Hashimoto, "High temperature properties of $La_{0.6}Sr_{0.4}Co_{0.8}Fe_{0.2}O_{3-\delta}$ phase structure and electrical conductivety", Solid State Ionics, 159 (2003) 71-78.
81. H. Ullmann, N. Trofimenko, F. Tietz, D. Stöver and A. Ahmad-Khanlou, "Correlation between thermal expansion and oxide ion transport in mixed conducting perovskite-type oxides for SOFC cathodes", Solid State Ionics, 138 (2000) 79-90.
82. B. Gilbu, H. Fjellvåg and A. Kjekshus, "Properties of $LaCo_{1-t}Cr_tO_3$. I. Solid Solubility, Thermal Expansion and Structural Transition", Acta Chemica Scandinavica, 48 (1994) 37-45.
83. R. D. Shannon, "Revised effective ionic radii and systematic studies of interatomic distances in halides and chalcogenides", Acte Cryst., A32 (1976) 751-767.
84. J. Mizusaki, M. Yoshihiro, S. Yamauchi and K. Fueki, "Nonstoichiometry and Defect Structure of the Perovskite-Type Oxides $La_{1-x}Sr_xFeO_{3-\delta}$", J. Solid State Chem.,58 (1985) 257-266.
85. J. Mizusaki, Y. Mima, S. Yamauchi, K. Fueki and A. Tagawa, "Nonstoichiometry of the Perovskite-Type Oxides $La_{1-x}Sr_xCoO_{3-\delta}$", J. Solid State Chem., 80 (1989) 102-111.
86. J. Mizusaki, "Nonstoichiometry, diffusion, and electrical properties of perovskite-type oxide electrode materials", Solid State Ionics, 52 (1992) 79-91.
87. W. Sitte, E. Bucher and W. Preis, "Nonstoichiometry and transport properties of strontium-substituted lanthanum cobaltites", Solid State Ionics, 154-155 (2002) 517-522.
88. A. N. Petrov, V. A. Cherepanov, O. F. Kononchuk and L. YA. Gavrilova, "Oxygen Nonstoichiometry of $La_{1-x}Sr_xCoO_{3-d}$ ($0<x<0.6$)", J. Solid State Chem., 87 (1990) 69-76.
89. V. V. Kharton, V. N Tikhonovich, S.B. Li, E. N Naumovich, A. V. Kovalevsky, A. P. Viskup, I.A. Bashmakov and A. A. Yaremchenko, "Ceramic microstructure and oxygen permeability of $SrCo(Fe,M)O_{3-\delta}$ (M = Cu or Cr) perovskite membranes", J. Electrochem. Soc., 145 (1998) 1363-1373.
90. H. L. Lein, K. Wiik and T. Grande, "Thermal and chemical expansion of $La_{0.5}Sr_{0.5}Fe_{1-x}Co_xO_{3-\delta}$ ($0\leq x\leq 1$) materials", paper I.
91. A. Atkinson and T. M. G. M. Ramos, "Chemically-induced stresses in ceramic oxygen ion-conducting membranes", Solid State Ionics, 129 (2000) 259-269.
92. T. R. Armstrong, J. W. Stevenson, L. R. Pederson and P. E. Raney, "Dimensional Instability of Doped Lanthanum Chromite", J. Electrochem. Soc., 143 [9] (1996) 2919-2925.
93. A. Zuev, L. Singheiser and K. Hilpert, "Defect structure and isothermal expansion of A-site and B-site substituted lanthanum chromites", Solis State Ionics, 147 (2002) 1-11.

94. S. Miyoshi, J.-O. Hong, K. Yashiro, A. Kaimai, Y. Nigara, K. Kawamura, T. Kawada and J. Mizusaki, "Lattice expansion upon reduction of perovskite-type $LaMnO_3$ with oxygen-deficit nonstoichiometry", Solid State Ionics 161 (2003) 209-217.
95. K. L. Ley, M. Krumpelt, R. Kumar, J. H. Meiser and I. Bloom, "Glass ceramic sealants for solid oxide fuel cells. Part I. Physical properties", J. Mater. Res., 11 (1996) 1489-1493.
96. A. Atkinson, "Chemically-induced stresses in gadolinium-doped ceria solid oxide fuel cell electrolytes", Solid State Ionics, 95 (1997) 249-258.
97. A. Fossdal, M.-A. Einarsrud and T. Grande, "Mechanical properties of $LaFeO_3$ ceramics", J. Euro. Ceram. Soc., 25 (2005) 927-933.
98. N. Orlovskaya, K. Kleveland, T. Grande and M.-A. Einarsrud, "Mechanical properties of $LaCoO_3$ based ceramics", J. Euro. Ceram. Soc., 20 (2000) 51-56.
99. H. L. Lein, E. Lara-Curzio, Ø. S. Andersen, P. E. Vullum, R. Holmestad, M.-A. Einarsrud and T. Grande, "Mechanical properties of $La_{0.5}Sr_{0.5}Fe_{1-x}Co_xO_{3-\delta}$ ($0 \leq x \leq 1$) materials", paper III.
100. Y.-S. Chou, J. W. Stevenson, T. R. Armstrong and L. R. Pederson, "Mechanical Properties of $La_{1-x}Sr_xCo_{0.2}Fe_{0.8}O_3$ Mixed-Conducting Perovskites Made by the Combustion Synthesis Technique", J. Am. Ceram. Soc., 83 (2000) 1457-1464.
101. A. Atkinson and A. Selcuk, "Mechanical behaviour of ceramic oxygen ion-conducting membranes", Solid State Ionics, 134 (2000) 59-66.
102. N. M. Sammes, R. Ratnaraj and M. G. Fee, "The effect of sintering on the mechanical properties of SOFC ceramic interconnect materials", J. Mater. Sci., 29 (1994) 4319-4324.
103. S. W. Paulik, S. Baskaran, T. R. Armstrong, "Mechanical properties of calcium- and strontium-substituted lanthanum chromite", J. Mater. Sci., 33 (1998) 2397-2404.
104. N. Nagendra and S. Bandopadhyay, "Strength and fracture toughness of LSFCO membranes exposed to reducing conditions", Scripta Materialia, 48 (2003) 37-42.
105. N. Nagendra and S. Bandopadhyay, "Room and elevated temperature strength of perovskite membrane tubes", J. Euro. Ceram. Soc., 23 (2003) 1361-1368.
106. Y. S. Chou, K. Kerstetter, L. R. Pederson and R. E. Williford, "Mechanical and thermal properties of combustion-synthesized perovskites, $La_{1-x}Sr_xCr_{0.2}Fe_{0.8}O_3$", J. Mater. Res., 16 [12] (2001) 3545-3553.
107. N. M Sammes and R. Ratnaraj, "High-temperature mechanical properties of $La_{0.7}Sr_{0.3}Cr_{1-y}Co_yO_3$ in reducing environments", J. Mater. Sci., 32 (1997) 687-692.
108. D. Y. Ostovoi, G. A. Gogotsi, S. A. Suvorov and A. P. Shevchik, "Strain and fracture of a ceramic based on lanthanum chromite", Refractories and Industrial Ceramics, 43 [7-8] (2002) 237-246.
109. D. L. Meixner and R. A. Cutler, "Sintering and mechanical characteristics of lanthanum strontium manganite", Solid State Ionics, 146 (2002) 273-284.

110. C. M. D'Souza and N. M. Sammes, "Mechanical Properties of Strontium-Doped Lanthanum Manganite", J. Am. Ceram. Soc., 83 (2000) 47-52.
111. C. S. Montross, H. Yokokawa, M. Dokiya and L. Bekessy, "Mechanical Properties of Magnesia-Doped Lanthanum Chromite versus Temperature", J. Am. Ceram. Soc., 78 (1995) 1869-1872.
112. J. Drennan, V. Zelizko, D. Hay, F. T. Ciacchi, S. Rajendran and S. P. S. Badwal, "Characterisation, conductivity and mechanical properties of the oxygen-ion conductor $La_{0.9}Sr_{0.1}Ga_{0.8}Mg_{0.2}O_{3-x}$", J. Mater. Chem., 7 [1] (1997) 79-83.
113. N. M. Sammes, F. M. Keppeler, H. Näfe and F. Aldinger, "Mechanical Properties of Solid-State-Synthesized Strontium- and Magnesium-Doped Lanthanum Gallate", J. Am. Ceram. Soc., 81 (1998) 3104-3108.
114. N. Nagendre, R. F. Klie, N. D. Browning and S. Bandhopadhyay, "Fracture characterization in tubular LSFCO ceramic membranes", Mater. Sci. Eng., A341 (2003) 236-246.
115. N. M Sammes and R. Ratnaraj, "High-temperature mechanical properties of $La_{1-x}Sr_xCr_{1-y}Co_yO_3$ for SOFC interconnect", J. Mater. Sci., 30 (1995) 4523-4526.
116. K. Kleveland, N. Orlovskaya, T. Grande, A. M. M. Moe, M.-A. Einarsrud, K. Breder and G. Gogotsi, "Ferroelastic Behovior of $LaCoO_3$-Based Ceramics", J. Am. Ceram. Soc., 84 (2001) 2029-2033.
117. Goldsmidt, V. N., "Skr. Nor. Vidensk.Akad. [K1] 1: Mat.-Naturvidensk. k1 No. 2", (1926).
118. S. Baskaran, C. A. Lewinsohn, Y.-S. Chou, M. Qian, J.W. Stevenson and T. R. Armstrong, "Mechanical properties of alkaline earth-doped lanthanum gallate", J. Mater. Sci., 34 (1999) 1-10.
119. J. B. Wachtman, "Mechanical properties of ceramics", John Wiley & Sons Inc., New York (1996).
120. W. B. Hillig, "Prospects for ultra-high-temperature ceramic composites", General Electric, Corporate Research and Development, No. 85CRD152, Aug 1985.
121. W. B. Hillig, "Prospects for ultra-high-temperature ceramic composites", Mater. Sci. Res., 20 (1986) 697-712.
122. B. L. Cheng, M. Gabbay, W Duffy Jr. and G. Fantozzi, "Mechanical loss and Young's modulus associated with phase transitions in barium titanate based ceramics", J. Mater. Sci., 31 (1996) 4951-4955.
123. A. Selçuk and A. Atkinson, "Elastic Properties of Ceramic Oxides Used in Solid Oxide Fuel Cells /SOFC)", J. Euro. Ceram. Soc., 17 (1997) 1523-1532.
124. Findley, W. N., Lai, J. S., Onaran, K., Creep and relaxation of nonlinear viscoelastic materials. With an introduction to Linear Viscoelasticity.,
125. J.-P. Poirier, "Creep of crystals. High-temperature deformation processes in metals, ceramics and minerals", Cambridge University Press, Cambridge (1985).
126. T. Bretheau, J. Castaing, J. Rabies and P. Veyssière, "Dislocation-motion and high-temperature plasticity of binary and ternary oxides", Advances in Physics, 28 (1979) 836-1014.

127. S. Kambe, G. Samukawa, K. Yamaguchi, O. Ishii, I. Shime, T. Nomura, S. Ohshima, K. Okuyama, T. Itoh, H. Suematsu and H. Yamauchi, "Physical properties and structure of $Ba_{2-x}La_xRuCuO_y$", Solid State Ionics, 108 (1998) 383-390.
128. N. Sakai, K. Yamaji, T. Horita, H. Negishi and H. Yokoka, "Chromium diffusion in lanthanum chromites", Solid State Ionics, 135 (2000) 469-474.
129. N. Sakai, T. Tsunoda, N. Fukumoto, I. Kojima, K. Yamaji, T. Horita, M. Ishikawa, H. Yokokawa and M. Dokiya, "TEM, XPS and SIMS analyzes on grain boundary of lanthanum chromites", J. Electroceram., 4;S1 (1999) 121-128.
130. T. Akashi, T. Maruyama and T. Goto, "Transport of lanthanum ion and hole in $LaCrO_3$ determined by electrical conductivity measurements", Solid State Ionics, 164 (2003) 177-183.
131. K. Kawamura, A. Saiki, T. Maruyama and K. Nagata, "Diffusion Coefficient of Yttrium in $YCrO_3$", J. Electrochem. Soc., 142 (1995) 3073-3077.
132. T. Akashi, Y. Mizuno, M. Nanko, T. Maruyama, A. Saiki, K. Tsukui and J. Tanabe, "Determination of Diffusion Coefficient of Nd^{3+} in $NdCrO_3$ Based on Solid State Reaction", Mater. Trans., 42 (2001) 1411-1416.
133. I. Værnhus, N. Sakai, H. Yokokawa, T. Grande and K. Wiik, "Cation Diffusion in $La_{1-x}Sr_xFeO_{3-\delta}$, x = 0 and 0.1, measured by SIMS", to be published.
134. O. Schulz, M. Martin, C. Argirusis and G. Borchardt, "Cation tracer diffusion of ^{138}La, ^{84}Sr and ^{25}Mg in polycrystalline $La_{0.9}Sr_{0.1}Ga_{0.9}Mg_{0.1}O_{2.9}$", Phys. Chem. Chem. Phys., 5 (2003) 2308-2313.
135. J. B. Smith and T. Norby, "Cation Self-Diffusion in $LaFeO_{3-\delta}$ Measured by the Solid State Reaction Method", to be published.
136. V. Buscaglia, F. Caracciolo, C. Bottino, M. Leoni and P. Nanni, "Reaction diffusion in the Y_2O_3-Fe_2O_3 system", Acta mater., 45 [3] (1997) 1213-1224.
137. V. Buscaglia, M. T. Buscaglia, L. Giordano, A. Martinelli, M. Viviani and C. Bottino, "Growth of ternary oxides in the Gd_2O_3–Fe_2O_3 system. A diffusion couple study", Solid State Ionics, 146 (2002) 257-271.
138. T. Horita, M. Ishikawa, K. Yamaji, N. Sakai, H. Yokokawa and M. Dokiya, "Calcium tracer diffusion in (La,Ca)CrO_3 by SIMS", Solid State Ionics, 124 (1999) 301-307.
139. K. Kleveland, A. Wereszczak, T. P. Kirkland, M.-A. Einarsrud and T. Grande, "Compressive creep performance of $SrFeO_3$", J. Am. Ceram. Soc., 84 [8] (2001) 1822-1826.
140. E. T. Park, P. Nash, J. Wolfenstine, K. C. Goretta and J. L. Routbort, "High-temperature creep of polycrystalline $BaTiO_3$", J. Mater. Res, 14 [2] (1999) 523-528.
141. C. Carry and A. Mocellin, "Superplastic Creep Fine-Grained $BaTiO_3$ in a Reducing Environment", J. Am. Ceram. Soc, 69 [9] (1986) C-215-C-216.
142. Z. Wang, S.-I. Karato and K. Fujino, "High temperature creep of single crystal strontium titanate ($SrTiO_3$): a contribution to creep systematics in perovskites", Phys. Earth Planet. Inter., 79 (1993) 299-312.

143. R. E. Cook, K. C. Goretta, J. Wolfenstine, P. Nash and J. L. Routbort, "High-temperature deformation and defect chemistry of $(La_{1-x}Sr_x)_{1-y}MnO_{3+\delta}$", Acta mater, 47 (1999) 2969-2980.
144. J. Wolfenstine, T. R. Armstrong, W. J. Weber, M. A. Boling-Risser, K. C. Goretta and J. L. Routbort, "Elevated temperature deformation of fine-grained $La_{0.9}Sr_{0.1}MnO_3$", J. Mater. Res., 11 (1996) 657-662.
145. J. Wolfenstine, K. C. Goretta, R. E. Cook and J. L. Routbort, "Use of diffusional creep to investigate mass transport in (La, Sr)MnO_3", Solid State Ionics 92 (1996) 75-83.
146. W. E. Luecke and T. R. Armstrong, "Creep of lanthanum gallate", J. Mater. Res., 17 (2002) 532-541.
147. J. Wolfenstine, P. Huang and A. Petric, "High-Temperature Mechanical Behavior of the Solid-State Electrolyte: $La_{0.8}Sr_{0.2}Ga_{0.85}Mg_{0.15}O_{2.825}$", J. Electrochem. Soc., 147 [5] (2000) 1668-1670.
148. J. Wolfenstine, "Rate-controlling species for creep of the solid state electrolyte: doped lanthanum gallate", Solid State Ionics, 126 (1999) 293-298.
149. J. Wolfenstine, P. Huang and A. Petric, "Creep behavior of doped lanthanum gallate versus cubic zirconia" Solid State Ionics, 118 (1999) 257-259.
150. G. Majkic, L. Wheeler, and K. Salma, "Characterization of Creep Behavior of $SrCo_{0.8}Fe_{0.2}O_{3-x}$", Mater. Res. Soc. Symp. Proc., 575 (2000) 349-54.
151. G. Majkic, L. Wheeler and K. Salama, "A transmission electron microscopy study of polycrystalline $SrCo_{0.8}Fe_{0.2}O_{3-\delta}$ creep in the diffusion-to-power law transition regime", Phil. Mag. A, 81 [11] (2001) 2675-2688.
152. G. Majkic, L. Wheeler and K. Salama, "Creep of polycrystalline $SrCo_{0.8}Fe_{0.2}O_{3-\delta}$", Acta mater. 48 (2000) 1907-1917.
153. G. Majkic, L. T. Wheeler and K. Salama, "High-temperature deformation of $La_{0.2}Sr_{0.8}Fe_{0.8}Cr_{0.2}O_{3-\delta}$-mixed ionic-electronic conductor", Solid State Ionics, 146 (2002) 393-404.
154. G. Majkic, L. T. Wheeler and K. Salama, "Stress-induced diffusion and defect chemistry of $La_{0.2}Sr_{0.8}Fe_{0.8}Cr_{0.2}O_{3-\delta}$. Part 1 – creep in controlled-oxygen atmosphere", Solid State Ionics, 164 (2003) 137-148.
155. G. Majkic, M. Mironova, L. T. Wheeler and K. Salama, "Stress-induced diffusion and defect chemistry of $La_{0.2}Sr_{0.8}Fe_{0.8}Cr_{0.2}O_{3-\delta}$. 2. Structural, elemental and chemical analysis", Solid State Ionics, 167 (2004) 243-254.
156. G. Majkic, A. J. Jacobson and K. Salama, "Stress-induced diffusion and defect chemistry of $La_{0.2}Sr_{0.8}Fe_{0.8}Cr_{0.2}O_{3-\delta}$. Part3. Defect-chemistry-based modeling", Solid State Ionics, 167 (2004) 255-262.
157. S. Aasland, I. L. Tangen, K. Wiik and R. Ødegård, "Oxygen permeation of $SrFe_{0.67}Co_{0.33}O_{3-d}$", Solid State Ionics, 135 (2000) 713-717.
158. Y. Teraoka, H. M. Zhang, S. Furukawa and N. Yamazoe, "Oxygen permeation through perovskite-type oxides", Chem. Lett., 11 (1985) 1743-1746.
159. Y. Teraoka, T. Nobunaga and N. Yamazoe, "Effect of cation substitution on the oxygen semipermeability of perovskite-type oxides", Chem. Lett., 3 (1988) 503-506.

160. K. Wiik, S. Aasland, H. L. Hansen, I. L. Tangen and R. Ødegård, "Oxygen permeation in the system $SrFeO_{3-x}$ – $SrCoO_{3-y}$", Solid State Ionics, 152-153 (2002) 675-680.
161. H. L. Lein, K. Wiik and T. Grande, "Oxygen permeation of $La_{0.5}Sr_{0.5}Fe_{1-x}Co_xO_{3-\delta}$ ($0 \leq x \leq 1$) materials", paper IV.
162. Z. Shao, G. Xiong, H. Dong, W. Yang and L. Lin, "Synthesis, oxygen permeation study and membrane performance of a $Ba_{0.5}Sr_{0.5}Co_{0.8}Fe_{0.2}O_{3-\delta}$ oxygen-permeable dense ceramic reactor for partial oxidation of methane to syngas", Separ. Purif. Technol., 25 (2001) 97-116.
163. Z. Shao, H. Dong, G. Xiong, Y. Cong and W. Yang, "Performance of a mixed-conducting ceramic membrane reactor with high oxygen permeability for methane conversion ", J. Membr. Sci., 183 (2001)
164. S. Stølen and T. Grande, "Chemical Thermodynamics of Materials. Macroscopic and Microscopic Aspects", John Wiley & Sons Ltd., West Sussex (2004).
165. M. Martin, "Materials in thermodynamic potential gradients", J. Chem. Thermodynamics, 35 (2003) 1291-1308.
166. M. Martin, "Materials in thermodynamic potential gradients", Pure Appl. Chem., 75 [7] (2003) 889-903.
167. D. Dimos, D. L. Kohlstedt and H. Schmalzried, "High-Temperature Creep and Kinetic Demixing in (Co, Mg)O", J. Am. Ceram. Soc., 71 [9] (1988) 732-741.
168. I. V. Belova, M. J. Brown and G. E. Murch, "Analysis of kinetic demixing in a mixed oxide (A,B)O in an oxygen potential gradient", Acta Mater., 51 (2003) 1821-1826.
169. H. Schmalzried, "Diffusion in oxides", Reactivity of Solids, 5 (1988) 268-278.
170. M. J. Brown, I. V. Belova and G. E. Murch, "Prediction of kinetic demixing in a quaternary mixed oxide (A,B,C)O in an oxygen potential gradient", Phil. Mag., 86 (2003) 1855-1865.
171. O. Teller and M. Martin, "Kinetic demixing of Heterovalently Doped CoO in an Electrical Field", Ber. Bunsenges. Phys. Chem, 110 (1997) 1377-1380.
172. O. Teller and M. Martin, "Steady State Demixing of Homovalent Oxide Solid Solutions in an Electrical Potential Gradient", J. Electrochem., 68 [6] (2000) 478-481.
173. O. Teller and M. Martin, "Kinetic demixing of (Co,Ni)O in an electric field", Solid State Ionics, 101-103 (1997) 475-478.
174. M. Martin, "Electrotransport and demixing in oxides" Solid State Ionics, 136-137 (2000) 331-337.
175. D. Monceau, M. Filial, M. Rebtoub, C. Petot and G. Petot-Ervas, "Kinetic demixing of ceramics in an electrical field", Solid State Ionics, 73 (1994) 221-225.
176. J.-O. Hong and H.-I. Yoo, "Electrotransport-induced demixing in semiconducting $(Mn_xFe_{1-x})_3O_4$", Solid State Ionics, 113-115 (1998) 265-270.
177. Y. Ueshima, H. Schmalzried and J. Koepke, "Demixing in Oxgen Potential Gradients: Two-Phase System and the Morphological Stability of the Interface", Ber. Bunsenges. Phys. Chem., 93 (1989) 24-29.

178. H. Schmalzried and W. Laqua, "Multicomponent Oxides in Oxygen Potential Gradients", Oxidation of Metals, 15 [3/4] (1981) 339-353.
179. S. Kim Y. L. Yang, R. Christoffersen and A. J. Jacobson, "Oxygen permeation, electrical conductivity and stability of the perovskite oxide $La_{0.2}Sr_{0.8}Cu_{0.4}Co_{0.6}O_{3-x}$", Solid State Ionics, 104 (1997) 57-65.
180. S. Diethelm, J. Sfeir, F. Clemens, J. Van herle and D. Favrat, „Planar and tubular perovskite type membrane reactors for the partial oxidation of methane to syngas", J. Solid State Electtrochem, 8 (2004) 611-617.
181. R. H. E. van Doorn, H. J. M. Bouwmeester and A. J. Burggraaf, "Kinetic decomposition of $La_{0.3}Sr_{0.7}CoO_{3-\delta}$ perovskite membranes during oxygen permeation", Solid State Ionics, 111 (1998) 263-272.
182. M. Martin, "Transport and degradation in transition metal oxides in chemical potential gradients", Materials Science Reports 7 (1991) 1-86.
183. J.-O. Hong, O. Teller, M. Martin and H.-I. Yoo, "Demixing of a mixed oxide (A,B)O in an oxygen potential gradient: numerical solution of the time evolution of the demixing process", Solid State Ionics, 123 (1999) 75-85.
184. T. Ishikawa, S. A. Akbar, W. Zhu and H. Sato, "Time Evolution of Demixing in Oxides under an Oxygen Potential Gradient", J. Am. Ceram. Soc, 71 [7] (1988) 513-521.
185. H. Schmalzried, W. Laqua and P. L. Lin, "Crystalline Oxide Solid Solutions in Oxygen Potential Gradients", Z. Naturforsch., 34a (1979) 192-199.

PAPER I

Thermal and chemical expansion of $La_{0.5}Sr_{0.5}Fe_{1-x}Co_xO_{3-\delta}$ ($0 \leq x \leq 1$) materials

Hilde Lea Lein, Kjell Wiik and Tor Grande*

Department of Materials Technology,
Norwegian University of Science and Technology,
7491 Trondheim, Norway.

Abstract

The oxygen non-stoichiometry of $La_{0.5}Sr_{0.5}Fe_{1-x}Co_xO_{3-\delta}$ (x = 0, 0.5, 1) have been measured as a function of temperature by thermogravimetry. The oxygen deficiency was increasing with increasing temperature and decreasing partial pressure of oxygen. This was coincident with the contribution of chemical expansion to the thermal expansion, due to larger unit cell volume. Below ~ 500°C in air and ~ 400°C in N_2, a constant oxygen deficiency was frozen in due to slow oxidation kinetics. Thermal and chemical expansion of the material have been measured by dilatometry and high temperature x-ray diffraction. The crystal structure of both x = 0.5 and x = 1 was rhombohedral at room temperature with a phase transition to the cubic perovskite at 350 ± 50°C. The thermal expansion of the materials up to the onset of thermal reduction was $15 - 18 \cdot 10^{-6}\ K^{-1}$. At high temperature, chemical expansion contributed to the thermal expansion and the linear thermal expansion coefficients were in the range $16 - 35 \cdot 10^{-6}\ K^{-1}$. The chemical expansion, ε_c, showed a maximum of 0.0045 for x = 0.5 and 0.0041 for x = 1 at 800-900°C. The normalized chemical expansion, $\varepsilon_c/\Delta\delta$, was 0.039 for x = 0.5 and 0.035 for x = 1 at 800°C. The chemical expansion can be correlated with the difference in ionic radius of the transition metals in various valence states.

* Correspondence to Tor.Grande@material.ntnu.no

Introduction

$La_{1-x}Sr_xFe_{1-y}Co_yO_{3-\delta}$ materials are potential candidates for oxygen permeable membranes due to high electronic and ionic conductivity.[1] Applications as gas sensors or electrodes in solid oxide fuel cells have also been suggested.[1-3] Chemical, thermal and mechanical stability of the materials are important for the utilization of these devices,[4] and one of the main challenges is to prevent mechanical failure during fabrication and operation.

The oxygen deficiency in $La_{1-x}Sr_xFe_{1-y}Co_yO_{3-\delta}$ materials increases with increasing temperature and decreasing partial pressure of oxygen.[1] This has been shown for both $La_{1-x}Sr_xFeO_{3-\delta}$ [5-6] and $La_{1-x}Sr_xCoO_{3-\delta}$ [7-12] materials in addition to $La_{1-x}Sr_xFe_{1-y}Co_yO_{3-\delta}$.[13-15] The gradient in the chemical potential used to permeate oxygen through $La_{1-x}Sr_xFe_{1-y}Co_yO_{3-\delta}$ materials results in a gradient in the oxygen non-stoichiometry across the membrane due to a reduction of the valence state of the transition metals in the materials with decreasing chemical potential of oxygen. The gradual increase in the oxygen deficiency (δ) is accompanied by a chemical expansion due to a change in the unit cell volume with decreasing valence state of the transition metals.[16] Oxygen permeable membranes are due to the lattice expansion subjected to a chemically induced stress when exposed to a gradient in partial pressure of oxygen. The magnitude of the stress, which might cause failure due to creep, fracture or even kinetic demixing, depends on the geometrical constrains, oxygen flux and the chemical expansion properties of the materials.[3, 5, 17] The chemical expansion comes in addition to the thermal expansion caused by anharmonic vibrations. The chemical expansion can be quantified by $\varepsilon/\Delta\delta$ where $\varepsilon = (a-a_o)/a_o$.[18] Here, $\Delta\delta$ and $a-a_o$ are the change in the oxygen deficiency and the pseudo cubic lattice cell parameter, for a change between two partial pressures of oxygen at constant temperature. For materials containing different transition metal ions, the normalized chemical strain is expected to vary. For $La_{0.7}Sr_{0.3}Cr_{1-x}Al_xO_3$-materials, the $\varepsilon/\Delta\delta$-ratio is determined to 0.034-0.036 at 1000°C,[19] 0.050-0.066 for $Ce_{1-x}Gd_xO_{2-d}$ at 1000°C [18] and 0.059 for $La_{0.5}Sr_{0.5}FeO_3$ at 800°C.[20] The chemical expansion of perovskite materials containing Co and Fe is significantly larger than for similar materials containing Cr. CeO_2 based materials, on the other hand, have significantly larger chemical expansion than perovskite based materials. The chemical expansion can be rationalized by the increase in ionic radii when the cation at B-site in the perovskite structure is reduced from M^{4+} to M^{3+} and/or M^{2+}.[21] For all transition metals, the ionic radii will increase up to 20 %. Volume expansion due to ordering of oxygen vacancies[22] has also been suggested.

We have recently started an experimental program focusing on $La_{0.5}Sr_{0.5}Fe_{1-x}Co_xO_{3-\delta}$ materials. The materials have been characterized with mechanical properties such as fracture strength and toughness,[23] compressive creep performance[24] and finally oxygen flux[25] and long term stability in chemical potential gradients.[26] Here, we report on the thermal properties of $La_{0.5}Sr_{0.5}Fe_{1-x}Co_xO_{3-\delta}$ materials measured by high temperature x-ray diffraction, thermogravimetry and dilatometry. Trends in the thermal behavior, including the chemical expansion of perovskite materials, are discussed in relation to the ionic radii of the transition metals.

Experimental

Materials preparation

$La_{0.5}Sr_{0.5}Fe_{1-x}Co_xO_{3-\delta}$ (x = 0, 0.5 and 1) were synthesized by spray drying. Aqueous solutions of stoichiometric amount cation nitrates (Merck or Fluka, p.a.) were made, and glycine (Merck, p.a.) was added as a complexing agent in a glycine/nitrate mole ratio of 5/9. The content of crystal water in the nitrates was determined by thermogravimetrical analysis. The total concentration of the cations was approximately 0.8 M. The solutions were dried in a Büchi Mini Spray Dryer B-191 with hot air (150°C) as the drying medium. The resulting solid precursors were ignited for decomposition to oxide by allowing it to fall through a vertical alumina tube preheated to 800-900°C. The resulting oxide powders were ball milled (Si_3N_4-balls) overnight in 100% ethanol or isopropanol. The milled powders were further calcined at 900°C (x = 0.5 and 1) or 1000°C/1050°C (x = 0) for 24 h in air. The powders were then ball milled (Si_3N_4-balls) for 24 h, and heat-treated at 600°C for 24 h.

The resulting powders were pressed uniaxially (37 or 60 MPa) into bars or cylinders, which were further pressed cold isostatically at 200 MPa. The materials with (x = 0.5 and 1) were sintered in air at 1150°C for 2 or 12 hours, respectively, while $La_{0.5}Sr_{0.5}FeO_{3-\delta}$ was sintered at 1250°C for 12 hours. To avoid cracking during cooling, the cooling rate after sintering was set to 50°C/h (1150-750°C), 6°C/h (750-450°C) and 100°C/h (450°C-room temperature). The ends of the sintered samples were finally ground parallel to each other and polished before the characterization by dilatometry.

Characterization

The density of the sintered materials was measured by the Archimedean method (ISO 5017) in isopropanol. The densities were, 95, 96, and 99 % for x = 0, 0.5 and 1, respectively. The theoretical densities for the three compositions, determined by x-ray diffraction, were 5.99 g cm^{-3}, 6.29 g cm^{-3} and 6.39 g cm^{-3} respectively.

The oxygen non-stoichiometry at room temperature of both calcined powders and sintered materials was determined by iodometric titration and/or thermogravimetrical analysis in hydrogen atmosphere. The reported oxygen deficiency is the mean value of the two methods. To avoid the influence of humidity, the powders were pre-heated to 500°C immediately before titration/reduction.

Iodometric titration was performed by mixing 100-150 mg of the powders with 0.8 - 1 mg KI and 25 ml deionized distilled water in a round-necked vessel. The vessel was flushed with N_2 gas to avoid air-oxidation of excess I^-. 25 ml of concentrated hydrochloric acid was added to dissolve the sample and the solution was immediate titrated against a 0.05 M sodium thiosulfate solution, using starch as the indicator. Iodometric titration of sintered materials was impossible due to problems to dissolve the samples completely in hydrochloric acid solution within an acceptable time. The uncertainty in the oxygen deficiency is given as the standard deviation of the titration.

Reduction in 5% H_2 in N_2 was performed by heating 250-300 mg of the powders to 1300°C for 24 hours. The total mass loss during reduction as measured gravimetrically and the non-stoichiometry was calculated according to the following reaction.

$$La_{0.5}Sr_{0.5}Fe_{1-x}Co_xO_{3-\delta} \rightarrow$$
$$\tfrac{1}{4}La_2O_3 + \tfrac{1}{2}SrO + (1-x)Fe + xCo + \frac{(3-\delta)-5/4}{2}O_2(g) \qquad (1)$$

The proposed reaction during reduction was confirmed by x-ray diffraction. The uncertainty in the oxygen deficiency by the gravimetrical analysis is estimated to ± 0.005.

Thermogravimetrical analysis (TG) was performed using a Netzsch STA 449C. The measurements were made on the calcined fine-grained powder. The powders were preheated to 500°C prior to the analysis to avoid

humidity. 100-200 mg of samples were heated stepwise (10°C/min) to every 100°C (100 - 500°C) or every 50°C (550 - 1000°C). The holding time for each step was 2 hours (100-650°C) or 1 hour (700-1000°C) in order to establish equilibrium. The same steps were used during cooling, and the loss/absorption of oxygen was measured. The average data from the second heating and cooling cycles in air are reported, while only the second heating cycles in N_2 are reported. Corrections were made for changes in buoyancy with the temperature. Combined with the oxygen non-stoichiometry obtained by titration/reduction at room temperature, the oxygen non-stoichiometry at different temperatures was calculated. The uncertainty at each temperature is estimated to ± 0.01. The partial pressure of oxygen in N_2 during the measurements was estimated to 10^{-4}. The specification of the nitrogen gas gives a maximum oxygen partial pressure of 3 ppm, but this level will be a lower limit due to the evolution of oxygen from the powders during heating.

Thermal expansion of the materials was determined by high temperature X-ray diffraction (HTXRD) and by dilatometry. Dilatometry was performed in air using a Netch DIL 402C. Rectangular bars (5 x 5 mm, length 20-25 mm) or cylinders (d = 8 mm, length ~ 12 mm) were heated to 1000°C with alumina spacers on both ends. The heating and cooling rates were 1°C/min.

HTXRD was carried by a Siemens D5005 θ-θ diffractometer, using $Cu_{K\alpha}$ radiation. Powders were made from sintered materials and were heat-treated in O_2 atmosphere at 400°C for 12 hours and cooled slowly (15°C/h) to room temperature prior to the diffraction experiments. The oxidized powders were then dispersed in isopropanol and applied on a Pt strip located in a high temperature camera (HTK 16, Anton Paar GmbH). Diffraction patterns were collected every 100°C from room temperature up to 1000°C in both air and N_2 atmospheres. The recording of the data delayed for 30 minutes at each temperature to establish equilibrium with the atmosphere. The diffraction data were recorded with a step size of 0.04° and a count time of 10s. The unit cell parameters were refined by the Rietveld method[27] using the Siemens Win-Rietveld programs, V 2.05. Both the perovskite and the platinum reflections were refined, using the cubic space group $Pm\bar{3}m$ or the rhombohedral space group $R\bar{3}c$ for the perovskite and cubic space group $Pm\bar{3}m$ for Pt. A Pearson VII peak shape function was used for both phases. The thermal expansion of Pt, determined from the temperature dependence of unit cell parameter, was in good accord with literature.[28]

Results

Oxygen non-stoichiometry

The oxygen non-stoichiometry, 3-δ, of the materials at room temperature is presented in Table 1. The materials did not oxidize completely during cooling and were oxygen deficient at ambient temperature.

Table 1: Ambient oxygen non-stoichiometry of $La_{0.5}Sr_{0.5}Fe_{1-x}Co_xO_{3-\delta}$ materials.

Composition	Type of powder	3-δ (reduction)	3-δ (iodometric titration)
x = 0	calcined	2.898± 0.005	2.970 ± 0.003
x = 0.5	calcined	2.974± 0.005	2.952 ± 0.005
	sintered	2.915± 0.005	-
x = 1	calcined	2.973± 0.005	2.953 ± 0.005
	sintered	2.913± 0.005	-

Oxygen non-stoichiometry for $La_{0.5}Sr_{0.5}FeO_{3-\delta}$ and $La_{0.5}Sr_{0.5}CoO_{3-\delta}$ is shown as a function of temperature in air and nitrogen in Figure 1. The raw data are given in Appendix I. The ambient oxygen deficiency is the mean value given in Table 1. The oxygen deficiency of $La_{0.5}Sr_{0.5}Fe_{0.5}Co_{0.5}O_{3-\delta}$ measured at several different partial pressures of oxygen is shown as a function of temperature in Figure 2. The oxygen deficiency of the materials is increasing with increasing temperature and decreasing partial pressure of oxygen according to the reaction:

$$La_{0.5}Sr_{0.5}Fe_{1-x}Co_xO_{3-\delta} \rightarrow La_{0.5}Sr_{0.5}Fe_{1-x}Co_xO_{3-\delta'} + \frac{\delta' - \delta}{2}O_2(g) \qquad (2)$$

For both data sets, the average from the second heating and cooling cycles in air and second heating in N_2 are reported due to chemical inhomogeneity of the powders even after calcining. TEM/EDS analysis of individual grains of the calcined powders have shown some variation in the La/Sr ratio.[29] After heat-treating at higher temperatures, the materials become homogeneous and the small deviation from cubic symmetry at ambient temperature become evident.

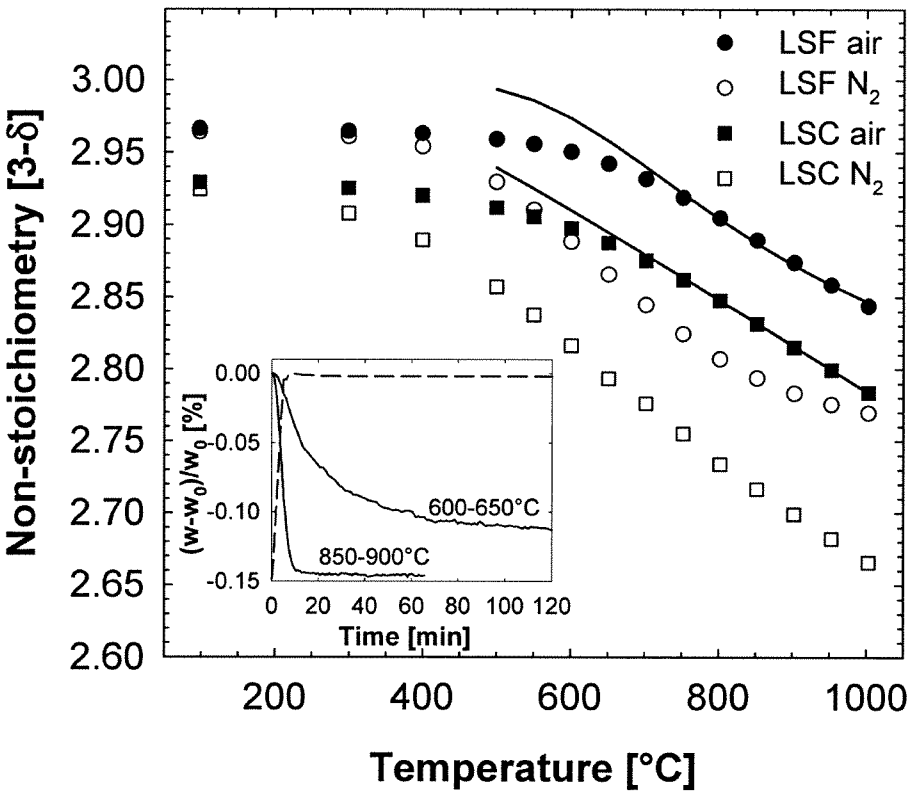

Figure 1: Oxygen non-stoichiometry, 3-δ, of $La_{0.5}Sr_{0.5}FeO_{3-\delta}$ (LSF) and $La_{0.5}Sr_{0.5}CoO_{3-\delta}$ (LSC) in air and in nitrogen atmosphere. The uncertainty in each point is estimated to ± 0.01. The solid lines are models, see text. Insert shows weight loss of LSC versus time for the temperature steps 600-650°C and 850-900°C. The broken line is the temperature profile.

The solid curves in Figure 1 correspond to models for the oxygen non-stoichiometry. In the case of $La_{1-x}Sr_xFeO_{3-\delta}$, the electrons are localized, and a point defect model has been shown to describe the non-stoichiometry.[5, 6, 30] In the $La_{1-x}Sr_xCoO_{3-\delta}$ system, the electrons are delocalized and can been modeled by a rigid band formalism.[7, 8] The line for $La_{0.5}Sr_{0.5}FeO_{3-\delta}$ is obtained by using the following constants in the point defect model; $K_3 = 1 \cdot 10^{-6}$, ΔH = 98.18 kJ/mol and ΔS = 69.81 J/Kmol.[6] In the case of $La_{0.5}Sr_{0.5}CoO_{3-\delta}$, the calculated oxygen non-stoichiometry was obtained by using the following constants; E_{ox} = -281 kJ/mol, S_{ox} = 0.0749 kJ/Kmol and

g(e) = 0.015 $(kJ/mol)^{-1}$. The models describe the oxygen deficiency relatively well at high temperatures. The discrepancy between the models and the experimental data at low temperatures is due to departure from equilibrium behavior. This is illustrated in the insert in Figure 1, where the weight loss versus time at for the steps 600-650°C and 850-900°C is shown. The broken line is the temperature profile. The relaxation time at 600 is significantly longer that at 850°C and the true equilibrium oxygen non-stoichiometry was not obtained below 600-650°C.

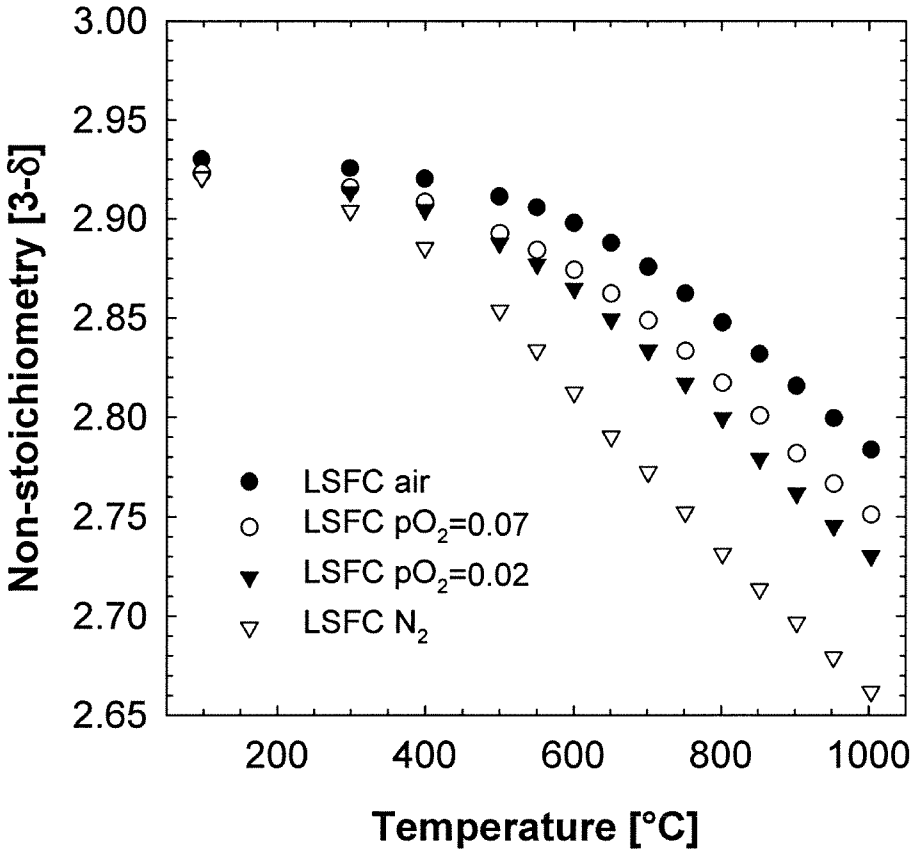

Figure 2: Oxygen non-stoichiometry of $La_{0.5}Sr_{0.5}Fe_{0.5}Co_{0.5}O_{3-\delta}$ (LSFC) as a function of oxygen partial pressure. The uncertainty in each point is estimated to ± 0.01.

Thermal expansion behavior

The HTXRD diffractograms of the powders were refined in the cubic space group $Pm\bar{3}m$ for all the temperatures in both atmospheres. At the lowest temperatures, a small splitting of the peaks indicates slightly rhombohedral distortion. However, the deviation from cubic structure was so small that the cubic refinement was easily performed. In addition to the cubic, the rhombohedral space group $R\bar{3}c$ was used to fit the diffractograms up to 300°C. The results are given in Table 2. Above 300°C the diffraction patters were refined only in the cubic space group $Pm\bar{3}m$ since the rhombohedral splitting of the diffraction lines had vanished. The second order cubic to rhombohedral phase transition of $La_{0.5}Sr_{0.5}Fe_{0.5}Co_{0.5}O_{3-\delta}$ and $La_{0.5}Sr_{0.5}CoO_{3-\delta}$ is located between 300 and 400°C. The phase transition temperature may also to a first approximation be defined as the temperature where the rhombohedral angle becomes 60°. The phase transition temperatures of the two materials according to this approach are 350 ± 50°C respectively. The corresponding phase transition of $La_{0.5}Sr_{0.5}FeO_{3-\delta}$ has been reported at 250 ± 50°C.[20]

Table 2: Rhombohedral unit cell parameters, $a_{rhombohedral}$ and α, and the calculated $a_{pseudo\ cubic}$ as function of temperature obtained from high temperature x-ray diffraction by refining a rhombohedral space group for $La_{0.5}Sr_{0.5}Fe_{1-x}Co_xO_{3-\delta}$.

Composition	Temperature [°C]	$a_{rhombohedral}$	α	$a_{pseudo\ cubic}$
x = 0.5	Rt	5.438	60.13	3.846
	200	5.455	60.09	3.857
	300	5.466	60.05	3.865
x = 1	Rt	5.412	60.17	3.827
	200	5.431	60.07	3.840
	300	5.443	60.01	3.849

The cubic lattice constant for the different materials as function of temperature and atmosphere are summarized in Appendix II. The cubic cell parameters for $La_{0.5}Sr_{0.5}Fe_{0.5}Co_{0.5}O_{3-\delta}$ and $La_{0.5}Sr_{0.5}CoO_{3-\delta}$ are shown as a function of temperature in Figure 3. The lattice constants obtained in both air and in nitrogen atmosphere ($pO_2 = 10^{-4}$ atm) are shown in the figure. The expansion of the lattice become more significant at high temperatures and in nitrogen atmosphere. The linear thermal expansion of the materials were obtained by a linear fit to the data at high and low temperature. The expansion coefficients at different conditions are summarized in Table 3.

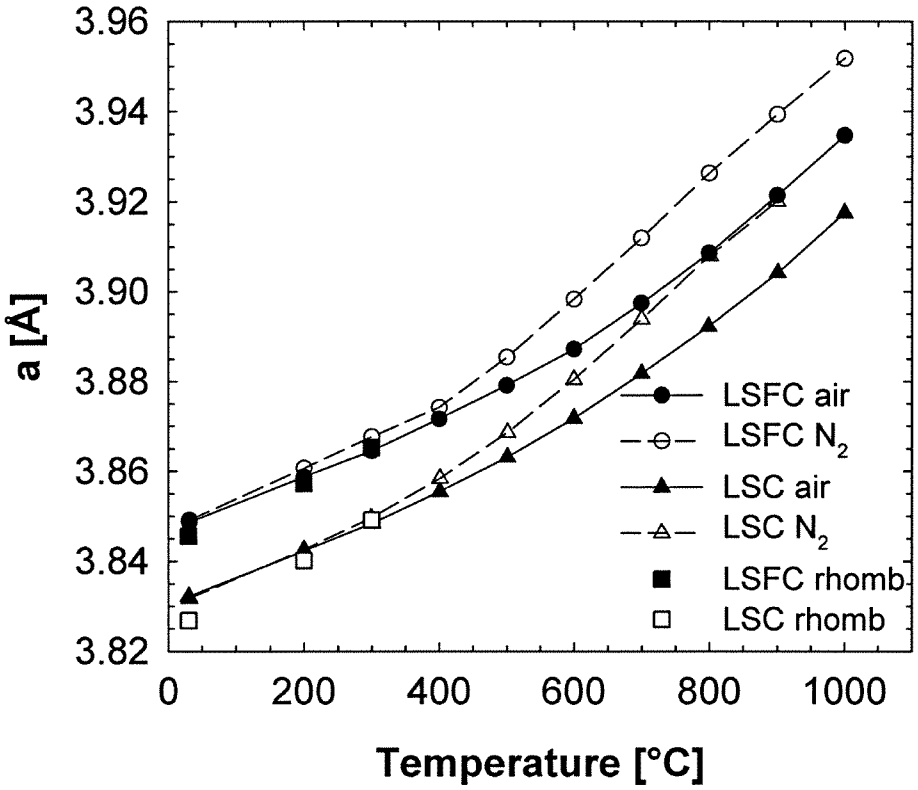

Figure 3: The cubic lattice constant of $La_{0.5}Sr_{0.5}Fe_{0.5}Co_{0.5}O_{3-\delta}$ (LSFC) and $La_{0.5}Sr_{0.5}CoO_{3-\delta}$ (LSC) as a function of temperature in air and in nitrogen atmosphere. The solid and dashed lines are guides to the eye. The squares are the pseudo cubic lattice constant in air obtained from rhombohedral model.

Table 3: Thermal expansion coefficient for $La_{0.5}Sr_{0.5}Fe_{1-x}Co_xO_{3-\delta}$ obtained by dilatometry (α_{dil}) and high temperature x-ray diffraction (α_{xrd}).

Composition	α_{dil} 10^{-6} K^{-1}	α_{xrd} 10^{-6} K^{-1}	Temperature range [°C]	Atmosphere
x = 0	15.31 ± 0.02	13.7 ± 1.0 *)	20-400	Air
	16.09 ± 0.02	22.1 ± 1.1 *)	700-800	Air
	16.30 ± 0.02	16.4 ± 0.3 *)	20-400	N_2
	16.55 ± 0.01	26.3 ± 0.8 *)	700-800	N_2
x = 0.5	16.93 ± 0.01	16.0 ± 0.5	20-400	Air
	28.57 ± 0.009	32.3 ± 0.9	700-1000	Air
	17.70 ± 0.01	17.7 ± 0.1	20-400	N_2
	32.99 ± 0.01	34.4 ± 0.8	700-1000	N_2
x = 1	17.87 ± 0.01	16.3 ± 0.5	20-400	Air
	30.59 ± 0.01	31.1 ± 1.2	700-1000	Air
	17.69 ± 0.02	18.6 ± 0.9	20-400	N_2
	32.72 ± 0.03	34.2 ± 1.3	700-900	N_2

*) From Fossdal et al.[20]

The linear thermal expansion of dense polycrystalline bars measured by dilatometry in air and nitrogen atmosphere is shown in Figure 4. For clarity, the two datasets for $La_{0.5}Sr_{0.5}Fe_{0.5}Co_{0.5}O_{3-\delta}$ and $La_{0.5}Sr_{0.5}CoO_{3-\delta}$ are shifted by 1% and 2 % to distinguish the different compositions. The data for the Co-containing materials demonstrate a clear shift in the thermal expansion at around 600°C. This is related to the onset of the thermal reduction of the materials, see Fig. 1 and 2. The corresponding shift for LSF is observed at higher temperature. Linear thermal expansion coefficients found by liner fit to the data are summarized in Table 3. There is generally a relatively good agreement between the expansion coefficients found by the two different methods.

A shift in thermal expansion coefficient from the first derivative of the dilatometry curves could have indicated the phase transition temperature from rhombohedral to cubic phase. No such shift could be observed and the thermal expansion of the two polymorphs are therefore quite similar.

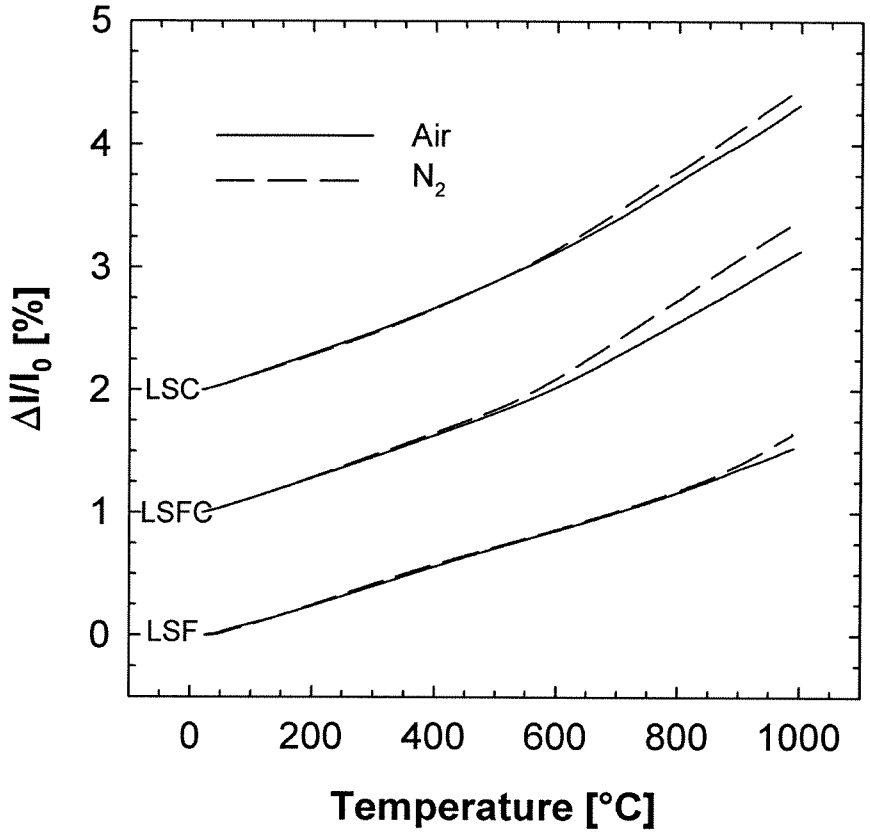

Figure 4: Linear thermal expansion of $La_{0.5}Sr_{0.5}FeO_{3-\delta}$ (LSF), $La_{0.5}Sr_{0.5}Fe_{0.5}Co_{0.5}O_{3-\delta}$ (LSFC) and $La_{0.5}Sr_{0.5}CoO_{3-\delta}$ (LSC) in air and nitrogen atmosphere measured by dilatometry.

Chemical expansion

The chemical expansion contributed to the overall thermal expansion above ~500°C in air and ~400°C in N_2, see Figure 3 and 4. The chemical expansion of the materials, calculated from the lattice constants in air and N_2 atmosphere, is shown in Figure 5 as function of the temperature. Here the chemical expansion is defined as $\varepsilon_c = \Delta a/a_o$, where $\Delta a = a - a_o$ is the change in the unit cell parameter from air to nitrogen at constant temperature. The reference state a_o correspond to the lattice constant in air.

The chemical expansion is increasing with increasing Fe content and seems to go through a maximum at around 800-900°C.

In order to compare different materials the chemical expansion can be normalized by the change in oxygen deficiency, $\varepsilon_c/\Delta\delta$, where $\Delta\delta = \delta - \delta_o$ is the change in the oxygen deficiency from the reference state δ_o. This normalized chemical expansion is also shown in Figure 5.

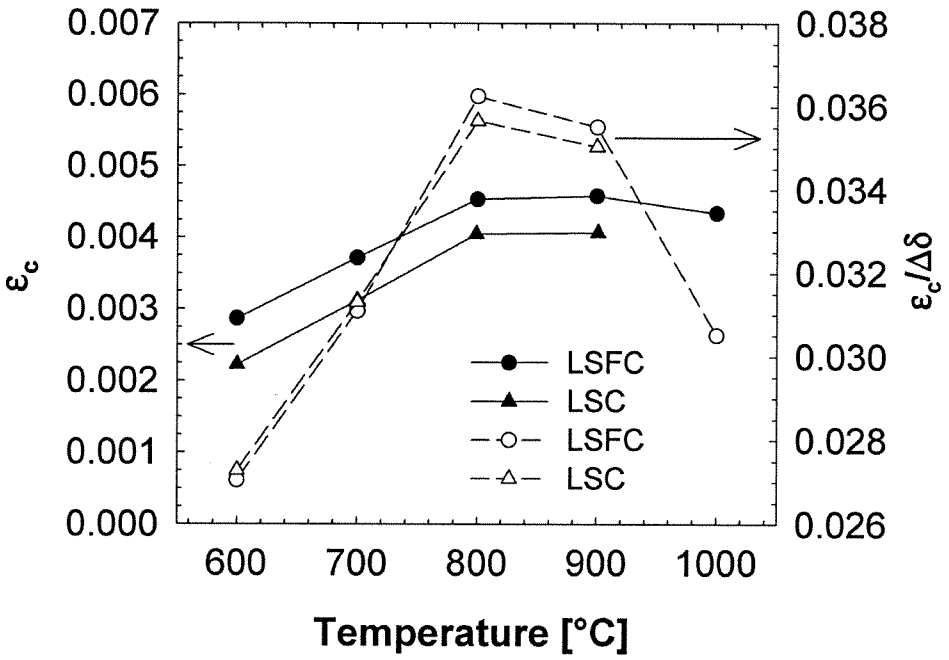

Figure 5: Chemical expansion, ε_c, (filled symbols) and normalized chemical expansion, $\varepsilon_c/\Delta\delta$, (open symbols) of $La_{0.5}Sr_{0.5}Fe_{0.5}Co_{0.5}O_{3-\delta}$ (LSFC) and $La_{0.5}Sr_{0.5}CoO_{3-\delta}$ (LSC) calculated from high temperature x-ray diffraction. The lines are guides to the eyes.

Discussion

Thermal expansion

A near linear expansion (anharmonic vibrations) is observed until ~500°C; the temperature region with essentially constant oxygen non-stoichiometry. The linear expansion coefficient (α) in this region is widely reported in literature. The magnitude of α at room temperature spans over a wide range for $La_{1-x}Sr_xFe_{1-y}Co_yO_{3-\delta}$–materials. Typical values are between 7 and $30 \cdot 10^{-6}$ K^{-1}.[15, 20, 31-33] In general, an increase in the thermal expansion is observed with increasing temperature and decreasing partial pressure of oxygen.

Thermal expansion coefficients have been measured for a whole range of compositions in the low temperature range, but no systematic contribution from chemical expansion at high temperature has appeared. By plotting data for $La_{1-x}Sr_xMO_3$ compositions as a function of Sr-doping on A-site with the B cation constant, there will be a clear increasing tendency with increasing doping concentration as shown in Figure 6. In the upper insert in the figure, ambient thermal expansion of $LaMO_3$ is shown as a function of M, the transition metal. No obvious trend is evident. The magnetic and electronic nature of the materials is probably governing the thermal expansion. Moreover, thermal expansion of materials with constant A-site composition is shown as function of the substitution level on the B-site in $La_{0.8}Sr_{0.2}Fe_{1-x}Co_xO_3$ and $LaCr_{1-x}Co_xO_3$ in the lower insert. Here the thermal expansion changes close to linearly with the substitution level. In this work, the linear thermal expansion coefficient for $La_{0.5}Sr_{0.5}Fe_{1-x}Co_xO_{3-\delta}$ in air and N_2 increase with increasing Co-content, see Table 2.

Chemical expansion

The onset temperature (T_o) is defined as the temperature where the total thermal expansion deviates from the linear (and only thermal) expansion. T_o seems to vary within the different composition, and seems to decrease with increasing Co/Fe-ratio. Fossdal et al.[20] have shown that this onset temperature decreases with increasing Sr/La ratio on A-site in the perovskite structure, and with decreasing partial pressure of oxygen.

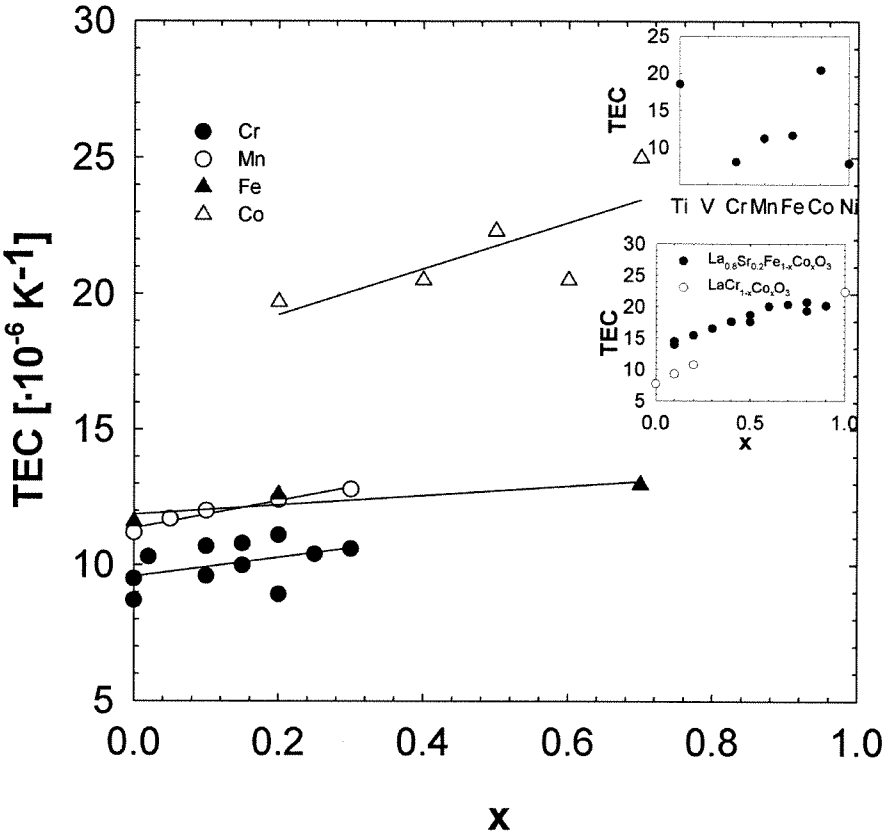

Figure 6: Thermal expansion coefficients (TEC) for $La_{1-x}Sr_xMO_3$ found in literature.[15, 34-40] The upper small plot shows TEC for $LaMO_3$ as a function of position in the periodic table.[20, 35, 41-51] The other small plot show the relationship of Co-doping on B-site in $La_{0.8}Sr_{0.2}Fe_{1-x}Co_xO_3$ [15] and $LaCr_{1-x}Co_xO_3$.[31]

All the materials studied here are nearly stoichiometric at room temperature and onset of thermal reduction is evident around 500°C in air and 400°C in N_2. This behavior is typical for Fe- and Co-containing perovskites.[33, 40, 52] The chemical expansion observed at higher temperatures is a result of the reduction of Fe^{4+} and Co^{4+} to the larger[21] Fe^{3+}, Fe^{2+}, Co^{3+} and Co^{2+} with a resulting increase in oxygen non-stoichiometry. Table 4 shows the $(r_{M^{3+}} - r_{M^{4+}})/r_{M^{4+}}$ radii ratio for the first row transition metals. As we can see, all the M^{3+} cations are larger than the M^{4+} cations and one would expect the reduction of the valence state of the metal ions to be accompanied by a volume expansion.

Table 4: Cation radii and relative radii ratio for the first row transition metals.[21]

Metal	$r_{M^{4+}}$ [Å]	$r_{M^{3+}}$ [Å]	$\frac{r_{M^{3+}} - r_{M^{4+}}}{r_{M^{4+}}}$
Ti	0.605	0.67	0.107
V	0.58	0.64	0.103
Cr	0.55	0.615	0.118
Mn	0.53	0.58 (LS)	0.094
		0.645 (HS)	0.217
Fe	0.585	0.645 (HS)	0.103
		0.55 (LS)	-0.060
Co	0.53 (HS)	0.545 (LS)	0.028
		0.61 (HS)	0.151
Ni	0.48 (LS)	0.6 (HS)	0.250
		0.53 (LS)	0.104

As shown in Figure 5, the chemical expansion, ε_c, increases with temperature until 800°C where it reaches a constant value. Above 900°C, a decrease in chemical expansion is observed. This behavior can be explained based on the assumption that the total thermal expansion will become equal in different atmospheres at high temperatures, when the oxygen vacancy concentration reaches its maximum value corresponding to only three valent transition metal ions. In the case of only Fe on B-site, this is when the vacancy concentration is equal to x/2, where x is the doping of Sr on La-site, corresponding to only Fe(III). In the case of the Co-containing materials the metals will be continuously reduced until they decompose, and a wide region with only Co(III) is not observed.

The chemical expansion will also vary with composition. As Figure 5 shows, for a fixed La/Sr-ratio at given temperatures, the chemical expansion decrease with increasing Co-content on B-site. Variations are also expected with different La/Sr-ratios and substitution of different cations. Reported chemical expansion found in literature show generally that the expansion of perovskite materials containing Co and Fe is almost the same for similar materials containing Cr. CeO_2 based materials, on the other hand, have significantly larger chemical expansion than the perovskite materials.[18]

For materials containing different transition metal ions, the normalized chemical strain is expected to vary. Atkinson et al.[18] have summarized this ratio for different chromites. In the literature, there is also data available for ferrites, cobaltites and compositions with other cations. Table 5 shows the

chemical expansion and normalized chemical expansion $\varepsilon_c/\Delta\delta$ ratio for different materials reported in the literature.

Table 5: Chemical expansion for different compositions found in the literature and the present work.

Composition	ε_c	$\Delta\delta$	$\varepsilon_c/\Delta\delta$	Temp[°C]	Ref.
$La_{0.5}Sr_{0.5}FeO_{3-\delta}$	0.0058	0.097	0.059	800	[20]
$La_{0.5}Sr_{0.5}Fe_{0.5}Co_{0.5}O_{3-\delta}$	0.0045	0.116	0.039	800	This work
$La_{0.5}Sr_{0.5}Fe_{0.5}Co_{0.5}O_{3-\delta}$	0.0043	0.122	0.036	1000	This work
$La_{0.5}Sr_{0.5}CoO_{3-\delta}$	0.0041	0.116	0.035	800	This work
$La_{0.7}Ca_{0.3}CrO_{3-\delta}$	0.0036	0.101	0.036	1000	[19]
$La_{0.7}Ca_{0.3}Cr_{0.9}Al_{0.1}O_{3-\delta}$	0.0040	0.118	0.034	1000	[19]
$La_{0.6}Sr_{0.4}Fe_{0.2}Co_{0.8}O_{3-\delta}$	0.0039	0.180	0.022	800	[39]
$La_{0.8}Sr_{0.2}Cr_{0.97}V_{0.03}O_{3-\delta}$	0.0013	0.044	0.030	1000	[53]
$La_{0.3}Sr_{0.7}FeO_{3-\delta}$	0.0040	0.125	0.032	875	[38]
$La_{0.7}Sr_{0.3}Fe_{0.6}Ga_{0.4}O_{3-\delta}$	0.0015	0.035	0.044	875	[38]
$LaMnO_{3+\delta}$			0.024		[54]
$La_{0.8}Sr_{0.2}CrO_{3-\delta}$			0.024		[53]

Figure 7 shows a plot of $\varepsilon_c/\Delta\delta$ versus $\Delta r/r_o$ for selected perovskite materials, where $\Delta r/r_o$ is the change in cation radii between the different oxidation states. The solid line indicates the expected tendency if only the change in valence for the transition metal ions causes the chemical expansion, and the experimental data show a relatively good correlation. The main contribution to the chemical expansion can therefore be related to the change in the ionic radii when the transition metal is reduced. Other factors which may contribute are for example ordering of oxygen vacancies, but this is out of the scope of the present work.

Chemical induced stresses

Above the onset temperatures for chemical expansion, and at operation temperatures for these materials, the oxygen non-stoichiometry will be quite large. If the materials are placed in a gradient of pO_2, there will be differences in the unit cell volume at each side of the material and the materials are subjected to a chemically induced stress. To describe these stresses, the variation in oxygen non-stoichiometry across the materials is

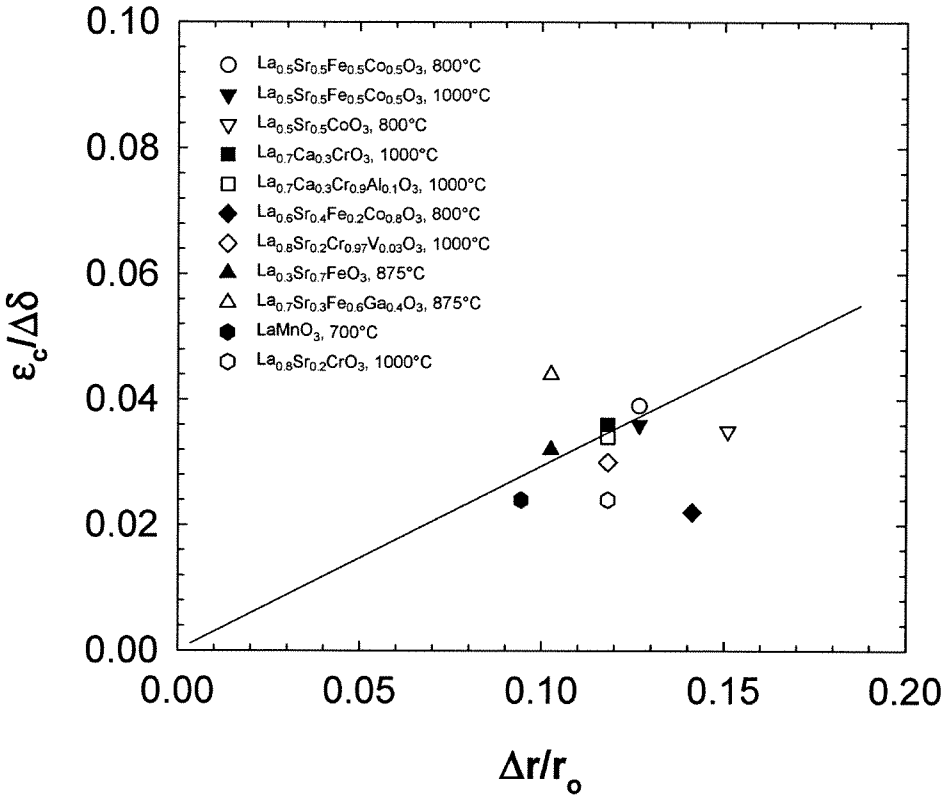

Figure 7: $\varepsilon_c/\Delta\delta$ versus $\Delta r/r_o$ for selected perovskite materials.[This work, 19, 38-39, 53-54] The solid line indicates the expected tendency if only the change in valence for the transition metal ions causes the chemical expansion.

important to investigate. The gradient in oxygen deficiency is dependent on the thickness of the membrane, oxygen diffusion and surface exchange kinetics.[3] The changes in dimensions caused by the increasing oxygen non-stoichiometry are of great importance due to potential applications at operation temperatures. The chemical induced stresses may cause failure of the devices due to creep or fracture, and the mechanical properties of the materials are of grate importance. The fracture strength and toughness and creep resistance of the present materials at the operation temperature will be followed up in two other contributions.

During cooling, an oxidation will take place from the surface of the materials and a stress gradient can easily be obtained. Tensile stresses may occur because of lower unit cell volume at the oxidized surface compared with the bulk. Therefore, cooling is the most critical step for this type of materials. To avoid cracking, a very slow cooling rate is required to allow the material to equilibrate. Most critical is the temperature range around the onset temperature for chemical expansion. Below this temperature, the bulk diffusion of oxygen is quite slow.

Conclusion

Oxygen non-stoichiometry, thermal and chemical expansion of materials $La_{0.5}Sr_{0.5}Fe_{1-x}Co_xO_{3-\delta}$ (x = 0, 0.5, 1) have been determined. Below an onset temperature of ~500°C in air and ~400°C in N_2, the oxygen deficiency remain constant and a linear thermal expansion is observed. At the onset temperature for thermal reduction of the valance state of Co and Fe, the thermal expansion is significantly increased due to the contribution from chemical expansion caused by the reduction of the valence state of Fe/Co. A reduction in the oxygen non-stoichiometry is observed simultaneously. The change in ionic radii of the transition metals is the main reason for the chemical expansion. The thermal expansion coefficient and the chemical expansion increases with increasing temperature and partial pressure of oxygen. The non-linear thermal expansion behavior of the oxygen permeable materials is a major challenge for potential applications for the materials.

Acknowledgement

The Research Council of Norway, Statoil and Hydro are acknowledged for financial support.

References

1. H. J. M. Bouwmeester and A. J. Burgraaf, in: P.J. Gellings and H.J.M. Bouwmeester (Eds), The CRC Handbook of Solid State Electrochemistry, CRC Press, Inc., New York (1997).
2. A. Atkinson and A. Selcuk, "Mechanical behaviour of ceramic oxygen ion-conducting membranes", Solid State Ionics, 134 (2000) 59-66.
3. P. V. Hendriksen, P. H. Larsen, M. Mogensen, F. W. Poulsen and K. Wiik, "Prospects and problems of dense oxygen permeable membranes", Catalysis Today, 56 (2000) 283-295.
4. J. Wolfenstine, K. C. Goretta, R. E. Cook and J. L. Routbort, "Use of diffusional creep to investigate mass transport in (La, Sr)MnO_3", Solid State Ionics 92 (1996) 75-83.
5. J. E. ten Elshof, H. J. M. Bouwmeester and H. Verweij, "Oxygen transport through $La_{1-x}Sr_xFeO_{3-\delta}$ membranes. I. Permeation in air/He gradients", Solid State Ionics, 81 (1995) 97-109.
6. J. Mizusaki, M. Yoshihiro, S. Yamauchi and K. Fueki, "Nonstoichiometry and Defect Structure of the Perovskite-Type Oxides $La_{1-x}Sr_xFeO_{3-\delta}$", J. Solid State Chem., 58 (1985) 257-266.
7. M. H. R. Lankhorst, H. J. M. Bouwmeester and H. Verweij, "High-Temperature Coulometric Titration of $La_{1-x}Sr_xCoO_{3-\delta}$: Evidence for the Effect of Electronic Band Structure on Nonstoichiometry Behavior", J. Solid State Chem., 133 (1997) 555-567.
8. J. Mizusaki, Y. Mima, S. Yamauchi, K. Fueki and A. Tagawa, "Nonstoichiometry of the Perovskite-Type Oxides $La_{1-x}Sr_xCoO_{3-\delta}$", J. Solid State Chem., 80 (1989) 102-111.
9. J. Mizusaki, "Nonstoichiometry, diffusion, and electrical properties of perovskite-type oxide electrode materials", Solid State Ionics, 52 (1992) 79-91.
10. W. Sitte, E. Bucher and W. Preis, "Nonstoichiometry and transport properties of strontium-substituted lanthanum cobaltites", Solid State Ionics, 154-155 (2002) 517-522.
11. A. N. Petrov, V. A. Cherepanov, O. F. Kononchuk and L. YA. Gavrilova, "Oxygen Nonstoichiometry of $La_{1-x}Sr_xCoO_{3-d}$ ($0 < x < 0.6$)", J. Solid State Chem., 87 (1990) 69-76.
12. M. H. R. Lankhorst and H. J. M. Bouwmeester, "Determination of Oxygen Nonstoichiometry and Diffusivity in Mixed Conducting Oxides by Oxygen Coulometric Titration. II. Oxygen Nonstoichiometry and Defect Model for $La_{0.8}Sr_{0.2}CoO_{3-\delta}$", J. Electrochem. Soc., 144 [4] (1997) 1268-1273.

13. M. Katsuki, A. Wang, M. Dokiya and T. Hashimoto, "High temperature properties of $La_{0.6}Sr_{0.4}Co_{0.8}Fe_{0.2}O_{3-\delta}$ oxygen nonstoichiometry and chemical diffusion constant", Solid State Ionics, 156 (2003) 453-461.
14. D. Mantzavinos, A. Hartley, I. S. Matcalfe and M. Sahibzada, "Oxygen stoichiometries in $La_{1-x}Sr_xCo_{1-y}Fe_yO_3$ perovskites at reduced oxygen partial pressures", Solid State ionics, 134 (2000) 103-109.
15. L.-W. Tai, M. M. Nasrallah, H. U. Anderson, D. M. Sparlin and S. R. Sehlin, "Structure and electrical properties of $La_{1-x}Sr_xCo_{1-y}Fe_yO_3$. Part 2. The system $La_{1-x}Sr_xCo_{0.2}Fe_{0.8}O_3$", Solid State Ionics, 76 (1995) 273-283.
16. S. B. Adler, "Chemical Expansivity of Electrochemical Ceramics", J. Am. Ceram. Soc., 84 [9] (2001) 2117-2119.
17. J. Mizusaki, M. Yoshihiro, S. Yamauchi and K. Fueki., "Nonstoichiometry and defect structure of the perovskite-type oxides $La_{1-x}Sr_xFeO_{3-\delta}$", J. Solid State Chem., 58 (1985) 257-266.
18. A. Atkinson and T. M. G. M. Ramos, "Chemically-induced stresses in ceramic oxygen ion-conducting membranes", Solid State Ionics, 129 (2000) 259-269.
19. T. R. Armstrong, J. W. Stevenson, L. R. Pederson and P. E. Raney, "Dimensional Instability of Doped Lanthanum Chromite", J. Electrochem. Soc., 143 [9] (1996) 2919-2925.
20. A. Fossdal, M. Menon, I. Værnhus, K. Wiik, M.-A. Einarsrud and T. Grande, "Crystal structure and thermal expansion of $La_{1-x}Sr_xFeO_{3-\delta}$ materials", J. Am. Ceram. Soc., 87 [10] (2004) 1952-1958.
21. R. D. Shannon, "Revised effective ionic radii and systematic studies of interatomic distances in halides and chalcogenides", Acte Cryst., A32 (1976) 751-767.
22. Kharton VV, Kovalevsky AV, Tsipis EV, Viskup AP, Naumovich EN, Jurado JR, Frade JR, "Mixed conductivity and stability of A-site-deficient $Sr(Fe,Ti)O_{3-\delta}$ perovskites", J. Solid State Electrochem., 7 (2002) 30-36.
23. H. L. Lein, E. Lara-Curzio, Ø. S. Andersen, P. E. Vullum, R. Holmestad, M.-A. Einarsrud and T. Grande, "Mechanical properties of $La_{0.5}Sr_{0.5}Fe_{1-x}Co_xO_{3-\delta}$ ($0 \leq x \leq 1$) materials", paper III.
24. H. L. Lein, E. Lara-Curzio, K. Wiik, M.-A. Einarsrud and T. Grande, "High temperature creep behavior of $La_{0.5}Sr_{0.5}Fe_{1-x}Co_xO_{3-\delta}$ ($0 \leq x \leq 1$) materials", paper II
25. H. L. Lein, K. Wiik and T. Grande, "Oxygen permeation of $La_{0.5}Sr_{0.5}Fe_{1-x}Co_xO_{3-\delta}$ ($0 \leq x \leq 1$) materials", paper IV.
26. H. L. Lein, K. Wiik and T. Grande, "Cation demixing of $La_{0.5}Sr_{0.5}Fe_{1-x}Co_xO_{3-\delta}$ ($0 \leq x \leq 1$) materials", paper V.
27. H. M. Rietveld, "A profile refinement method for nuclear and magnetic structures", J. Appl. Cryst. 2, 2 (1969) 65.

28. J. W. Edwards, R. Speiser and H. L. Johnston, "High Temperature Structure and Thermal Expansion of Some Metals as Determined by X-Ray Diffraction Data. I. Platinum, Tantalum, Niobium, and Molybdenum", J. Appl. Phys., 22 [4] (1951) 424-428.
29. P. E. Vullum, Project work, Department of Physics, Norwegian University of Science and Technology, 2000.
30. J. Nowotny and M. Rekas, "Defect Chemistry of (La,Sr)MnO_3", J. Am. Ceram. Soc., 81 [1] (1998) 67-80.
31. B. Gilbu, H. Fjellvåg and A. Kjekshus, "Properties of $LaCo_{1-t}Cr_tO_3$. I. Solid Solubility, Thermal Expansion and Structural Transition", Acta Chemica Scandinavica, 48 (1994) 37-45.
32. V. V. Kharton, V. N Tikhonovich, S.B. Li, E. N Naumovich, A. V. Kovalevsky, A. P. Viskup, I.A. Bashmakov and A. A. Yaremchenko, "Ceramic microstructure and oxygen permeability of $SrCo(Fe,M)O_{3-\delta}$ (M = Cu or Cr) perovskite membranes", J. Electrochem. Soc., 145 (1998) 1363-1373.
33. V. V. Kharton, A. A. Yaremchenko, A. V. Kovalevsky, A. P. Viskup, E. N. Naumovich and P. F. Kerko, "Perovskite-type oxides for high-temperature oxygen separation membranes", J. Membr. Sci., 163 (1999) 307-317.
34. N. G. Minh, "Ceramic Fuel Cells", J. Am. Ceram. Soc, 76 [3] (1993) 563-588.
35. S. Srilomsak, D. P. Schilling, H. U. Anderson, in: S. C. Singhal (Ed.), Proceedings of the First International Symposium on Solid Oxide Fuel Cells, The Electrochemical Society, Pennington, NJ, 1989.
36. P. Duran, J. Tartaj, F. Capel and C. Moure, "Formation, sintering and thermal expansion behavior of Sr- and Mg – doped $LaCrO_3$ as AOFC interconnector prepared by the ethylene glycol polymerized complex solution synthesis method", J. Euro. Ceram. Soc., 24 (2004) 2619-2629.
37. J. W. Fergus, "Lanthanum chromite-based materials for solid oxide fuel cell interconnects", Solid State Ionics, 171 (2004) 1-15.
38. V. V. Kharton, A. A. Yaremchenko, M. V. Patrakeev, E. N Naumovich and F. M. B. Marques, "Thermal and chemical induced expansion of $La_{0.3}Sr_{0.7}(Fe,Ga)O_{3-\delta}$ ceramics", J Euro. Ceram. Soc, 23 (2003) 1417-1426.
39. S. Wang, M. Katsuki, M. Dokiya and T. Hashimoto, "High temperature properties of $La_{0.6}Sr_{0.4}Co_{0.8}Fe_{0.2}O_{3-\delta}$ phase structure and electrical conductivety", Solid State Ionics, 159 (2003) 71-78.
40. H. Ullmann, N. Trofimenko, F. Tietz, D. Stöver and A. Ahmad-Khanlou, "Correlation between thermal expansion and oxide ion transport in mixed conducting perovskite-type oxides for SOFC cathodes", Solid State Ionics, 138 (2000) 79-90.

41. M. M Nasrallah, J. D. Carter, H. U. Anderson and R. Koc, in: Proceedings of the Second International Symposium on Solid Oxide Fuel Cells. Commission of The European Communities, Luxembourg, 1991.
42. V. V. Kharton, A. A. Yaremchenko and E. N. Naumovich, "Research on the electrochemistry of oxygen ion conductors in the formed Soviet Union. II. Perovskite-related oxides", J. Solid State Electrochem. 3 (1999) 303-326.
43. M. Mori and Y. Hiei, "Thermal Expansion Behavior of Titanium-Doped La(Sr)CrO_3 Solid Oxide Fuel Cell Interconnects", J. Am. Ceram. Soc., 84 [11] (2001) 2573-2578.
44. M. Mori, Y. Hiei and T. Yamamoto, "Control of the Thermal Expansion of Strontium-Doped Lanthanum Chromite Perovskites by B-site Doping for High-Temperature Solid Oxide Fuel Cell Separators", J. Am. Ceram. Soc., 84 [4] (2001) 781-786.
45. H. Hayashi, M. Watanabe and H. Inaba, "Measurement of thermal expansion coefficient of $LaCrO_3$", Thermichimica Acta, 359 (2000) 77-85.
46. N. Sakai and S. Stølen, "Heat capacity and thermodynamic properties of lanthanum(III) chromate(III): $LaCrO_3$, at temperatures from 298.15 K. Evaluation of the thermal conductivity", J. Chem. Thermodynamics, 27 (1995) 493-506.
47. C. S. Montross, H. Yokogawa and M. Dokiya, "Thermal stresses in planar solid oxide fuel cells due to thermal expansion differences", Br. Ceram. Trans., 101 [3] (2002) 85-93.
48. W. Ma, G. Xie and H. Wang, "Thermal Expansion Behavior of $La_{1-x}Sr_xMn_{1-y}Co_yO_{3-\delta}$ Perovskites", J. Mater. Sci. Technol., 18 [3] (2002) 286-287.
49. B. Yan, J. Zhang and J. Liu, "Thermal Expansion of $LaCoO_3$", J. Rare Earths", 22 [2] (2004) 259-262.
50. J. Hemberger, H. A. Krug von Nidda, V. Fritsch, J. Deisenhofer, S. Lobina, T. Rudolf, P. Lunkenheimer, F. Lichtenberg, A. Loidl, D. Bruns ans B. Büchner, "Evidence for Jahn-Teller distortions at the Antiferromagnetic transition in $LaTiO_3$", Phys. Rev. Lett., 91 [6] (2003) 066403.
51. M. Cwik, T. Lorenz, J. Baier, R. Müller, G. André, F. Bourée, F. Lichtenberg, A. Freimuth, R. Smitz, E. Müller-Hartmann and M. Braden, "Crystal and magnetic structure of $LaTiO_3$: Evidence for nondegenerate t_{2g} orbitals", Phys. Rew. B, 68 (2003) 060401.
52. V. V. Kharton, A. V. Kovalevsky, ,A. P. Viskup, J. R. Jurado, F. M. Figueiredo, E. N Naumovich and J. R. Frade, "Transport Properties and Thermal Expansion of $Sr_{0.97}Ti_{1-x}Fe_xO\ O_{3-\delta}$ (x = 0.2-0.8), J. Solid State Chem., 156 (2001) 437-444.

53. A. Zuev, L. Singheiser and K. Hilpert, "Defect structure and isothermal expansion of A-site and B-site substituted lanthanum chromites", Solis State Ionics, 147 (2002) 1-11.
54. S. Miyoshi, J.-O. Hong, K. Yashiro, A. Kaimai, Y. Nigara, K. Kawamura, T. Kawada and J. Mizusaki, "Lattice expansion upon reduction of perovskite-type $LaMnO_3$ with oxygen-deficit nonstoichiometry", Solid State Ionics 161 (2003) 209-217.

PAPER II

High temperature creep behavior of $La_{0.5}Sr_{0.5}Fe_{1-x}Co_xO_{3-\delta}$ ($0.5 \leq x \leq 1$) materials

Hilde Lea Lein, [a] Edgar Lara-Curzio, Kjell Wiik,
Mari-Ann Einarsrud and Tor Grande*

Department of Materials Technology,
Norwegian University of Science and Technology,
7491 Trondheim, Norway.

[a] High Temperature Materials Laboratory,
Oak Ridge National Laboratory,
Oak Ridge TN 37831, USA

Abstract

Steady state compressive creep rate was measured in $La_{0.5}Sr_{0.5}Fe_{0.5}Co_{0.5}O_{3-\delta}$ (LSFC) and $La_{0.5}Sr_{0.5}CoO_{3-\delta}$ (LSC) materials at temperatures between 900 and 1050°C and stresses from 5 to 28 MPa. The stress exponent has been found to be close to unity for both materials while the apparent activation energy for creep was considerably higher for LSC (619 ± 56 kJ/mol) than for LSFC (392 ± 28 kJ/mol). The grain size exponent for LSC was determined to be 1.28 ± 0.14. Considerably higher creep rates were observed for both materials in N_2 atmosphere at 900°C compared to air. Based on the present findings possible creep relaxation of mechanical or chemical induced stresses in oxygen permeable membranes have been addressed, especially at reducing conditions.

* Correspondence to Tor.Grande@material.ntnu.no

Introduction

$La_{1-x}Sr_xFe_{1-y}Co_yO_{3-\delta}$ materials have recently received considerable attention due to their combined electronic and ionic conductivity at elevated temperatures. They are potential candidates for oxygen permeable membranes, gas sensors and electrodes in high temperature electrochemical devices.[1-3] Oxygen permeable membranes are of particular interest for production of syngas ($CO + H_2$) by direct conversion of methane or for oxygen production from air.[1, 4]

Chemical, thermal and mechanical stability of the materials are important for the utilization of such devices.[5] They must be chemical compatible with supports, tolerate thermal cycling during preparation and operation, and have sufficient mechanical properties. The creep resistance is important for the dimensional stability of the devices. Considerable mechanical stresses may be present due to chemically induced stresses and gradient in the absolute pressure across membranes. Creep relaxation may also to some extent be beneficial to avoid failure. For this reasons the creep performance of the materials in various atmospheres is of importance. Creep data are also fundamentally of importance for the understanding of cation diffusion in these materials and related phenomena such as sintering and grain growth.[6-15]

Several studies of the creep performance in perovskite materials have been performed. Kleveland et al.[12] measured creep behavior in Sr-deficient and Sr-excess $SrFeO_{3-\delta}$ materials in the temperature range 800-1000°C in air. The stress exponent for these materials was close to unity, and the activation energy was 260 ± 30 kJ/mol. The creep rate is faster in the Sr-deficient material compared to the Sr-excess material.

A few studies have been investigating titanates. Park et al.[10] measured creep behavior in $BaTiO_3$ in the temperature range 1200-1300°C by varying partial pressure of oxygen and grain size. The stress exponent was 1 and the grain size exponent 2. Obtained activation energy was 720 kJ/mol. The assumed mechanism for creep was grain boundary sliding accommodated by lattice cation diffusion. Carry et al.[16] measured a stress exponent of 2 and an activation energy of 800 kJ/mol in the temperature range 1150-1250°C for fine-grained $BaTiO_3$. Wang et al.[17] have measured compressive creep in single crystals of $SrTiO_3$ in the temperature range 1250-1520°C. They found a stress exponent of 3.5 ± 0.1. A strong plastic anisotropy is observed, and the creep is easier along the <110> orientation than the <100> orientation. Simultaneously, the activation energy is higher for the <100> orientation

(730-770 kJ/mol) compared to the <110> orientation (620 kJ/mol). They also investigated the effect of different atmospheres, and found differences between the two orientations by a stronger relationship between creep and atmosphere for low partial pressures of oxygen in the <110> orientation. Wang et al.[18] investigated also creep in $YAlO_3$ single crystals in the temperature range 1490-1610°C and found the same anisotropic effects as for the $SrTiO_3$ single crystals.

Several authors have reported creep data for Sr-substituted $LaMnO_3$. Cook et al. [11] investigated creep for 10, 20 and 30% Sr-doped $LaMnO_3$ as a function of partial pressure of oxygen at 1250°C. They found that the materials were deformed by grain-boundary sliding accommodated by lattice diffusion. Depending on partial pressure of oxygen and Sr-concentration, either cation vacancies or oxygen vacancies controlled the creep rate. Wolfenstine et al.[19] measured compressive creep behavior of $La_{0.9}Sr_{0.1}MnO_3$ between 1150-1300°C in air. They found a creep exponent close to unity and the activation energy was 490 kJ/mol. The deformation was controlled by a diffusional creep mechanism by lattice diffusion of cations, either La or Mn. Wolfenstine et al.[5] investigated further other Sr-doped $LaMnO_3$ materials in the temperature range 1150-1300°C, and found out that the steady-state creep rate decreased with decreasing Sr content. The mechanism for creep was the same as for $La_{0.9}Sr_{0.1}MnO_3$.[19]

Luecke et al.[20] measured creep in four-point bending for $(La_{0.9}Sr_{0.1})_zGa_{0.8}Mg_{0.2}O_{3-\delta}$ (z = 1.0, 0.98 and 0.95) in the temperature range 950-1350°C. The stress exponent for all compositions was 1.49 ± 0.10 and the activation energy was 426 ± 9 kJ/mol. The inverse grain size exponent was dependent of the composition (z) and calculated to 3.1 (z = 0.98) and 1.9 (z = 0.95).

Wolfenstine et al.[6, 21-22] investigated the creep rate in $La_{0.8}Sr_{0.2}Ga_{0.85}Mg_{0.15}O_{2.825}$ and compared the results of this composition to cubic zirconia. The temperature range for creep measurements in $La_{0.8}Sr_{0.2}Ga_{0.85}Mg_{0.15}O_{2.825}$ was 1200-1300°C and they found a stress exponent close to unity and an activation energy of 521 ± 15 kJ/mol. The creep rate is controlled by cation lattice diffusion. They compared the creep behavior at 1300°C with cubic zirconia at the same temperature, and found out that the creep rate of zirconia is about 25 times lower.

Majkic et al.[9, 23-24] investigated the creep behavior in $SrCo_{0.8}Fe_{0.2}O_{3-x}$ materials with different grain size in the temperature range 850-975°C in air. The stress exponent was close to unity in the low stress range, indicating diffusion controlled creep. In the high stress range, the stress exponent is

temperature dependent and measured to 2.2 - 2.9. This increase from unity indicates that the material undergoes a transition from diffusion to dislocation creep in this stress range. The activation energy is determined to 457 kJ/mol below 925°C and 268 kJ/mol above 925°C. The values indicate a cation diffusion controlled creep. The change in activation energy indicates that the A and B site cations switch being the rate controlling specie. The inverse grain size exponent resulting from a linear fit to the data has been found to be close to unity.

The creep behavior for $La_{0.2}Sr_{0.8}Fe_{0.8}Cr_{0.2}O_{3-\delta}$ in the temperature range 1100-1200°C with different grain size and in different pO_2-atmospheres, was investigated by Majkic et al.[25-28] In air, a stress exponent of 1.4 in the lower stress range indicates diffusion-controlled creep. In the higher stress range, the material undergoes a transition from diffusion to power-law creep. The diffusion is controlled by the slowest cation with an activation energy of 566 kJ/mol. The inverse grain exponent in air is found to be 2.3 and indicates diffusion mainly through the bulk. The creep behavior is characterized by an oxygen partial pressure exponent of $m = 0.04$ at $pO_2 > 10^{-11}$ atm. At even lower pO_2, the creep rates increases and the behavior is characterized by an oxygen partial pressure exponent of -0.5. At the same time, the activation energy increases from values between 532 and 479 kJ/mol in the $m = 0.04$ pO_2-range to 885 kJ/mol in the $m = -0.5$ pO_2-range. The inverse grain exponent changes with changing pO_2 to 2.07 in the $m = -0.5$ pO_2-range and indicates that the contribution of bulk diffusion changes from predominant to nearly pure bulk diffusion.

We have recently started an experimental program focusing on $La_{0.5}Sr_{0.5}Fe_{1-x}Co_xO_{3-\delta}$ materials. The materials have been characterized with respect to thermal expansion, chemical expansion and oxygen stoichiometry,[29] mechanical properties such as fracture strength and toughness [30] and oxygen permeation and long term stability in chemical potential gradients.[31-32] Here we report on the compressive creep performance of the corresponding materials. The stress exponent, the inverse grain size exponent, the oxygen partial pressure exponent and the activation energy are found, and the mechanism for creep discussed.

Experimental

Materials preparation and characterization

$La_{0.5}Sr_{0.5}Fe_{1-x}Co_xO_{3-\delta}$ (x = 0.5 (LSFC) and 1 (LSC)) powders were synthesized by a modified glycine-nitrate method and calcined as described previously.[29]

The powders were single phase according to X-ray diffraction, but thermogravimetry showed a weight loss around 920°C due to the phase transition of Co_3O_4 to CoO. The Co_3O_4 content was determined by using the weight loss obtained while heating crushed sintered samples (2°C/min) to 1100°C. The results are summarized in Table 1. The density of the cylinders was measured by the Archimedean method (ISO 5017) in isopropanol and the result is summarized in Table 1. The theoretical densities used were 6.29 g cm^{-3} (LSFC) and 6.42 g cm^{-3} (LSC), calculated from x-ray diffraction patterns and oxygen non-stoichiometry. The oxygen non-stoichiometry, δ, at room temperature is found for both materials by iodometric titration and reduction in hydrogen.[29] The characteristics of the two materials are given in Table 1.

Table 1: Density, oxygen non-stoichiometry and Co_3O_4-content in $La_{0.5}Sr_{0.5}Fe_{1-x}Co_xO_{3-\delta}$.

Composition	Label	Co_3O_4 [wt%]	Density [%]	3-δ
x = 0.5	LSFC	0.99	97	2.963 ± 0.016
x = 1	LSC	0.98	99	2.963 ± 0.014

Calcined powders were pressed uniaxially into cylinders (diameter 10 mm, 60 MPa), which were finally pressed isostatically at 200 MPa. The relative green densities obtained were 52-54 %. LSFC was sintered in air at 1150°C for 12 hours. LSC was sintered in air at 1150°C for 12 hours and at 1250°C for 36 hours in order to obtain samples with different grain size. The heating rate was 200°C/h. To avoid cracking during cooling, the cooling rates were 50°C/h (1150/1250-750°C), 6°C/h (750-450°C) and 100°C/h (450°C-room temperature).

The end faces of the cylinders were grinded to a height-to-diameter ratio of approximately 2:1 and polished (until diamond size of 1 μm) to verify parallelism. The uncertainty in sample height is measured to ± 20 μm.

X-ray powder diffraction (XRD) of powders and crushed sintered samples was performed on a Siemens D5005 diffractometer (CuKα radiation) in the 2θ range 20-80° with a 0.030° step and step time 8 s. Investigation of the calcined powders and crushed sintered samples showed single phase materials. The cubic cell parameters obtained from the diffraction patterns for powder calcined at 900°C were 3.842 ± 0.001 Å and 3.833 ± 0.002 Å for LSFC and LSC, respectively.

Microstructural analysis was performed using a Hitachi S3500 N scanning electron microscope. The grain size was measured by a linear intercept method after thermal etching (1130°C, 0.2 h). Ten SEM images were taken from different parts of the polished and etched surfaces of sintered samples. The number of grain boundaries of six different lines at constant distance across the pictures was counted and the grain size was calculated. Here, we have assumed that the grain size is equal to the intercept length without further notice. The microstructure of samples after creep measurements was investigated by SEM. Samples of both compositions were polished and thermally etched after the creep experiments to look for differences in grain shape.

Experimental setup

The setups for the compression creep tests in different atmospheres are shown in Figures 1 and 2. For the setup in air atmosphere, the samples were placed between two alumina push-rods. The specimen and the push-rods were heated to set-point temperature with a resistance-heated furnace (80 mm vertical hot zone). A thermocouple was positioned close to the specimen and controlled the temperatures to ± 1°C by a Yokogawa LIP550E controller. Another thermocouple was also positioned close to the specimen, and operated as a safety thermocouple connected to a Yokogawa UT350L controller. A high temperature capacitive extensometer (Instron) was used to measure the displacement of the push-rods. A load cell was griped to the lower alumina tube and controlled the load.

For the measurements in inert atmosphere, the specimens were placed between two SiC push-rods. The upper push-rod had a hole in the end towards the specimen. Between the specimen and this hole, a semi-spherical piece of WC was placed to intercept possible variations in the parallelism of the specimen. The sample and the push-rods were placed in a furnace with

carbon heating element inside a controlled atmosphere chamber. A thermocouple was positioned close to the specimen and controlled the temperature to ± 1°C by a Yokogawa UP550E controller. A high temperature capacitive extensometer (Instron) was used to measure the displacement of the push-rods. A load cell, which was gripped to the upper push rod, controlled the load.

The test temperatures were 900, 950, 1000°C and 1050°C in air and 900°C in N_2. The stress was increased in steps of 5 MPa from 5 MPa to 25 MPa. In addition, a stress of 28 MPa was used for some of the measurements. Before terminating the measurements, the load was again set to 5 MPa (labeled 5 MPa-2). At each stress level, the specimens were kept at constant stresses for 24 h and the strains were measured. The creep rates were calculated from data points between 18 and 24 h for every stress level. In addition, stress relaxations were measured by exposing the sample to 25 MPa before keeping the strain constant and let the stress relax as a function of time. These results are given in Appendix III. For all creep rate data, the engineering strain is calculated. The strains were not large enough to give any differences between true strain and engineering strain.

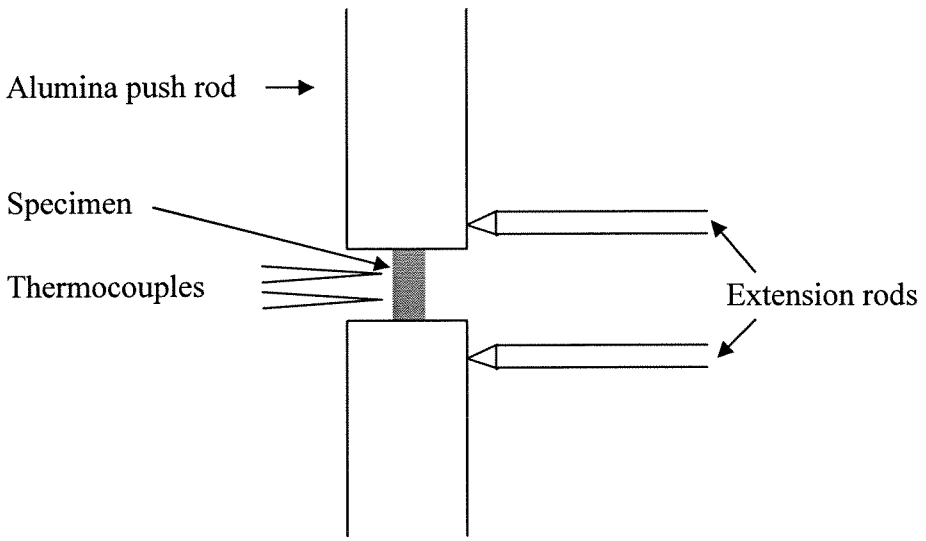

Figure 1: Schematic drawing of compression creep tests in air. Cylindrical specimens were used.

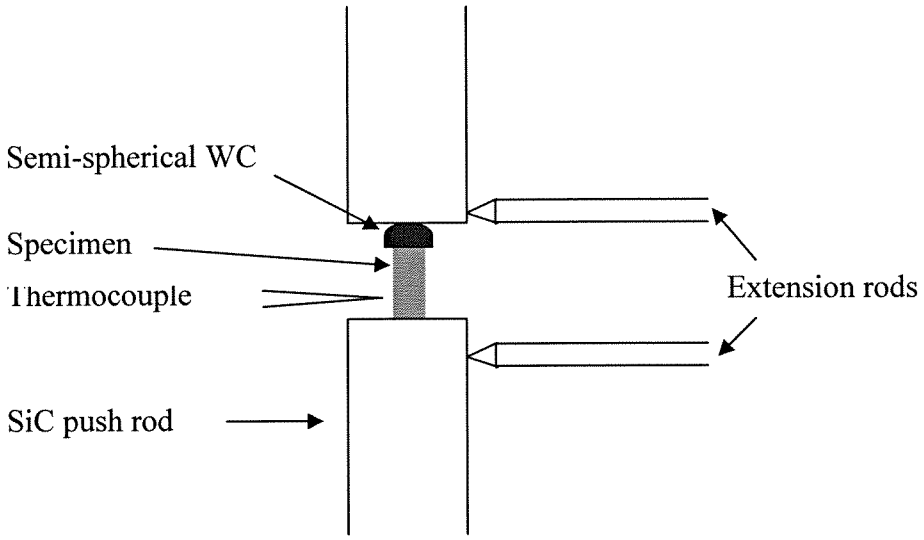

Figure 2: Schematic drawing of compression creep tests in N_2. Cylindrical specimens were used.

Results

Phase composition and microstructure

Figure 3 a) shows a SEM image of the LSC material sintered at 1150°C and then thermally etched. The average grain sizes are given in Table 2.

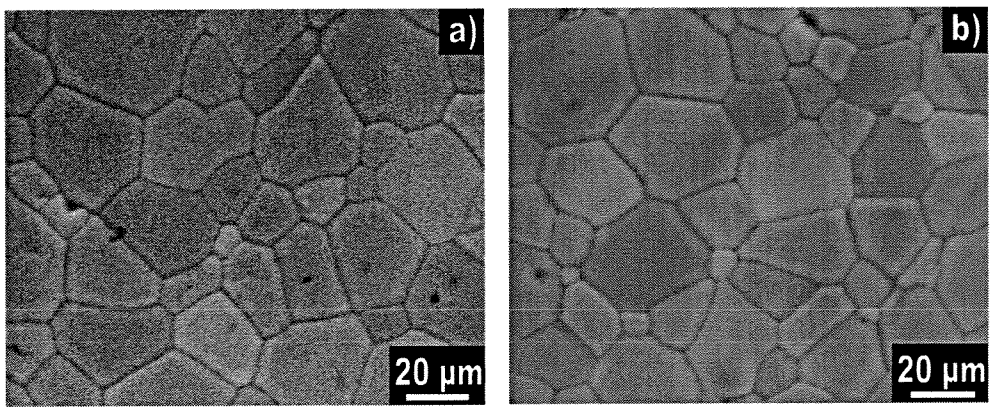

Figure 3: Microstructure of thermally etched $La_{0.5}Sr_{0.5}CoO_{3-\delta}$ (LSC1) material. a) Sintered at 1150°C and b) after creep measurements.

Table 2: Average grain size for $La_{0.5}Sr_{0.5}Fe_{1-x}Co_xO_{3-\delta}$ sintered at different temperatures.

Composition	Sintering temperature [°C]	Grain size before creep [μm]	Grain size after creep [μm]
LSFC	1150	1.1 ± 0.2	1.5 ± 0.2
LSC1	1150	1.7 ± 0.4	2.2 ± 0.4
LSC2	1250	10.3 ± 2.6	-

Figure 3b) shows an etched surface of a LSC bulk sample. As seen, there are no changes in the grain shape compared to before creep measurements. The grain sizes after creep are given in Table 2. This means that there is no significant grain growth in any of the compositions during creep, and the creep rates are not affected by it.

Previous TEM investigations[30] have shown that the secondary phase Co_3O_4, which transforms to CoO above 920°C in air, was observed as ~0.5 μm grains located at grain boundaries. The low content of cobalt oxide is assumed to have insignificant effect on the creep performance, except the effect of Co-excess on the grain boundary chemistry as discussed further below.

Creep data

An example of typical creep curves is given in Figure 4 where strain vs. time is given for LSFC and different stress levels at 950°C. The minimum creep rates are calculated from the linear region between 16 and 24 hours. The parameters for creep were obtained by fitting the experimental data to a generalized steady-state creep relationship[33] given in equation (1)

$$\dot{\varepsilon} = A\left(\frac{1}{d}\right)^{p} (pO_2)^{m} \sigma^{n} \exp\left(-\frac{Q}{RT}\right) \quad (1)$$

where $\dot{\varepsilon}$ is the steady-state creep rate, A is a constant, d is the grain size, p is the inverse grain size exponent, pO_2 is the partial pressure of oxygen, m is the oxygen partial pressure exponent, σ is the applied stress, n is the stress

exponent, Q is the activation energy, R is the gas constant and T is the absolute temperature.

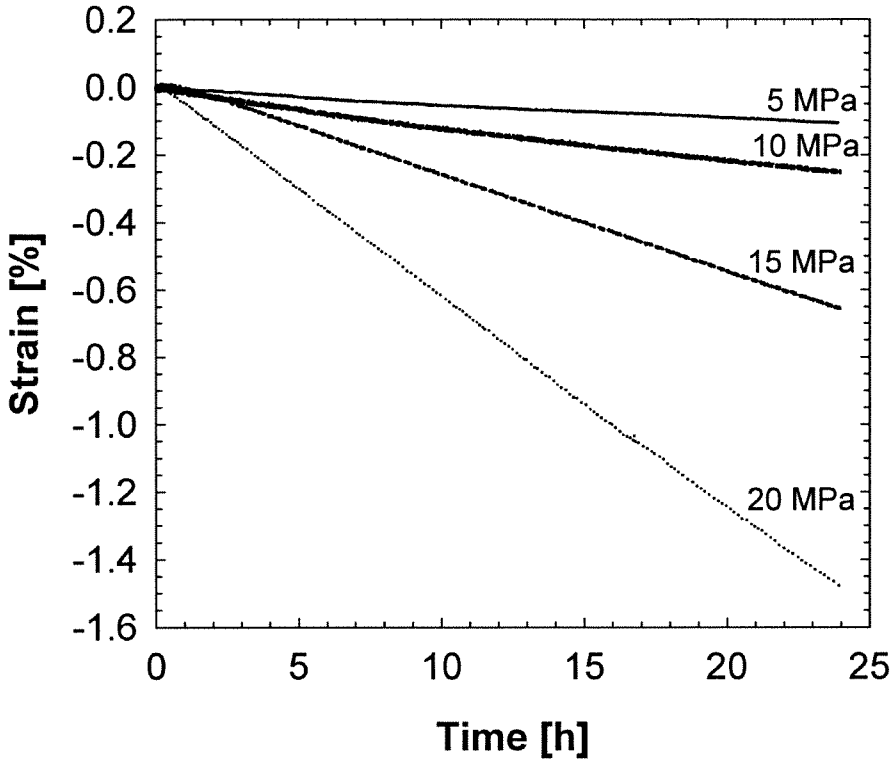

Figure 4: Strain vs. time for different stress levels for $La_{0.5}Sr_{0.5}Fe_{0.5}Co_{0.5}O_{3-\delta}$ at 950°C.

A summary of the obtained creep rates at different stresses, temperatures, oxygen partial pressures and grain sizes are given in Tables 3 and 4. Table 3 shows the data for LSFC while Table 4 shows the data for LSC.

Table 3: Minimum creep rates for $La_{0.5}Sr_{0.5}Fe_{0.5}Co_{0.5}O_{3-\delta}$ at different stresses, temperatures and oxygen partial pressures.

Temperature [°C]	Grain size [μm]	pO_2 [atm]	Stress [MPa]	Steady-state creep rate [$\cdot 10^{-9}$ s^{-1}]
900	1.1	0.21	5.00	1.53
			10.00	3.67
			15.01	3.91
			20.01	7.59
			25.01	8.90
			28.01	15.6
			5.00	1.33
950	1.1	0.21	5.00	10.1
			10.00	24.2
			15.00	78.4
			19.99	166
			25.00	249
			5.00	2.90
1000	1.1	0.21	5.00	6.57
			10.00	36.1
			15.00	100
			19.99	189
			24.99	290
			27.92	356
			5.00	6.40
1050	1.1	0.21	5.00	57.6
			10.00	342
			15.01	614
900	1.1	10^{-5}	5.02	33.8
			9.99	36.4
			15.02	50.8
			20.03	65.5
			25.03	87.5
			28.02	102
			5.00	7.71

Table 4: Minimum creep rates for $La_{0.5}Sr_{0.5}CoO_{3-\delta}$ at different stresses, temperatures, oxygen partial pressures and grain sizes.

Temperature [°C]	Grain size [µm]	pO_2 [atm]	Stress [MPa]	Steady-state creep rate [$\cdot 10^{-9}$ s^{-1}]
900	1.7	0.21	5.00	0.780
			10.00	1.02
			15.00	1.37
			20.00	1.60
			25.00	1.76
			28.00	1.92
			5.00	0.763
950	1.7	0.21	5.00	7.28
			10.00	13.8
			15.00	20.4
			19.99	30.7
			25.00	48.7
			5.00	2.57
1000	1.7	0.21	5.00	18.9
			10.00	81.8
			15.00	184
			19.99	290
			24.99	393
			5.00	9.90
1000	10.3	0.21	4.99	2.50
			9.98	10.6
			14.97	17.6
			19.96	21.9
			24.94	31.8
			4.99	4.55
900	1.7	10^{-5}	5.01	88.3
			9.99	94.4
			15.02	114
			20.03	145
			25.03	225

By plotting logarithmic creep rate versus logarithmic stress and adjust a linear regression, the stress exponent n in equation (1) can be calculated from the slope. This is shown for the two materials in Figure 5a) and b). The different stress exponents for the different compositions, temperatures and atmospheres are given in Table 5.

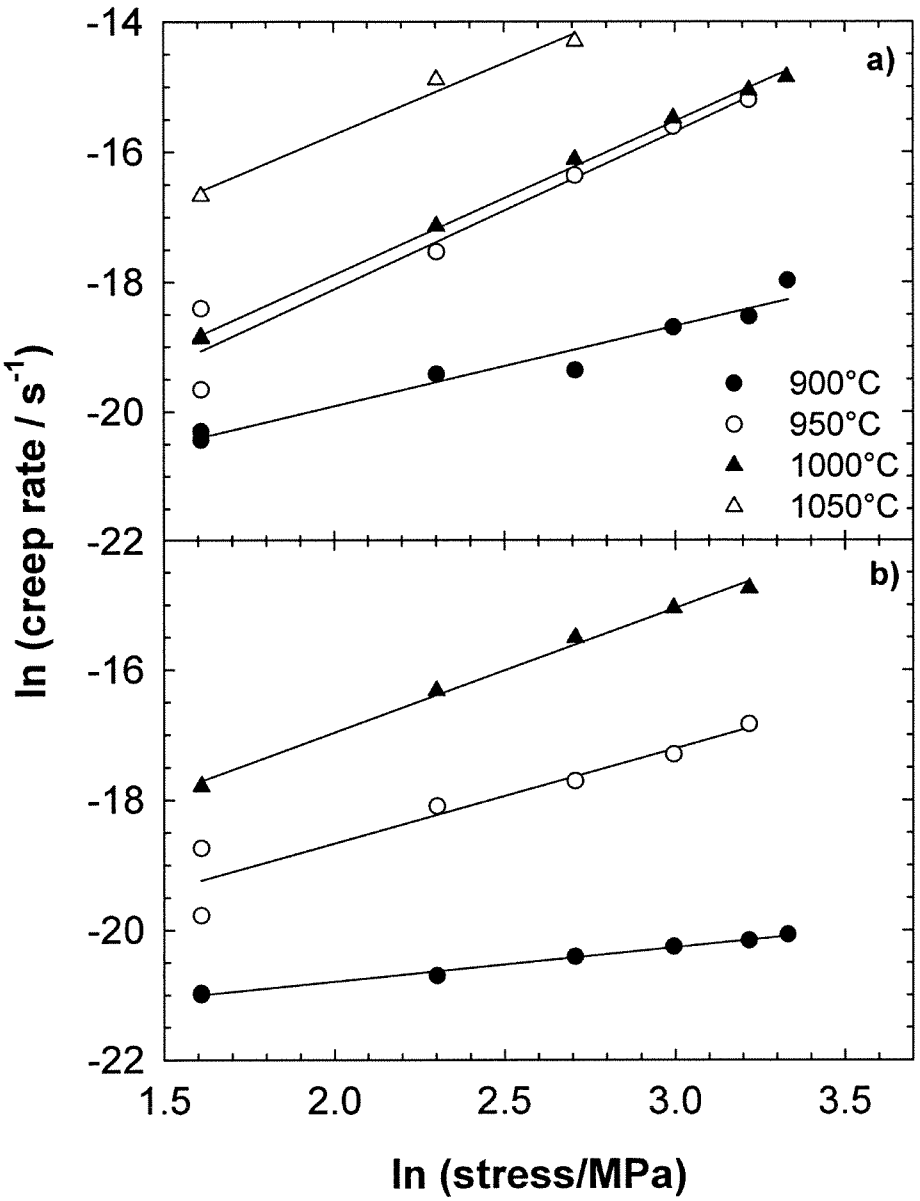

Figure 5: Presentation of ln creep rate vs. ln stress for $La_{0.5}Sr_{0.5}Fe_{0.5}Co_{0.5}O_{3-\delta}$ (a) and $La_{0.5}Sr_{0.5}CoO_{3-\delta}$ (b) at different temperatures. The slope of the curves gives the stress exponent n.

Table 5: Stress exponents for $La_{0.5}Sr_{0.5}Fe_{1-x}Co_xO_{3-\delta}$ at different temperatures, oxygen partial pressures and grain sizes.

Composition x	Temperature [°C]	Grain size [μm]	pO_2 [atm]	Stress exponent [n]
0.5	900	1.1	0.21	1.24 ± 0.12
	950	1.1	0.21	2.42 ± 0.29
	1000	1.1	0.21	2.36 ± 0.04
	1050	1.1	0.21	2.20 ± 0.30
	900	1.1	10^{-5}	1.05 ± 0.27
1	900	1.7	0.21	0.53 ± 0.02
	950	1.7	0.21	1.45 ± 0.25
	1000	1.7	0.21	1.91 ± 0.08
	1000	10.3	0.21	1.54 ± 0.15
	900	1.7	10^{-5}	0.90 ± 0.22

The activation energy, Q in equation (1), can be calculated from the linear regression of a plot of ln creep rate versus inverse temperature at constant load. The data is shown in Figure 6. The calculated activation energies are 398 ± 28 kJ/mol for LSFC and 619 ± 56 kJ/mol for LSC. However, the activation energies seem to increase with increasing stress. Table 6 shows the activation energy for LSC at the different stresses.

Table 6: Activation energy for $La_{0.5}Sr_{0.5}CoO_{3-\delta}$ at different stresses and temperatures between 900°C and 1000°C.

Stress [MPa]	Activation energy [kJ/mol]
10	545 ± 46
15	609 ± 22
20	647 ± 35
25	673 ± 72

The inverse grain size exponent (p) can be found from a linear regression of a log-log plot of strain rate versus inverse grain size at constant stress and temperature, shown in Figure 7 for LSC at 1000°C in air. The average value obtained is 1.28 ± 0.14.

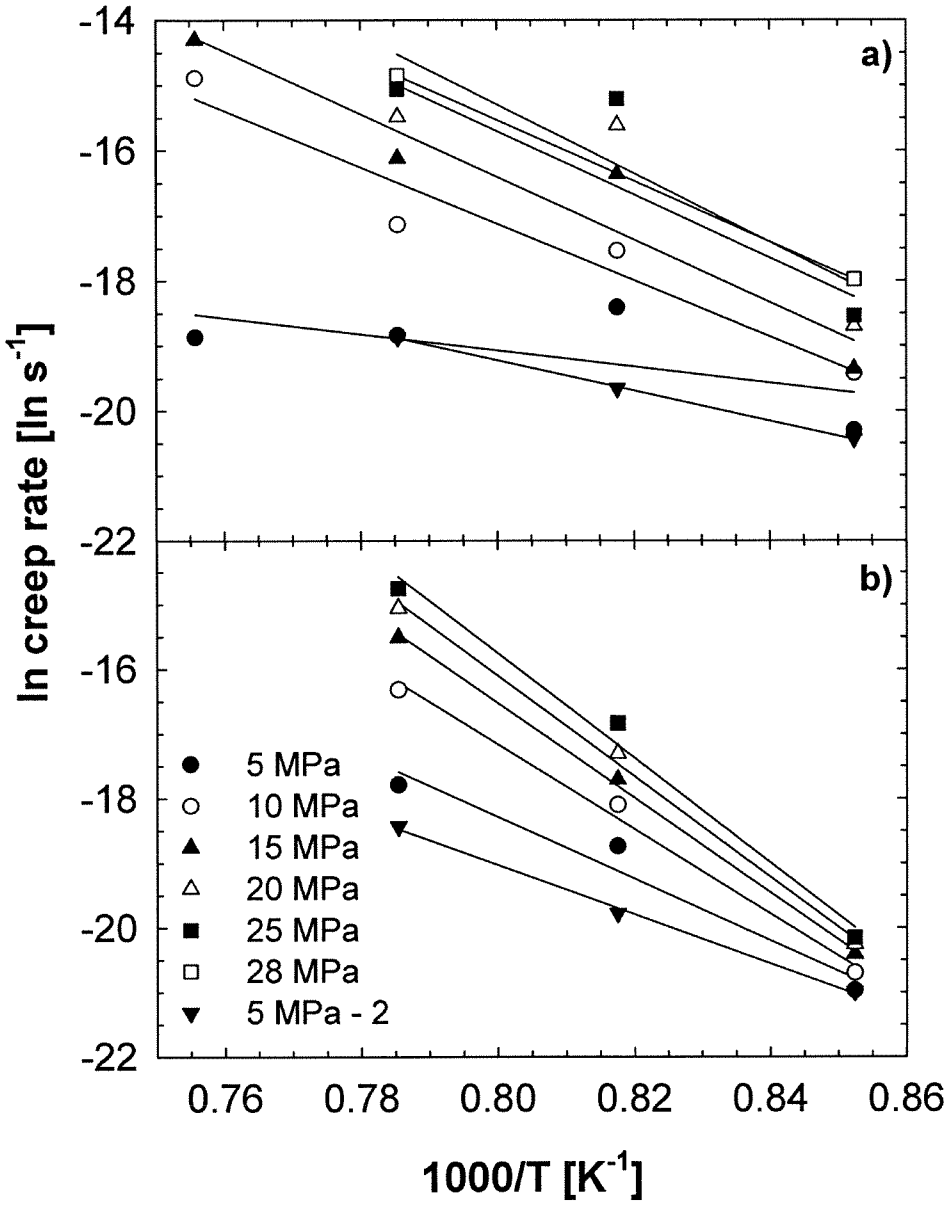

Figure 6: Plot of ln creep rate vs. inverse absolute temperature for $La_{0.5}Sr_{0.5}Fe_{0.5}Co_{0.5}O_{3-\delta}$ (a) and $La_{0.5}Sr_{0.5}CoO_{3-\delta}$ (b). The slopes give the activation energy. 5 MPa-2 indicates second time 5 MPa.

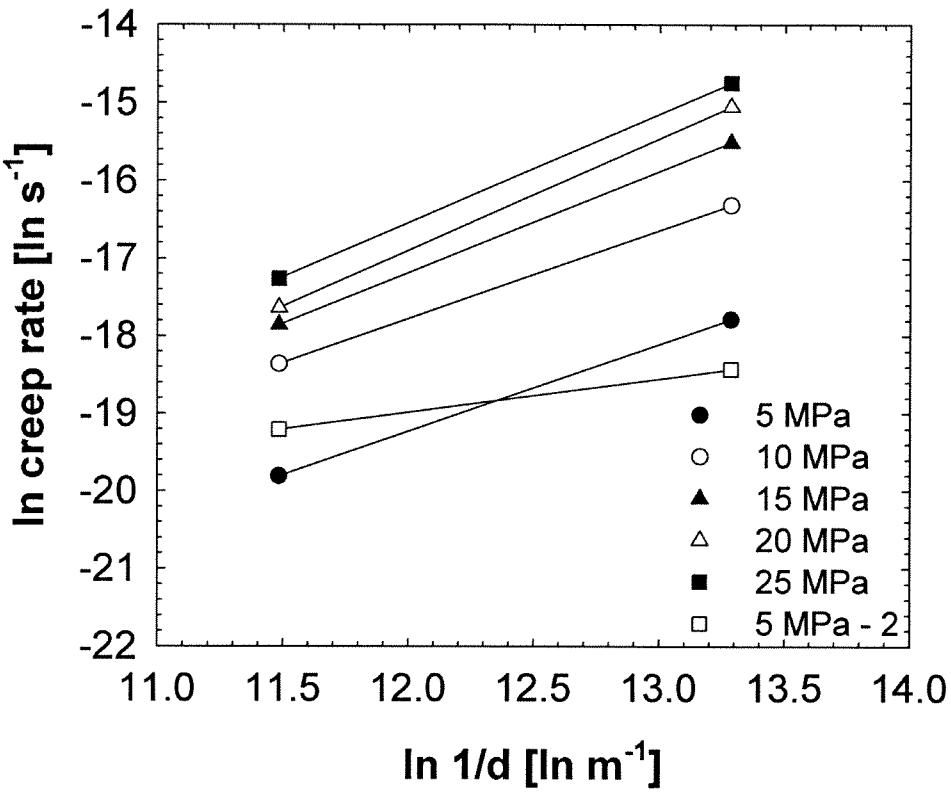

Figure 7: Presentation of ln creep rate vs. ln of inverse grain size for $La_{0.5}Sr_{0.5}CoO_{3-\delta}$ at 1000°C. Slope of the curve gives the inverse grain size exponent p.

By plotting ln creep rate versus ln pO_2 at constant temperature and stress, the oxygen partial pressure exponent m can be calculated. Figure 8 shows the plots for LSFC (a) and LSC (b) at 900°C. m is determined to -0.23 ± 0.04 and -0.46 ± 0.02 respectively, assuming an oxygen partial pressure of 10^{-5} in nitrogen. The pO_2 may be higher due to oxygen release from the sample. By assuming an oxygen partial pressure of 10^{-4}, m will change to -0.31 ± 0.05 for LSFC and -0.60 ± 0.02 for LSC.

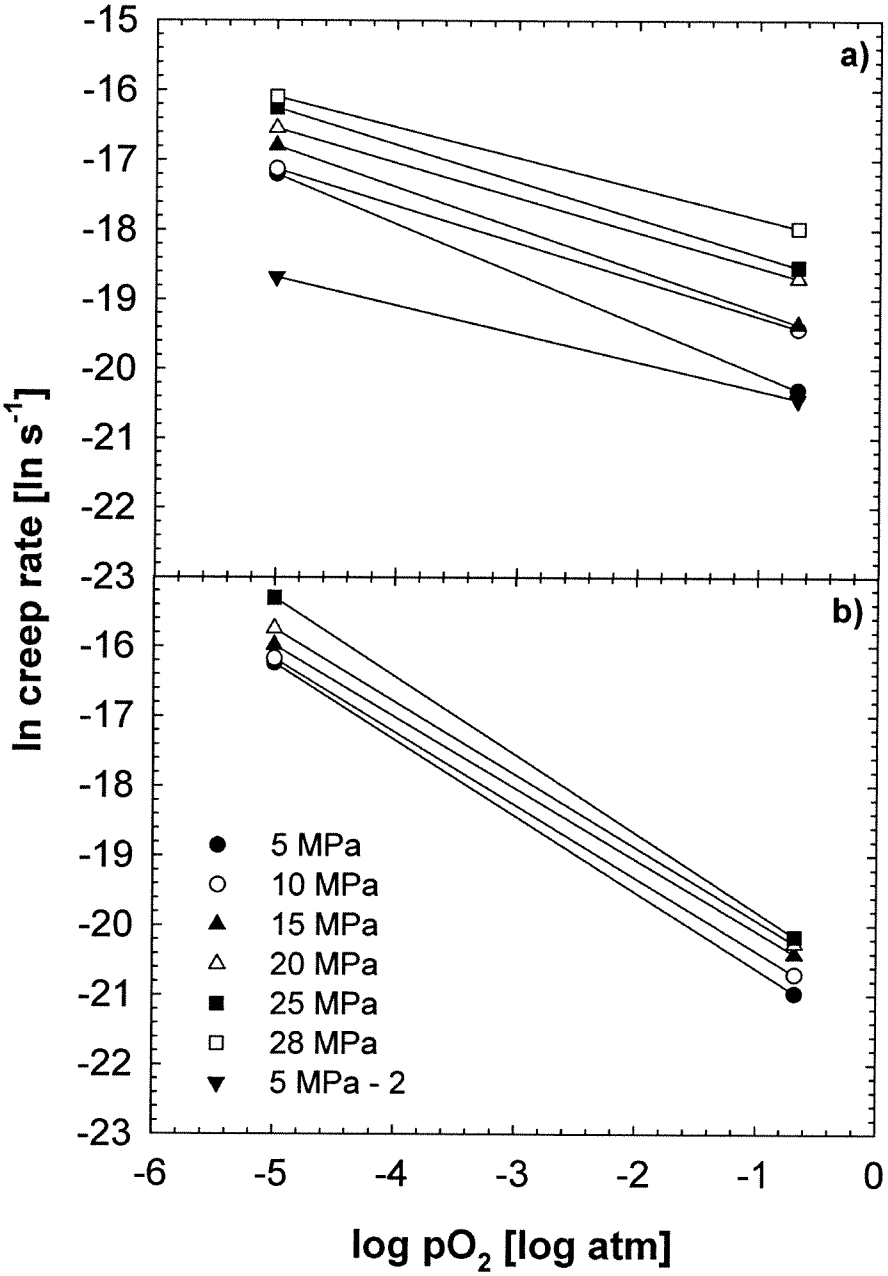

Figure 8: Presentation of ln creep rate vs. log pO_2 for $La_{0.5}Sr_{0.5}Fe_{0.5}Co_{0.5}O_{3-\delta}$ (a) and $La_{0.5}Sr_{0.5}CoO_{3-\delta}$ (b) at 900°C. Slope of the curve gives the oxygen partial pressure exponent m.

The temperature-compensated creep rate (TCCR) is calculated by dividing both sides of equation (1) by the exponential temperature term exp(-Q/RT). Plot of TCCR versus ln stress for the different compositions are shown in Figure 9. The slope of the plots gives the mean stress exponent for the different materials. For LSFC, n is equal to 1.83 ± 0.23 and for LSC, n is 1.32 ± 0.21.

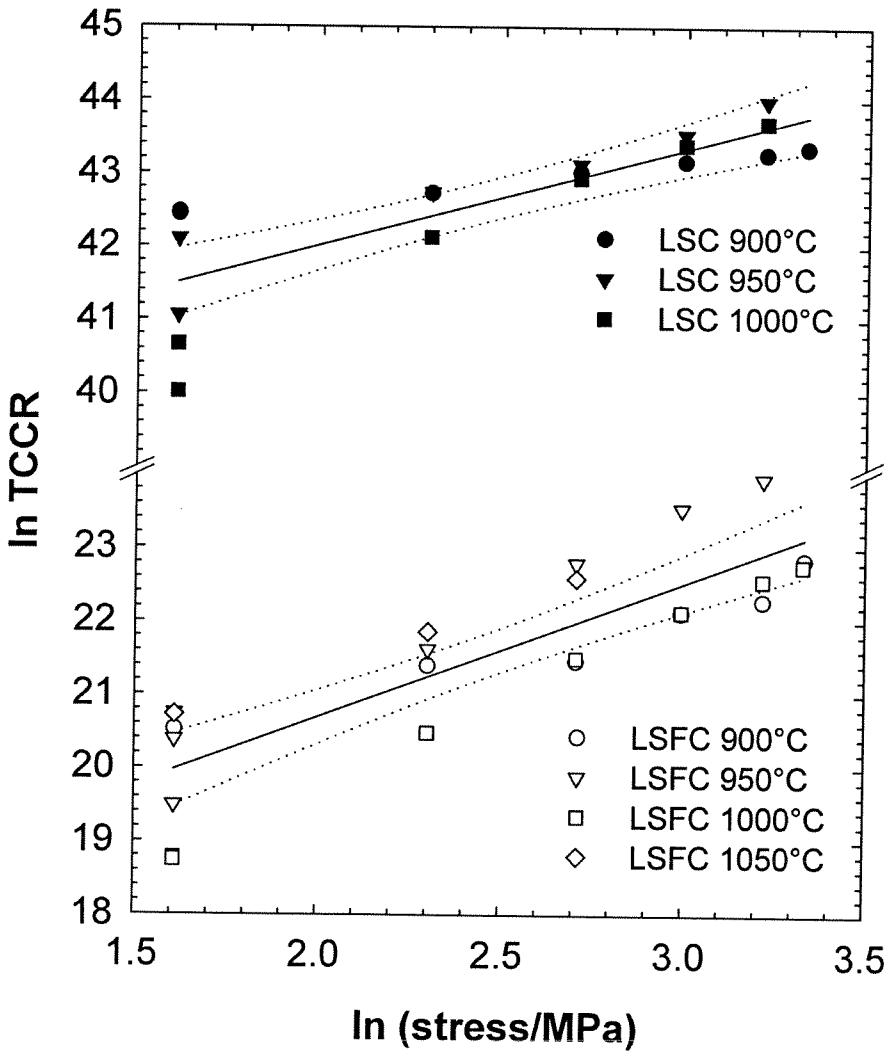

Figure 9: Plot of temperature-compensated creep rate (TCCR) versus ln stress for $La_{0.5}Sr_{0.5}Fe_{0.5}Co_{0.5}O_{3-\delta}$ (LSFC) and $La_{0.5}Sr_{0.5}CoO_{3-\delta}$ (LSC). The dotted lines indicate the 95% confidence interval.

Discussion

Microstructure

The microstructure analysis of the materials confirmed that the grains remained equiaxed after creep. No significant grain growth and no indication of elongation of the grains could be observed, as shown in Figure 3. Some kind of diffusion accommodated grain boundary sliding has been suggested as the mechanism for creep based on similar observations in $La_{0.2}Sr_{0.8}Fe_{0.8}Cr_{0.2}O_{3-\delta}$ and $SrCo_{0.8}Fe_{0.2}O_{3-\delta}$.[9, 25-27, 33] A purely diffusional creep mechanism such as Herring-Nabarro or Coble creep[34] would imply uniform elongation of all grains.

The materials in this study have been sintered at 1150°C. The sintering rate of green bodies has also been investigated by dilatometry and the onset for sintering of calcined powder is observed at 810°C for LSC and 840°C for LSFC with maximum sintering rate around 1065°C for LSC and 1100°C for LSFC. Figure 10 shows sintering performance for cold isostatic pressed LSFC and LSC green bodies, both containing minor amounts of secondary phase Co_3O_4. The sintering curves show that sintering occurs at lower temperatures for LSC compared to LSFC, both the onset for sintering and the maximum sintering rate. This is in good accordance with the higher creep rates for LSC, and the mechanisms for creep and sintering in these materials seem to be related.

The materials used in this study where not phase pure but contained some minor content of a Co_3O_4, which transformed to CoO at high temperatures. Since we have no creep data on phase pure materials, the influence of the secondary phase is not clear. However, it is previous seen[30] that powder with increasing amount of secondary phase need longer sintering time. It is believed that this may influence the creep rates in the same way. In addition, the grain boundary chemistry is obviously affected by the excess amount of Co, and if grain boundary diffusion is the dominant diffusion mechanism, a change in the overall cation stoichiometry might change the creep performance.

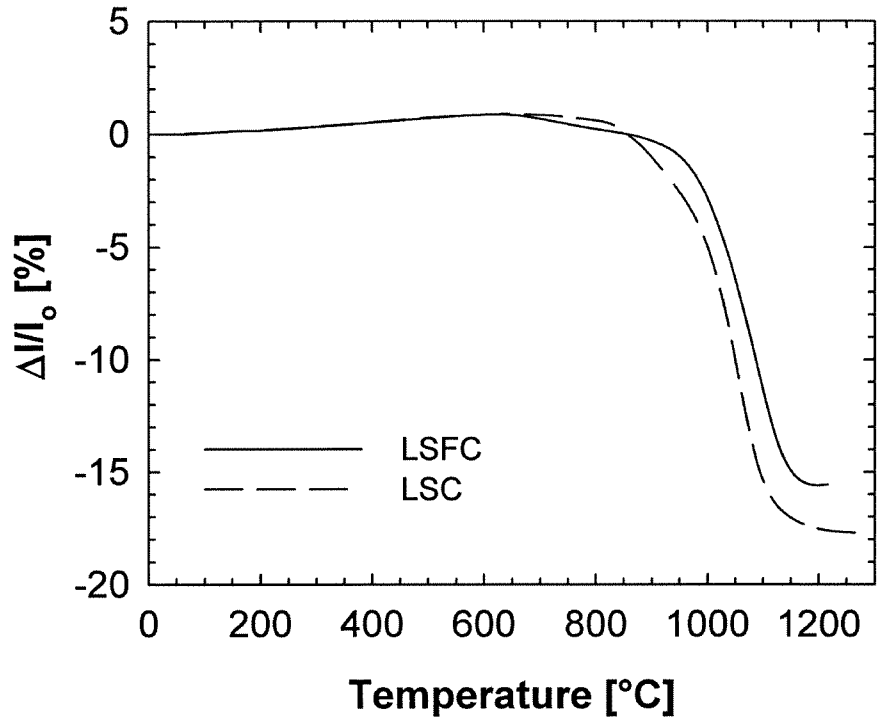

Figure 10: Sintering curves for green bodies of $La_{0.5}Sr_{0.5}Fe_{0.5}Co_{0.5}O_{3-\delta}$ (LSFC) and $La_{0.5}Sr_{0.5}CoO_{3-\delta}$ (LSC) as a function of temperature.

Stress exponent

The values for the stress exponent alone indicate a diffusion controlled mechanism in the stress range investigated. Traditional diffusional creep models (Herring-Nabarro and Coble) as well as models involving grain rotation or sliding[34] all predicts n = 1. Stress exponent close to unity has been observed in a number of different perovskite materials[6, 9, 12, 16, 19-28] Table 7 shows creep parameters for selected compositions. At higher stress levels than used here, a sharp transition to power law creep has been observed in similar materials.[25-28]

For deformation to occur in diffusional creep, the entire unit cell of the compound must be transported. For a multi component material, the diffusion rate will be controlled by the slowest moving specie along its

fastest path. In this material, the activation energy for oxygen ion diffusion is considerably lower than the activation energy found for creep, and it is clear that cation diffusion is rate limiting. The diffusion of Co/Fe in these materials has been observed to be faster than Sr/La[31] and grain boundary or bulk diffusion of Sr/La are most likely controlling the creep performance.

Table 7: Creep parameters of perovskite materials in air. GBS = grain boundary sliding, LD = lattice diffusion

Composition	Temp [°C]	n	Ea [kJ/mol]	p	Ref
$SrFeO_{3-d}$	800-1000	unity	260±30		12
$BaTiO_3$	1200-1300	1	720	2	10
$BaTiO_3$	1150-1250	2	800		16
$La_{0.8}Sr_{0.2}MnO_3$	1165-1265	1.3±0.2	530±40		11
$La_{0.9}Sr_{0.1}MnO_3$	1150-1300	unity	490		19
$(La_{0.9}Sr_{0.1})_zGa_{0.8}Mg_{0.2}O_3$ (z=1, 0.98, 0.95)	950-1350	1.49±0.10	426±9	3.1 (z=0.98) 1.9 (z=0.95)	20
$La_{0.8}Sr_{0.2}Ga_{0.85}Mg_{0.15}O_3$	1200-1300	unity	521±15		6, 21-22
$SrCo_{0.8}Fe_{0.2}O_{3-d}$	850-975	unity 2.2-2.9	457 (T<925) 268 (T>925)	Unity	9, 23-24
$La_{0.2}Sr_{0.8}Fe_{0.8}Cr_{0.2}O_{3-d}$	1100-1200	1.4	566	2.3	25-28

Inverse grain size exponent

For LSC an inverse grain size exponent of 1.28 ± 0.14 was determined. Such a low inverse grain size exponent and stress exponent close to unity is relatively rare. In perovskite materials grain size exponents closed to 2 has been reported for $BaTiO_3$,[10] $(La_{0.9}Sr_{0.1})_zGa_{0.8}Mg_{0.2}O_{3-\delta}$ [20] and $La_{0.2}Sr_{0.8}Fe_{0.8}Cr_{0.2}O_{3-\delta}$,[25-28] while in $SrCo_{0.8}Fe_{0.2}O_{3-\delta}$ a similar low value have been reported.[9, 13, 24] An inverse grain size exponent of 2 indicates grain boundary diffusion, while 3 indicates bulk diffusion.[34] The seemingly unusual low influence of the grain size on the strain rate observed here indicates that grain boundary diffusion might be dominating. However, the presence of the secondary cobalt oxide phase might have an influence on the grain size exponent.

Activation energy

The apparent activation energies of the two materials were significantly different. Apparent activation energies for creep in perovskite materials reported in the literature is included in Table 7, and varies considerably in the range 260-800 kJ/mole. As shown in Table 6, the apparent activation energy for LSC seems to depend on the stress level. The reason for this behavior is not clear. There is also no obvious reason for the relatively large change in activation energy between the two materials. Generally in materials with high content of secondary phases low activation energies have been reported.[17] Here, the two materials have the same amount of secondary phase. However, it might be possible that this phase affect the creep rates in different ways. In addition, the secondary phase undergoes a phase transition from Co_3O_4 to CoO at 920°C. This can affect the calculation of activation energy since the transition occurs between the lowest temperature and the other temperatures for creep measurement. More creep data around the phase transition temperature are necessary to be sure of the influence.

As mentioned previously these activation energies are far higher than reported for oxygen ionic diffusion in perovskites (< 100 kJ/mole). Activation energies for tracer diffusion of cations in perovskites are in the same range as reported for creep.[35-46] In those cases where grain boundary diffusion has been differentiated from bulk diffusion, activation energy for grain boundary diffusion has been reported to be considerably higher.

Oxygen partial pressure exponent

The oxygen partial pressure exponents, -0.23 ± 0.04 and -0.46 ± 0.02 at 900°C for LSFC and LSC respectively, show a larger creep rate at low oxygen partial pressures than in air. There are few reports on creep in perovskite materials in variable atmosphere. Cook et al.[11] reported $m < 0$ for $La_{1-x}Sr_xMnO_{3+\delta}$ and $pO_2 > 10^{-3}$ and assumed the oxygen vacancies to be rate controlling. Majkic et al.[26, 28] report the same trend for $La_{0.2}Sr_{0.8}Fe_{0.8}Cr_{0.2}O_{3-\delta}$ at $pO_2 < 10^{-11}$ atm. The standard random defect model based on non-interacting point defects could not describe the observed creep behavior. They explain the creep mechanism by a model taking account of $\left\langle B_B^{'} - V_O^{\cdot\cdot} - B_B^{'} \right\rangle$ cluster formation. The effect of the

clusters on the diffusion rate arose from cluster interactions forming channels with low B site cation diffusion.

We have no reasons to assume a similar mechanism for creep in these materials. However, the oxygen non-stoichiometry, δ, and then the molar volume is seen to be very dependent on temperature and atmosphere above 500°C.[29] The oxygen vacancy concentration is high at the temperatures where the creep measurements are performed. The chemical expansion due to the oxygen vacancy formation causes larger unit cell volume and hence more space for the diffusing ions. This may cause higher diffusion rates. Therefore it is assumed that the oxygen vacancies contribute to the creep mechanism, especially in inert atmosphere where the concentration is higher. This may give rise to different mechanisms for cation diffusion with possible lower activation energy in N_2 compared to air. The cation vacancy concentration is assumed to be independent of oxygen partial pressure at such high oxygen vacancy concentrations.

Influence of creep for applications of the materials

The creep rates observed here were dependent on the oxygen partial pressure. For a membrane exposed to oxygen partial pressure gradients, there will be a gradual change in creep resistance from oxidant to fuel side. The material close to the fuel side will experience a drastic increase in the rate of deformation compared to the high pO_2 side. In addition, higher fracture toughness can be expected at this side because of possible diffusional crack blunting and crack healing.[26] How creep influences in a membrane, depends on the pO_2 profile. Hendriksen et al.[3] have calculated an approximately linear profile for a $La_{0.6}Sr_{0.4}Co_{0.2}Fe_{0.8}O_{3-\delta}$ membrane under operating conditions. Other conditions may give rise to different profiles. It is previously seen[47] that the surface exchange coefficient, k_{chem}, decreases with decreasing pO_2 for LSC, and this may affect the profile. An assumed behavior of almost constant values from the low pO_2 side followed by a larger increase close to the high pO_2 side may cause an almost constant creep rate until close to the oxidizing surface followed by a significant decrease.

High creep rates gives possibilities for creep relaxation in the materials. Table 8 gives absolute creep rates for different materials at 1200°C in air and at 5 MPa load. For most of the compositions the reported values are estimated from other temperatures and/or different loads. In addition the

grain size is varying. However, the values are useful for general discussions. A limited number of compositions make it difficult to draw particular conclusions, but A-deficient materials seem to have lower creep rates. By keeping a fixed La/Sr ratio on A-site, a change or substitution on B-site will change the creep rate dramatically. Removing of La in La-Sr-Fe-Co materials seems to increase the creep rate and few cations may give the impression of higher creep rates than high substitution level. At high applied stresses on a membrane, the membranes with high creep rates will deform instead of failure due to fracture. Other materials with lower creep rates have larger potential for fracture during operation. Too high creep rates will on the other hand give rise to problems with the dimension stability.

Table 8: Creep rates at 1200°C in air and 5 MPa load for different compositions.

Composition	Creep rate [s-1]	Grain size [μm]	Ref
$SrFeO_{3-d}$, 5% A excess	$4 \cdot 10^{-6}$	<5	12
$SrFeO_{3-d}$, 5% B excess	$3 \cdot 10^{-6}$	<5	12
$BaTiO_3$	$6 \cdot 10^{-6}$	19.3	10
$La_{0.9}Sr_{0.1}MnO_3$	$1 \cdot 10^{-6}$	5	19
$La_{0.9}Sr_{0.1}Ga_{0.8}Mg_{0.2}O_3$	$1 \cdot 10^{-8}$	19.6	20
$(La_{0.9}Sr_{0.1})_{0.98}Ga_{0.8}Mg_{0.2}O_3$	$4 \cdot 10^{-9}$	16.2	20
$(La_{0.9}Sr_{0.1})_{0.95}Ga_{0.8}Mg_{0.2}O_3$	$3 \cdot 10^{-9}$	21.2	20
$La_{0.8}Sr_{0.2}Ga_{0.85}Mg_{0.15}O_3$	$2 \cdot 10^{-7}$	8	21
$La_{0.5}Sr_{0.5}Fe_{0.5}Co_{0.5}O_{3-\delta}$	$3 \cdot 10^{-6}$	1.1	This paper
$La_{0.5}Sr_{0.5}CoO_{3-\delta}$	$4 \cdot 10^{-5}$	1.7	This paper
$SrCo_{0.8}Fe_{0.2}O_{3-d}$	$9 \cdot 10^{-3}$	2.4	9
$La_{0.2}Sr_{0.8}Fe_{0.8}Cr_{0.2}O_{3-d}$	$6 \cdot 10^{-6}$	3.2	25

Experimental difficulties

The creep measurements were performed by increasing the load from 5 MPa to the maximum load, and then back to 5 MPa. At this lowest load, the creep rates sometimes differ from the expected linear relationship versus load, both at first and second loading. We do not have any explanation for this non-reproducibility. Non parallel edges of the samples could have given a larger creep rate until the edges are parallel, but this can not explain the behavior for the second time at 5 MPa. Therefore, all the data obtained are used in the calculations of the exponents and the activation energy.

The assumed oxygen partial pressure for measurements in inert atmosphere is a moment of uncertainty. The pressure is only measured in the flow into the furnace chamber, not out of the chamber. However, calculations show that the oxygen partial pressure exponents are not so sensitive to the oxygen partial pressure and the given exponents and standard deviations are within the assumed pO_2 variation.

Previous studies have shown that the phase transition $Co_3O_4 \rightarrow CoO$ give rise to a volume expansion of 16.4 vol% at 920°C.[30] This may cause stresses in the perovskite matrix surroundings and further crack trapping and enhancement of the fracture toughness. Most likely, the creep can cause relaxation of the material and reduce the stresses. Figure III-1 in Appendix III shows that by keeping the strain constant, the stress will relax until 50% of original value within a time aspect of three hours.

Conclusion

The steady state compressive creep performance of the perovskite materials $La_{0.5}Sr_{0.5}Fe_{0.5}Co_{0.5}O_{3-\delta}$ (LSFC) and $La_{0.5}Sr_{0.5}CoO_{3-\delta}$ (LSC) has been determined at temperatures between 900 and 1050°C and stresses from 5 to 28 MPa. The stress exponent has been found to be close to unity. The microstructure after creep gave no indication of grain growth and elongated grains, only equiaxed grains were observed after creep. These two observations point to a diffusion related mechanism for the creep. The grain size exponent for the LSC material was determined to be 1.28 ± 0.14, which is an unusually low grain size exponent for ceramics. The apparent activation energy for creep was considerably higher for LSC (619 ± 56 kJ/mol) than for LSFC (392 ± 28 kJ/mol). The influence of a secondary phase due to deviation from the nominal cation stoichiometry is proposed as a plausible explanation for the large difference in the activation energy. The creep performance in inert atmosphere of both materials was also determined at 900°C. Considerably higher creep rates were observed for both materials in N_2 atmosphere at 900°C compared to air. The higher creep rate under reducing conditions suggest that creep relaxation of mechanical or chemical induced stresses is proposed to enhance the mechanical stability of oxygen permeable membranes.

Acknowledgement

The authors would like to thank Rosa Trejo and Miladin Radovic for help to perform the creep experiments. The Research Council of Norway, Statoil and Hydro are acknowledged for financial support.

References

1. H. J. M. Bouwmeester and A. J. Burgraaf, in: P.J. Gellings and H.J.M. Bouwmeester (Eds), The CRC Handbook of Solid State Electrochemistry, CRC Press, Inc., New York (1997).
2. A. Atkinson and A. Selcuk, "Mechanical behaviour of ceramic oxygen ion-conducting membranes", Solid State Ionics, 134 (2000) 59-66.
3. P. V. Hendriksen, P. H. Larsen, M. Mogensen, F. W. Poulsen and K. Wiik, "Prospects and problems of dense oxygen permeable membranes", Catal. Today, 56 (2000) 283-295.
4. V. V. Kharton, E. N. Naumovich and A. V. Nikolaev, "Materials of high-temperature electrochemical oxygen membranes", J. Membr. Sci., 111 (1996) 149-157.
5. J. Wolfenstine, K. C. Goretta, R. E. Cook and J. L. Routbort, "Use of diffusional creep to investigate mass transport in (La, Sr)MnO_3", Solid State Ionics 92 (1996) 75-83.
6. J. Wolfenstine, P. Huang and A. Petric, "Creep behavior of doped lanthanum gallate versus cubic zirconia" Solid State Ionics, 118 (1999) 257-259.
7. A. R. De Arellano-Lopez, U. Balachandran, K. C. Goretta, B. Ma and J. L. Routbort, "High-temperature deformation of $Sr(FeCo)_{1.5}O_x$ ceramics", Acta mater., 49 (2001) 3109-3116.
8. K. C. Goretta, E. T. Park, J. Guan, U. Balachandran, S. E. Dorris and J. L. Routbort, "Diffusional creep of $BaCe_{0.8}Y_{0.2}O_{3-\alpha}$ mixed conductors", Solid State Ionics, 111 (1998) 295-299.
9. G. Majkic, L. Wheeler and K. Salama, "Creep of polycrystalline $SrCo_{0.8}Fe_{0.2}O_{3-\delta}$", Acta mater. 48 (2000) 1907-1917.
10. E. T. Park, P. Nash, J. Wolfenstine, K. C. Goretta and J. L. Routbort, "High-temperature creep of polycrystalline $BaTiO_3$", J. Mater. Res, 14 [2] (1999) 523-528.
11. R. E. Cook, K. C. Goretta, J. Wolfenstine, P. Nash and J. L. Routbort, "High-temperature deformation and defect chemistry of $(La_{1-x}Sr_x)_{1-y}MnO_{3+\delta}$", Acta mater, 47 (1999) 2969-2980.

12. K. Kleveland, A. Wereszczak, T. P. Kirkland, M.-A. Einarsrud and T. Grande, "Compressive creep performance of $SrFeO_3$", J. Am. Ceram. Soc., 84 [8] (2001) 1822-1826.
13. J. L. Routbort, K. C. Goretta, R. E. Cook and J. Wolfenstine, "Deformation of perovskite elecronic ceramics – a review", Solid State Ionics, 129 (2000) 53-62.
14. J. E. ten Elshof, H. J. M. Bouwmeester and H. Verweij, "Oxygen transport through $La_{1-x}Sr_xFeO_{3-\delta}$ membranes. I. Permeation in air/He gradients", Solid State Ionics, 81 (1995) 97-109.
15. J. Mizusaki, M. Yoshihiro, S. Yamauchi and K. Fueki., "Nonstoichiometry and defect structure of the perovskite-type oxides $La_{1-x}Sr_xFeO_{3-\delta}$", J. Solid State Chem., 58 (1985) 257-266.
16. C. Carry and A. Mocellin, "Superplastic Creep Fine-Grained $BaTiO_3$ in a Reducing Environment", J. Am. Ceram. Soc, 69 [9] (1986) C-215-C-216.
17. Z. Wang, S.-I. Karato and K. Fujino, "High temperature creep of single crystal strontium titanate ($SrTiO_3$): a contribution to creep systematics in perovskites", Phys. Earth Planet. Inter., 79 (1993) 299-312.
18. Z. -C. Wang, C. Dupas-Bruzek and S. Karato, "High temperature creep of an orthorhombic perovskite—$YAlO_3$", Phys. Earth Planet. Inter., 110 (1999) 51-69.
19. J. Wolfenstine, T. R. Armstrong, W. J. Weber, M. A. Boling-Risser, K. C. Goretta and J. L. Routbort, "Elevated temperature deformation of fine-grained $La_{0.9}Sr_{0.1}MnO_3$", J. Mater. Res., 11 (1996) 657-662.
20. W. E. Luecke and T. R. Armstrong, "Creep of lanthanum gallate", J. Mater. Res., 17 (2002) 532-541.
21. J. Wolfenstine, P. Huang and A. Petric, "High-Temperature Mechanical Behavior of the Solid-State Electrolyte: $La_{0.8}Sr_{0.2}Ga_{0.85}Mg_{0.15}O_{2.825}$", J. Electrochem. Soc., 147 [5] (2000) 1668-1670.
22. J. Wolfenstine, "Rate-controlling species for creep of the solid state electrolyte: doped lanthanum gallate", Solid State Ionics, 126 (1999) 293-298.
23. G. Majkic, L. Wheeler and K. Salama, "Characterization of creep behavior of $SrCo_{0.8}Fe_{0.2}O_{3-x}$", Mat. Res. Soc. Symp. Proc, 575 (2000) 349-354.
24. G. Majkic, L. Wheeler and K. Salama, "A transmission electron microscopy study of polycrystalline $SrCo_{0.8}Fe_{0.2}O_{3-\delta}$ creep in the diffusion-to-power law transition regime", Phil. Mag. A, 81 [11] (2001) 2675-2688.

25. G. Majkic, L. T. Wheeler and K. Salama, "High-temperature deformation of $La_{0.2}Sr_{0.8}Fe_{0.8}Cr_{0.2}O_{3-\delta}$-mixed ionic-electronic conductor", Solid State Ionics, 146 (2002) 393-404.
26. G. Majkic, L. T. Wheeler and K. Salama, "Stress-induced diffusion and defect chemistry of $La_{0.2}Sr_{0.8}Fe_{0.8}Cr_{0.2}O_{3-\delta}$. Part 1 – creep in controlled-oxygen atmosphere", Solid State Ionics, 164 (2003) 137-148.
27. G. Majkic, M. Mironova, L. T. Wheeler and K. Salama, "Stress-induced diffusion and defect chemistry of $La_{0.2}Sr_{0.8}Fe_{0.8}Cr_{0.2}O_{3-\delta}$. 2. Structural, elemental and chemical analysis", Solid State Ionics, 167 (2004) 243-254.
28. G. Majkic, A. J. Jacobson and K. Salama, "Stress-induced diffusion and defect chemistry of $La_{0.2}Sr_{0.8}Fe_{0.8}Cr_{0.2}O_{3-\delta}$. Part3. Defect-chemistry-based modeling", Solid State Ionics, 167 (2004) 255-262.
29. H. L. Lein, K. Wiik and T. Grande, "Thermal and chemical expansion of $La_{0.5}Sr_{0.5}Fe_{1-x}Co_xO_{3-\delta}$ ($0 \leq x \leq 1$) materials", paper I.
30. H. L. Lein, E. Lara-Curzio, Ø. S. Andersen, P. E. Vullum, R. Holmestad, M.-A. Einarsrud and T. Grande, "Mechanical properties of $La_{0.5}Sr_{0.5}Fe_{1-x}Co_xO_{3-\delta}$ ($0 \leq x \leq 1$) materials", paper III.
31. H. L. Lein, K. Wiik and T. Grande, "Oxygen permeation and cation demixing of $La_{0.5}Sr_{0.5}Fe_{1-x}Co_xO_{3-\delta}$ ($0 \leq x \leq 1$) materials", paper IV.
32. H. L. Lein, K. Wiik and T. Grande, "Cation demixing of $La_{0.5}Sr_{0.5}Fe_{1-x}Co_xO_{3-\delta}$ ($0 \leq x \leq 1$) materials", paper V.
33. T. Bretheau, J. Castaing, J. Rabies and P. Veyssière, "Dislocation-motion and high-temperature plasticity of binary and ternary oxides", Advances in Physics, 28 (1979) 836-1014.
34. J.-P. Poirier, "Creep of crystals. High-temperature deformation processes in metals, ceramics and minerals", Cambridge University Press, Cambridge (1985).
35. S. Kambe, G. Samukawa, K. Yamaguchi, O. Ishii, I. Shime, T. Nomura, S. Ohshima, K. Okuyama, T. Itoh, H. Suematsu and H. Yamauchi, "Physical properties and structure of $Ba_{2-x}La_xRuCuO_y$", Solid State Ionics, 108 (1998) 383-390.
36. N. Sakai, K. Yamaji, T. Horita, H. Negishi and H. Yokoka, "Chromium diffusion in lanthanum chromites", Solid State Ionics, 135 (2000) 469-474.
37. I. Værnhus, N. Sakai, H. Yokokawa, T. Grande and K. Wiik, "Cation Diffusion in $La_{1-x}Sr_xFeO_{3-\delta}$, x = 0 and 0.1, measured by SIMS", to be published.
38. T. Akashi, T. Maruyama and T. Goto, "Transport of lanthanum ion and hole in $LaCrO_3$ determined by electrical conductivity measurements", Solid State Ionics, 164 (2003) 177-183.

39. O. Schulz, M. Martin, C. Argirusis and G. Borchardt, "Cation tracer diffusion of ^{138}La, ^{84}Sr and ^{25}Mg in polycrystalline $La_{0.9}Sr_{0.1}Ga_{0.9}Mg_{0.1}O_{2.9}$", Phys. Chem. Chem. Phys., 5 (2003) 2308-2313.
40. V. Buscaglia, F. Caracciolo, C. Bottino, M. Leoni and P. Nanni, "Reaction diffusion in the Y_2O_3-Fe_2O_3 system", Acta mater., 45 [3] (1997) 1213-1224.
41. V. Buscaglia, M. T. Buscaglia, L. Giordano, A. Martinelli, M. Viviani and C. Bottino, "Growth of ternary oxides in the Gd_2O_3–Fe_2O_3 system. A diffusion couple study", Solid State Ionics, 146 (2002) 257-271.
42. T. Horita, M. Ishikawa, K. Yamaji, N. Sakai, H. Yokokawa and M. Dokiya, "Calcium tracer diffusion in (La,Ca)CrO_3 by SIMS", Solid State Ionics, 124 (1999) 301-307.
43. T. Akashi, Y. Mizuno, M. Nanko, T. Maruyama, A. Saiki, K. Tsukui and J. Tanabe, "Determination of Diffusion Coefficient of Nd^{3+} in $NdCrO_3$ Based on Solid State Reaction", Mater. Trans., 42 (2001) 1411-1416.
44. K. Kawamura, A. Saiki, T. Maruyama and K. Nagata, "Diffusion Coefficient of Yttrium in $YCrO_3$", J. Electrochem. Soc., 142 (1995) 3073-3077.
45. J. B. Smith and T. Norby, "Cation Self-Diffusion in $LaFeO_{3-\delta}$ Measured by the Solid State Reaction Method", to be published.
46. N. Sakai, T. Tsunoda, N. Fukumoto, I. Kojima, K. Yamaji, T. Horita, M. Ishikawa, H. Yokokawa and M. Dokiya, "TEM, XPS and SIMS analyzes on grain boundary of lanthanum chromites", J. Electroceram., 4;S1 (1999) 121-128.
47. G. Watterud, K. Wiik and S. Julsrud, "Oxygen transport in $La_{1-x}Sr_xCoO_{3-\delta}$ (x = 0, 0.2 and 0.5) assessed with electrical conductivity relaxation. Part I: Bulk diffusion and k_{chem}", to be published.

PAPER III

Mechanical properties of $La_{0.5}Sr_{0.5}Fe_{1-x}Co_xO_{3-\delta}$ ($0 \leq x \leq 1$) materials

Hilde Lea Lein, [b] Edgar Lara-Curzio, Øystein Skottun Andersen, [a] Per Erik Vullum, [a] Randi Holmestad, Mari-Ann Einarsrud and Tor Grande*

Department of Materials Technology,
[a] Department of Physics,
Norwegian University of Science and Technology,
7491 Trondheim, Norway.

[b] High Temperature Materials Laboratory,
Oak Ridge National Laboratory,
Oak Ridge TN 37831, USA.

Abstract

The Young's modulus, strain-stress behavior, fracture strength and fracture toughness of $La_{0.5}Sr_{0.5}Fe_{1-x}Co_xO_{3-\delta}$ ($0 \leq x \leq 1$) materials have been investigated in the temperature range 20-1000°C. The Young's modulus at room temperature measured by resonant ultrasound spectroscopy of the materials with $x = 0.5$ and $x = 1$ were 130 ± 1 and 133 ± 3 GPa, respectively. A non-linear stress-strain relationship during 4-point bending observed at room temperature was inferred as a signature of ferroelastic behavior. Above the ferroelastic to paraelastic transition temperature the materials showed elastic behavior, however, at temperatures from about 800°C a non-elastic respond was observed due to creep. The room temperature fracture strength measured by four-point bending was in the range 107-128 MPa. The fracture toughness measured by SEVNB method was 1.16 ± 0.12 $MPa \cdot m^{1/2}$ at room temperature for the material with $x = 0.5$. The measured fracture strength and fracture toughness were observed to increase with increasing temperature. Possible reasons for this increase in fracture strength and fracture toughness were discussed. Tensile stress gradient caused by oxygen non-stoichiometry gradients frozen in during cooling was proposed to explain the low ambient fracture strength and toughness.

* Correspondence to Tor.Grande@material.ntnu.no

Introduction

Sr-substituted $LaFe_{1-x}Co_xO_{3-\delta}$ materials are candidates for oxygen permeable membranes, gas sensors and electrodes in high temperature electrochemical devices due to their high electronic and ionic conductivity at elevated temperatures.[1-6] One of the main challenges for these applications is to prevent mechanical failure during fabrication and operation. Therefore, knowledge of mechanical properties of these materials is essential. Of special importance are the mechanical properties at operation temperatures, due to the desired long lifetime and estimation of reliability. Several reports on the fracture strength and fracture toughness of various perovskite materials with ionic or mixed conductivity have been published over the last two decades. However, only a few studies of the temperature dependency of the mechanical properties for these perovskite materials have been reported. The room temperature fracture strength of perovskite materials based on $LaMO_3$ (M = La, Co, Mn, Cr, Ga) measured by four point bending is typically 100-160 MPa.[7-11] The corresponding room temperature fracture toughness of the materials are reported in the range 1.3-2.8 $MPa \cdot m^{1/2}$,[7-8, 12-13] where orthorhombic perovskites have higher fracture toughness than rhombohedral and cubic perovskites. For rhombohedral and cubic materials, the fracture strength generally decreases with increasing temperature.[8, 11, 14] The fracture toughness is either constant or decreasing with increasing temperature.[8, 12-13] There are conflicting reports on the Young's modulus of these materials. Young's modulus in the range 100-200 GPa have been reported, but there is no physical explanation for the large variation. Different methods have however been applied, but when data from the most reliable techniques[15] are considered, the Young's modulus of $LaMO_3$-materials is in the range 120-200 GPa.[10, 12, 16-17]

$La_{0.5}Sr_{0.5}Fe_{1-x}Co_xO_{3-\delta}$ materials are rhombohedral perovskites at room temperature, but transforms to cubic structure around 300°C.[18] From ambient temperature to 1000°, a linear expansion of 1.5-2.3 % in air or 1.7-2.5 % in N_2 is found. At the same time the oxygen non-stoichiometry, 3-δ, decreases from 2.93-2.97 to 2.78-2.84 in air or 2.66-2.77 in N_2.[18] Recently, it has been shown that rhombohedral and orthorhombic perovskite materials demonstrate a ferroelastic behavior,[7, 11, 13, 19-20] i.e. a hysteresis behavior in stress-strain relationship. $La_{0.5}Sr_{0.5}Fe_{1-x}Co_xO_{3-\delta}$ materials fulfils the criteria to be ferroelastic, i.e. a phase transition between the ferroelastic phase and a high temperature paraelastic phase (cubic) introducing twin boundaries or domains in the materials and secondly that these domains can be reoriented by external stress.[21] The reorientation of the ferroelastic domains under mechanical stress may lead to toughening of the materials

and the temperature dependence of the fracture toughness of rhombohedral and orthorhombic perovskites have been related to the ferroelastic behavior.[7, 13] In the paraelastic phase no domains are present and the materials show elastic behavior.

$La_{0.5}Sr_{0.5}Fe_{1-x}Co_xO_{3-\delta}$ materials show low creep resistance at elevated temperatures.[22-24] Creep rates in the range $1 \cdot 10^{-9} - 2 \cdot 10^{-8}$ s^{-1} are reported at 900°C for $x = 0.5$ and $x = 1$, and even larger creep rates at higher temperatures or in inert atmosphere.[22] Even at operating temperatures around 800°C for devices with these materials, compressive creep rates are found to be significant. Creep may also give rise to systematic errors in bending experiments as shown in this paper.

We have recently performed an experimental study focusing on $La_{0.5}Sr_{0.5}Fe_{1-x}Co_xO_{3-\delta}$ materials. Here, we report on Young's modulus, strain-stress behaviour, ferroelasticity, fracture strength and fracture toughness of these materials. Particular attention is devoted to the observed temperature variation of the measured mechanical properties.

Experimental

Materials preparation

$La_{0.5}Sr_{0.5}Fe_{1-x}Co_xO_{3-\delta}$ (x = 0.5 (LSFC), 0.75 (LSF25C75) and 1 (LSC)) powders were synthesized by spray drying of glycine/nitrate solutions as described elsewhere.[18] Calcined powders were uniaxially pressed (60 MPa) into bars (8x8x58 mm, for four-point bending) or cylinders (diameter 10 mm and length 20 mm, for resonant ultrasound spectroscopy), and finally pressed isostatically at 200 MPa. The relative green densities obtained were 52-54 % of theoretical. The samples were sintered in air at 1150°C for 2 (LSFC1, LSF25C75) or 12 h (LSFC2, LSC). The heating rate was 200°C/h. To avoid cracking during cooling, the cooling rate was 50°C/h (1150-750°C), 6°C/h (750-450°C) and 100°C/h (450°C-room temperature).

Bars for mechanical testing were machined (Mil. Spec. 1942) to 3x4x45 mm^3. All the edges were chamfered. After machining, some of the bars were annealed at 500°C for 2 h to eliminate possible preferential orientation of ferroelastic domains caused by the machining. The end faces

of the cylinders were ground and polished (until diamond size of 1 μm) for determination of Young's modulus.

Characterization of microstructure and phase composition

The microstructure of the materials before and after the mechanical testing was investigated with a Hitachi S3500N scanning electron microscope (SEM) and a JEOL 2010F transmission electron microscope (TEM) equipped with a field emission gun (FEG), operating at 200 kV. The grain sizes were estimated by a linear intercept method from SEM-images of polished (1 μm diamond finish) and thermally etched (0.2 hours, 1130°C) surfaces. Ten images were taken from different parts of the polished samples. To verify the phase purity, X-ray powder diffraction (XRD) of calcined powders and sintered materials were performed on a Siemens D 5005 θ-θ diffractometer using CuK radiation. Thermogravimetry (TG) was performed using a heating rate of 2K/min on the crushed sintered samples using a Netzsch STA 449C instrument up to 1100°C. Dilatometry (DIL) was performed on sintered samples using a Netch DIL 402C instrument up to 1000°C.

Characterization of mechanical properties

Four-point bending strength of machined specimens was measured at different temperatures between room temperature and 1000°C using a fully articulating 40/20 span SiC bend fixture (MTS Model 642.85). Deflection of the specimens during loading was measured with a MTS Model 632.70-03 Bend Bar Extensiometer with three extensiometer pushrods (Model 602.81). The two outer pushrods were placed in correspondence with the two upper rollers of the bend fixture, while the third was placed in the center of the sample. Details are given in Appendix IV. A total of 5-11 bars were tested for each temperature. Fracture toughness (K_{IC}) was measured by the single edge notch beam (SENB) method or single edge V-notch beam (SEVNB) method at different temperatures using the same fixture as described above. The notch depths of the SENB specimen were ~ 0.8 or 1.2 mm and the widths were ~ 0.2 mm. For the SEVNB specimen, the notches were machined to 0.8 mm and further cut with a razor blade to totally 0.9-1.0 mm to make a V-notch. The fracture toughness was calculated using equations from ISO 15732,[25-26] see Appendix V. A total of 3-4 bars were tested at

each temperature. The mechanical testing was performed by using a Cormet 20 kN electromechanical machine with a 2 kN HBM load cell and a Sigmatest controlled-atmosphere furnace with a Kanthal A heating element and nickel radiation shields. The heating rate was 200°C/h while the cooling rate was 300°C/h. The furnace chamber was evacuated and backfilled with synthetic air before the high temperature measurements, and the measurements were performed in flowing synthetic air. The bars were equilibrated at the measurement temperature for one hour prior to the measurements. For the high temperature measurements, the samples were exposed to a load of 14 MPa at during the heating to avoid any movements in the fixture during the heating. The measurements were performed in position control with a rate of 8 μm/s for four-point bending and 1 μm/s for SENB and SEVNB measurements. The dimensions of the specimens were corrected for thermal expansion.[18] One of the LSF25C75 bars was kept at 800°C at constant stress (25 MPa) for 18 hours and the creep rate in the steady state region at the end of the relaxation was calculated. The fracture surfaces were examined by SEM to determine the fracture origins.

Selected LSFC2 samples were also heat treated in flowing N_2 ($pO_2 \sim 10^{-4}$ atm) at 800 or 1000°C to prepare samples for measurement of fracture strength and fracture toughness at elevated temperature in N_2. Heating and cooling rates in the ranges 15-100°C/h and 50-100°C/h, respectively, were tried. Due to extended fracture of the samples after cooling, only two samples were tested for fracture strength at room temperature according to the procedure described above.

The Young's modulus of the LSFC and LSF materials was measured by resonant ultrasound spectroscopy (RUS). Cylinders were placed on the top of three piezoelectric transducers, and further placed in a resistance heated furnace with controlled atmosphere. Measurements were performed for each sample in the 50-400 Hz frequency range with a resolution of 0.035 Hz. A multidimensional algorithm (Quasar International) were used to analyze the spectra by fitting the obtained frequency peaks to theoretical peaks based on dimensions, density and a set of guessed elastic constants. New elastic constants were then calculated. Young's modulus for the materials was obtained for every 100°C from room temperature up to 1200°C in air and N_2 atmospheres ($pO_2 \sim 10^{-4}$ atm).

Results and discussion

Microstructure and phase composition

The relative density, average grain size, and excess Co_3O_4 content in the materials[22] are given in Table 1. The theoretical densities used for the calculation of theoretical density were 6.29 gcm^{-3} (LSFC), 6.30 gcm^{-3} (LSF25C75) and 6.42 gcm^{-3} (LSC) calculated from x-ray diffractograms and oxygen non-stoichiometry.[18] The influence of secondary phases was neglected in the calculation of theoretical densities.

Table 1: Relative density, average grain size and excess Co_3O_4 content for the $La_{0.5}Sr_{0.5}Fe_{1-x}Co_xO_{3-\delta}$ materials sintered at different temperatures.

Composition x	Label	Sintering time at 1150°C [h]	Rel. density [%]	Grain size [μm]	Co_3O_4 content [wt%]
0.5	LSFC1	2	97	0.8 ± 0.1	0.10
0.5	LSFC2	12	95	1.1 ± 0.2	0.99
0.75	LSF25C75	2	97	1.4 ± 0.3	2.8
1	LSC1	12	99	1.7 ± 0.4	0.39
1	LSC2	12	99	1.7 ± 0.4	0.98

A typical image of the microstructure of these materials is shown in Figure 1. The pores in the materials were sub-micron in size as seen in the insert in Figure 1. Larger flaws observed as the fracture origins did also contribute to the closed porosity.

Thermogravimetrical analysis showed that small amounts of Co_3O_4 were present in the samples (Table 1), indicating a small deviation from nominal composition.[22] The excess Co_3O_4 was located in grains about 0.5 μm in size consisting of several Co_3O_4 crystallites as shown in the TEM-image in Figure 2. The Co_3O_4 crystallites were formed according to reaction (1) when excess CoO was oxidized to Co_3O_4 during cooling of the material from the sintering temperature.

$$3CoO + \tfrac{1}{2}O_2(g) \rightarrow Co_3O_4 \qquad (1)$$

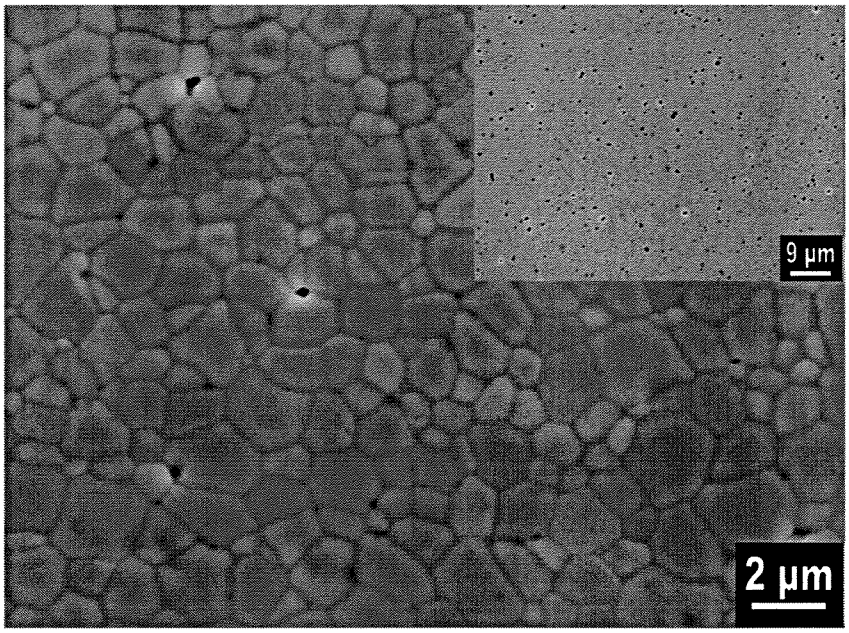

Figure 1: SEM image of etched surface of $La_{0.5}Sr_{0.5}Fe_{0.5}Co_{0.5}O_{3-\delta}$ material sintered at 1150°C for 12 hours (LSFC2). Insert: Polished surface of the same material.

The expansion due to reaction (1) is 16.4 vol%, which introduces compressive "radial" stresses and tensile hoop stresses in the perovskite matrix surrounding the Co_3O_4 inclusions. For LSF25C75 containing 2.8 wt% Co_3O_4, the expansion was observed by dilatometry between 950°C to 910°C to be 0.3 vol%.[27] For the other materials, the effect of the Co_3O_4 inclusions was not detected by dilatometry. The stresses generated around the Co_3O_4 inclusions due to the volume expansion may result in crack trapping and enhancement of the fracture toughness.[28]

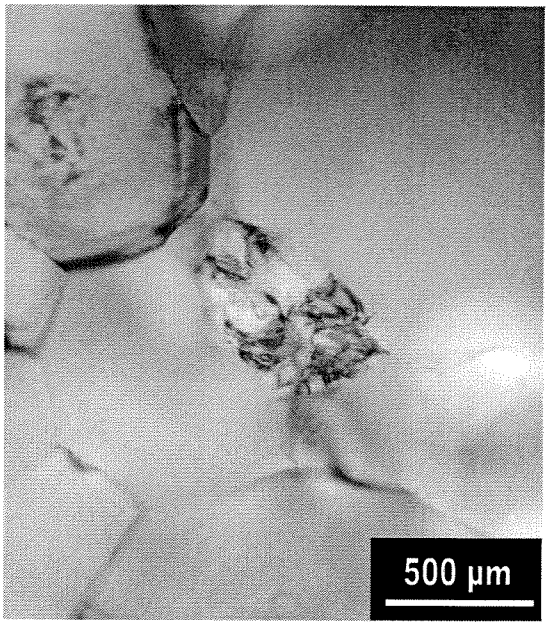

Figure 2: TEM image of $La_{0.5}Sr_{0.5}Fe_{0.5}Co_{0.5}O_{3-\delta}$ (LSFC1) with an inclusion consisting of several Co_3O_4 crystallites.

Young's modulus

The Young's modulus of the LSFC2 and LSC2 materials measured by RUS in air and N_2 is shown as a function of temperature in Figure 3.

The average value of the Young's modulus for LSFC and LSC for $T < 400°C$ is 130 ± 1 and 133 ± 3 GPa, respectively, independent on atmosphere. Generally a decrease of about 1% per hundred Kelvin in Young's modulus is expected with increasing temperature for polycrystalline ceramics without grain boundary softening.[28] Two of the data sets actually demonstrate a depression of the Young's modulus with increasing temperature. The temperature dependence of Young's modulus can also generally be described by equation (2) according to Hillig[29-31]

$$\frac{E}{E_0} = 1 - \left(\frac{T}{T_m}\right)^3 \qquad (2)$$

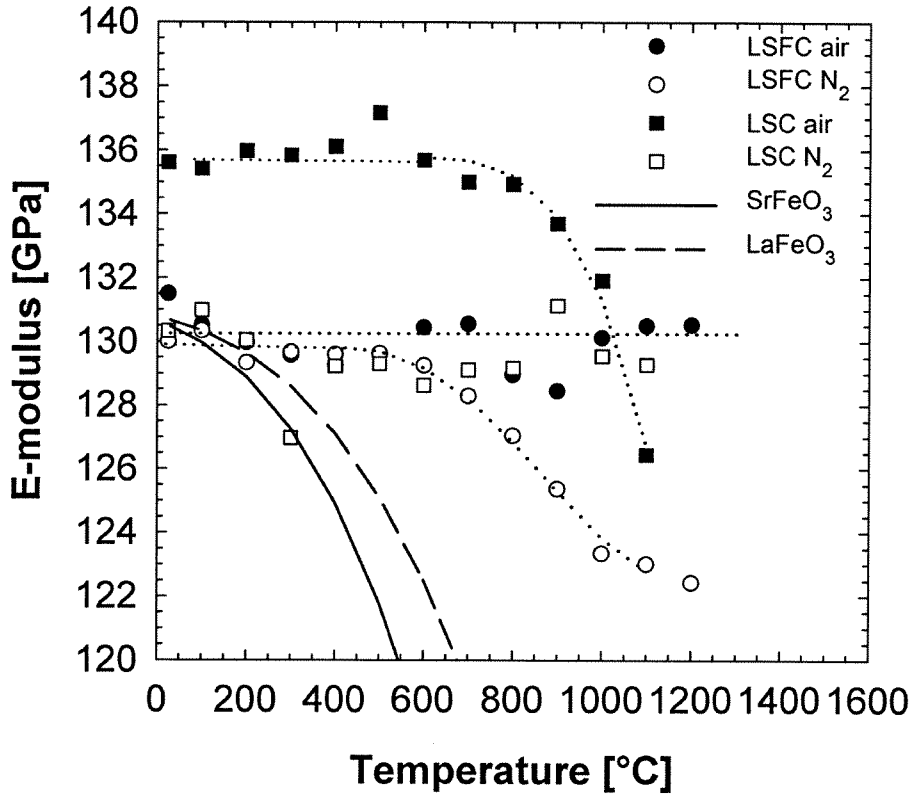

Figure 3: Young's modulus of $La_{0.5}Sr_{0.5}Fe_{0.5}Co_{0.5}O_{3-\delta}$ (LSFC2) and $La_{0.5}Sr_{0.5}CoO_{3-\delta}$ (LSC2) in air and N_2 as a function of temperature, measured by resonant ultrasound spectroscopy. The solid and the dashed lines represent the model from Hillig[29-31] and the dotted lines are guides to the eye.

where E_0 is the Young's modulus at room temperature, T is the actual temperature and T_m is the melting temperature of the material. The model is compared to the measured data in Figure 3 using E_0 = 131 GPa and the melting point of $LaFeO_3$ [32] (dashed line) and $SrFeO_3$ [33-34] (solid line). The model predicts a considerably sharper reduction of the Young's modulus with increasing temperature than observed. Hence, the thermal and chemical expansion[18] is not significantly influencing the value of the Young's modulus of these materials. Neither is a possible contribution from frozen in tensional stresses at the surface as discussed later in the fracture strength chapter. The Young's modulus of the materials is therefore considered quite constant in the whole temperature range studied.

Strain-stress relationship and apparent Young's modulus

The strain-stress relationship for LSFC2 and LSF25C75 at different temperatures measured by four-point bending is given in Figures 4 and 5. LSC1 investigated at room temperature and 800°C showed a similar behavior as LSF25C75. At room temperature, the strain-stress relationship is non-linear and for LSFC2 an inflection point around 80 ± 10 MPa is observed (Figure 4). This non-linear behavior is interpreted as the signature of ferroelasticity in the materials as a part of a hysteresis curve in strain-stress is observed.[7, 13] For LSF25C75 and LSC, the inflection point in strain-stress behavior is at a higher stress level than the maximum stress level obtained here. A higher value is expected because an inflection point of 215 MPa has been observed for $La_{0.7}Ca_{0.3}CoO_3$ in compression studies.[19] By increasing substitution of Ca for La in $LaCoO_3$, an inflection point at a higher stress level was observed consistent with the present data.[19] $LaFeO_3$ has previously been shown to be a soft ferroelastic material with a very narrow hysteresis loop[7] also consistent with an increasing value for the inflection point with increasing x in $La_{0.5}Sr_{0.5}Fe_{1-x}Co_xO_{3-\delta}$ materials. The strain-stress data observed at room temperature for the present materials demonstrates that they are ferroelastic. At 400°C and higher temperatures, the stress-strain relationship does not show any inflection point, which is in accordance with the transition to a paraelastic phase above 300°C.[18] A linear stress-strain behavior is therefore expected above the transition temperature.

However, an increasing degree of non-linearity is again observed for measurements at high temperatures, especially at 1000°C. The steady state creep rate of LSF25C75 at 800°C and 25 MPa calculated from four-point bending was $6.8 \cdot 10^{-10}$ s^{-1} and by extrapolating creep data obtained at different temperatures and different loads, the compressive creep rate for LSFC2 at 800°C and at 175 MPa (load corresponding to the fracture strength) was estimated to $4 \cdot 10^{-8}$ s^{-1} by assuming the same creep rate-stress relationship as the one measured for 1000°C.[22] The creep rate in tension is expected to be even larger than this value.[28] These significant creep rates at 800°C and higher temperatures are therefore responsible for the observed non-linear behavior in the strain-stress behavior.

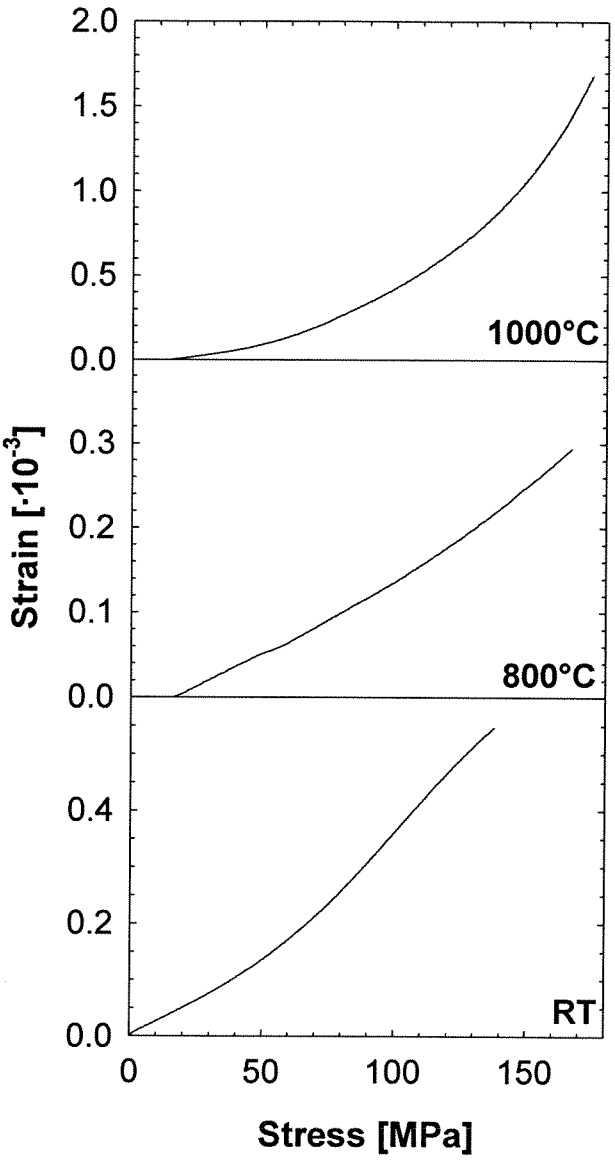

Figure 4: Strain vs. stress relationship for $La_{0.5}Sr_{0.5}Fe_{0.5}Co_{0.5}O_{3-\delta}$ (LSFC2) at room temperature, 800°C and 1000°C. Note that for testing at elevated temperature a pre-stress of 14 MPa was applied to the sample during heating.

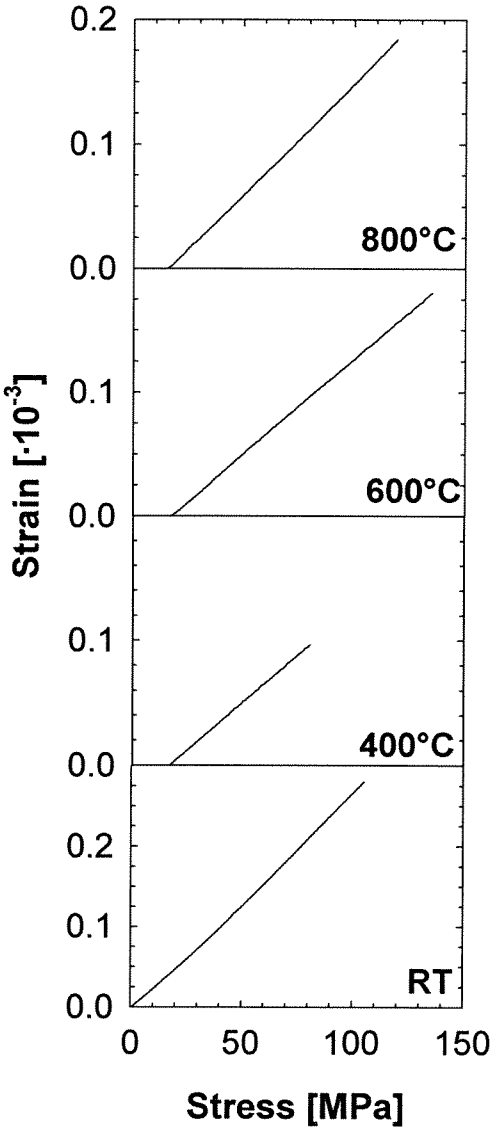

Figure 5: Strain vs. stress relationship for $La_{0.5}Sr_{0.5}Fe_{0.25}Co_{0.75}O_{3-\delta}$ (LSF25C75) at room temperature, 400°C, 600°C and 800°C. Note that for testing at elevated temperature a pre-stress of 20 MPa was applied to the sample during heating.

The Young's modulus is proportional to the inverse slope of strain-stress curves for elastic materials with symmetric deformation behavior. The apparent Young's modulus obtained from strain-stress relationships of the

present materials is summarized in Table 2. The apparent Young's modulus is calculated using the inverse slope from the first measured 5-10 MPa of the strain-stress curves if non-linear behavior is observed.

Table 2: Apparent Young's modulus and fracture strength of $La_{0.5}Sr_{0.5}Fe_{1-x}Co_xO_{3-\delta}$ materials at different temperatures measured by 4-point bending. The given uncertainty is the standard deviation between the different bars.

Composition	Temperature [°C]	Apparent Young's modulus [GPa]	Fracture strength [MPa]	Number of bars
LSFC1	RT, non-annealed	115 ± 5	107 ± 15	11
	RT, annealed	116 ± 10	121 ± 7	5
	800	160 ± 10	181 ± 13	5
LSFC2	RT, annealed	118 ± 7	128 ± 12	8
	800	169 ± 8	166 ± 15	6
	1000	121 ± 11	181 ± 23	5
LSF25C75	RT, annealed	115 ± 3	71 ± 7	6
	400, annealed	176 ± 8	61 ± 20	3
	600	177 ± 4	121 ± 11	3
	800	160 ± 10	120 ± 11	5
LSC1	RT, non-annealed	122 ± 5	138 ± 12	8
	800	157 ± 7	181 ± 18	6

The apparent Young's modulus given in Table 2 is not in good agreement with the values obtained by RUS. Particularly, the temperature dependence of the apparent Young's modulus determined by 4-point bending is non-physical as the Young's modulus should decrease with increasing temperature.[28] The increasing apparent Young's modulus from room temperature to 400°C and above is probably related to the ferroelastic behavior of the materials below 300°C.

At high temperatures and high stresses, where creep contributes to the stress-strain relationship, a systematic depression of the apparent Young's modulus is expected. At low stress levels the creep is not considered to affect the stress-strain relationship, and we therefore have no reliable explanation for the non-physical behavior of the apparent Young's modulus from 4-point bending. However, RUS is considered to be a more reliable method,[15] and the Young's modulus of the materials obtained by RUS is the far most credible.

Fracture strength

The fracture strength of the materials obtained by four-point bending is included in Table 2. This fracture strength value is the linear-elastically computed strength value for all data even if they are non-elastic. These calculated values are unrealistic high when non-linear strain-stress relationship is observed due to the non-symmetric deformation behavior in tension and compression.[35-36]

Machining of the bars prior to the mechanical testing may induce preferential orientation of the ferroelastic domains due to the stresses applied. This preferential orientation of domains may reduce the fracture strength. Here, it is seen that heat-treatment at 500°C for 2 hours gives a small increase in the fracture strength for LSFC1 at room temperature from 107 ± 15 MPa to 121 ± 7 MPa and a decrease in standard deviation is observed. These results show that the bars should be heat-treated before measurements at temperatures below the ferroelastic to paraelastic phase transition temperature in accordance with previous reports.[13] For temperatures above the phase transition, the materials are expected to relax before the measurements and a heat-treatment is not considered to be necessary.

The fracture origins of all samples were porous regions or flaws with extension up to 100 μm. In a few cases a secondary phase was observed as the origin. The fracture mirrors are also easily seen, especially for the fracture surfaces of bars tested at room temperature. An example of a porous fracture origin and fracture mirror of LSFC1 is shown in Figure 6. More images are shown in Appendix VI. At room temperature and 400°C a intragranular fracture mode was generally observed while at temperatures above 600°C an intergranular fracture mode was observed as can be seen from the fracture surfaces of LSFC2 at room temperature and 800°C given in Figure 7.

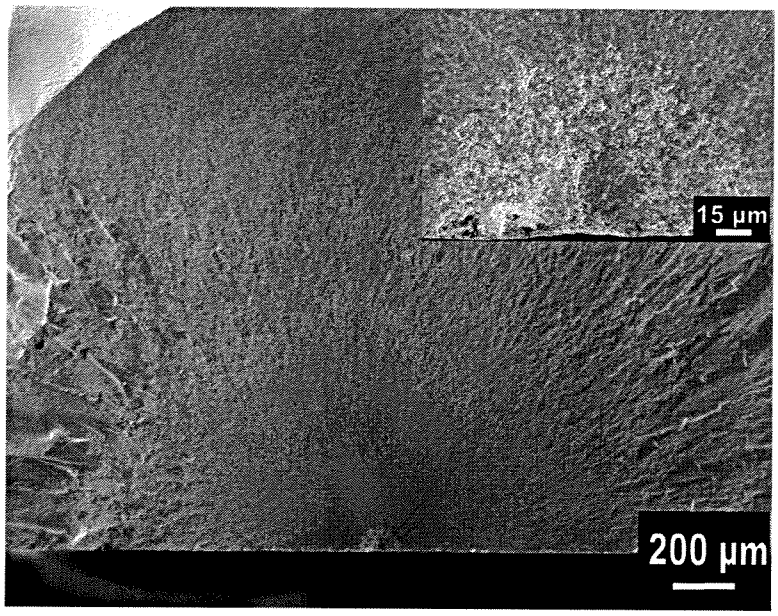

Figure 6: SEM image of a fracture surface after four-point bending of a $La_{0.5}Sr_{0.5}Fe_{0.5}Co_{0.5}O_{3-\delta}$ (LSFC1) bar. The fracture mirror is easily seen. The insert is the fracture origin.

Table 2 shows that the fracture strength increases with increasing temperature, however, several factors contribute to the uncertainty of these values. In the following a discussion about these factors is given. Deviation from linear and symmetrical deformation will lead to systematic errors in the calculated fracture strength. Since the deviation from linear deformation is largest at temperatures below 300°C (due to ferroelasticity) and at the high temperatures (due to creep), a minimum in calculated fracture strength is expected at around 4-600°C where an elastic behavior is observed. Since such a minimum in calculated fracture strength is not observed (Table 2), the non-elastic behavior and error related to this is not the major factor giving the increase in fracture strength with increasing temperature. The effect of the Co_3O_4 secondary phase is not expected to significantly affect the fracture strength. However, if it did a decrease in fracture strength with increasing temperature is expected as the cobalt oxide phase will be reduced upon heating at high temperatures. The loss of the ferroelastic behavior above the phase transition temperature will also cause a reduction in the expected fracture strength of the materials.

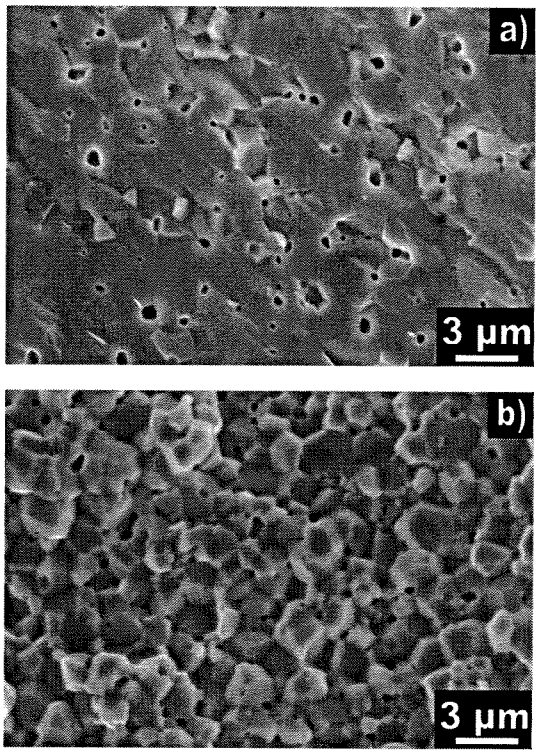

Figure 7: SEM images of a fracture surface of $La_{0.5}Sr_{0.5}Fe_{0.5}Co_{0.5}O_{3-\delta}$ (LSFC2) after four-point bending measurements at a) room temperature and b) 800°C.

The factor which we believe is the most significant for explaining the observed increase in fracture strength with increasing temperature is the fact that a gradient in oxygen content could have been generated during the cooling of these materials from the sintering temperature. During the cooling the interior of the samples will have lower oxygen content than the exterior introducing tensile stresses on the surface of the materials compared to the interior. The stress gradients hence generated will weaken the material at low temperatures. During testing at elevated temperatures where the oxygen diffusivity becomes sufficient for equilibration of the oxygen content, the oxygen gradient will be eliminated and hence a higher fracture strength value is obtained. We therefore suggest that fracture strength values observed at elevated temperatures is more representative for the fracture strength of stress free materials than the fracture strength values obtained at room temperature. The significant effect of the stress gradients is supported by the fact that a very large fraction of samples cracked when reduced samples were prepared by cooling in nitrogen atmosphere. The change from

transgranular to intergranular fracture mode with increasing temperature may contribute to the observed increase in nominal fracture strength.

Based on dilatometry of polycrystals,[18] the oxygen content of the bulk is frozen in at 400-600°C. In N_2 the oxygen loss and chemical expansion is considerably higher. Stresses in membranes induced by the gradient in δ are conveniently normalized with respect to the magnitude of the maximum possible biaxial stress, s_{max}, expressed as[37]

$$|s_{\max}| = \hat{E}|\varepsilon_{c,\max}| \tag{3}$$

where $\varepsilon_{c,\max}$ is the maximum chemical strain and Ê is related to the Young's modulus, E, and the Poisson's ratio, υ, by

$$\hat{E} = \frac{E}{1-\upsilon} \tag{4}$$

By using a Young's modulus of 130 GPa (LSFC2), Poisson's ratio of 0.33 and maximum stress of 166 MPa, $\varepsilon_{c,\max}$ is calculated to $9 \cdot 10^{-4}$. The chemical expansion, ε_c, found for LSFC at 800°C between air and N_2 atmosphere was $4.5 \cdot 10^{-3}$,[18] and hence above $\varepsilon_{c,\max}$. This calculation can explain the built-in stresses in the materials during cooling. The materials will be oxidized, but when the temperature is lowered to a certain point, the transport from bulk will be too slow and remain in the reduced condition while the surface still will be oxidized. The difference in oxidation state between bulk and surface may give stresses in the in the order of what give failure.

Fracture toughness

Fracture toughness of the materials obtained by single edge notch beam (SENB) method and single edge V-notch beam (SEVNB) are summarized in Table 3.

Table 3: Fracture toughness measured by single edge notch beam (SENB) method and by single edge V-notch beam (SEVNB) method for $La_{0.5}Sr_{0.5}Fe_{1-x}Co_xO_{3-\delta}$ materials at different temperatures.

Comp.	Method	Notch length [mm]	Temperature [°C]	Fracture toughness [MPa·m$^{1/2}$]	No. of bars
LSFC1	SENB	0.75-0.78	RT, non-annealed	1.31 ± 0.11	3
		1.14-1.16	RT, non-annealed	1.84 ± 0.33	3
LSFC2	SEVNB	0.87-0.96	RT, annealed	1.16 ± 0.12	5
		0.92-0.95	800	1.48 ± 0.16	5
		0.92-0.95	1000	2.26 ± 0.20	4
LSC1	SENB	1.17-1.20	RT, non-annealed	1.47 ± 0.44	3
		1.16-1.19	RT, annealed	1.49 ± 0.30	3
		1.16-1.18	800	2.88 ± 0.44	3

The annealing of the LSC bars did not influence the absolute values of the toughness. The standard deviation for the measurements performed by the SEVNB method is smaller compared to the SENB method due to the better defined notch as is illustrated in Figure 7.

The fracture toughness increases with temperature. Both the fracture toughness and the fracture strength shows the same temperature dependency as is shown in Figure 8 which is in accordance with equation (3)[28, 38]

$$\sigma_f = K_{IC}/Yc^{1/2} \tag{5}$$

where Y is a dimensionless factor dependent on the crack configuration and c is the half of the crack length or the entire length of an edge crack. The stress gradient developed due to the difference in oxygen stoichiometry is therefore also influencing on the fracture toughness values.

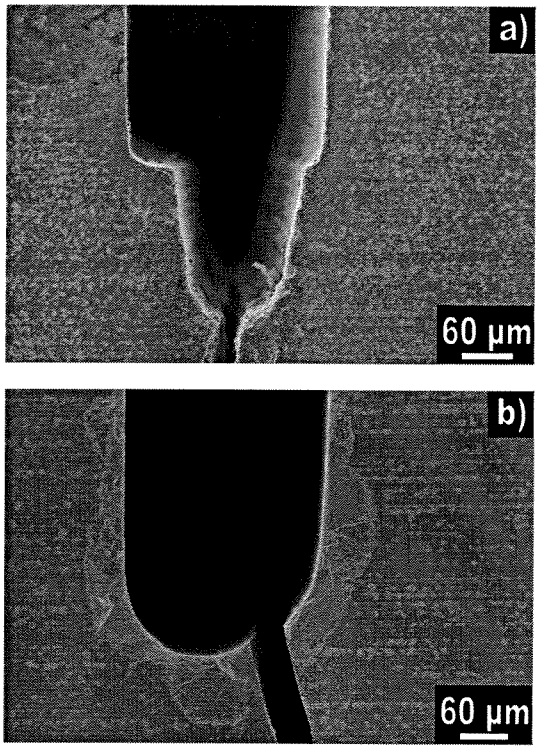

Figure 7: Notch shape for a) a SEVNB-bar (LSFC2) and b) a SENB-bar (LSFC1) of $La_{0.5}Sr_{0.5}Fe_{0.5}Co_{0.5}O_{3-\delta}$ materials.

Fracture strength of reduced samples

The measured fracture strength of two LSFC2 bars pre-reduced in nitrogen atmosphere was 13 and 24 MPa. After cooling in nitrogen atmosphere the surface of the samples appeared cracked as can be seen from Figure 9 giving the low fracture strength. It was also a large fraction of the samples that fractured during the cooling in nitrogen atmosphere, showing that considerable stress gradients develop in the materials due to gradient in oxygen concentration. This is also in agreement with the proposed effect of the stresses due to oxygen concentration gradient on the nominal fracture strength of the samples.

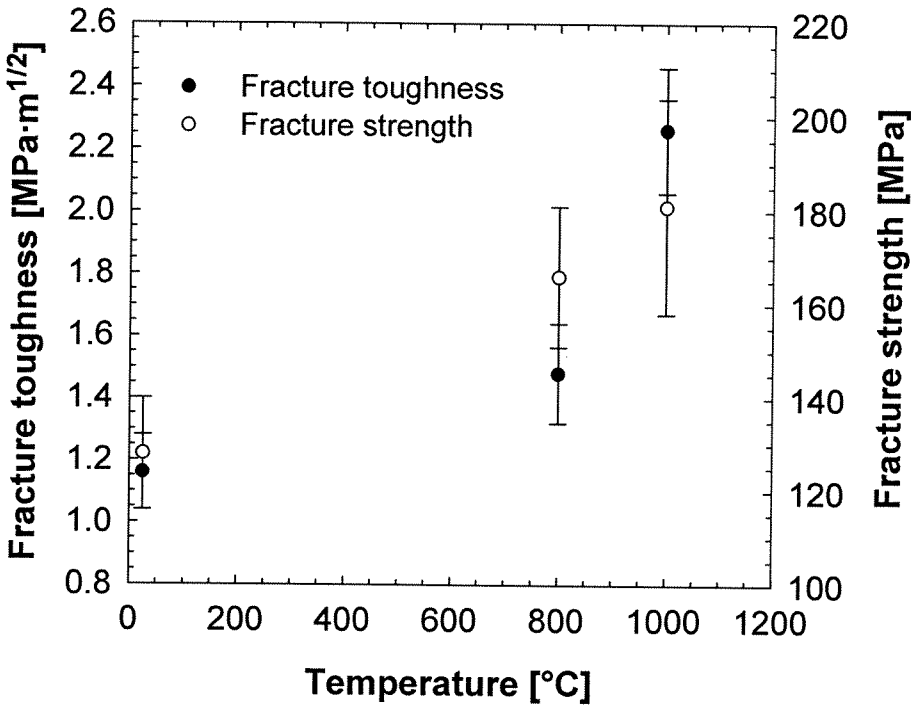

Figure 8: Fracture strength and fracture toughness for $La_{0.5}Sr_{0.5}Fe_{0.5}Co_{0.5}O_{3-\delta}$ bars.

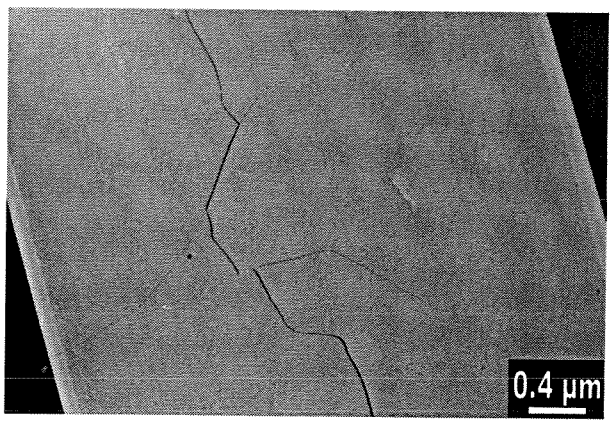

Figure 9: Surface of a $La_{0.5}Sr_{0.5}Fe_{0.5}Co_{0.5}O_{3-\delta}$ bar (LSFC2) heat-treated in N_2 prior to fracture strength measurement.

Conclusion

$La_{0.5}Sr_{0.5}Fe_{1-x}Co_xO_{3-\delta}$ materials, $0.5 \leq x \leq 1$, are ferroelastic and show a non-linear strain-stress relationship below the ferroelastic to paraelastic phase transition temperature of 300°C. Above this temperature a liner strain-stress relationship is observed, however, at temperatures exceeding about 800°C the materials again shows non-linear behaviour due to creep. The room temperature values for fracture strength (4-point bending) and fracture toughness (SEVNB) were 107-128 MPa and 1.16-1.84 $MPa \cdot m^{1/2}$, respectively, and these values were observed to increase with increasing temperature. This increase was attributed to frozen-in stress gradients in the materials during cooling due to different oxygen stoichiometry. These stress gradients caused the low-temperature fracture strength and fracture toughness values to be low. The Young's modulus at room temperature measured by resonant ultrasound spectroscopy of the materials with $x = 0.5$ and $x = 1$ were 130 ± 1 and 133 ± 3 GPa, respectively. Apparent Young's modulus values calculated from strain-stress relationships were not in good agreement with the values obtained by RUS. The present findings have demonstrated the importance of understanding ferroelasticity and chemically induced stresses in order to understand the mechanical properties of mixed valence state rhombohedral perovskite materials.

Acknowledgement

The Research Council of Norway, Statoil and Hydro are acknowledged for financial support. A special thank to Miladin Radovic for help performing the RUS measurements.

References

1. H. J. M. Bouwmeester and A. J. Burgraaf, in: P.J. Gellings and H.J.M. Bouwmeester (Eds), The CRC Handbook of Solid State Electrochemistry, CRC Press, Inc., New York (1997).
2. A. Atkinson and A. Selcuk, "Mechanical behaviour of ceramic oxygen ion-conducting membranes", Solid State Ionics, 134 (2000) 59-66.
3. P. V. Hendriksen, P. H. Larsen, M. Mogensen, F. W. Poulsen and K. Wiik, "Prospects and problems of dense oxygen permeable membranes", Catalysis Today, 56 (2000) 283-295.
4. J. E. ten Elshof, H. J. M. Bouwmeester and H. Verweij, "Oxygen transport through $La_{1-x}Sr_xFeO_{3-\delta}$ membranes. I. Permeation in air/He gradients", Solid State Ionics, 81 (1995) 97-109.
5. J. Mizusaki, M. Yoshihiro, S. Yamauchi and K. Fueki, "Nonstoichiometry and defect structure of the perovskite-type oxides $La_{1-x}Sr_xFeO_{3-\delta}$ " J. Solid State Chem., 58 (1985) 257-266.
6. V. V. Kharton, E. N. Naumovich and A. V. Nikolaev, "Materials of high-temperature electrochemical oxygen membranes", J. Membr. Sci., 111 (1996) 149-157.
7. A. Fossdal, M.-A. Einarsrud and T. Grande, "Mechanical properties of $LaFeO_3$ ceramics", J. Euro. Ceram. Soc., 25 (2005) 927-933.
8. C. S. Montross, H. Yokokawa, M. Dokiya and L. Bekessy, "Mechanical Properties of Magnesia-Doped Lanthanum Chromite versus Temperature", J. Am. Ceram. Soc., 78 (1995) 1869-1872.
9. S. W. Paulik, S. Baskaran, T. R. Armstrong, "Mechanical properties of calcium- and strontium-substituted lanthanum chromite", J. Mater. Sci., 33 (1998) 2397-2404.
10. Y.-S. Chou, J. W. Stevenson, T. R. Armstrong and L. R. Pederson, "Mechanical Properties of $La_{1-x}Sr_xCo_{0.2}Fe_{0.8}O_3$ Mixed-Conducting Perovskites Made by the Combustion Synthesis Technique", J. Am. Ceram. Soc., 83 (2000) 1457-1464.
11. N. Orlovskaya, K. Kleveland, T. Grande and M.-A. Einarsrud, "Mechanical properties of $LaCoO_3$ based ceramics", J. Euro. Ceram. Soc., 20 (2000) 51-56.
12. S. Baskaran, C. A. Lewinsohn, Y.-S. Chou, M. Qian, J.W. Stevenson and T. R. Armstrong, "Mechanical properties of alkaline earth-doped lanthanum gallate", J. Mater. Sci., 34 (1999) 1-10.
13. K. Kleveland, N. Orlovskaya, T. Grande, A. M. M. Moe, M.-A. Einarsrud, K. Breder and G. Gogotsi, "Ferroelastic Behavior of $LaCoO_3$-Based Ceramics", J. Am. Ceram. Soc., 84 (2001) 2029-2033.

14. N. M Sammes and R. Ratnaraj, "High-temperature mechanical properties of $La_{1-x}Sr_xCr_{1-y}Co_yO_3$ for SOFC interconnect", J. Mater. Sci., 30 (1995) 4523-4526.
15. M. Radovic, E. Lara-Curzio and L. Riester, "Comparison of different experimental techniques for determination of elastic properties of solids", Mater. Sci. Eng., A368 (2004) 56-70.
16. Y. S. Chou, K. Kerstetter, L. R. Pederson and R. E. Williford, "Mechanical and thermal properties of combustion-synthesized perovskites, $La_{1-x}Sr_xCr_{0.2}Fe_{0.8}O_3$", J. Mater. Res., 16 [12] (2001) 3545-3553.
17. D. L. Meixner and R. A. Cutler, "Sintering and mechanical characteristics of lanthanum strontium manganite", Solid State Ionics, 146 (2002) 273-284.
18. H. L. Lein, K. Wiik and T. Grande, "Thermal and chemical expansion of $La_{0.5}Sr_{0.5}Fe_{1-x}Co_xO_{3-\delta}$ ($0 \leq x \leq 1$) materials", paper I.
19. S. Faaland, P.E. Vullum, T. Grande, R. Holmestad, and M.-A. Einarsrud, "Stress-strain behavior during compression of polycrystalline $La_{1-x}Ca_xCoO_3$ ceramics", J. Am. Ceram. Soc., in print.
20. D. Y. Ostovoi, G. A. Gogotsi, S. A. Suvorov and A. P. Shevchik, "Strain and fracture of a ceramic based on lanthanum chromite", Refractories and Industrial Ceramics, 43 [7-8] (2002) 237-246.
21. E.K.H. Salje, Phase Transitions in Ferroelastic and Co-elastic Crystals, Cambridge University Press, Cambridge, 1990.
22. H. L. Lein, E. Lara-Curzio, K. Wiik, M.-A. Einarsrud and T. Grande, "High temperature creep behavior of $La_{0.5}Sr_{0.5}Fe_{1-x}Co_xO_{3-\delta}$ ($0 \leq x \leq 1$) materials", paper II.
23. K. Kleveland, A. Wereszcak, and T.P. Kirkland, "Compressive creep of $SrFeO_3$", J. Am. Cer. Soc., 84 (2001) 1822-26.
24. G. Majkic, L. Wheeler, and K. Salma, "Characterization of Creep Behavior of $SrCo_{0.8}Fe_{0.2}O_{3-x}$", Mater. Res. Soc. Symp. Proc., 575 (2000) 349-54.
25. ISO/CD 15732 Fine Ceramics (Advanced ceramics, Advanced technical ceramics) – Test method for fracture toughness at room temperature by single edge precracked beam (SEPB) method, International Organization for Standardization, Geneva, Switzerland.
26. ASTM STP 1409 Fracture Resistance Testing of Monolithic and Composite Brittle Materials, J. Kübler, "Fracture Toughness of Ceramics using the SEVNB Method: From a Preliminary Study to a Standard Test method", 93-106.
27. Ø. S. Andersen, "Thermal and mechanical properties of $La_{1-x}Sr_xFe_{1-y}Co_yO_{3-\delta}$", diploma thesis, Norwegian University of Science and Technology, Trondheim, Norway (2003).

28. J. B. Wachtman, "Mechanical properties of ceramics", John Wiley & Sons Inc., New York (1996).
29. W. B. Hillig, "Prospects for ultra-high-temperature ceramic composites", General Electric, Corporate Research and Development, No. 85CRD152, Aug 1985.
30. W. B. Hillig, "Prospects for ultra-high-temperature ceramic composites", Mater. Sci. Res., 20 (1986) 697-712.
31. W.S. Hillig, "A methodology for estimating the mechanical properties of oxides at high temperature", J. Am. Ceram. Soc., 76 (1993) 129-138.
32. V. L. Moruzzi and M. W. Shafer, "Phase equilibria in the system La_2O_3-iron oxide in air", J. Am. Ceram. Soc., 43 (1960) 367-372.
33. A. Fossdal, M.-A. Einarsrud and T. Grande, "Phase equilibria in the pseudo binary system SrO-Fe_2O_3 in air", in print.
34 P. Batti, "Diagramma d'equilibrio del sistema SrO-Fe_2O_3", Ann. Chim. (Rome), 52 (1962) 941-961.
35. T. Fett, D. Munz and G. Thun, "Nonsymmetric Deformation Behavior of Lead Zirconate Titanate Determined in Bending Tests", J. Am. Ceram. Soc., 81 [1] (1998) 269-272.
36. T. Fett, D. Munz and G. Thun, "Bending strength of a PZT ceramic under electric fields", J. Euro. Ceram. Soc., 23 (2003) 195-202.
37. A. Atkinson and T. M. G. M. Ramos, "Chemically-induced stresses in ceramic oxygen ion-conducting membranes", Solid State Ionics, 129 (2000) 259-269.
38. D. W. Richerson, "Modern Ceramic Engineering", Marcel Dekker Inc., New York (1992).

PAPER IV

Oxygen permeability of $La_{0.5}Sr_{0.5}Fe_{1-x}Co_xO_{3-\delta}$ ($0 \leq x \leq 1$) materials

Hilde Lea Lein, Tor Grande and Kjell Wiik*

Department of Materials Technology,
Norwegian University of Science and Technology,
7491 Trondheim, Norway.

Abstract

Oxygen flux through $La_{0.5}Sr_{0.5}Fe_{1-x}Co_xO_{3-\delta}$ (x = 0, 0.5 and 1) membranes has been found as a function of oxygen partial pressure and temperature. In a He - air gradient at 1148°C for relative thin membranes (0.81-0.97 mm), the fluxes varied between 0.4 and 2.8 ml/min·cm^{-3} dependent on composition. The activation energies was calculated to 67-105 kJ/mol for the temperature range of 970-1148°C, with the highest values for x = 0. For the smallest pO_2 gradients, diffusion controlled the permeability. Larger pO_2 gradients caused a surface exchange controlled flux. The fluxes were seen to decrease for the largest gradients, due to the oxygen partial pressure dependency of the surface exchange coefficient.

* Correspondence to Kjell.Wiik@material.ntnu.no

Introduction

Due to the mixed conductivity, $La_{1-x}Sr_xFe_{1-y}Co_yO_{3-\delta}$ materials are potential candidates as oxygen permeable membranes. In such a dense membrane, there is transport of oxygen ions and electrons at elevated temperatures without an external electrical circuit, and the driving force for the oxygen ions is the difference in oxygen partial pressure on each side of the membrane.[1-4]

The oxygen permeation is determined by either surface exchange processes on one or both of the surfaces, or solid-state oxygen ion bulk diffusion. The bulk diffusion depends on the temperature, oxygen partial pressure and microstructure of the bulk. The surface exchange depends in addition on surface structure and area.[1] The oxygen transport in bulk is described by the Wagner equation

$$j_{O_2} = -\frac{RT}{4^2 F^2 L} \int_{\ln P'_{O_2}}^{\ln P''_{O_2}} \frac{\sigma_{el}\sigma_{ion}}{\sigma_{el}+\sigma_{ion}} d\ln P_{O_2} \qquad (1)$$

where R is the gas constant, T is the temperature, L is the membrane thickness, σ_{el} and σ_{ion} are the electronic and the ionic conductivity, and P'_{O2} and P''_{O2} are the oxygen partial pressures on the different sides of the membrane.[1]

For materials with high bulk diffusion or in the case of very thin membranes, the surface exchange processes may be the rate controlling step for oxygen transport. This transition from predominant control by diffusion to control by surface exchange corresponds to the critical thickness, L_c, of the membrane.[1] L_c is reported to vary in the range from 20 to 3000 μm dependent on composition, temperature and pO_2.[5]

Here we report the oxygen permeation of $La_{0.5}Sr_{0.5}Fe_{1-x}Co_xO_{3-\delta}$ (x = 0, 0.5 and 1) materials as a function of temperature, oxygen partial pressure across the membrane and time. Special attention is made to a decrease in oxygen flux in the surface exchange controlled regime. There are many studies of these properties for similar compositions in the literature,[5-14] however, the temperature where the measurements have been performed is lower than used here.

Experimental

Materials preparation and characterization

$La_{0.5}Sr_{0.5}Fe_{1-x}Co_xO_{3-\delta}$ (x = 0 (LSF), 0.5 (LSFC) and 1 (LSC)) powders were synthesized by spraydrying of glycine/nitrate solution as described elsewhere.[15] Oxide powders were calcined at 900°C (LSFC and LSC) or 1050°C (LSF) for 24 h in air. The powders were then ball milled (Si_3N_4-balls) for 24 h, and heat-treated at 600°C for 24 h.

The stoichiometries of the materials were shown to deviate from the nominal, resulting in the presence of small amount of a cobalt oxide secondary phase. The amount of cobalt excess was determined by thermogravimetrical analysis using the weight loss due to the phase transition of Co_3O_4 to CoO. In order to obtain an A-excess membrane, a small amount of calcined LSFC powder was added Sr-nitrate to a SrO excess of 0.66 wt%. The strontium nitrate was dissolved in water and the calcined powder was added. The water was then removed by evaporation.

The calcined powders were pressed uniaxially into discs (57 MPa) and pressed cold isostatic (200 MPa). The relative green densities obtained were 52-54 %. The compositions LSFC and LSC were sintered in air at 1150°C for 2 or 12 hours respectively. The composition LSF was sintered in air at 1250°C for 12 hours. The Sr-added LSFC was sintered at 1250°C for 24 hours. To avoid cracking during cooling, the cooling rate for all compositions was set to 50°C/h (sintering temperaure-750°C), 6°C/h (750-450°C) and 100°C/h (450°C-room temperature). The surfaces of the sintered samples were grinded parallel and to wanted thicknesses (~ 1 mm), and then polished (until 1μm diamond size). Table 1 gives a summary of the different membranes investigated.

Table 1: Average grain size and relative densities for $La_{0.5}Sr_{0.5}Fe_{1-x}Co_xO_{3-\delta}$ sintered at different temperatures.

Membrane Name	Composition x	Sintering temperature [°C]	Sintering time [h]	B-excess Co_3O_4 [wt%]	A-excess SrO [wt%]
LSFC 3	0.5	1150	2	0.10	-
LSFC 4	0.5	1150	2	0.10	-
LSF 5	0	1250	12	-	-
LSC 6	1	1150	12	0.98	-
LSFC 7	0.5	1250	24	-	0.66

The microstructure of the materials before and after the permeation experiments was investigated with a Hitachi S3500 N scanning electron microscope (SEM). The grain sizes were estimated by a linear intercept method of 2-dimentional SEM-images of the polished (1μm diamond finish) and thermal etched (0.2 hours, 1130°C) surfaces. Ten images were taken from different parts of the polished samples. To verify the phase purity, X-ray powder diffraction (XRD) of calcined powders and sintered materials were performed on a Siemens D 5005 θ-θ diffractometer using CuK radiation. The data were collected with a step size of 0.03° and a count time of 8 s. The densities of the membranes were determined by the Archimedean method (ISO 5017) in isopropanol. Table 2 gives the thicknesses, average grain sizes and the relative densities of the membranes. Here the theoretical densities used are 5.99 g cm^{-3} (LSF), 6.29 g cm^{-3} (LSFC) and 6.42 g cm^{-3} (LSC) calculated from x-ray diffraction and oxygen non-stoichiometry.

Table 2: Average grain size and relative densities for $La_{0.5}Sr_{0.5}Fe_{1-x}Co_xO_{3-\delta}$ sintered at different temperatures.

Membrane Name	Composition x	Thickness [mm]	Grain size [μm]	Relative density [%]
LSFC 3	0.5	0.81	0.8 ± 0.1	97
LSFC 4	0.5	0.94	0.8 ± 0.1	97
LSF 5	0	0.94	1.2 ± 0.2	95
LSC 6	1	0.97	1.7 ± 0.4	99
LSFC 7	0.5	0.88	3.1 ± 0.6	95

The pores in all the materials were sub-micron in size, except for the A-excess LSFC which had pores up to 10μm.

Permeation experiments

The experimental setup for the oxygen permeation measurements is shown in Figure 1.

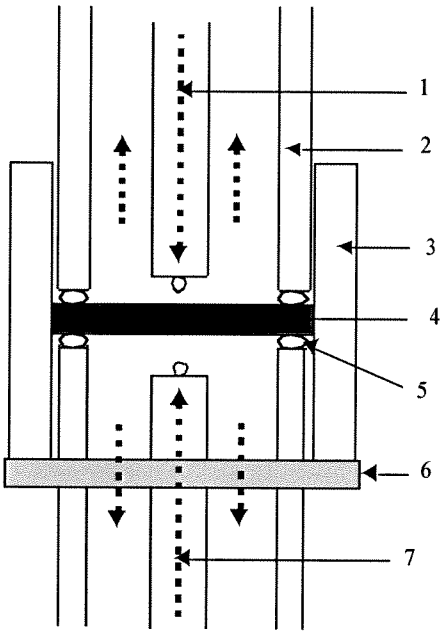

Figure 1: Experimental setup for the oxygen permeation measurements. 1: Alumina tube with inlet gas and thermocouple. 2: Alumina tube. 3. Alumina support. 4. Membrane. 5. Sealing (Pt). 6. Alumina disk. 7. Alumina tube with inlet gas and thermocouple.

The membrane is placed between two vertical alumina tubes with platinum as the sealing material. Above the membrane, an alumina tube with inlet secondary gas and a thermocouple is placed. Under the membrane, there is another alumina tube with inlet primary gas and an additional thermocouple. Outside the membrane there is an alumina support tube to prevent movement in horizontal direction.

The O_2 and N_2 concentrations in the secondary gas were measured by a Varian Micro-GC (Gas Chromatograph) Bench model CP-2003 with Ar as the carrier gas. The data were analyzed by Star Chromatography Workstation Version 5. Three different calibration gases with different O_2 and N_2 content were used. The reported oxygen fluxes were corrected for

leakages by using the difference in N_2 content from secondary gas in to secondary gas out and the fixed ratio between O_2 and N_2 in air.

All membranes were heated to approximately 1150°C. The oxygen flux were measured as a function of pO_2 by using air on the primary side and He or a mixture of He and air on the secondary side. The oxygen partial pressures were determined by analyzing the oxygen content in the outlet gas from the secondary side of the membrane. The temperature dependency of the flux was investigated by varying the temperature in the range from 1150°C to 970°C. Here, He on the secondary side and air on the primary side were used. The gas flows were kept at 200 ml/min for all gases and gas mixtures. The flux values were calculated by using the fractions of oxygen in the total flow and the active membrane areas inside the sealing material.

After both the pO_2 and temperature dependency were investigated, the gases were changed to 50 ml/min flow of O_2 on the primary side and N_2 on the secondary side, respectively. This pO_2 gradient was maintained constant for approximately three weeks. Before the experiments were terminated, the gases were changed to air and He, and the oxygen flux was measured once more. The membranes were cooled in a pO_2 gradient by keeping the primary and secondary gases flowing.

Results

Oxygen flux measurements

The normalized oxygen fluxes of the materials as function of the partial pressure of oxygen on the secondary side are given in Figure 2. The raw data are given in Appendix VI. The temperature is kept constant at 1148 ± 2 °C. At highest partial pressures, the flux increases with increasing pO_2 difference over the membrane due to a bulk controlled diffusion. The flux is almost constant for $pO_2 = 10^{-1.5} - 10^{-2}$ or lower oxygen partial pressures due to a surface exchange process becoming rate controlling. The broken lines indicate this trend. At even lower oxygen partial pressures the fluxes tend to decrease. The reason for this will be discussed later.

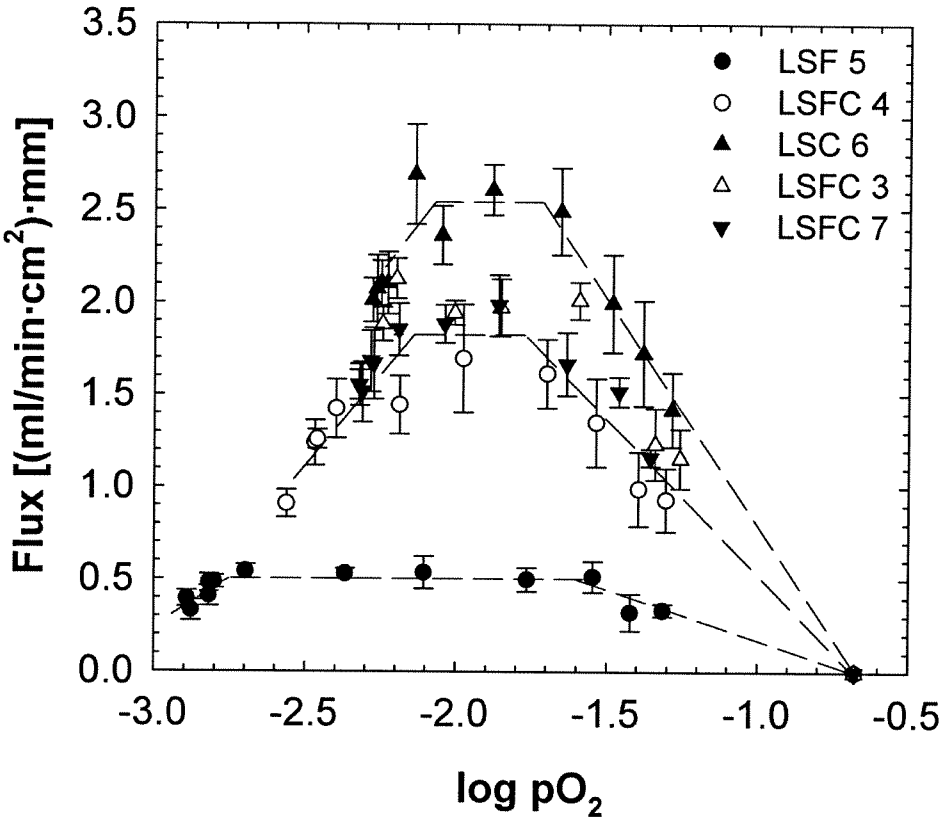

Figure 2: Normalized oxygen flux versus pO_2 on secondary side of the membrane for $La_{0.5}Sr_{0.5}FeO_{3-\delta}$ (LSF), $La_{0.5}Sr_{0.5}Fe_{0.5}Co_{0.5}O_{3-\delta}$ (LSFC) and $La_{0.5}Sr_{0.5}CoO_{3-\delta}$ (LSC) at 1148°C. Dashed lines are trend lines.

The temperature dependency of the oxygen flux by using He on the secondary side and air on the primary side is shown in an Arrhenius plot in Figure 3. The activation energies obtained by the linear fit of the data are given in Table 3.

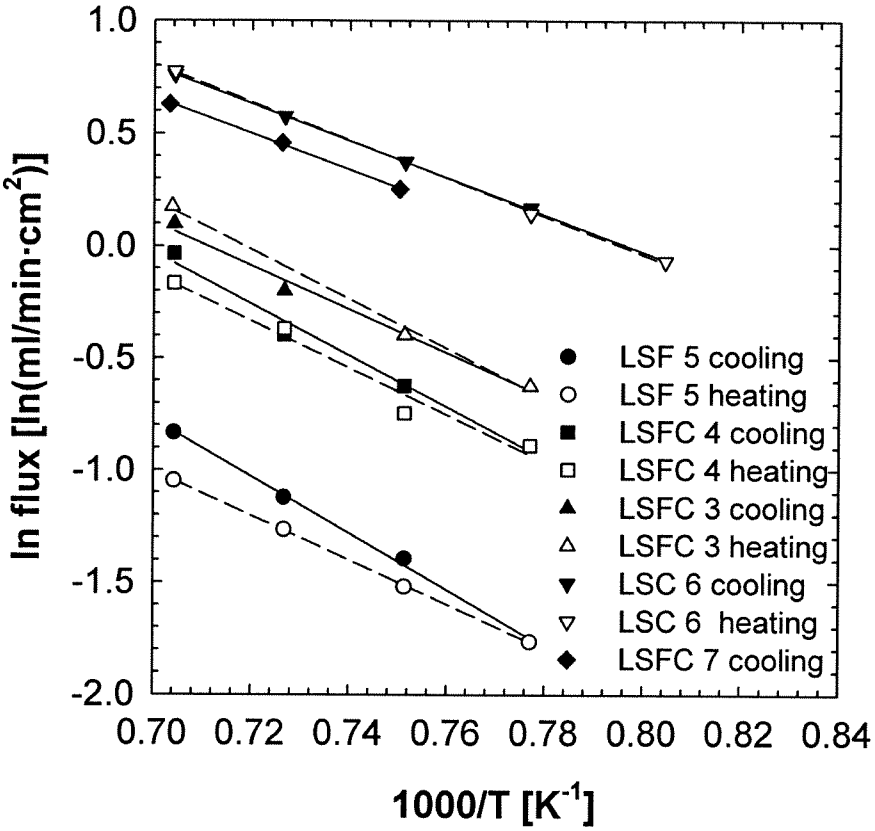

Figure 3: Oxygen flux versus temperature for $La_{0.5}Sr_{0.5}FeO_{3-\delta}$ (LSF), $La_{0.5}Sr_{0.5}Fe_{0.5}Co_{0.5}O_{3-\delta}$ (LSFC) and $La_{0.5}Sr_{0.5}CoO_{3-\delta}$ (LSC). The solid lines are linear regression to the points. Primary side: Air. Secondary side: He.

Table 3: Activation energies for $La_{0.5}Sr_{0.5}Fe_{1-x}Co_xO_{3-\delta}$ from oxygen flux measurements.

Membrane name	Activation energy [kJ/mol] cooling	Activation energy [kJ/mol] heating
LSFC 3	81 ± 6	92 ± 6
LSFC 4	96 ± 8	87 ± 11
LSF 5	105 ± 4	82 ± 1
LSC 6	68 ± 1	70 ± 2
LSFC 7	67 ± 3	-

Figure 4 shows the normalized flux as function of composition for $La_{0.5}Sr_{0.5}Fe_{1-x}Co_xO_{3-\delta}$ materials. The figure shows both the behavior in a bulk controlled pO_2 gradient (5 % O_2 in He as the secondary gas) and in a surface exchange controlled pO_2 gradient (He as the secondary gas). As seen, the flux increases with increasing Co content in both cases.

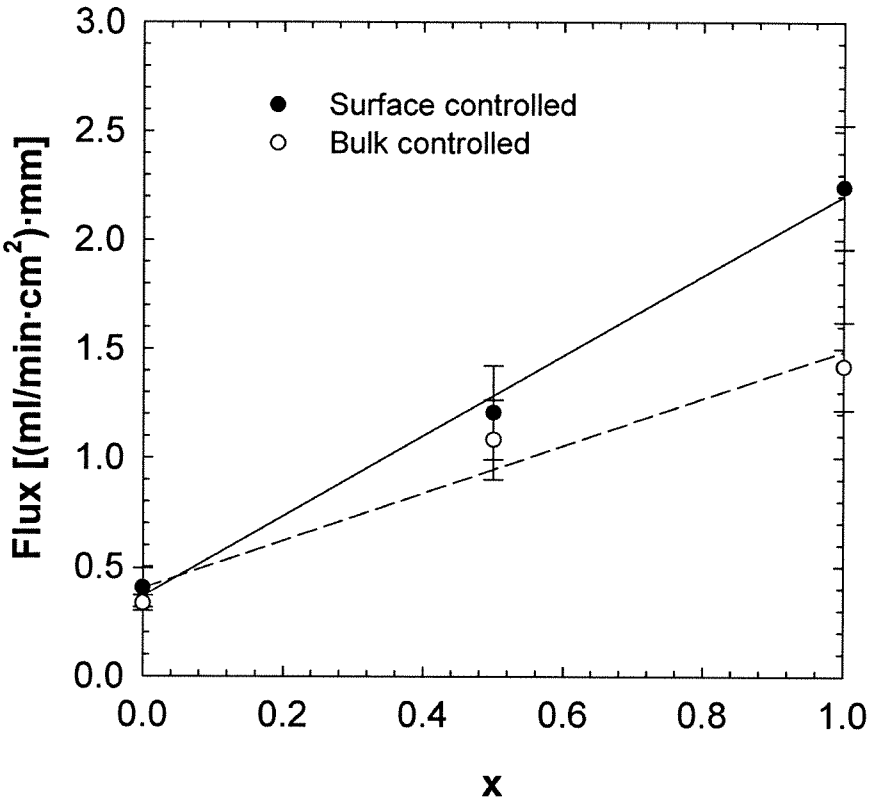

Figure 4: Normalized oxygen flux versus composition for $La_{0.5}Sr_{0.5}Fe_{1-x}Co_xO_{3-\delta}$ materials.

The oxygen flux through the membrane was measured as a function of time for all membranes, and the data are given in Figure 5. The broken lines are guides to the eye. For the LSF 5 membrane, the flux is seen to decrease with time and then tend to be constant. It is assumed that the formation of a $SrFe_{12}O_{19}$ layer slows the oxygen flux through the membrane. Still, this phase is oxygen permeable due to the measured fluxes during the entire time period. Detailed information about formation of secondary phases is given elsewhere.[16] For the LSFC membranes the oxygen flux is almost constant with time. A minimum is seen for the time aspect around the temperature

changes, but reaches earlier values afterwards. For the A-excess membrane, the flux decreases until a constant value after 10 days. For the LSC membrane, the flux is constant the first time in a pO_2 gradient, followed by a small increase.

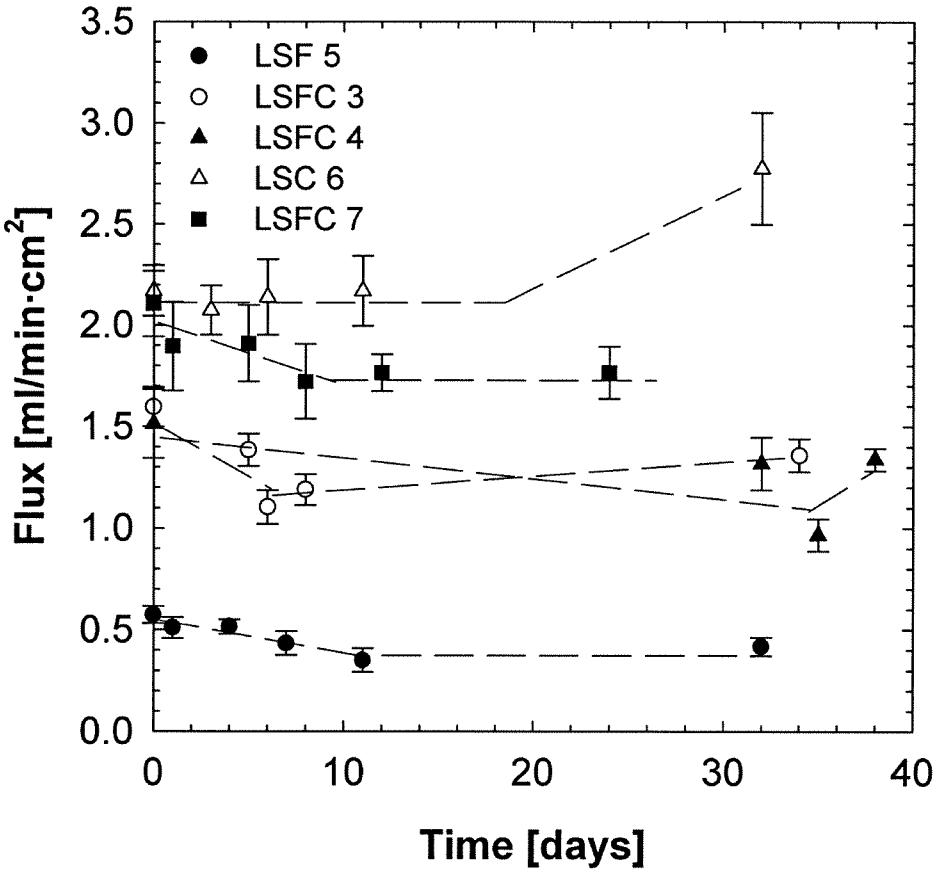

Figure 5: Oxygen flux as a function of time for a $La_{0.5}Sr_{0.5}Fe_{1-x}Co_xO_{3-\delta}$ membrane. The broken lines are guides to the eye.

Discussion

The flux is bulk controlled for the smallest gradients and the oxygen flux increase with increasing pO_2-gradient, consistent with the Wagner equation (1). At a certain point, the flux reaches a plateau and does not change by further increase in the gradient. That is, the flux becomes controlled by surface exchange instead of controlled by bulk diffusion, and the surface kinetics will determine the oxygen flux through the membrane. At even higher oxygen partial pressure gradients, the oxygen flux decreases with increasing gradients for all compositions. The behavior of decreasing oxygen flux with increasing driving force is intuitively unexpected, and it is reasoned that the surface exchange kinetics is responsible. The decreasing oxygen flux with increasing driving force occurs at low oxygen partial pressures at the secondary side of the membrane, indicating that the rate of oxygen exchange decreases with decreasing oxygen partial pressure below some critical pO_2. This behavior is supported by Watterud et al.[17] who have assessed surface exchange coefficients and bulk diffusion coefficients in the system $La_{1-x}Sr_xCoO_3$ ($x = 0$, 0.2 and 0.5) by means of conductivity relaxation experiments. Results for $x = 0.5$ at 1000°C are reported in Figure 6, where D_{chem} is the chemical oxygen diffusion coefficient whereas k_{chem} is the surface exchange coefficient for a reduction process. Figure 6 predict an overall trend consistent with an increasing flux with driving force at high and medium pO_2's, following the curve for D_{chem}. At lower pO_2 the flux becomes controlled by surface exchange at the reduced side and should decline with decreasing pO_2 in accordance with the observed pO_2 dependency for k_{chem}. It is assumed that the same trends as shown for LSC are valid for the other compositions. Lane et al.[14] have seen the same small decreasing flux tendency for the largest pO_2 gradients for $La_{0.6}Sr_{0.4}Co_{0.2}Fe_{0.8}O_{3-\delta}$ at 800°C. Their results are supported by a model indicating the same trend calculated on the basis of pO_2 dependence of D_T (tracer diffusion coefficient) and k, and the oxygen non-stoichiometry. At 1000°C, they do not see the same tendency due to smaller pO_2 gradient.

There is a linear relationship between the inverse temperature and the logarithmic oxygen flux, as seen in Figure 3. The linear behavior suggests that the same rate controlling process dominates in the whole temperature region reported. Since all fluxes reported in Figure 3 refer to conditions where the partial pressure at the secondary side is low and hence controlled by surface exchange, the corresponding activation energy is likely to be associated with some rate controlling surface reaction at the reduced side of the membrane. It is seen from Table 3 that there is a tendency of decreasing

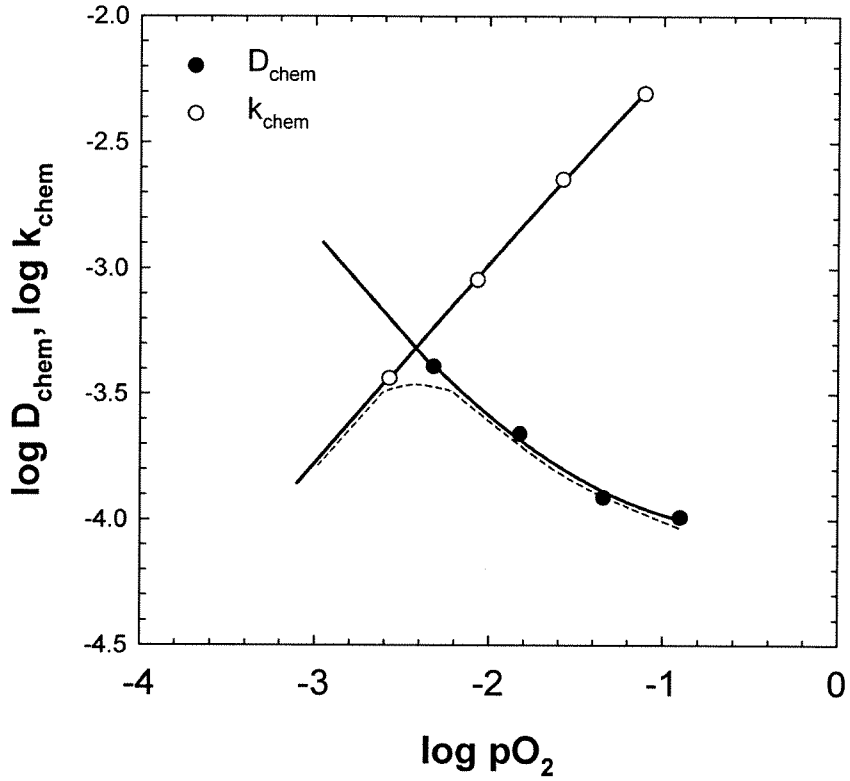

Figure 6: log D_{chem} and log k_{chem} for $La_{0.5}Sr_{0.5}CoO_{3-\delta}$ at 1000°C, from[17]. A tentative flux trend is indicated by the dotted line.

activations energy with increasing Co content, consistent with findings reported elsewhere.[1, 17] Apparently, a somewhat more pronounced temperature dependency (high activation energy) is observed for cooling compared with heating for all compositions. The reason for this behavior is not clear, however, for LSF the difference between cooling and heating may be due to the formation of $SrFe_{12}O_{19}$ on the primary side.[16] With reference to Figure 3 and Table 3 the activation energies seem to be slightly higher for B-excess materials (LSFC 3 and LSFC 4) compared with A-excess materials (LSFC 7). However, the grain sizes are different and this may affect the activation energy. The oxygen permeability is seen to be higher for $La_{0.3}Sr_{0.7}CoO_{3-\delta}$ membranes with large grains compared to smaller grains.[9] The fluxes have larger temperature dependency with large grains in the membranes compared to small grains, giving rise to higher activation energy.

The absolute oxygen fluxes increases with increasing Co content, both in the surface controlled and the bulk controlled pO_2 regime. This is in accordance with observations reported for similar compounds, e.g. in the $SrFeO_{3-x} - SrCoO_{3-y}$ system.[12]

The obtained fluxes are in the same order of magnitude as corresponding compositions found in the literature. For $La_{0.6}Sr_{0.4}Fe_{0.2}Co_{0.8}O_{3-\delta}$, fluxes of 0.05 ml/min·cm^2 is found at 800°C or 0.43 ml/min·cm^2 at 1000°C for a membrane with thickness 0.96 mm.[14] For $La_{0.7}Sr_{0.3}FeO_{3-\delta}$, a flux of 0.23 ml/min·cm^2 at 1000°C is reported for a 1.0 mm membrane,[18] while 0.42 ml/min·cm^2 is reported at 1000°C for a 1.1 mm $La_{0.3}Sr_{0.7}CoO_{3-\delta}$ membrane.[7] The values reported here is somewhat higher due to higher performance temperature. Only the reported LSF fluxes are possible lower than expected, taken into consideration the earlier reported increasing fluxes with increasing Sr-doping in $La_{1-x}Sr_xFeO_{3-\delta}$.[18] The formation of the covering $SrFe_{12}O_{19}$ layer may have slowed the oxygen permeation.

Conclusion

Oxygen flux through $La_{0.5}Sr_{0.5}Fe_{1-x}Co_xO_{3-\delta}$ (x = 0, 0.5, 1) membranes are found as a function of oxygen gradient and temperature. The fluxes increases with decreasing pO_2 on the secondary side until the surface exchange becomes rate limiting where the fluxes reaches a constant value. By further increase of the pO_2 gradient, the fluxes decreases according to the pO_2 dependent surface exchange coefficient. The fluxes at 1148°C increase with increasing content of cobalt, both in the bulk diffusion and in the surface exchange controlled regime. The obtained activation energies seem to decrease with increasing cobalt content in the membranes. Different activation energies obtained for cooling and heating can be explained by secondary phases on the primary side which may slow the transport processes.

Acknowledgement

The Research Council of Norway, Statoil and Hydro are acknowledged for financial support.

References

1. H. J. M. Bouwmeester and A. J. Burgraaf, in: P.J. Gellings and H.J.M. Bouwmeester (Eds), The CRC Handbook of Solid State Electrochemistry, CRC Press, Inc., New York (1997).
2. A. Atkinson and A. Selcuk, "Mechanical behaviour of ceramic oxygen ion-conducting membranes", Solid State Ionics, 134 (2000) 59-66.
3. P. V. Hendriksen, P. H. Larsen, M. Mogensen, F. W. Poulsen and K. Wiik, "Prospects and problems of dense oxygen permeable membranes", Catalysis Today, 56 (2000) 283-295.
4. J. E. ten Elshof, H. J. M. Bouwmeester and H. Verweij, "Oxygen transport through $La_{1-x}Sr_xFeO_{3-\delta}$ membranes. I. Permeation in air/He gradients", Solid State Ionics, 81 (1995) 97-109.
5. S. Aasland, I. L. Tangen, K. Wiik and R. Ødegård, "Oxygen permeation of $SrFe_{0.67}Co_{0.33}O_{3-d}$", Solid State Ionics, 135 (2000) 713-717.
6. C.-Y. Tsai, A. G. Dixon, Y. H. Ma, W. R. Moser and M. R. Pascucci, "Dense Perovskite, $La_{1-x}A'_xFe_{1-y}Co_yO_{3-\delta}$ (A' = Ba, Sr, Ca), Membrane Synthesis, Applications, and Characterization", J. Am. Ceram. Soc., 81 [6] (1998) 1437-1444.
7. C. H. Chen, H. M. J. Bouwmeester, R. H. E. van Doorn, H. Kruidhof and A. J. Burggraaf, "Oxygen permeation of $La_{0.3}Sr_{0.7}CoO_{3-\delta}$", Solid State Ionics, 98 (1997) 7-13.
8. K. Huang and J. B. Goodenough, "Oxygen Permeation Through Cobalt-Containing Perovskites. Surface Oxygen Exchange vs. Lattice Oxygen Diffusion", J. Electrochem. Soc., 148 [5] (2001) E203-E214.
9. V. V. Kharton and F. M. B. Marques, "Mixed ionic-electronic conductors: effects of ceramic microstructure on transport properties", Curr. Op. in Solid State and Mater. Sci., 6 (2002) 261-269.
10. V. V. Kharton, A. A. Yaremchenko, A. V. Kovalevsky, A. P. Viskup, E. N. Naumovich and P. F. Kerko, "Perovskite-type oxides for high-temperature oxygen separation membranes", 163 (1999) 307-317.
11. Z. Shao, G. Xiong, H. Dong, W. Yang and L. Lin, "Synthesis, oxygen permeation study and membrane performance of a $Ba_{0.5}Sr_{0.5}Co_{0.8}Fe_{0.2}O_{3-\delta}$ oxygen-permeable dense ceramic reactor for partial oxidation of methane to syngas", Separ. Purif. Technol., 25 (2001) 97-116.
12. K. Wiik, S. Aasland, H. L. Hansen, I. L. Tangen and R. Ødegård, "Oxygen permeation in the system $SrFeO_{3-x}$ – $SrCoO_{3-y}$", Solid State Ionics, 152-153 (2002) 675-680.
13. S. Diethelm, J. Van herle, P. H. Middleton and D. Favrat, "Oxygen permeation and stability of $La_{0.4}Ca_{0.6}Fe_{1-x}Co_xO_{3-\delta}$ (x = 0, 0.25, 0.5) membranes", J. Power Sources, 118 (2003) 270-275.

14. J. A. Lane, S. J. Benson, D. Waller and J. A. Kilner, "Oxygen transport in $La_{0.6}Sr_{0.4}Co_{0.2}Fe_{0.8}O_{3-\delta}$", Solid State Ionics, 121 (1999) 201-208.
15. H. L. Lein, K. Wiik and T. Grande, "Thermal and chemical expansion of $La_{0.5}Sr_{0.5}Fe_{1-x}Co_xO_{3-\delta}$ ($0 \leq x \leq 1$) materials", paper I.
16. H. L. Lein, K. Wiik and T. Grande, "Cation demixing of $La_{0.5}Sr_{0.5}Fe_{1-x}Co_xO_{3-\delta}$ ($0 \leq x \leq 1$) materials", paper V.
17. G. Watterud, K. Wiik and S. Julsrud, "Oxygen transport in $La_{1-x}Sr_xCoO_{3-\delta}$ (x = 0, 0.2 and 0.5) assessed with electrical conductivity relaxation. Part I: Bulk diffusion and k_{chem}", to be published.
18. J. E. ten Elshof, H. J. M. Bouwmeester and H. Verweij, "Oxygen transport through $La_{1-x}Sr_xFeO_{3-\delta}$ membranes. II. Permeation in air/CO, CO_2 gradients", Solid State Ionics, 89 (1996) 81-92.

PAPER V

Cation demixing and decomposition of $La_{0.5}Sr_{0.5}Fe_{1-x}Co_xO_{3-\delta}$ ($0 \leq x \leq 1$) materials

Hilde Lea Lein, Kjell Wiik and Tor Grande*

Department of Materials Technology,
Norwegian University of Science and Technology,
7491 Trondheim, Norway.

Abstract

The stability of $La_{0.5}Sr_{0.5}Fe_{1-x}Co_xO_{3-\delta}$ (x = 0, 0.5, 1) membranes have been investigated at 1150°C in an oxygen permeation cell with flowing air/O_2 at the primary side and He/N_2 at the secondary side. After about five weeks of operation, kinetic demixing and decomposition of the membranes were demonstrated by electron microscopy and electron probe microanalysis. Secondary phases at the primary side were observed in all the membranes. For all the cobalt containing materials, grains of cobalt oxide were observed at and near the surface. A dense 17 μm layer of the secondary phase $SrFe_{12}O_{19}$ covered completely the surface of the $La_{0.5}Sr_{0.5}FeO_{3-\delta}$ membrane. The secondary phases were also influenced by the overall (Sr+La)/(Fe+Co) stoichiometry in the materials. Electron microprobe analysis of the cross section of the membranes demonstrated evidence for kinetic demixing of all the membranes particularly near the two surfaces. The formation of Fe/Co rich secondary phases at the primary side was accompanied by a Sr/La excess in the bulk of the compositions where x = 0 and 1. Finally, the membranes were also observed to swell during operation due to pore expansion, and grain growth was observed in Co-containing membranes. The demonstration of kinetic demixing and decomposition of the present oxygen permeable perovskite materials show that the long term stability is one of the main obstacles for the oxygen permeation membranes, particularly for reactor designs based on thin films on porous substrate.

* Correspondence to Tor.Grande@material.ntnu.no

Introduction

Mixed conductors with perovskite structure are candidates for use in high temperature electrochemical devices and oxygen permeable membranes.[1-3] These devices are operated in non-equilibrium conditions under exposure to gradients in temperature and possibly pressure in addition to electrical/chemical gradients.[4-5] Such gradients act as driving forces on atoms in a crystalline material, and fluxes of atoms result.[6] In oxygen permeable membranes, the combination of oxygen ionic conductivity and electronic conductivity leads to a flux of oxygen due to any gradient in the electrochemical potential of oxygen. Diffusion of cations on the other hand, is usually neglected, but this can not be done if there is a difference in mobility of the cations.[7-8]

The cation fluxes may lead to degradation phenomena of the materials.[6, 8-11] A material which was originally chemically homogeneous may become chemically inhomogeneous. This is called kinetic demixing. There are also possibilities for kinetic decomposition by formation of new phases in the initially single phase material. The original morphology of the material may also become unstable and a new morphology may be established. This is called morphological instability. These phenomena are purely kinetic in nature. If the gradient is removed, the directed fluxes will disappear and the material will relax, secondary phases will disappear and the material will become homogeneous.[6, 9]

The fluxes of cations cause migration of the membrane as a whole towards the primary (high pO_2) side. Crystal planes are subtracted from the secondary (low pO_2) side at the same time as the material loses oxygen. New crystal planes are added at the primary side due to reaction with oxygen atoms from the gas.[6-7, 12-14] The physical reason for the demixing process is the difference in the mobilities of the cations. In a pO_2 gradient, the cations move towards the high pO_2 and the most mobile cation will be enriched on this side. The degree of demixing is dependent on the difference in mobility between the cations and the gradient of the driving force. A large difference in mobility and a thinner material increase this degree of demixing.[5-6, 14-17]

The physical and the chemical properties of oxygen permeable materials are controlled through careful optimization of the composition. The occurrence of kinetic demixing results in a degradation since local composition changes, secondary phases and perhaps morphological changes may destroy the functionality of the materials and give rise to a decrease in the lifetime.[4, 10-11, 18-22] Therefore, the understanding of the demixing process is

of great fundamental and practical importance due to prediction of the durability and reliability of these materials.

For a homovalent ideal solution of AO and BO, the demixing equation can be written as

$$\nabla\mu_B = (D_A/D_B)\cdot\nabla\mu_A \tag{1}$$

where $\nabla\mu$ is the gradient of the potential and D is the diffusion coefficients.[9] For an ideal solution of AO and BO,

$$\nabla\mu_A + \tfrac{1}{2}\nabla\mu_{O_2} = \nabla\mu_{AO} = RT\nabla\ln x_A \tag{2}$$

$$\nabla\mu_B + \tfrac{1}{2}\nabla\mu_{O_2} = \nabla\mu_{BO} = RT\nabla\ln x_B \tag{3}$$

where x is the molar fraction. Then the equation for the steady state can be written

$$\left(\frac{1}{1-x_A} + \frac{D_A}{D_B}\cdot\frac{1}{x_A}\right)\cdot RT\nabla\ln x_A = \left(\frac{D_A}{D_B} - 1\right)\cdot\frac{1}{2}\nabla\mu_{O_2} \tag{4}$$

Equation (4) shows that the ratio D_A/D_B determines whether the kinetic demixing occurs and at which side the different cations become enriched.

Since cation diffusion in oxygen ion conductors is very slow, the steady-state can be reached in reasonable times only for very thin membranes. For example, if the slowest diffusion coefficient is $D = 10^{-14}$ cm^2 s^{-1}, the steady state is reached after 15000 years for a 1 mm thick membrane, while it is only 1.5 years for a 1 μm thick membrane.[20] However, already during the transient time to the steady state, demixing at the oxide surfaces might become important. Recently, thin membrane films of about 10 μm is developed as a new design, placed upon a porous support. For such thin materials, the cation demixing and degradation are even more important phenomena for the long term stability.

Cation demixing in binary and tertiary oxides is widely reported, but only limited studies on kinetic demixing and decomposition in perovskite materials have been reported. Kim et al.[23] have investigated $La_{0.36}Sr_{0.64}Co_{0.65}Cu_{0.35}O_{3-x}$ membrane after permeation experiments. The original perovskite phase was enriched on La and Co at the reducing side and grains of a non-perovskite Sr-Cu oxide had been formed. La was enriched along cracks or grain boundaries. Diethelm et al.[24] found three

layers of phases in $La_{0.6}Ca_{0.4}Fe_{0.75}Co_{0.25}O_{3-\delta}$ at the secondary side (CH_4). La was enriched and Fe and Co was found as metallic clusters. On the primary side, Ca and Co oxide was formed. A corresponding study of $La_{0.3}Sr_{0.7}CoO_{3-\delta}$ membranes by Doorn et al.[8] showed formation of a thin porous layer of mainly $SrCO_3$ at the secondary side. A Sr enriched phase was discovered between the surface layer and bulk. There were no changes at the primary side. Finally, $La_{0.4}Ca_{0.6}Fe_{1-x}Co_xO_{3-\delta}$ (x = 0, 0.25 and 0.5) membranes[25] decomposed at secondary side, and an enrichment of transition metals was found. However, no composition change across the membrane was detected.

In this contribution we present an investigation of the microstructure, phase composition and chemical composition profiles of $La_{0.5}Sr_{0.5}Fe_{1-x}Co_xO_{3-\delta}$ (x = 0, 0.5, 1) membranes exposed to a chemical gradient in oxygen partial pressure at 1150°C in more than a month. In a separate paper, the preparation of the membranes and the procedure for the permeation experiments along with the oxygen flux performance have been reported.[26] This report is to the authors' knowledge the first systematic study of kinetic demixing and decomposition of ternary and quaternary oxide perovskite materials with high oxygen permeability.

Experimental

Preparation of membranes

The powders used to prepare the membranes were synthesized by spraydrying of glycine-nitrate solutions as described elsewhere.[27] Membrane preparation, flux characterization and experimental setup for the permeation experiments are described in a previous contribution.[26]

The relative densities of the materials and the amount of secondary phase determined by thermogravimetrical analysis[28] are given in Table 1. The theoretical densities used are 5.99 gcm^{-3} (LSF), 6.29 gcm^{-3} (LSFC) and 6.42 gcm^{-3} (LSC) calculated from x-ray diffraction and oxygen non-stoichiometry.[27]

Permeation experiments

The membranes were first investigated with respect to the oxygen flux, see [26]. The membranes were then exposed to a chemical gradient at 1150°C for an extended time period as seen in Table 2. During this period the gas flows were 50 ml/min of O_2 on the primary side and 50 ml/min of N_2 on the secondary side. Before termination of the experiments, the atmospheres on the two sides of the membranes were finally changed to air and He and the oxygen flux was measured before the membranes were cooled to room temperature. The membranes were cooled in a pO_2 gradient by keeping the primary and secondary gases flowing.

Table 1: Amount secondary phase and relative density of the $La_{0.5}Sr_{0.5}Fe_{1-x}Co_xO_{3-\delta}$ membranes.

Membrane name	Composition x	B-excess Co_3O_4 [wt%]	A-excess SrO [wt%]	Relative density [%]
LSFC1	0.5	0.10	-	97
LSFC2	0.5	0.10	-	97
LSFC3	0.5	0.10	-	97
LSFC4	0.5	0.10	-	97
LSF5	0	-	-	95
LSC6	1	0.98	-	99
LSFC7	0.5	-	0.66	95

Table 2: Experimental conditions for the investigation of the long time stability of membranes.

Membrane name	Temperature [°C]	Time in pO_2 gradient [days]
LSFC1	1100	133
LSFC2	1144	41
LSFC3	1147	37
LSFC4	1146	40
LSF5	1147	34
LSC6	1147	36
LSFC7	1149	30

The microstructure of the membranes was investigated by a Hitachi S3500 N scanning electron microscope (SEM). The average grain sizes were estimated by a linear intercept method from SEM-images of polished

(1 μm diamond finish) and thermally etched (0.2 hours, 1130°C) surfaces. Ten images were taken from different parts of the polished samples. The element concentration profiles across the membrane were determined by a JXA-8900 Superprobe microprobe. The data were collected by a step size of 10 μm, an electron beam defocus of 10 μm and a count time of 60 seconds. As the standard for the quantitative analysis, a sintered and polished material of $La_{0.5}Sr_{0.5}Fe_{0.5}Co_{0.5}O_{2.915}$ was used. The oxygen content in these materials was determined by reduction in hydrogen.[27]

Results

Microstructure of membranes

The surface microstructures of the membranes at the primary (air) and secondary (inert) side after long time in an oxygen partial pressure gradient are shown for 6 different membranes in Figures 1-6. Micrographs of the cross section close to the primary side of the membranes are also shown in the figures.

The surfaces at the secondary inert side of all the membranes were phase pure with only the "initial" perovskite phase, see Figure 1-6. The grain size was easily recognized by the topographic effect of the dihedral angle of the grain boundaries. The average grain size of the secondary side of the membranes is summarized in Table 3. No major difference in grain size at the primary and secondary side could be observed within the uncertainty of the measurements.

No grain growth in the LSF material could be observed, see Figure 4 and Table 3. Similar observation was evident for the A-excess LSFC membrane (LSFC7), see Figure 6. In the LSFC membranes (LSFC1-4), a moderate grain growth was recorded, see Figure 1-3. On the other hand in the LSC material (LSC6), there had been a significant grain growth during the permeation experiments, see Figure 5.

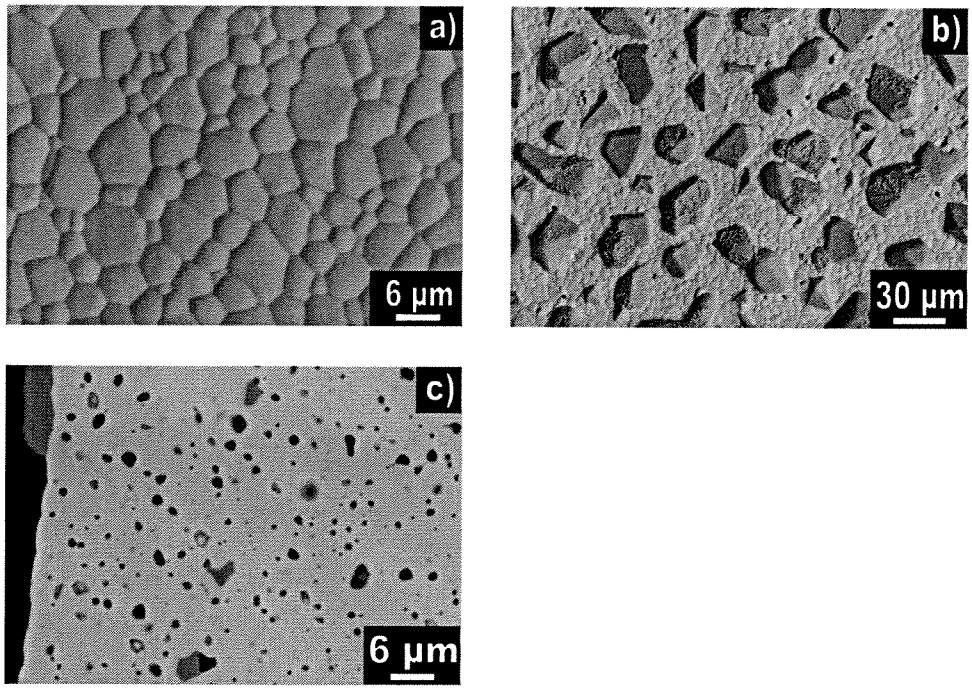

Figure 1: Surfaces of secondary side (a), primary side (b) and cross section at primary side (c) of the LSFC2 membrane ($La_{0.5}Sr_{0.5}Fe_{0.5}Co_{0.5}O_{3-\delta}$) after 41 days in a pO_2 gradient.

Table 3: The average grain size of $La_{0.5}Sr_{0.5}Fe_{1-x}Co_xO_{3-\delta}$ membranes before and after extended period of time in a pO_2 gradient.

Membrane name	Grain size before [µm]	Grain size after [µm]
LSFC1	0.8 ± 0.1	4.8 ± 0.6
LSFC2	0.8 ± 0.1	4.4 ± 0.6
LSFC3	0.8 ± 0.1	3.9 ± 0.6
LSFC4	0.8 ± 0.1	4.5 ± 0.8
LSF5	1.2 ± 0.2	1.1 ± 0.2
LSC6	1.7 ± 0.4	12.6 ± 2.5
LSFC7	3.1 ± 0.6	3.2 ± 0.8

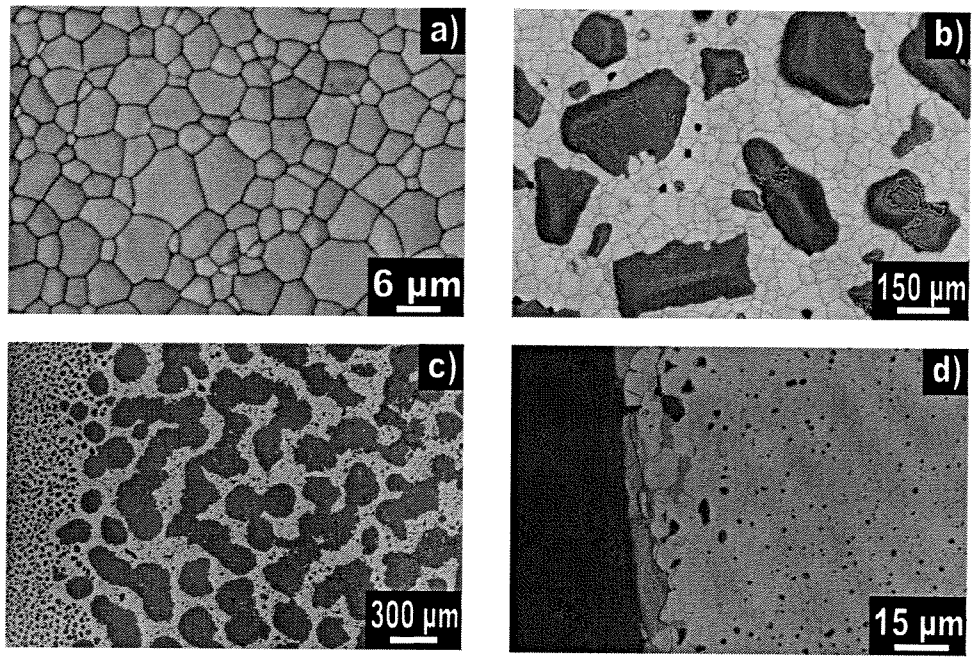

Figure 2: Surfaces of secondary side (a), primary side (b and c) and cross section at primary side (d) of the LSFC3 membrane ($La_{0.5}Sr_{0.5}Fe_{0.5}Co_{0.5}O_{3-\delta}$) after 37 days in a pO_2 gradient.

All of the membranes were observed to expand during the oxygen permeation experiments. The linear expansion of the membranes, calculated by the measured thickness of the membranes before and after the experiment, is summarized in Table 4. The Co-containing membranes expanded significantly during the time in an oxygen partial pressure gradient, mainly due to pore expansion. The initial pore size was sub-micron, except for the A-excess LSFC7 which had pores up to 10 µm. The electron microscopy investigations demonstrated a same small pore growth in the LSF material, while a significant pore growth was observed in LSFC and LSC membranes.

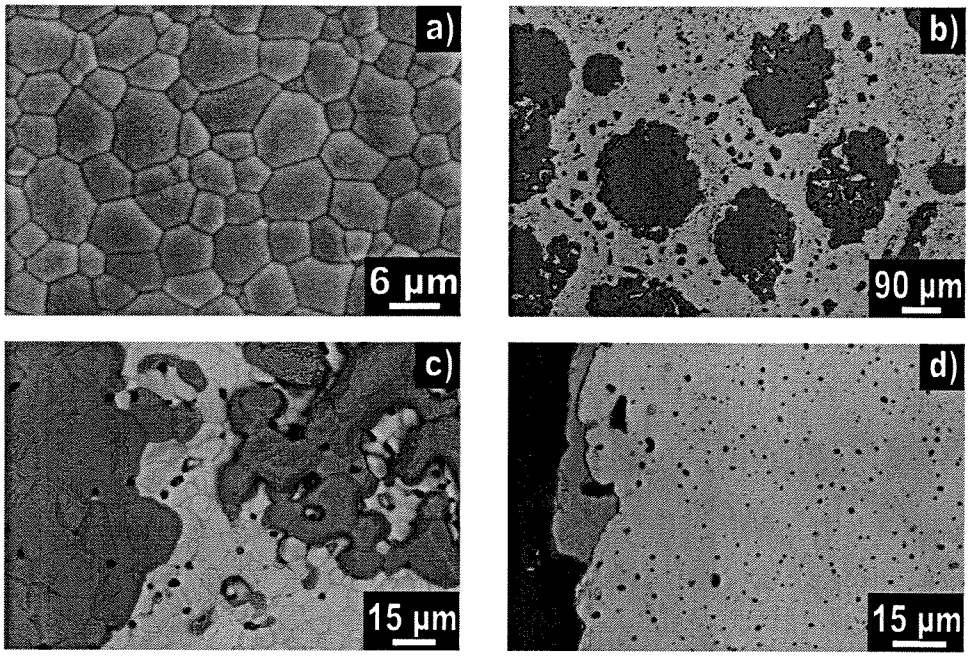

Figure 3: Surfaces of secondary side (a), primary side (b and c) and cross section at primary side (d) of the LSFC4 membrane ($La_{0.5}Sr_{0.5}Fe_{0.5}Co_{0.5}O_{3-\delta}$) after 40 days in a pO_2 gradient.

Table 4: Thickness of the $La_{0.5}Sr_{0.5}Fe_{1-x}Co_xO_{3-\delta}$ membranes before and after the permeation experiments and the linear expansion calculated by the change in thickness.

Membrane name	Thickness before [mm]	Thickness after [mm]	Expansion [%]
LSFC 1	2.62	2.84	8.4
LSFC 2	2.00	2.14	7.0
LSFC 3	0.81	0.91	12
LSFC 4	0.94	1.02	8.5
LSF 5	0.94	0.953	1.4
LSC 6	0.97	1.07	10.3
LSFC 7	0.88	0.96	9.1

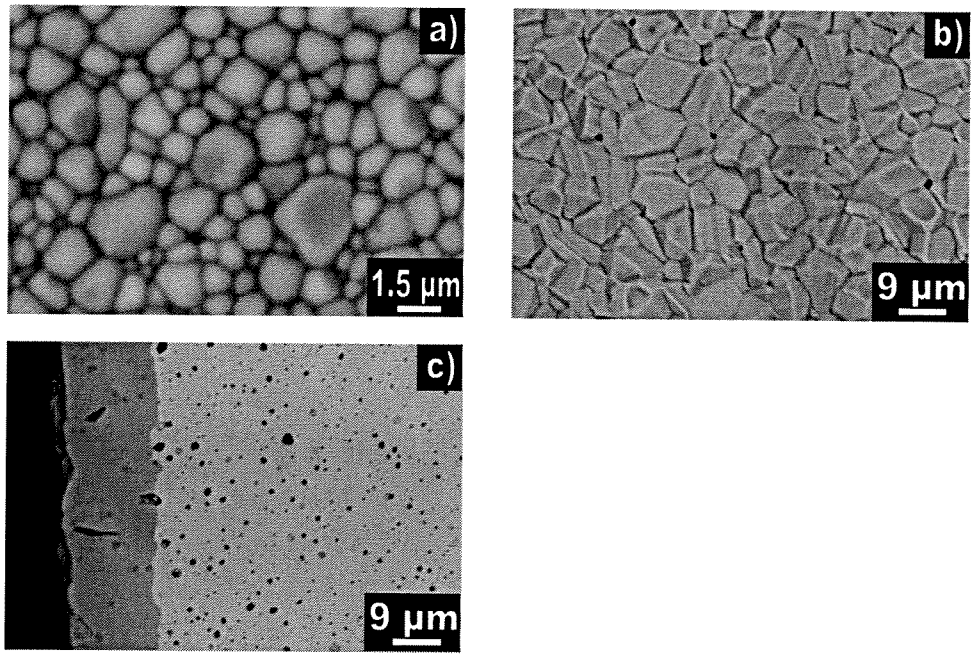

Figure 4: Surfaces of secondary side (a), primary side (b) and cross section at primary side (c) of the LSF5 membrane ($La_{0.5}Sr_{0.5}FeO_{3-\delta}$) after 34 days in a pO_2 gradient.

In the first experiment, using the LSFC1 membrane, a sealing material of 46.5% Ag, 46.5% Pd and 7% Cu was used. Figure 7 shows the cross section of this membrane at the secondary side and the primary side close to the sealing material. At the primary side a significant pore expansion has taken place, while a much less pore growth is evident on the secondary side. At the primary side Cu in the sealing materials had oxidized to CuO, and diffusion of CuO into the membrane was demonstrated by EDS. The creep resistance of the materials is low[28] and a presence of CuO in the material seems to increase the creep rates, enhance the expansion of the pores and enlarge deformation of the membrane around the sealing material. Significant deformation of the membranes is seen for all the membranes. To avoid the presence of CuO, Pt was used for sealing for the other membranes.

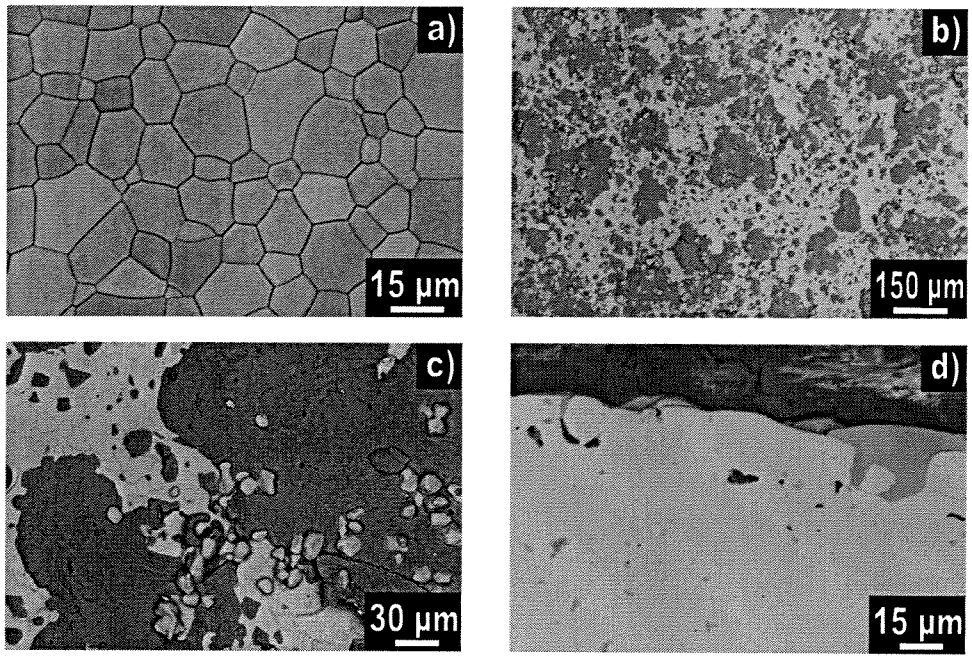

Figure 5: Surfaces of secondary side (a), primary side (b and c) and cross section at primary side (d) of the LSC6 membrane ($La_{0.5}Sr_{0.5}CoO_{3-\delta}$) after 36 days in a pO_2 gradient.

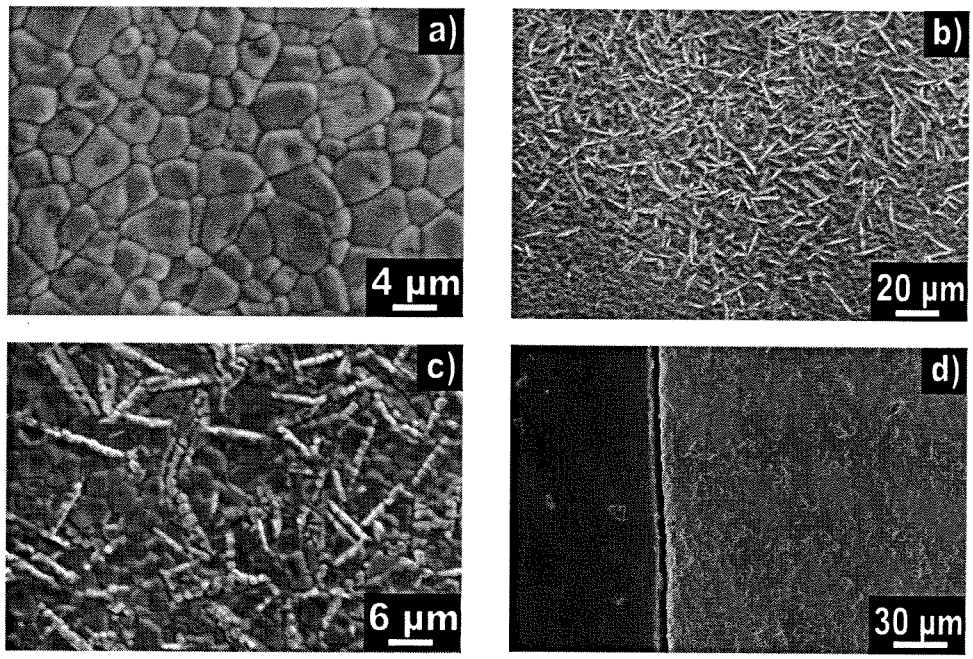

Figure 6: Surfaces of secondary side (a), primary side (b and c) and cross section at primary side (d) of the LSFC7 membrane ($La_{0.5}Sr_{0.5}Fe_{0.5}Co_{0.5}O_{3-\delta}$) after 30 days in a pO_2 gradient.

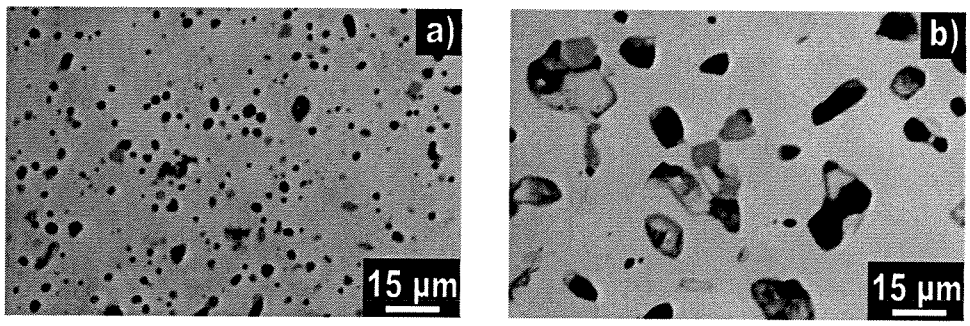

Figure 7: Cross section close to the sealing material at the secondary side (a) and the primary side (b) of the LSFC1 membrane ($La_{0.5}Sr_{0.5}Fe_{0.5}Co_{0.5}O_{3-\delta}$) after ~ 5 weeks in a pO_2 gradient.

Kinetic decomposition

The primary surfaces of all the membranes were partly or completely covered by a secondary phase, significantly different from the initial perovskite phase. In case of the LSFC and LSC materials, isolated grains or clusters of grains of cobalt oxide could be detected. The grain size of cobalt oxide was observed to depend on the oxygen flux. Small miss-alignment of the Pt sealing rings resulted in lower oxygen flux at the edge. In this region the cobalt oxide crystals were significantly smaller than in the middle of the membrane as shown in Figure 2c). Areas where the flux had been higher, larger clusters or grains where created, see Figure 2b). In case of the LSFC2 membrane, the entire primary surface was covered with smaller grains since the flux was lower due to a thicker membrane.

Cobalt oxide grains were also formed inside the membrane close to the primary side, seen in the cross section image Figure 2d). It is important to note that the LSFC and LSC materials were shown to be slightly Co-excess and cobalt oxide was also detected initially in these membranes.

In the case of LSF5, the primary side was completely covered by a ~ 17 μm thick layer of a new phase, see Figure 4c). EDS measurements of the layer evidenced that the composition of the new phase was $SrFe_{12}O_{19}$. $SrFe_{12}O_{19}$ has been shown to coexist with LSF at 1150°C and air by Fossdal et al.[29]

The accumulation of Co or Fe rich phases at the primary side clearly demonstrate that mobility of the cations at the A and B site in the perovskite is different. Based on these observations it seems that the B-cations Fe and Co are significantly more mobile than the A-cations Sr and La.

In the last permeation experiments, the overall composition of the membranes were adjusted by adding some Sr nitrate to the LSFC powder in order ensure that the material was Sr-excess. Unfortunately, the resulting membranes became less homogeneous with large pores, but the LSFC7 membrane was gas tight. At the primary side in this membrane, a completely different phase had formed during the permeation experiment, see Figure 6a) and 6b). Needles and/or plates of an A_2BO_4 composition as could be demonstrated by EDS analysis. This analysis showed an enrichment of Sr at A-site and Fe at B-site pointing to an overall composition close to Sr_2FeO_4. However, Sr_2FeO_4 is not stable at 1150°C,[29] and some content of La is expected. The LSFC7 experiment demonstrates that the cation diffusion in the materials is influenced by the overall stoichiometry of the material. In the original LSFC materials and in the LSC material, which both had a slightly Co-excess (see Table 1), Co was

observed to be the fastest moving cation. Since the presence of cobalt in the bulk will reduce the vacancy concentration on the B-site, it is most reasonable that grain boundary diffusion of Co is causing the formation of cobalt oxide at the primary surface. Correspondingly, by changing the overall composition to Sr-excess, Sr-diffusion seems to be favored. Here again grain boundary diffusion of Sr seems more likely than bulk diffusion. If our preliminary conclusion is correct, the stability of the membranes is very dependent on the overall cation stoichiometry of the membrane material.

In the LSF material, the grain boundary diffusion is proposed to be of less importance. $SrFeO_{3-\delta}$ has been shown to tolerate considerable Sr/Fe non-stoichiometry, which means that the compound can be described as $Sr_{1\pm\delta}FeO_{3-\delta}$.[29] We therefore anticipate that also LSF tolerates some cation non-stoichiometry, which will prevent the formation of secondary phases and accumulation of these at the grain boundaries. In LSF we therefore propose that cation non-stoichiometry will rather result in a difference in the cation vacancy concentration on the A and B site and thereby change the cation mobilities. The formation of $SrFe_{12}O_{19}$ at the air side demonstrates that Fe is the most mobile cation in LSF. Dominating Fe diffusion compared to La has also been shown in diffusion couples of Fe_2O_3 and La_2O_3.[30] As shown in the next paragraph the LSF membrane became Fe-deficient and give additional support the above suggestions.

Kinetic demixing

The concentrations of the cations across the membranes after the permeation experiments were measured by electron microprobe analysis. The resulting cation fraction as a function of position from the secondary side ($\xi/L = 0$, the surface with low pO_2) to the primary side ($\xi/L = 1$, the surface with high pO_2) of 6 membranes are shown in Figure 8-13. The nominal compositions are given as straight lines in the diagrams. The long time exposure in an oxygen gradient had no drastic effect on the cation fraction profiles. Only minor changes in the compositions are seen. The most pronounced effects are evident near the two surfaces. This phenomena suggests that the chemical gradient where more pronounced near the surfaces due to surface exchange kinetics. A more careful examination of the data is necessary in order to see any trends in the data. In the following the compositional data are analysed with respect to Sr/Fe-ratio, Co/Fe ratio and (Sr+La)/(Fe+Co) ration across the membranes.

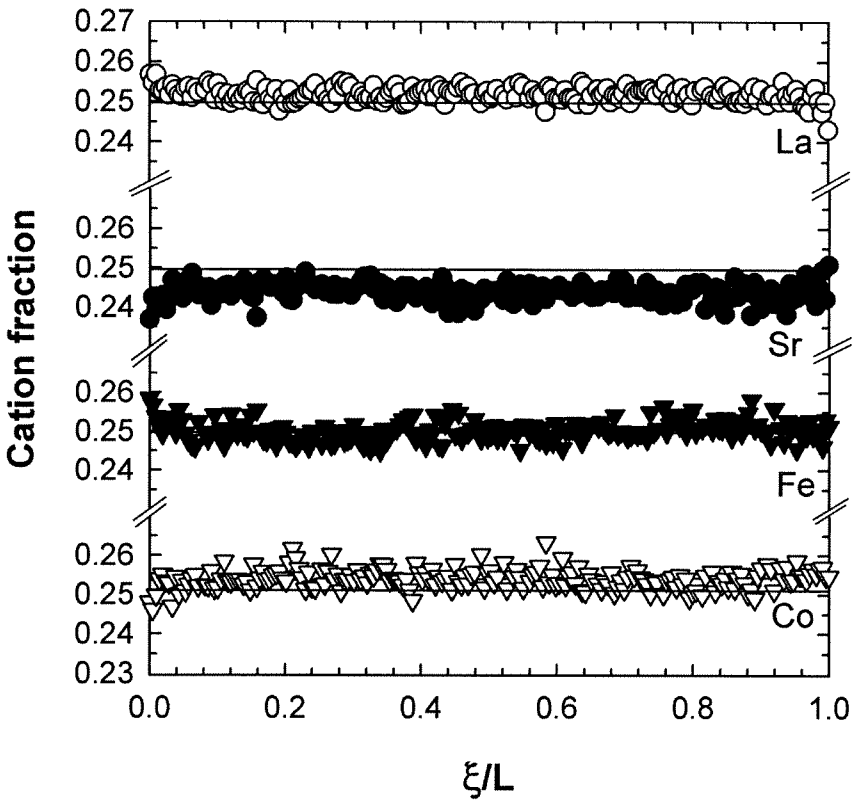

Figure 8: Cation fractions across the LSFC2 ($La_{0.5}Sr_{0.5}Fe_{0.5}Co_{0.5}O_{3-\delta}$) membrane as a function of position from secondary (low pO_2) side ($\xi/L = 0$) to primary (high pO_2) side ($\xi/L = 1$). The solid lines are the nominal compositions.

The (Sr+La)/(Fe+Co) or A/B ratio across the membrane is of particular interest. The A/B ratio is shown in Figure 14. Across the three LSFC membranes there is no dramatic change in the A/B ratio. A minor increase in the A/B ratio towards the primary side is evident for LSFC3 and LSFC4. This is in good accordance with the depletion of the B-cation due to formation of cobalt oxide phase at the primary side. The LSF and LSC membranes, on the other hand, have become A-excess across the whole cross section, with no significant gradient across the membrane. The A-excess is in good accordance with the formation of Co and Fe rich phases at the primary side. A simple mass balance for LSF5 membrane gives an average A/B ratio equal to 1.04, taking into account the formation of the

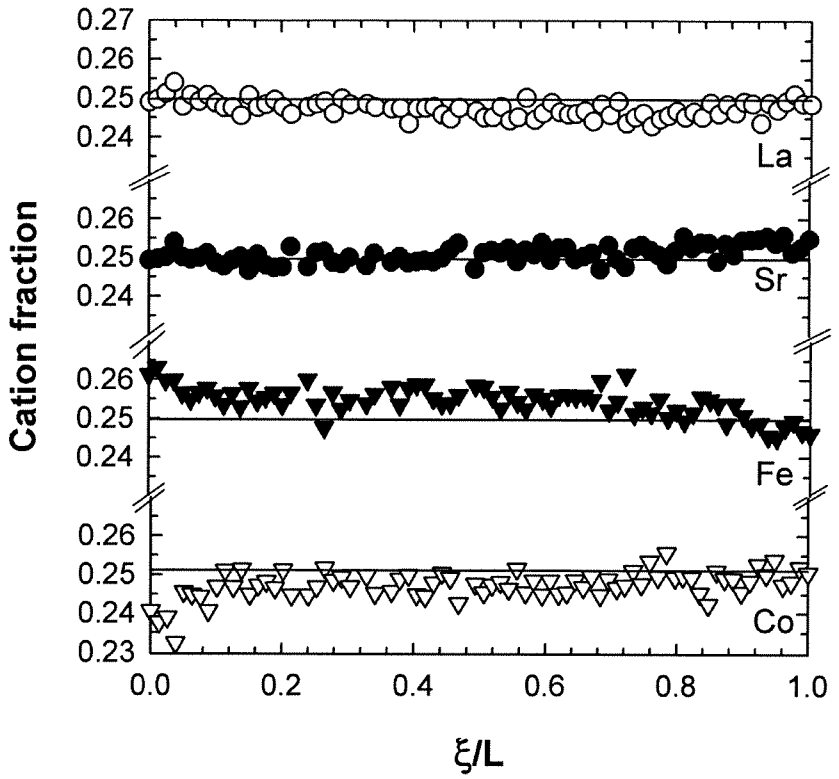

Figure 9: Cation fractions across the LSFC3 ($La_{0.5}Sr_{0.5}Fe_{0.5}Co_{0.5}O_{3-\delta}$) membrane as a function of position from secondary (low pO_2) side ($\xi/L = 0$) to primary (high pO_2) side ($\xi/L = 1$). The solid lines are the nominal compositions.

~ 17 μm $SrFe_{12}O_{19}$ layer. This is in good accord with the average value of the A/B ratio equal to 1.07. The average A/B ratio observed for LSC6 is 1.05. This A/B ratio corresponds to the formation of an about 18 μm thick layer of Co_3O_4. This is also in good accordance with the experimental observations except that Co_3O_4 formed separated grains at the surface and near the primary surface rather than a continuous layer.

A significant large scatter is evident for the A/B ratio across the LSFC7 membrane as shown in Figure 14. This is probably related to the less homogenous microstructure of this membrane compared to the others. The average A/B ratio is higher than 1 in line with the nominal composition.

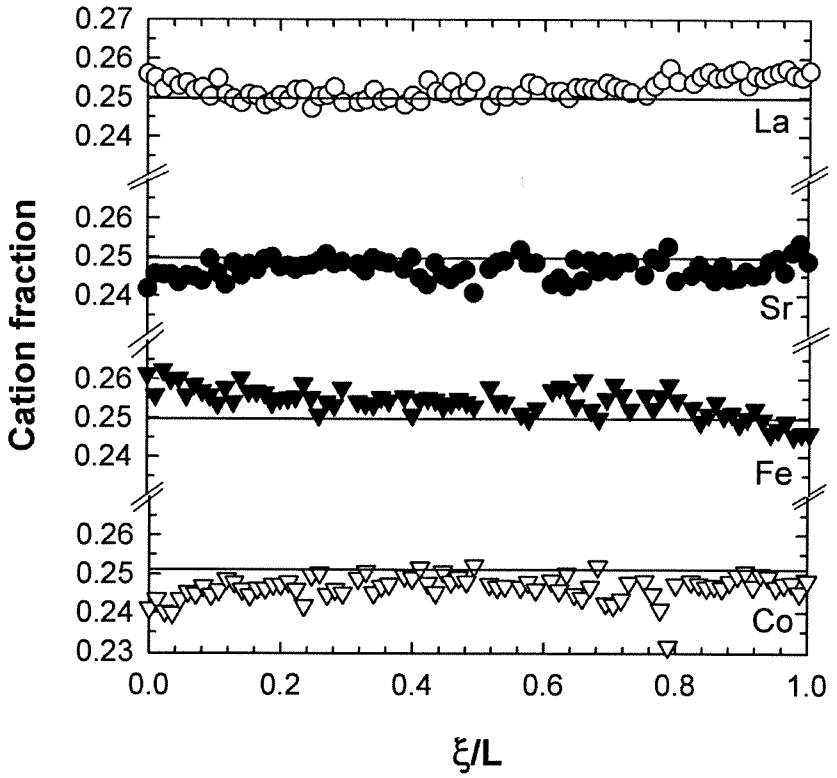

Figure 10: Cation fraction across the LSFC4 ($La_{0.5}Sr_{0.5}Fe_{0.5}Co_{0.5}O_{3-\delta}$) membrane as a function of position from secondary (low pO_2) side ($\xi/L = 0$) to primary (high pO_2) side ($\xi/L = 1$). The solid lines are the nominal compositions.

The La/Sr ratio across the 6 membranes as a function of position is given in Figure 15. The nominal compositions of all the membranes correspond to a ratio of unity. Here again only minor differences from the nominal compositions are observed. For the LSFC membranes the La/Sr ratio seems to be dependent on the thickness of the membrane. In the thin membranes, LSFC3 and LSFC4, no pronounced gradient is evident, while for the thick membrane LSFC2, which has twice the thickness, a clear depletion of Sr is evident at the secondary side and an enrichment of Sr at the primary side. This is a clear demonstration that the mobility of Sr is fast relative to La. The pronounced gradient in the thickest membrane gives additional evidence for the effect of slow surface kinetics. Only in the thick membrane,

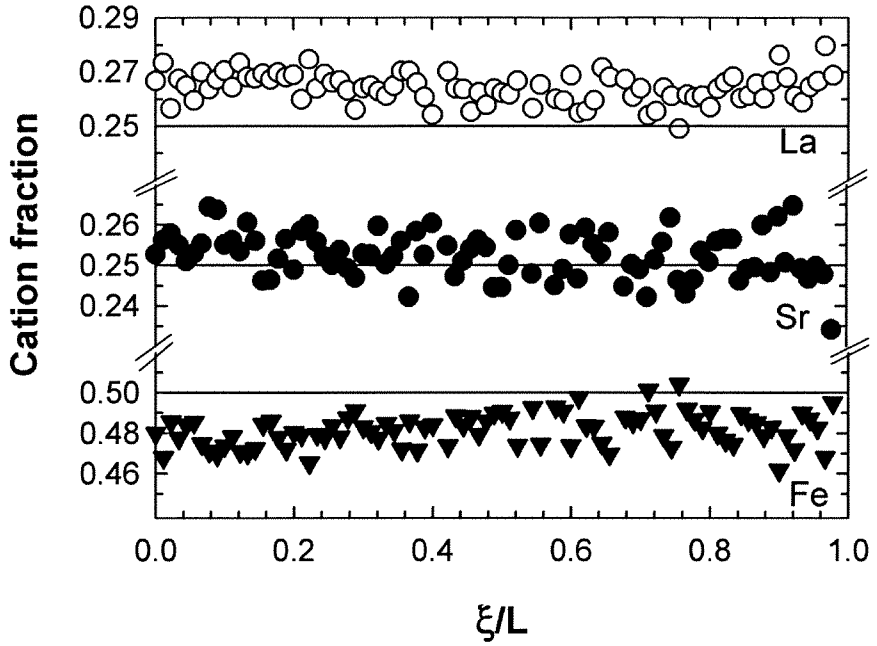

Figure 11: Cation fraction across the LSF5 ($La_{0.5}Sr_{0.5}FeO_{3-\delta}$) membrane as a function of position from secondary (low pO_2) side ($\xi/L = 0$) to primary (high pO_2) side ($\xi/L = 1$). The solid lines are the nominal compositions.

bulk diffusion was rate limiting resulting in a steeper gradient in the partial pressure of oxygen and a cation demixing of La and Sr. As shown in Figure 14 the demixing of Sr and La is not accompanied by a change in the A/B ratio.

The corresponding demixing of Sr and La on the A-site in the perovskite structure is also evident for the LSC membrane, see Figure 15. Here, again La is enriched on the secondary side and Sr on the primary side pointing to a higher mobility of Sr compared to La. The LSF membrane has been depleted on Sr and the La/Sr ratio is higher than the nominal as shown in Figure 15. Near the $SrFe_{12}O_{19}$ layer the La/Sr ratio is observed to increase. These observations are in accordance with the formation of the $SrFe_{12}O_{19}$ layer. Finally, the profile does also demonstrate that Sr is also diffusing faster than La in this material.

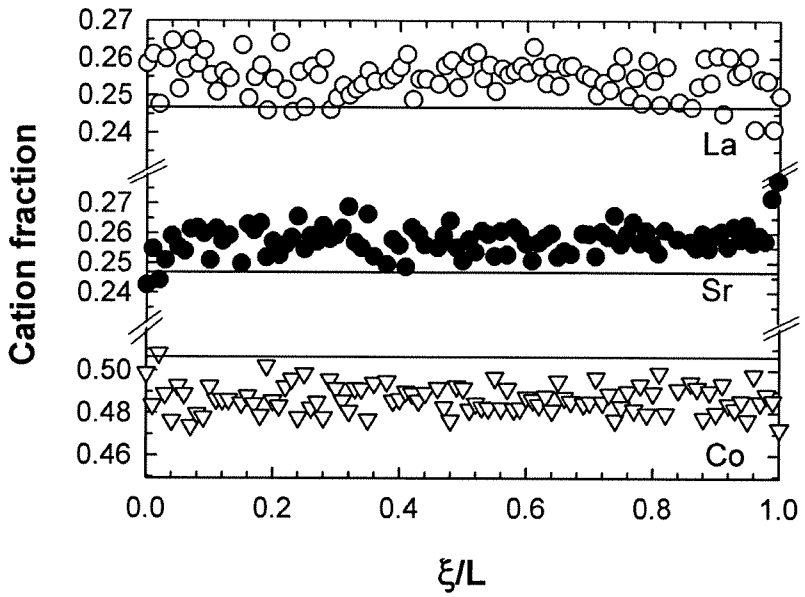

Figure 12: Cation fraction across the LSC6 ($La_{0.5}Sr_{0.5}CoO_{3-\delta}$) membrane as a function of position from secondary (low pO_2) side ($\xi/L = 0$) to primary (high pO_2) side ($\xi/L = 1$). The solid lines are the nominal compositions.

For the Sr-excess LSFC7 membrane, the La/Sr ratio is almost constant and lower than 1, see Figure 15. But in this case, the nominal was also lower than 1. Some minor enrichment of La towards the primary side is in accordance with the formation of a Sr-rich phase and point to a faster diffusion of Sr. We can therefore conclude that Sr has a relative higher mobility of La in all the studied materials.

The calculated Fe/Co ratio across the four LSFC membranes is given in Figure 16. The nominal ratio corresponding to a ratio close to unity is shown by the solid lines. For the three Co-excess membranes Fe is slightly enriched against the secondary side. This is also in accordance with formation of a cobalt oxide phase at the primary surface. These observations demonstrate the faster diffusion of Co compared to Fe.

In the LSFC7 membrane, the Fe/Co ratio is approximately constant and lower than 1 through the material. This is in accordance with the EDS

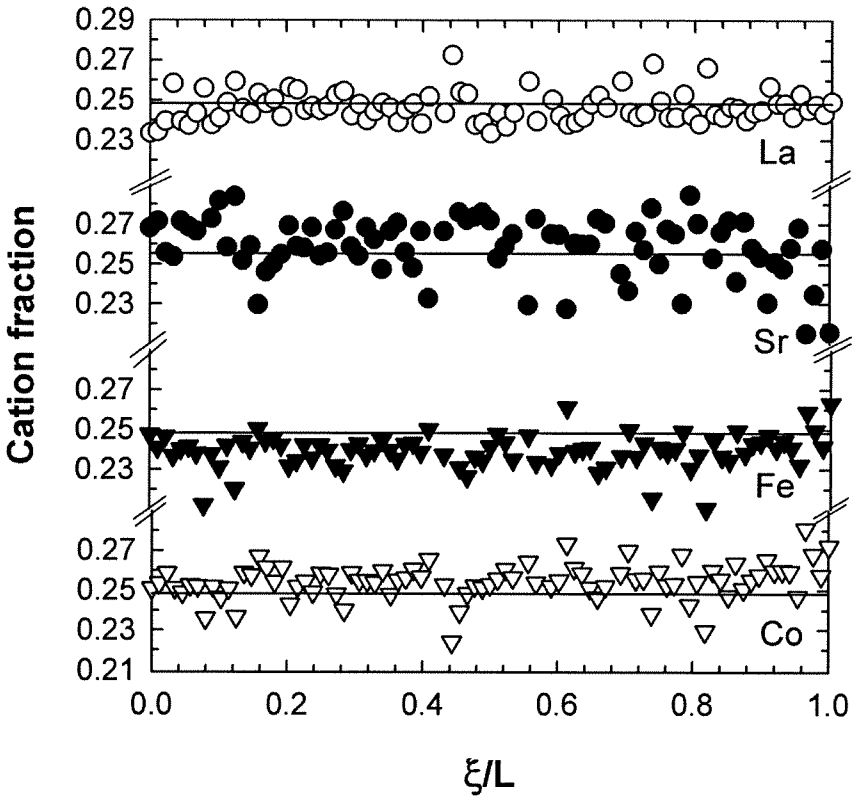

Figure 13: Cation fraction across the LSFC7 ($La_{0.5}Sr_{0.5}Fe_{0.5}Co_{0.5}O_{3-\delta}$) membrane as a function of position from secondary (low pO_2) side ($\xi/L = 0$) to primary (high pO_2) side ($\xi/L = 1$). The solid lines are the nominal compositions.

results of the secondary phase at the primary side that shows a phase with Fe enrichment at B-site. It therefore seems that diffusion of Fe relative to Co is enhanced by the Sr/La-excess in the material. It also interesting to note that the scatter in the Fe/Co ratio is far less than the corresponding scatter in the La/Sr ratio. Fe and Co was homogenously distributed in the powder used to prepare the membrane, while Sr originated both from the powder and the added strontium nitrate. The large scatter in the La/Sr ratio compared to the Fe/Co ratio clearly demonstrate that inhomogeneous distribution of Sr was still present after 30 days of operation. We can not rule out that the inhomogeneous distribution of Sr and La has a strong influence on the final microstructure and demixing and decomposition phenomena.

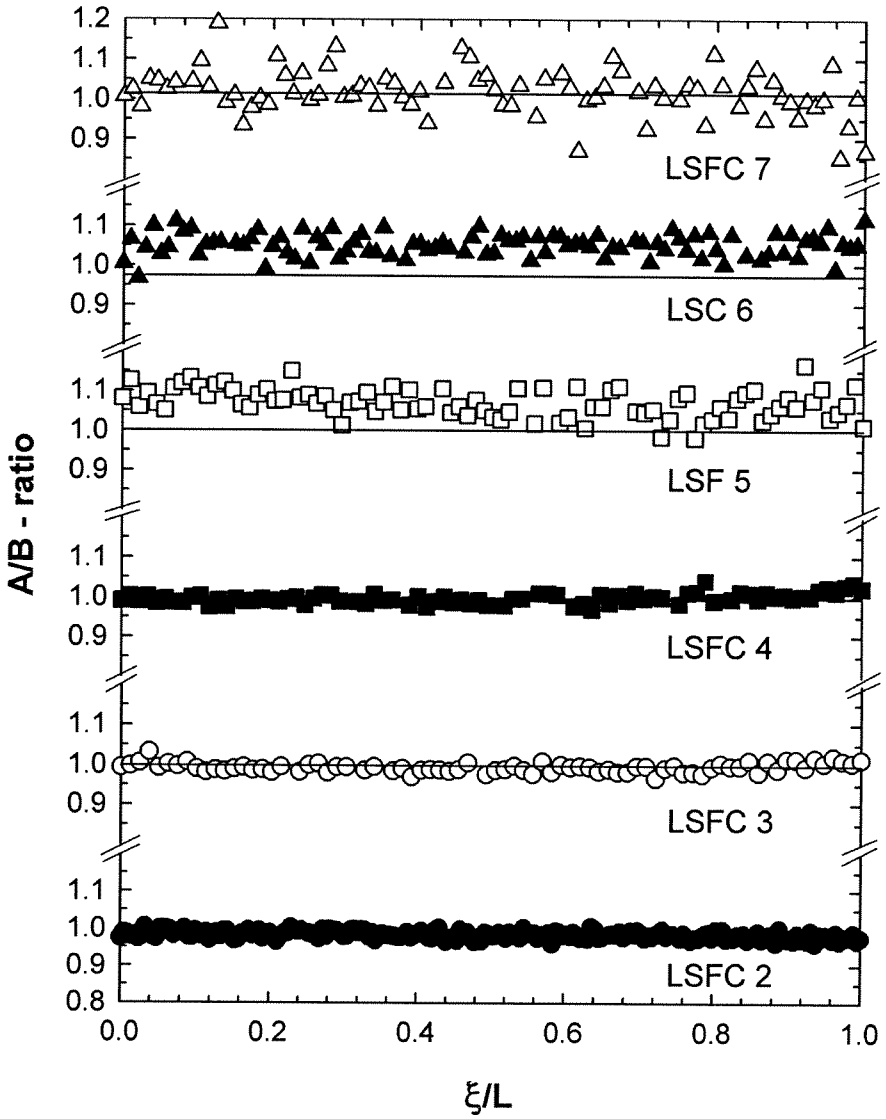

Figure 14: A/B ratio across $La_{0.5}Sr_{0.5}FeO_{3-\delta}$ (LSF), $La_{0.5}Sr_{0.5}Fe_{0.5}Co_{0.5}O_{3-\delta}$ (LSFC) and $La_{0.5}Sr_{0.5}CoO_{3-\delta}$ (LSC) membranes as a function of position from secondary (low pO_2) side ($\xi/L = 0$) to primary (high pO_2) side ($\xi/L = 1$). The solid lines are the nominal compositions.

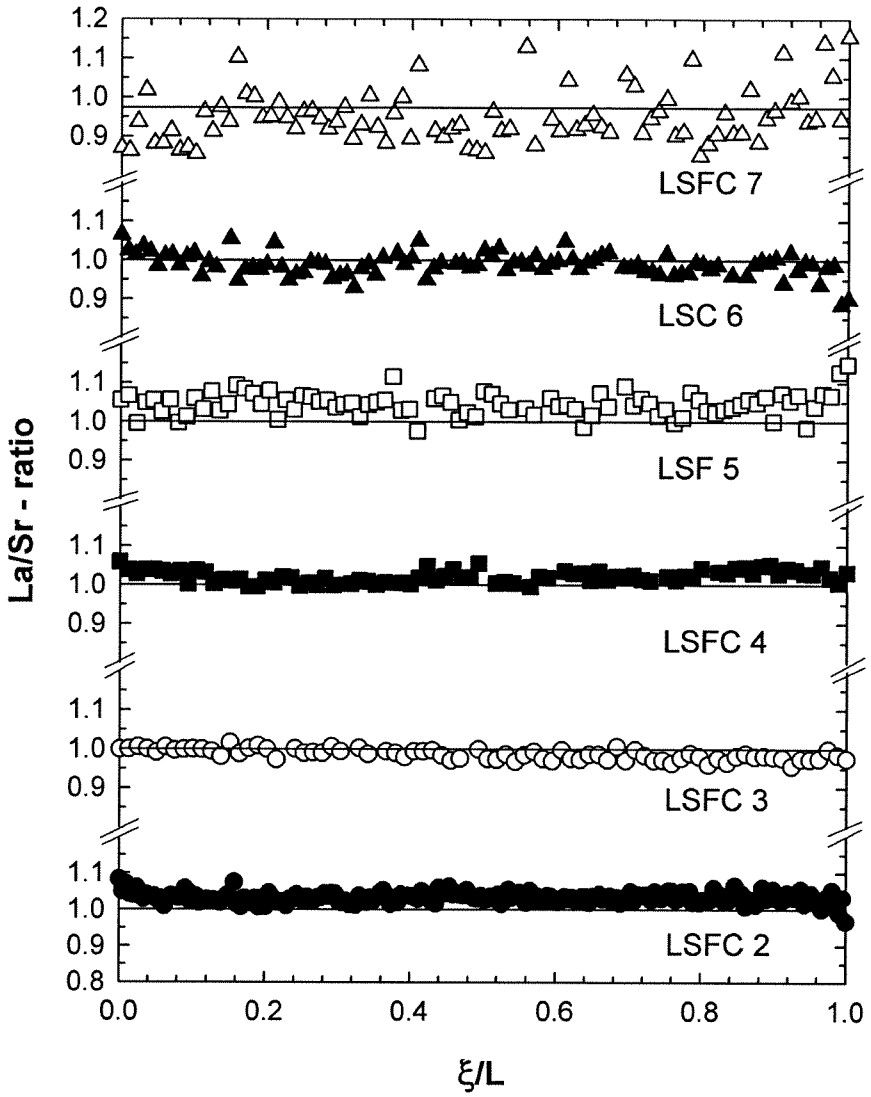

Figure 15: La/Sr ratio across $La_{0.5}Sr_{0.5}FeO_{3-\delta}$ (LSF), $La_{0.5}Sr_{0.5}Fe_{0.5}Co_{0.5}O_{3-\delta}$ (LSFC) and $La_{0.5}Sr_{0.5}CoO_{3-\delta}$ (LSC) membranes as a function of position from secondary (low pO_2) side ($\xi/L = 0$) to primary (high pO_2) side ($\xi/L = 1$). The solid lines are the nominal compositions.

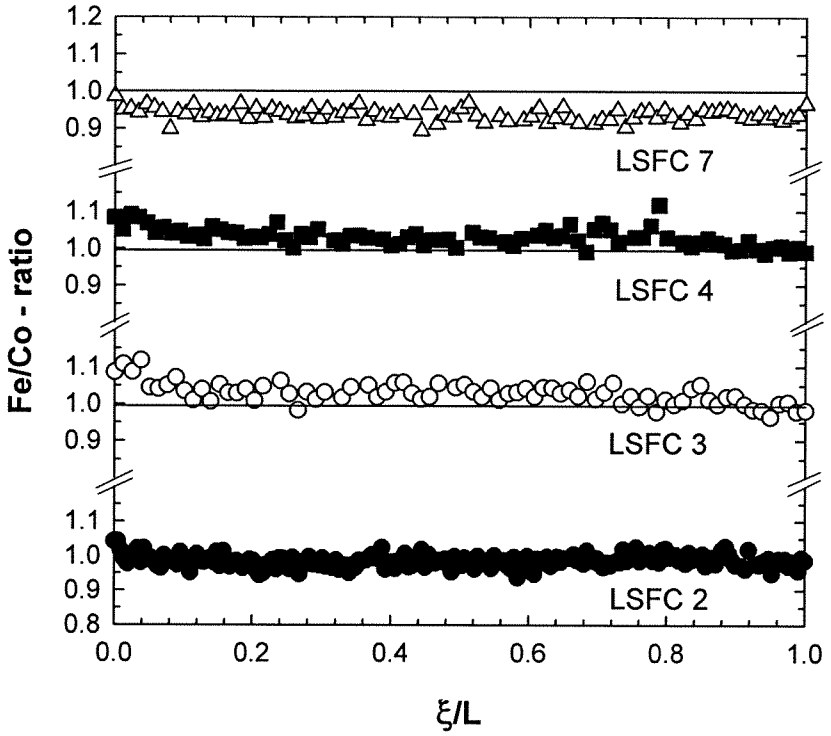

Figure 16: Fe/Co ratio across the $La_{0.5}Sr_{0.5}Fe_{0.5}Co_{0.5}O_{3-\delta}$ (LSFC) membranes as a function of position from secondary (low pO_2) side ($\xi/L = 0$) to primary (high pO_2) side ($\xi/L = 1$). The solid lines are the nominal compositions.

The measured oxygen content across the membranes after the experiments is given in Figure 17. The uncertainty in the absolute oxygen content is considered to be significant, but the profiles across the membranes should give a realistic picture of the relative oxygen content across the membranes. To our surprise the oxygen content was observed to increase towards the inert side and decreasing towards the air side. If one neglect any gradients in the metal concentrations these gradients are unphysical since the gradient is in opposite direction of the gradient in the partial pressure of oxygen. A more careful analysis is therefore necessary in order to explain these oxygen concentration profiles.

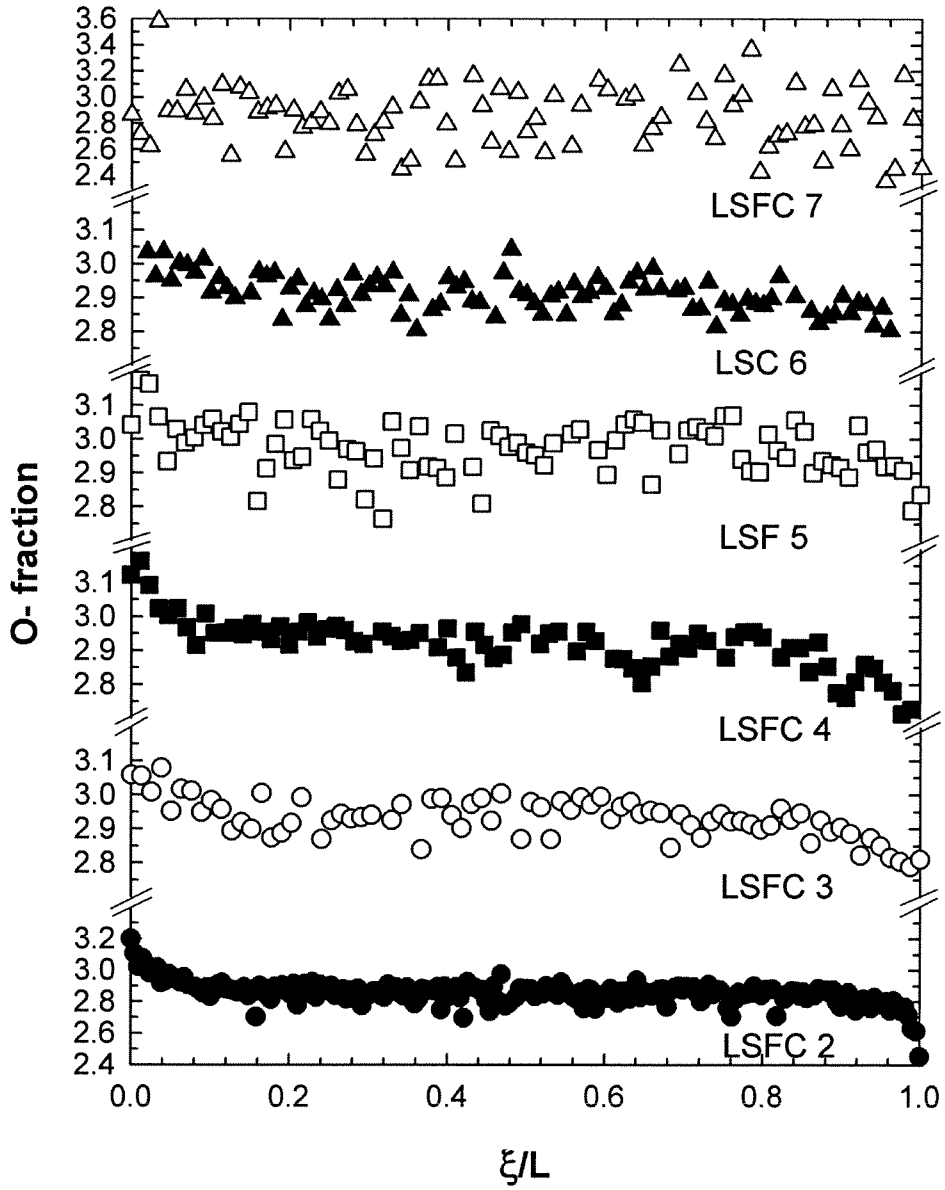

Figure 17: Oxygen fraction of $La_{0.5}Sr_{0.5}FeO_{3-\delta}$ (LSF), $La_{0.5}Sr_{0.5}Fe_{0.5}Co_{0.5}O_{3-\delta}$ (LSFC) and $La_{0.5}Sr_{0.5}CoO_{3-\delta}$ (LSC) membranes after ~ 5 weeks in a pO_2 gradient as a function of position from secondary (low pO_2) side ($\xi/L = 0$) to primary (high pO_2) side ($\xi/L = 1$).

The observed oxygen content may also reflect the oxidation of the membranes taking place during cooling, but this can not explain oxygen enrichment on the secondary side. We therefore propose that the change in oxygen content across the membrane reflects differences in the relative metal content across the membranes. From the cation profiles discussed earlier we have concluded that the secondary side is enriched on Fe and La, while Sr and Co are enriched on the primary side. High Sr and Co content will result in a lower oxygen content due to lower valence state of Sr relative to La and Co relative to Fe. For example $SrCoO_{3-\delta}$ is known to have an oxygen deficiency as low as 0.5-0.7.[31] Correspondingly pure $LaFeO_3$ is stoichiometric even in inert atmosphere.[32]

Discussion

Changes in the microstructure

All the membranes were observed to swell during the permeation experiments at 1150°C (Table 4), essentially due to pore expansion. The only membrane which did not expand significantly was LSF5, and in this membrane only a minor grain growth was observed (Table 3). The pore expansion in the other membranes was accompanied by a significant grain growth, and the pore expansion is therefore most likely linked to pore coalescence due to this grain growth. These observations demonstrate that it is of importance that oxygen permeable membranes should be as dense as possible to avoid expansion due to this phenomenon. The significant change in the microstructure will influence on the mechanical properties of the membrane and it might be challenging to predict the mechanical performance of the material with time.

The incorporation of CuO on the air side in LSFC1 demonstrated how easily contaminations may affect the microstructure of the materials. Good chemical compatibility with sealing materials or support is therefore important for the development of oxygen permeable membranes.

Kinetic decomposition

The thermodynamic stability of the present materials at high temperature and varying oxygen partial pressure is not well established for all compositions. In case of LSF, studies by Fossdal et al.[33] have shown that this phase is stable both in air and inert atmosphere. In another publication by Fossdal et al.,[34] the phase formed at the primary side of the LSF5 membrane, $SrFe_{12}O_{19}$, is reported to be coexistent with LSF in air at 1150°C. We can therefore conclude that in the case of the LSF membrane kinetic decomposition had occurred at the air side during the permeation experiments.

The phase investigation of LSC after sintering support the coexistence of CoO (which transform to Co_3O_4 during cooling) with LSC in air at 1150°C. Kinetic decomposition of LSC is therefore also expected, although the LSC material was initially slightly Co-excess (Table 1). It is also interesting to note that LSC is not a thermodynamic stable phase in inert atmosphere above 1000°C. LSC was observed to decompose in nitrogen during high temperature X-ray diffraction.[27] Therefore, from thermodynamic consideration, we should expect to observe a Ruddlesden-Popper type of secondary phase coexisting with a La-rich perovskite at the secondary side of the membrane. This was indeed not observed as shown in Figure 5a). As discussed in the following, we may explain the lack of decomposition by a slow surface exchange kinetics at this side. If the surface exchange is rate limiting, the effective partial pressure of oxygen at the secondary surface may be higher than in the sweep gas due to a steep gradient in oxygen chemical potential at the surface.

The similar behavior of LSC and LSFC1-4 membranes points to a kinetic decomposition of LSFC materials at the air side. However, it is again important to note the presence of a cobalt oxide secondary phase in the original membranes.

A "Sr_2FeO_4" like phase was formed at the air side of the LSFC7 membrane. The coexistence of LSF and $La_{2-x}Sr_xFeO_4$ in air at 1100-1300°C has been reported by Fossdal et al.[29] However, due to the inhomogeneous nature of LSFC7 as discussed in the previous chapter, it is not possible to conclude that kinetic decomposition of the LSFC7 membrane has occurred at the primary side. However, the data obtained for the LSFC7 membrane have clearly shown the importance of the cation non-stoichiometry with regard to the chemical stability of the materials. If a secondary phase is formed due to deviation from the nominal cation stoichiometry, this may strongly influence on the nature of the phase formed at the primary side of a

membrane. The effect of the A/B ratio in homogeneous membranes should be followed up more thoroughly in future experiments. In previous reports on the formation of secondary phases at the surfaces of oxygen permeable membranes, deviation from nominal cation stoichiometry and the inherent thermodynamic stability of the materials have not been in focus.[8, 23-25] Before any conclusion can be made, one needs to know the thermodynamic stability of the material and the content of secondary phases due to offsets in the cation stoichiometry. Unfortunately, even with very careful control, deviation from the nominal composition must be expected on the level of the uncertainty of the stoichiometry, which is typically 0.1 wt% of each metal oxide. One should therefore look for grain boundary phases by electron microscopy to establish the offset from the nominal composition. Simple X-ray diffraction analysis is not sufficient to establish the phase purity, but this is the far most used method for phase purity analysis in solid state ionics. Finally, cation non-stoichiometry may not result in secondary phases due to solid solution, but so far solid solution has only been reported for $SrFeO_{3-\delta}$ [29] and $LaMnO_{3\pm\delta}$.[35]

Cation demixing

The gradient in the oxygen chemical potential, μ_O, inside a multi-component oxide $A_{1-x}A'_xB_{1-y}B'_yO_{3-\delta}$ induces a corresponding but inverse gradient of the cation chemical potential.[8, 36] This can be described by the Gibbs-Duhem equation[1], written in differential form

$$(1-x)\nabla\mu_A + x\nabla\mu_{A'} + (1-y)\nabla\mu_B + y\nabla\mu_{B'} + (3-\delta)\nabla\mu_O = 0 \qquad (5)$$

The cation diffusion in perovskite materials is many orders of magnitude lower than oxygen diffusion,[37-38] and the cations do not contribute to the electrical conductivity. The oxygen flux through the membranes is determined by the bulk diffusion of oxygen ions, the electronic conductivity and the surface exchange process taking place at the two surfaces.[26] Cation diffusion is therefore only interesting with regard to the long term stability and changes in the performance of the membrane due to changes caused by difference in cation mobility.

The Gibbs-Duhem equation demonstrates that the driving force for demixing or decomposition is actually reduced by increasing the number of metal components in the membrane. The gradient in the chemical potential

of oxygen is balanced by the sum of the opposing gradients of the cations, and the higher number of metal ions in the material, the smaller is the chemical potential for each cation. Here, we have seen that changes in the cation concentration and kinetic demixing are more dramatic in LSF and LSC compared to LSFC. In the ternary oxides LSF and LSC, both kinetic demixing (departure from the nominal A/B ratio, see Figure 14) and kinetic decomposition were observed. The more pronounced effect in the ternary oxide membranes can then be explained by a shallower gradient in the chemical potential of the metal ions when going from three to four metal components.

For an ternary oxide, e.g. LSF, the bulk flux of a cation, j, can be expressed as

$$j(La) = -L_{LaLa}\nabla\eta(La) - L_{LaSr}\nabla\eta(Sr) - L_{LaFe}\nabla\eta(Fe) - L_{LaO}\nabla\eta(O) - L_{Lah}\nabla\eta(h) \quad (6)$$

$$j(Sr) = -L_{SrLa}\nabla\eta(La) - L_{SrSr}\nabla\eta(Sr) - L_{SrFe}\nabla\eta(Fe) - L_{SrO}\nabla\eta(O) - L_{Srh}\nabla\eta(h) \quad (7)$$

$$j(Fe) = -L_{FeLa}\nabla\eta(La) - L_{FeSr}\nabla\eta(Sr) - L_{FeFe}\nabla\eta(Fe) - L_{FeO}\nabla\eta(O) - L_{Feh}\nabla\eta(h) \quad (8)$$

$$j(O) = -L_{OLa}\nabla\eta(La) - L_{OSr}\nabla\eta(Sr) - L_{OFe}\nabla\eta(Fe) - L_{OO}\nabla\eta(O) - L_{Oh}\nabla\eta(h) \quad (9)$$

$$j(h) = -L_{hLa}\nabla\eta(La) - L_{hSr}\nabla\eta(Sr) - L_{hFe}\nabla\eta(Fe) - L_{hO}\nabla\eta(O) - L_{hh}\nabla\eta(h) \quad (10)$$

using linear irreversible thermodynamics.[39] Lij are the Onsager transport coefficients and the η_i the electrochemical potential given by $\eta_i = \mu_i + z_i \cdot F \cdot \Phi$ where μ_i is the chemical potential, z_i·the charge number and Φ the electric potential.[9] In oxides with only one sub-lattice, the cross coefficients are often neglected as a first approximation. The A/B ratio profiles across the membranes shown in Figure 14, indicates that the cross coefficient between cations on the A and B sites can not be neglected. Large deviation from the nominal ABO_3 cation stoichiometry is energetically unfavorable and diffusion on the A and B site should be to some degree coupled. On the other hand, the cross coefficients of cations on the same sublattice may be disregarded to a first approximation as usually assumed for simpler binary oxides.[20]

The movement of the cations towards the oxygen rich side will lead to growth and dissociation of the mixed conductors at the two surfaces, in analogy with what is going on in pure ion conductors.[20] The surface reactions for the two sublattices of trivalent cations can generally be expressed as

$$A_2O_3 + 2V_A + 6h^{\cdot} \underset{\text{oxidizing side}}{\overset{\text{reduced side}}{\rightleftharpoons}} 2A^{3+} + \tfrac{3}{2}O_2(g) \quad (11)$$

$$B_2O_3 + 2V_B + 6h^{\cdot} \underset{\text{oxidizing side}}{\overset{\text{reduced side}}{\rightleftharpoons}} 2B^{3+} + \tfrac{3}{2}O_2(g) \qquad (12)$$

where h$^{\cdot}$ are electron holes and V are cation vacancies. Here, we have assumed that no new phases appear at the primary air side. The sum of the reactions will be

$$2ABO_3 + 2V_A + 2V_B + 12h^{\cdot} \underset{\text{oxidizing side}}{\overset{\text{reduced side}}{\rightleftharpoons}} 2A^{3+} + 2B^{3+} + 3O_2(g) \qquad (13)$$

In the case of formation of CoO on the primary surface, the reaction will be

$$CoO + V_{Co} + 3h^{\cdot} \underset{\text{oxidizing side}}{\overset{\text{reduced side}}{\rightleftharpoons}} Co^{3+} + \tfrac{1}{2}O_2(g) \qquad (14)$$

As a consequence of these reactions, both the membrane surfaces will move towards the oxygen rich side. As a first approximation, the sub lattice of the slowest cation may be regarded as a frame of reference for the relative movement of the two surfaces.

Similar experiments on simple binary oxide solid solutions having the rock salt structure have shown that steady state can be reached within a few days.[20] At steady state the concentration profile of the cations remain unchanged with time, which means that the flux of the cations divided by the concentration is constant for all cations. In the perovskite crystal structure, this picture is questionable since the flux of cations on the A and B site is not necessarily linked as in a case of a oxide with only a single cation sub-lattice.

At present we have no numerical model that can be used to predict the cation concentration profile across the membranes. It is therefore not clear if the concentration profiles that are reported here reflect a transient or a steady state situation. Several factors are important with this respect. First, the measured oxygen permeation rates were surprisingly stable with time despite of the fact that the surface morphology on the primary side changes. The membrane has therefore been operating through the whole time period. Secondly, the largest departure from the nominal La/Sr ratio was observed in the LSFC2 membrane, see Figure 15, which is the thickest membrane investigated. The concentration profiles of the metal ions across the membranes are, except near the surfaces, relatively flat. This can be interpreted in two different ways. First, the profiles reflect a transient stage after the exposed time, which means that a steady state situation will take considerably longer time than about 30-40 days. However, it is previously

seen[28] that the sintering rates are high at these temperatures and hence a considerable mass transport favors the steady state presence. Secondly, the profiles may reflect that the driving force, i.e. the chemical gradient in the partial pressure of oxygen, has only a minor gradient in the bulk of the membranes. The latter points to a surface control of the oxygen flux and that the drop in oxygen chemical potential from air on the primary side to the inert gas on the secondary side is basically taking place close to the two surfaces. This is illustrated in Figure 18. As discussed in Paper IV[26], surface exchange on secondary side may be rate limiting for the oxygen flux at these pO_2 gradients. This may even be the case at the primary side. This suggests that the critical thickness of the membrane becomes rather large due to small surface exchange coefficients. Moreover, the phase composition changes at the primary side of the membranes may also slow the surface exchange rate at the primary side. The bulk diffusion of oxygen ions may therefore be sufficiently high, relative to the two surface exchange processes, to cause a reduction of the chemical gradient in the bulk. For the thickest membrane (LSFC2), the bulk diffusion may be rate limiting due to a membrane possibly thicker than the critical thickness, and hence the chemical gradient will be larger. This is in accordance with the largest departure from the nominal La/Sr ratio seen for this membrane. However, without a thorough numerical analysis of the data these considerations are only preliminary, and future work on this subject should also be followed up with numerical analysis. Additional information on the cation diffusion of the corresponding materials by tracer diffusion, diffusion couples and creep would also be very helpful to evaluate the relative mobility of cations on the A and B site.

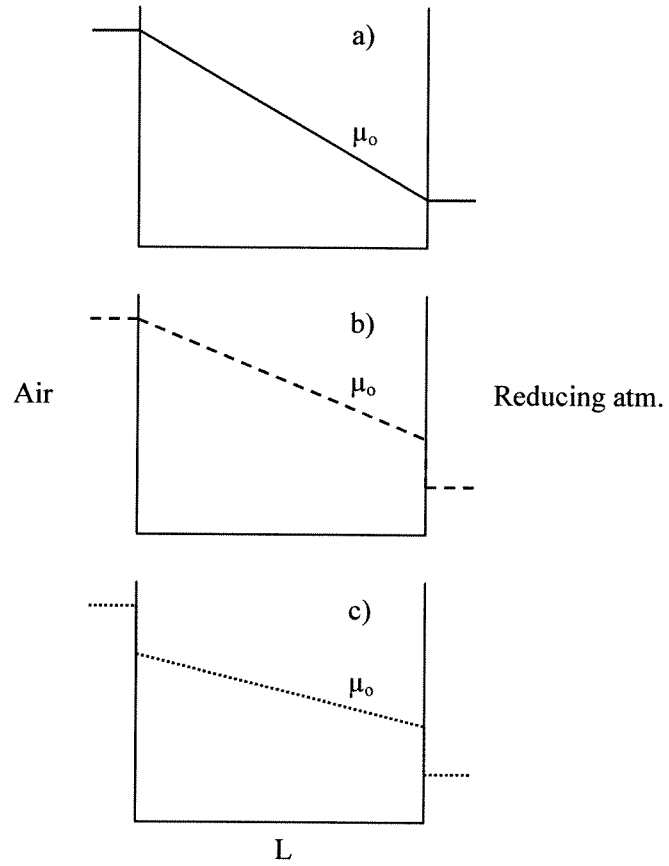

Figure 18: Oxygen chemical potential profiles through bulk of an oxygen permeable membrane for different contributions from surface exchange processes. a) Only bulk diffusion, b) contribution of surface processes at secondary side and c) contribution of surface processes at both sides.

Conclusion

Kinetic decomposition has been demonstrated in $La_{0.5}Sr_{0.5}Fe_{1-x}Co_xO_{3-\delta}$ ($0 \leq x \leq 1$) oxygen permeable membranes operating for more than ~30 days at 1150°C. At the primary side of $La_{0.5}Sr_{0.5}Fe_{0.5}Co_{0.5}O_{3-\delta}$ (LSFC) and $La_{0.5}Sr_{0.5}CoO_{3-\delta}$ (LSC) membranes, cobalt oxide was formed, while the $La_{0.5}Sr_{0.5}FeO_{3-\delta}$ (LSF) membrane was a completely covered by a layer of $SrFe_{12}O_{19}$. It was also shown that the nature of the phase formed is probably affected by the overall (Sr+La)/(Fe+Co) stoichiometry of the materials. The observations of the Co and Fe rich phases at the primary side indicate that diffusion of Co or Fe is dominant over diffusion of La and Sr in these materials. Evidence for kinetic demixing was also observed. Diffusion of Sr cations was fastest on A-site in all the materials, while Co cations were fastest on the B-site in LSFC. In all the membranes the most pronounced changes in the metal content was observed near the two surfaces. These observations point to a surface exchange control of the oxygen flux through ~ 1 mm membranes operating at 1150°C. Finally, the oxygen permeability was not severely changed by the kinetic demixing and decomposition.

Acknowledgement

The Research Council of Norway, Statoil and Hydro are acknowledged for financial support.

References

1. H. J. M. Bouwmeester and A. J. Burgraaf, in: P.J. Gellings and H.J.M. Bouwmeester (Eds), The CRC Handbook of Solid State Electrochemistry, CRC Press, Inc., New York (1997).
2. A. Atkinson and A. Selcuk, "Mechanical behaviour of ceramic oxygen ion-conducting membranes", Solid State Ionics, 134 (2000) 59-66.
3. P. V. Hendriksen, P. H. Larsen, M. Mogensen, F. W. Poulsen and K. Wiik, "Prospects and problems of dense oxygen permeable membranes", Catalysis Today, 56 (2000) 283-295.
4. M. Martin, "Transport and degradation in transition metal oxides in chemical potential gradients", Materials Science Reports 7 (1991) 1-86.
5. H. Schmalzried, "Behavior of (semiconducting) oxide crystals in oxygen potential gradients", Reactivity of Solids, 1 (1986) 117-137.
6. S. Stølen and T. Grande, "Chemical Thermodynamics of Materials. Macroscopic and Microscopic Aspects", John Wiley & Sons Ltd., West Sussex (2004).
7. M. Martin and H. Schmalzried, "Tracer diffusion in chemical potential gradients", Solid State Ionics, 20 (1986) 75-80.
8. R. H. E. van Doorn, H. J. M. Bouwmeester and A. J. Burggraaf, "Kinetic decomposition of $La_{0.3}Sr_{0.7}CoO_{3-\delta}$ perovskite membranes during oxygen permeation", Solid State Ionics, 111 (1998) 263-272.
9. M. Martin, "Materials in thermodynamic potential gradients", J. Chem. Thermodynamics, 35 (2003) 1291-1308.
10. T. Ishikawa, S. A. Akbar, W. Zhu and H. Sato, "Time Evolution of Demixing in Oxides under an Oxygen Potential Gradient", J. Am. Ceram. Soc, 71 [7] (1988) 513-521.
11. H. Schmalzried, W. Laqua and P. L. Lin, "Crystalline Oxide Solid Solutions in Oxygen Potential Gradients", Z. Naturforsch., 34a (1979) 192-199.
12. H. Schmalzried and W. Laqua, "Multicomponent Oxides in Oxygen Potential Gradients", Oxidation of Metals, 15 [3/4] (1981) 339-353.
13. Y. Ueshima, H. Schmalzried and J. Koepke, "Demixing of oxide solid solutions in oxygen potential gradients: Two-phase systems and the morphological stability of the interface", Solid State Ionics, 40-41 (1990) 232-235.
14. M. J. Brown, I. V. Belova and G. E. Murch, "Prediction of kinetic demixing in a quaternary mixed oxide (A,B,C)O in an oxygen potential gradient", Phil. Mag., 86 (2003) 1855-1865.

15. D. Dimos, D. L. Kohlstedt and H. Schmalzried, "High-Temperature Creep and Kinetic Demixing in (Co, Mg)O", J. Am. Ceram. Soc., 71 [9] (1988) 732-741.
16. I. V. Belova, M. J. Brown and G. E. Murch, "Analysis of kinetic demixing in a mixed oxide (A,B)O in an oxygen potential gradient", Acta Mater., 51 (2003) 1821-1826.
17. H. Schmalzried, "Diffusion in oxides", Reactivity of Solids, 5 (1988) 268-278.
18. O. Teller and M. Martin, "Kinetic demixing of Heterovalently Doped CoO in an Electrical Field", Ber. Bunsenges. Phys. Chem, 110 (1997) 1377-1380.
19. O. Teller and M. Martin, "Kinetic demixing of (Co,Ni)O in an electric field", Solid State Ionics, 101-103 (1997) 475-478.
20. M. Martin, "Electrotransport and demixing in oxides" Solid State Ionics, 136-137 (2000) 331-337.
21. J.-O. Hong, O. Teller, M. Martin and H.-I. Yoo, "Demixing of a mixed oxide (A,B)O in an oxygen potential gradient: numerical solution of the time evolution of the demixing process", Solid State Ionics, 123 (1999) 75-85.
22. Y. Ueshima, H. Schmalzried and J. Koepke, "Demixing in Oxgen Potential Gradients: Two-Phase System and the Morphological Stability of the Interface", Ber. Bunsenges. Phys. Chem., 93 (1989) 24-29.
23. S. Kim Y. L. Yang, R. Christoffersen and A. J. Jacobson, "Oxygen permeation, electrical conductivity and stability of the perovskite oxide $La_{0.2}Sr_{0.8}Cu_{0.4}Co_{0.6}O_{3-x}$", Solid State Ionics, 104 (1997) 57-65.
24. S. Diethelm, J. Sfeir, F. Clemens, J. Van herle and D. Favrat, "Planar and tubular perovskite type membrane reactors for the partial oxidation of methane to syngas", J. Solid State Electtrochem, 8 (2004) 611-617.
25. S. Diethelm, J. Van herle, P. H. Middleton and D. Favrat, "Oxygen permeation and stability of $La_{0.4}Ca_{0.6}Fe_{1-x}Co_xO_{3-\delta}$ (x = 0, 0.25, 0.5) membranes", J. Power Sources, 118 (2003) 270-275.
26. H. L. Lein, K. Wiik and T. Grande, "Oxygen permeation of $La_{0.5}Sr_{0.5}Fe_{1-x}Co_xO_{3-\delta}$ ($0 \leq x \leq 1$) materials", paper IV.
27. H. L. Lein, K. Wiik and T. Grande, "Thermal and chemical expansion of $La_{0.5}Sr_{0.5}Fe_{1-x}Co_xO_{3-\delta}$ ($0 \leq x \leq 1$) materials", paper I.
28. H. L. Lein, E. Lara-Curzio, K. Wiik, M.-A. Einarsrud and T. Grande, "High temperature creep behavior of $La_{0.5}Sr_{0.5}Fe_{1-x}Co_xO_{3-\delta}$ ($0 \leq x \leq 1$) materials", paper II.
29. A. Fossdal, M.-A. Einarsrud and T. Grande, "Phase equilibria in the pseudo-binary system $SrO\text{-}Fe_2O_3$", J. Solid State Chem., 177 (2004) 2933-2942.

30. J. B. Smith and T. Norby, "Cation Self-Diffusion in $LaFeO_{3-\delta}$ Measured by the Solid State Reaction Method", to be published.
31. V. V. Vashook, M. V. Zinkevich, H. Ullmann, J. Paulsen, N. Trofimenko and K. Teske, "Oxygen non-stoichiometry and electrical conductivity of the binary strontium cobalt oxide $SrCoO_x$", Solid State Ionics, 99 (1997) 23-32.
32. J. Mizusaki, M. Yoshihiro, S. Yamauchi and K. Fueki, "Nonstoichiometry and defect structure of the perovskite-type oxides $La_{1-x}Sr_xFeO_{3-\delta}$", J. Solid State Chem., 58 (1985) 257-266.
33. A. Fossdal, M. Menon, I. Værnhus, K. Wiik, M.-A. Einarsrud and T. Grande, "Crystal structure and thermal expansion of $La_{1-x}Sr_xFeO_{3-\delta}$ materials", J. Am. Ceram. Soc., 87 [10] (2004) 1952-1958.
34. A. Fossdal, M.-A. Einarsrud and T. Grande, "Phase relations in the pseudo ternary La_2O_3 – SrO – Fe_2O_3 system at 1100°C and 1300°C in air", J. Am. Ceram. Soc., in print.
35. J. A. M. van Roosmalen, P. van Vlaanderen, E. H. P. Cordfunke, W. L. IJdo and D. J. W. IJdo, "Phases in the Perovskite-Type $LaMnO_{3+\delta}$ Solid Solution and the La_2O_3-Mn_2O_3 Phase Diagram", J. Solid State Chem., 114 (1995) 516-523.
36. H. J. M. Bouwmeester, "Dense ceramic membranes for methane conversion", Catalysis Today, 82 (2003) 141-150.
37. O. Schulz and M. Martin, "Preparation and characterisation of $La_{1-x}Sr_xGa_{1-y}Mg_yO_{3-(x+y)/2}$ for the investigation of cation diffusion processes", Solid State Ionics, 135 (2000) 549-555.
38. T. Horita, M. Ishikawa, K. Yamaji, N. Sakai, H. Yokokawa and M. Dokiya, "Cation diffusion in (La,Ca)CrO_3 perovskite by SIMS", Solid State Ionics 108 (1998) 383-390.
39. S. R. de Groot, P. Mazur, Non-Equilibrium Thermodynamics, North-Holland, Amsterdam (1962).

APPENDICES

APPENDIX I

RAW DATA OF OXYGEN NON-STOICHIOMETRY

Table I-1 – I-3 show raw data of oxygen non-stoichiometry as a function of temperature in different atmospheres for $La_{0.5}Sr_{0.5}FeO_{3-\delta}$, $La_{0.5}Sr_{0.5}Fe_{0.5}Co_{0.5}O_{3-\delta}$ and $La_{0.5}Sr_{0.5}CoO_{3-\delta}$.

Table I-1: Raw data of oxygen non-stoichiometry as a function of temperature in different atmospheres for $La_{0.5}Sr_{0.5}FeO_{3-\delta}$.

Temperature [°C]	Atm	3-δ
97.6	Air	2.966
299.1	Air	2.965
399.4	Air	2.963
500.0	Air	2.959
550.2	Air	2.956
600.5	Air	2.951
650.8	Air	2.942
701.0	Air	2.932
751.4	Air	2.919
801.7	Air	2.905
852.0	Air	2.889
902.2	Air	2.874
952.6	Air	2.858
1003.1	Air	2.844
97.5	N_2	2.964
299.1	N_2	2.961
399.4	N_2	2.954
499.9	N_2	2.930
550.2	N_2	2.910
600.5	N_2	2.888
650.8	N_2	2.866
701.0	N_2	2.845
751.4	N_2	2.824
801.7	N_2	2.807
851.9	N_2	2.794
902.2	N_2	2.783
952.6	N_2	2.775
1003.0	N_2	2.770

Table I-2: Raw data of oxygen non-stoichiometry as a function of temperature in different atmospheres for $La_{0.5}Sr_{0.5}Fe_{0.5}Co_{0.5}O_{3-\delta}$.

Temperature [°C]	Atm	3-δ
97.5	Air	2.930
299.0	Air	2.926
399.4	Air	2.920
499.9	Air	2.911
550.1	Air	2.906
600.4	Air	2.898
650.8	Air	2.888
701.0	Air	2.876
751.3	Air	2.862
801.6	Air	2.848
851.9	Air	2.832
902.2	Air	2.816
952.6	Air	2.799
1003.0	Air	2.784
97.5	N_2	2.921
299.1	N_2	2.904
399.4	N_2	2.885
500.0	N_2	2.854
550.1	N_2	2.837
600.4	N_2	2.813
650.8	N_2	2.790
700.9	N_2	2.772
751.3	N_2	2.752
801.7	N_2	2.731
851.9	N_2	2.714
902.2	N_2	2.698
952.6	N_2	2.679
1003.0	N_2	2.662

Table I-3: Raw data of oxygen non-stoichiometry as a function of temperature in different atmospheres for $La_{0.5}Sr_{0.5}CoO_{3-\delta}$.

Temperature [°C]	Atm	3-δ
97.5	Air	2.929
299.0	Air	2.925
399.4	Air	2.920
499.9	Air	2.912
550.1	Air	2.906
600.4	Air	2.898
650.7	Air	2.888
701.0	Air	2.876
751.3	Air	2.862
801.6	Air	2.848
851.9	Air	2.831
902.2	Air	2.815
952.6	Air	2.799
1003.0	Air	2.784
97.5	N_2	2.925
299.0	N_2	2.908
399.4	N_2	2.890
499.9	N_2	2.857
550.1	N_2	2.838
600.4	N_2	2.816
650.8	N_2	2.794
701.0	N_2	2.776
751.3	N_2	2.755
801.6	N_2	2.734
851.9	N_2	2.716
902.2	N_2	2.699
952.6	N_2	2.682
1003.0	N_2	2.666

APPENDIX II

RAW DATA OF HIGH-TEMPERATURE X-RAY DIFFRACTION

Table II-1 – II-2 show raw data of high-temperature x-ray diffraction for $La_{0.5}Sr_{0.5}Fe_{0.5}Co_{0.5}O_{3-\delta}$ and $La_{0.5}Sr_{0.5}CoO_{3-\delta}$ as a function of temperature in different atmospheres.

Table II-1: Cubic cell parameter as a function of temperature in different atmospheres for $La_{0.5}Sr_{0.5}Fe_{0.5}Co_{0.5}O_{3-\delta}$. The obtained cell parameter for Pt is also reported.

Temperature [°C]	Atm	a [Å]	a Pt [Å]
31	Air	3.849	3.924
200	Air	3.859	3.930
300	Air	3.865	3.933
400	Air	3.872	3.937
500	Air	3.879	3.940
600	Air	3.887	3.944
700	Air	3.897	3.948
800	Air	3.909	3.953
900	Air	3.921	3.957
1000	Air	3.935	3.962
31	N_2	3.849	3.924
200	N_2	3.861	3.930
300	N_2	3.868	3.933
400	N_2	3.874	3.937
500	N_2	3.885	3.941
600	N_2	3.898	3.945
700	N_2	3.912	3.949
800	N_2	3.926	3.953
900	N_2	3.939	3.957
1000	N_2	3.952	3.959

Table II-2: Cubic cell parameter as a function of temperature in different atmospheres for $La_{0.5}Sr_{0.5}CoO_{3-\delta}$. The obtained cell parameter for Pt is also reported.

Temperature [°C]	Atm	a [Å]	a Pt [Å]
30	Air	3.832	3.922
200	Air	3.842	3.929
301	Air	3.848	3.932
401	Air	3.855	3.936
501	Air	3.863	3.940
600	Air	3.872	3.944
700	Air	3.882	3.948
799	Air	3.892	3.953
901	Air	3.904	3.957
1000	Air	3.918	3.962
31	N_2	3.832	3.924
200	N_2	3.843	3.931
299	N_2	3.850	3.934
401	N_2	3.858	3.938
501	N_2	3.869	3.942
600	N_2	3.880	3.946
700	N_2	3.894	3.950
801	N_2	3.908	3.954
900	N_2	3.920	3.956

APPENDIX III

CREEP RELAXATION

Stress relaxation curves were obtained for both $La_{0.5}Sr_{0.5}Fe_{0.5}Co_{0.5}O_{3-\delta}$ and $La_{0.5}Sr_{0.5}CoO_{3-\delta}$ cylinders at 900°C in N_2 atmosphere. Two relaxations of each composition were measured. Figure III-1 shows an example of one of the stress relaxations where the stress is normalized by dividing the measured stress by the initial stress. Such a stress relaxation can then be fitted to the following equation

$$\frac{\sigma}{\sigma_0} = c_1 \cdot e^{-t/t_1} + c_2 \cdot e^{-t/t_2} + c_3 \cdot e^{-t/t_3} \ldots \qquad \text{(III-1)}$$

where σ_0 is the initial stress, t is the time, t_1, t_2, t_3... are time constants with a decade in difference and c_1, c_2, c_3... are constants ($c_1 + c_2 + c_3 \ldots = 1$).

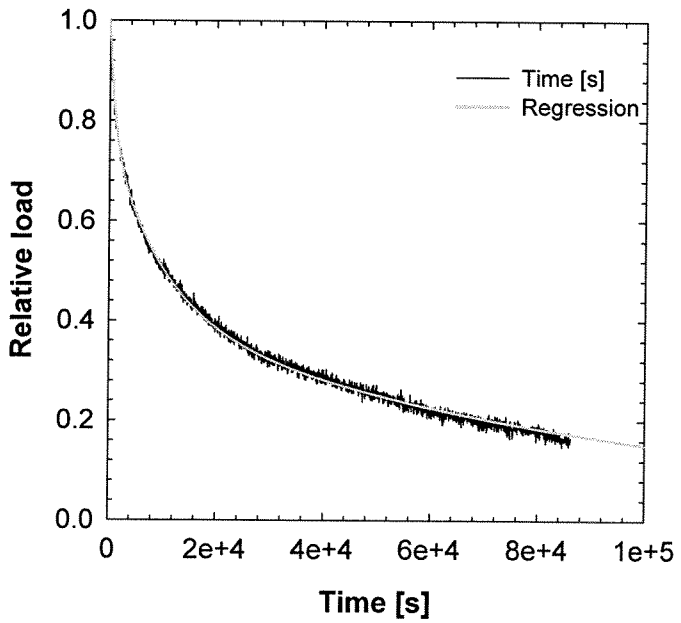

Figure III-1 Stress relaxation curve for $La_{0.5}Sr_{0.5}CoO_{3-\delta}$ at 900°C in N_2. The load is normalized by dividing the measured load by the initial load (25 MPa).

By setting the time constants, the curve can be refined to equation (2) by fitting the constants. Figure III-1 shows the obtained curve for this stress relaxation. Table III-1 gives the obtained values for the different stress relaxations. The constants t_1, t_2 and t_3 is set to $1 \cdot 10^{-3}$, $1 \cdot 10^{-4}$ and $1 \cdot 10^{-5}$ respectively.

Table III-1 Time constants for $La_{0.5}Sr_{0.5}Fe_{1-x}Co_xO_{3-\delta}$ for different relaxations at 900°C in N_2 atmosphere.

Composition x	c_1	c_2	c_3
0.5	0.3747	0.1258	0.4995
0.5	0.3720	0.1135	0.5145
1	0.2201	0.3700	0.4098
1	0.4169	0.2797	0.3034

APPENDIX IV

HIGH TEMPERATURE MECHANICAL TESTING RIG

A schematic of the setup for measurement of Young's modulus, bending strength and fracture toughness is shown in Figure IV-1.

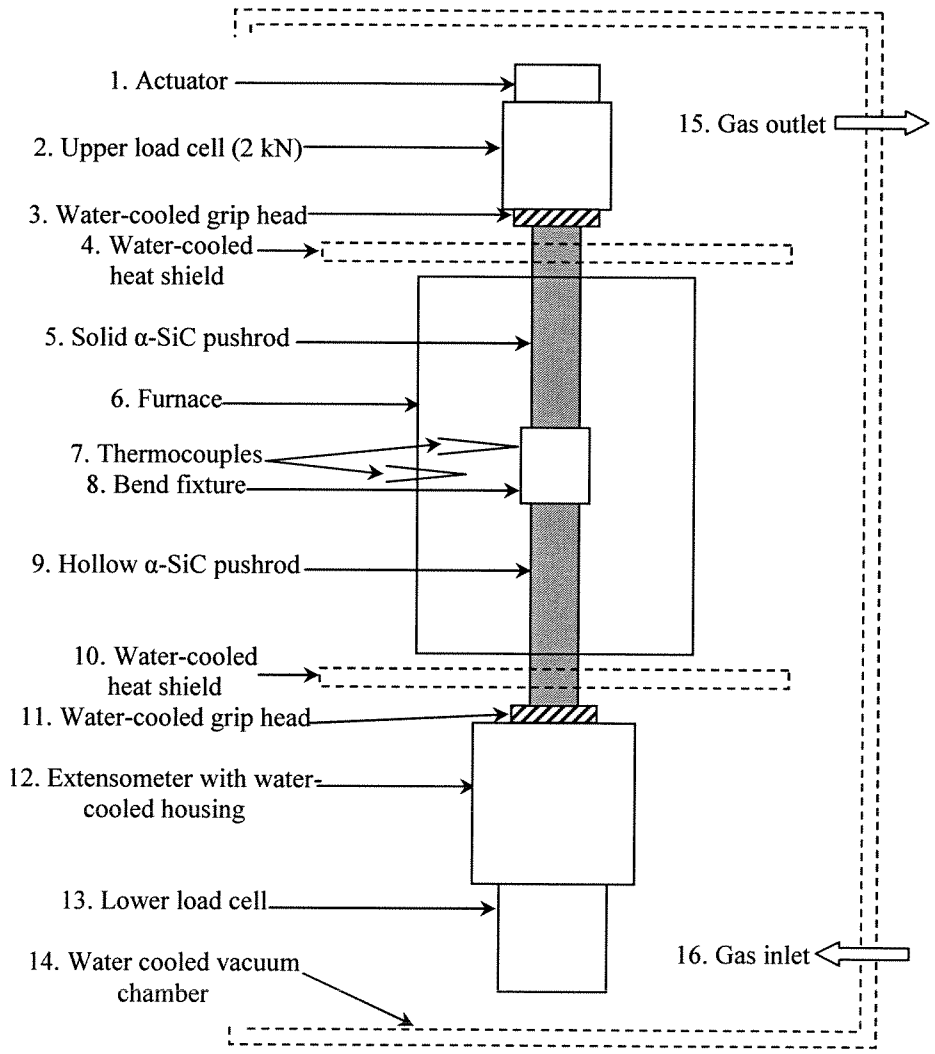

Figure IV-1: Schematic representation of the setup used for measurement of Young's modulus, bending strength and fracture toughness

The setup consisted of one fully dense (upper) and one hollow (lower) high-purity α-SiC pushrod attached to water-cooled grips in an electromechanical test machine (Cormet) with a 20 kN uniaxial actuator (Cormet digital control), a Cormet 20 kN or HBM 1 kN load cell (lower) and a 2 kN HBM load cell (upper), the latter used for data recording. Loading was controlled by the Cormet SSRT software. The load signal from the 2 kN load cell was amplified in HBM amplifiers and was recorded by a FLUKE logging system. The sample was mounted in a MTS high-temperature bend fixture (642.85, Figure IV-2), constructed of α-SiC and designed to comply with ASTM Standard C1211-92 for high-temperature bend testing. The fixture was fully articulating to minimize high contact stresses, its rollers designed to both roll and pivot to ensure a line contact on the specimen.

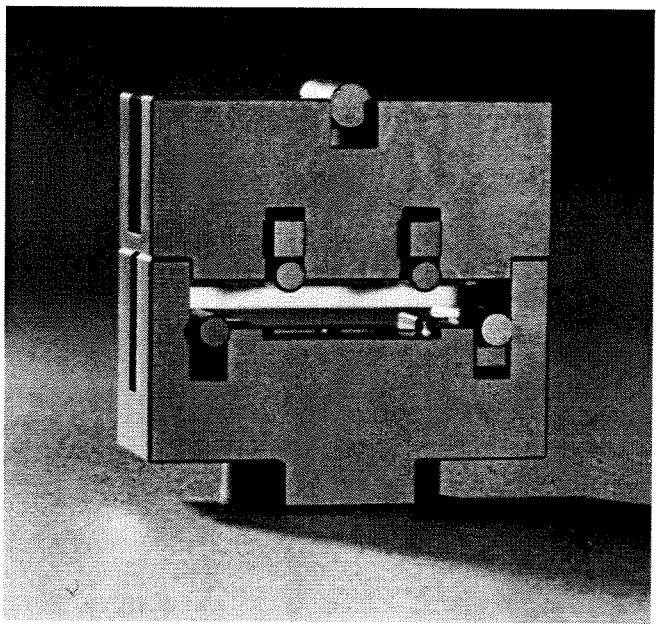

Figure IV-2 MTS Model 642.85 High Temperature Bend Fixture

Specimen deflection during loading was measured during bending strength tests with a MTS bend bar extensometer (632.70-03) with a strain gauge based deflectometer and three measurement rods (MTS 602.81) which extend from the extensometer up to the test specimen. The two outer rods were spaced to correspond with the location of the upper two rollers of the bend fixture (Figure IV-3). All three rods contacted the specimen. During the test, the extensometer measured the deflection of the center rod with respect to the outer rods.

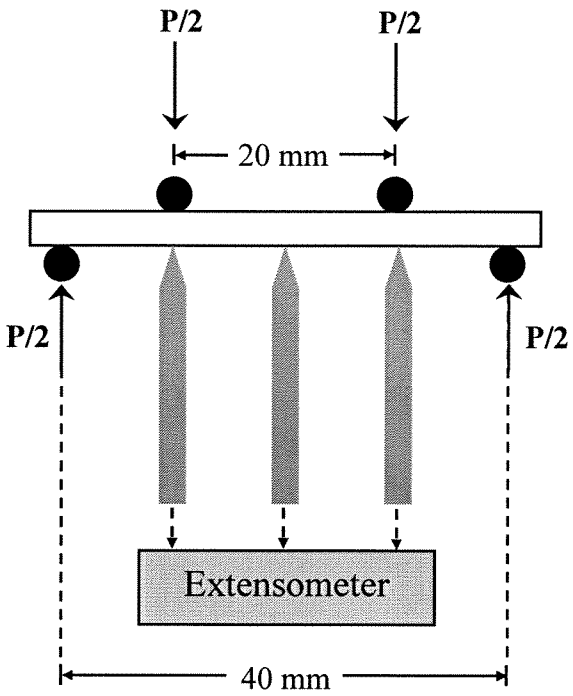

Figure IV-3 Schematic representation of sample configuration prior to a bending strength measurement. P is the applied load

The mechanical testing rig was fitted with a split single phase Kanthal A heating element (SIGMATEST Materialprüftechnik GmbH, 200 mm vertical hot zone) and Ni radiation shields. The front half of the furnace was mounted at the door to allow specimen access. The temperature in the furnace was controlled through a thermocouple mounted close to the sample, using a Eurotherm 2408 controller (Eurotherm Controls Ltd.) A second thermocouple (type S) was mounted near the heating element and was connected to a high-temperature alarm on the temperature controller in order to avoid overheating of the element. The furnace could be used up to 800°C in air, vacuum and inert gas.

The entire setup was mounted inside a water-cooled vacuum chamber (approx. 400 x 300 x 600 mm) connected to a rotary pump and a gas supply system.

The load frame was designed and built at SINTEF. It is overdimensioned with respect to the maximum load of 20 kN, providing a good stiffness of the frame. This is especially important in testing of brittle materials.

A photograph of the entire system is shown in Figure IV-4.

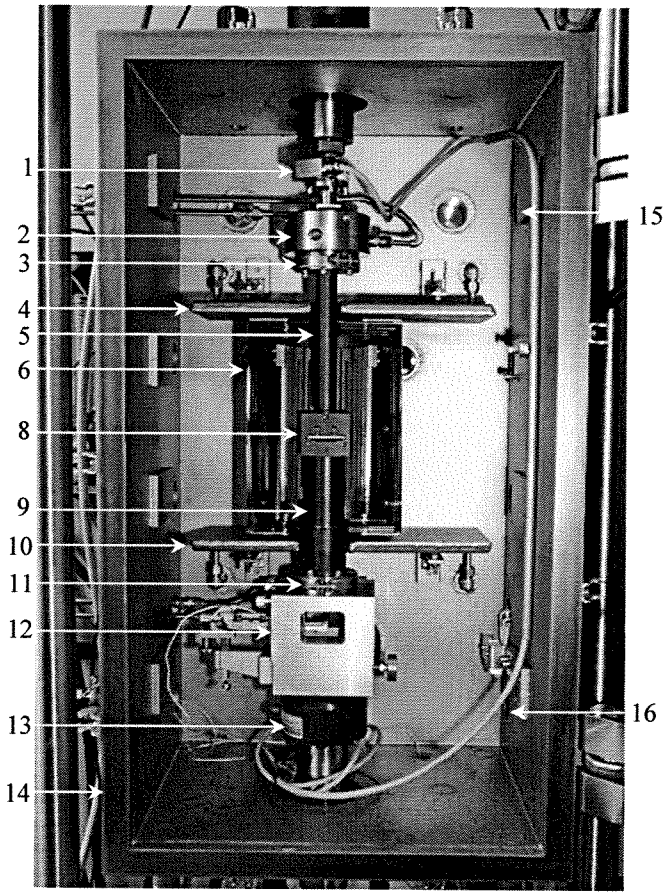

Figure IV-4 Room temperature setup of the mechanical testing rig used to measure bending strength and fracture toughness. The high-temperature setup is identical, with the exception of installation of two thermocouples. The numbers correspond to those defined in Figure IV-1

APPENDIX V

MEASUREMENT OF MECHANICAL PROPERTIES

Bending strength

The bending strength, σ_f, was calculated from four-point bend testing. Sample bars were machined to MIL SPEC 1942 and dimensions 4 x 3 x ca. 45 mm^3 (*b* x *h* x *l*) by Chand Associates, MA, USA or by Kadco Ceramics, PA, USA. All the edges were chamfered. The bending strength was calculated using equation (V-1).[1]

$$\sigma_f = \frac{3 \cdot P_f \cdot a}{b \cdot h^2} \qquad \text{(V-1)}$$

where a is given as

$$a = \frac{S_1 - S_2}{2} \qquad \text{(V-2)}$$

and P_f is the maximum load at fracture [N], b is width [m], h is height [m], S_1 is the support roller span (40 mm) and S_2 is the load roller span (20 mm).

A total of up to 11 specimens were tested at each temperature. A preload of ~0.5 N was applied to the specimens tested at room temperature, whereas the specimens tested at elevated temperatures were preloaded with ~20 N prior to testing. The preload of the high temperature samples was maintained by using load control of the rig during heating. Position control, with a crosshead rate of 8 μm/s, was used during the bending strength measurements.

Young's modulus

Young's modulus was calculated from a plot of the load (P) versus the deflection of the bar (δ_c) during four-point bend testing. Here, the deflection of the center extensometer rod with respect to the outer rods (see Appendix IV) is taken as the deflection of the bar.[2]

$$\delta_c = \frac{Pl^3}{8 \cdot EJ} \cdot \frac{a}{l}\left(1 - \frac{4a^2}{3l^2}\right) - \frac{Pl^3}{2 \cdot EJ} \cdot \frac{a^2}{l^2}\left(1 - \frac{4a}{3l}\right) \quad \text{(V-3)}$$

where

$$J = \frac{bh^3}{12} \quad \text{(V-4)}$$

Rearranging equation (II-3), inserting J and substituting $P(\delta_c)/\delta_c$ with the slope of the curve of load versus deflection (S [N/m]) found by regression analysis, gives the expression for the E-modulus:

$$E = \frac{12}{bh^3} \cdot \frac{a}{4}\left(\frac{l^2}{4} - la + a^2\right) \cdot S \quad \text{(V-5)}$$

A total of up to 11 specimens were tested for each composition.

Fracture toughness

The fracture toughness was measured using the single edge notched beam method (SENB) or single edge V-notched beam method (SEVNB). Sample bars were machined to MIL SPEC 1942 and dimensions 3 x 4 x ca. 45 mm^3 (b x h x l) by Chand Associates, MA, USA or by Kadco Ceramics, PA, USA. Note the differing definitions of width (b) and height (h) between bending strength measurements and fracture toughness measurements. The depth of the notches was 0.75-0.80 ± 0.03 or 1.14-1.18 ± 0.02 mm and the width 0.21-0.24 ± 0.01 mm. The fracture toughness was calculated using equation (II-6)[3, 4]

$$K_{IC} = \frac{P_f(S_1 - S_2)}{b \cdot h^{3/2}} \cdot \left(\frac{3}{2} \frac{\alpha^{1/2}}{(1-\alpha)^{3/2}} \cdot F(\alpha)\right) \quad \text{(V-6)}$$

where

$$F(\alpha) = 1.9887 - 1.326 \cdot \alpha - \frac{(3.49 - 0.68 \cdot \alpha + 1.35 \cdot \alpha^2) \cdot \alpha \cdot (1-\alpha)}{(1+\alpha)^2} \quad \text{(V-7)}$$

and

$$\alpha = \frac{c}{h} \tag{V-8}$$

where c is the length of the notch [m].

A crosshead rate of 1 μm/s was used. A total of 3-4 specimens were tested at each temperature.

References

1. J. B. Wachtman, "Mechanical properties of ceramics", John Wiley & Sons, Inc., New York (1996).
2. F. Sass, C. Bouché and A. Leitner, "Dubbels Taschenbuch für den Maschinenbau", Springer-Verlag, Berlin (1961).
3. ISO/CD 15732, "Fine ceramics (Advanced ceramics, Advanced technical ceramics) - Test method for fracture toughness at room temperature by single edge precracked beam (SEPB) method", International Organization for Standardization, Geneva, Switzerland.
4. ASTM STP 1409 Fracture Resistance Testing of Monolithic and Composite Brittle Materials, J. Kübler, "Fracture Toughness of Ceramics using the SEVNB Method: From a Preliminary Study to a Standard Test method", 93-106.

APPENDIX VI

FRACTURE ORIGINS FROM FOUR-POINT BENDING

Figure VI-1 shows selected fracture origins from $La_{0.5}Sr_{0.5}Fe_{0.5}Co_{0.5}O_{3-\delta}$ and $La_{0.5}Sr_{0.5}CoO_{3-\delta}$ bars obtained from four-point bending.

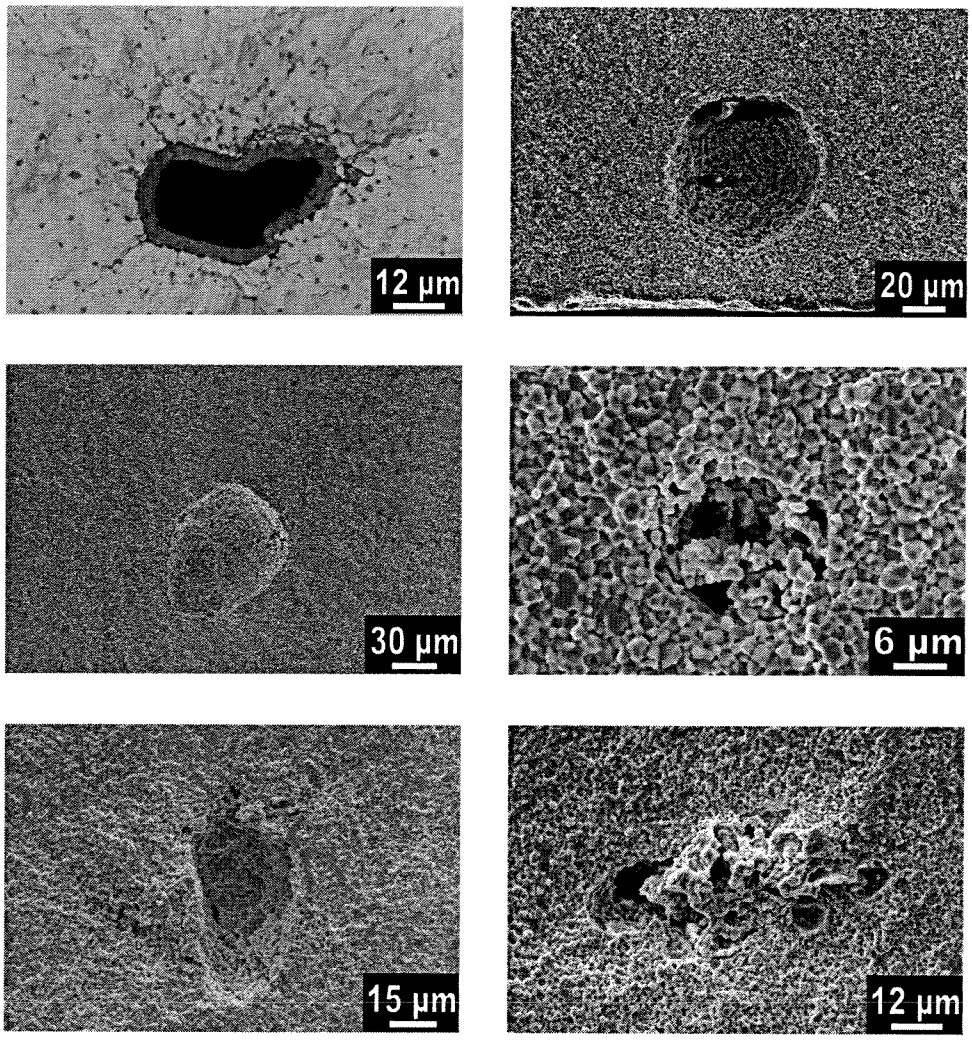

Figure VI-1: Selected images of fracture origins of $La_{0.5}Sr_{0.5}Fe_{0.5}Co_{0.5}O_{3-\delta}$ and $La_{0.5}Sr_{0.5}CoO_{3-\delta}$ bars.

APPENDIX VII

RAW DATA OF OXYGEN FLUX MEASUREMENTS

Table VII-1 – VII-5 show raw data of oxygen flux measurements of $La_{0.5}Sr_{0.5}FeO_{3-\delta}$ $La_{0.5}Sr_{0.5}Fe_{0.5}Co_{0.5}O_{3-\delta}$ and $La_{0.5}Sr_{0.5}CoO_{3-\delta}$ membranes at different pO_2 on secondary side and at different temperatures.

Table VII-1: Oxygen flux for LSFC3 ($La_{0.5}Sr_{0.5}Fe_{0.5}Co_{0.5}O_{3-\delta}$) membrane for different pO_2 on secondary side and different temperatures.

Temperature [°C]	log pO_2	Oxygen flux [ml/min·cm^2]	Standard deviation
1147	-2.40	1.60	0.10
1147	-1.67	2.14	0.11
1147	-1.39	1.31	0.20
1147	-1.98	1.92	0.16
1147	-2.16	1.74	0.07
1147	-2.45	1.39	0.08
1147	-1.30	1.20	0.16
1147	-2.32	1.77	0.13
1147	-2.55	1.10	0.08
1103	-2.65	0.82	0.02
1058	-2.72	0.67	0.01
1014	-2.81	0.54	0.02
1058	-2.70	0.67	0.03
1148	-2.50	1.19	0.08
1148	-2.50	1.19	0.08

Table VII-2: Oxygen flux for LSFC4 ($La_{0.5}Sr_{0.5}Fe_{0.5}Co_{0.5}O_{3-\delta}$) membrane for different pO_2 on secondary side and different temperatures.

Temperature [°C]	log pO_2	Oxygen flux [ml/min·cm^2]	Standard deviation
1146	-2.40	1.51	0.17
1146	-4.67	1.32	0.13
1146	-2.19	1.54	0.17
1146	-1.98	1.80	0.31
1146	-1.70	1.72	0.20
1146	-1.40	1.05	0.21
1146	-1.31	0.99	0.18
1146	-1.54	1.44	0.25
1146	-2.56	0.97	0.08
1146	-2.46	1.34	0.05
1146	-2.56	0.97	0.08
1103	-2.68	0.67	0.02
1058	-2.76	0.54	0.01
1014	-2.83	0.41	0.01
1058	-2.80	0.47	0.04
1103	-2.67	0.69	0.03
1147	-2.62	0.85	0.03

Table VII-3: Oxygen flux for LSF5 ($La_{0.5}Sr_{0.5}FeO_{3-\delta}$) membrane for different pO_2 on secondary side and different temperatures.

Temperature [°C]	log pO_2	Oxygen flux [ml/min·cm^2]	Standard deviation
1147	-2.70	0.57	0.04
1147	-2.82	0.51	0.05
1147	-2.80	0.52	0.04
1147	-2.37	0.56	0.03
1147	-2.11	0.57	0.09
1147	-1.76	0.53	0.07
1147	-1.55	0.55	0.09
1147	-1.42	0.34	0.11
1147	-1.31	0.35	0.04
1147	-2.82	0.44	0.06
1147	-2.88	0.35	0.06
1147	-2.89	0.42	0.05
1147	-2.82	0.43	0.06
1103	-2.89	0.33	0.04
1058	-2.96	0.25	0.04
1014	-3.04	0.17	0.03
1058	-2.99	0.22	0.04
1103	-2.93	0.28	0.04
1147	-2.88	0.35	0.06

Table VII-4: Oxygen flux for LSC6 ($La_{0.5}Sr_{0.5}CoO_{3-\delta}$) membrane for different pO_2 on secondary side and different temperatures.

Temperature [°C]	log pO_2	Oxygen flux [ml/min·cm^2]	Standard deviation
1147	-2.25	2.17	0.13
1147	-2.28	2.07	0.12
1147	-2.05	2.44	0.16
1147	-1.88	2.69	0.14
1147	-1.65	2.57	0.24
1147	-1.48	2.06	0.27
1147	-1.38	1.78	0.29
1147	-1.29	1.46	0.21
1147	-2.26	2.14	0.19
1147	-2.14	2.77	0.28
1147	-2.26	2.14	0.19
1103	-2.34	1.78	0.19
1058	-2.42	1.45	0.15
1014	-2.51	1.19	0.13
970	-2.61	0.94	0.09
1014	-2.52	1.15	0.12
1147	-2.23	2.17	0.17

Table VII-5: Oxygen flux for LSFC7 ($La_{0.5}Sr_{0.5}Fe_{0.5}Co_{0.5}O_{3-\delta}$) membrane for different pO_2 on secondary side and different temperatures.

Temperature [°C]	log pO_2	Oxygen flux [ml/min·cm^2]	Standard deviation
1149	-2.19	2.11	0.16
1149	-2.27	1.90	0.22
1149	-2.28	1.91	0.19
1149	-2.04	2.14	0.12
1149	-1.86	2.25	0.19
1149	-1.63	1.89	0.20
1149	-1.46	1.72	0.09
1149	-1.36	1.32	0.05
1149	-2.31	1.72	0.19
1149	-2.32	1.77	0.13
1149	-2.31	1.88	0.19
1104	-2.37	1.58	0.17
1060	-2.44	1.29	0.14
1149	-2.32	1.77	0.09